



Max-Planck-Institut für Metallforschung
Stuttgart

Mechanical Properties of Ultra Thin Metallic Films Revealed by Synchrotron Techniques

Patric Alfons Gruber

Dissertation
an der
Universität Stuttgart

Bericht Nr. 200
Juli 2007

Mechanical Properties of Ultra Thin Metallic Films Revealed by Synchrotron Techniques

Von der Fakultät Chemie der Universität Stuttgart
zur Erlangung der Würde eines Doktors der
Naturwissenschaften (Dr. rer. nat.) genehmigte Abhandlung

Vorgelegt von
Dipl.-Ing. Patric Alfons Gruber
aus Salzburg, Österreich

Hauptberichter: Prof. Dr. phil. Eduard Arzt
Mitberichter: Prof. Dr. rer. nat. Ralph Spolenak
Tag der mündlichen Prüfung: 20.07.2007

Institut für Metallkunde der Universität Stuttgart
und
Max-Planck-Institut für Metallforschung Stuttgart

Stuttgart, Juli 2007

Patric Alfons Gruber

Mechanical Properties of Ultra Thin Metallic Films Revealed by Synchrotron Techniques

176 pages, 65 figures, 13 tables

Abstract

A prerequisite for the study of the scaling behavior of mechanical properties of ultra thin films is a suitable testing technique. Therefore synchrotron-based *in situ* testing techniques were developed and optimized in order to characterize the stress evolution in ultra thin metallic films on compliant polymer substrates during isothermal tensile tests. Experimental procedures for polycrystalline as well as single crystalline films were established. These techniques were used to systematically investigate the influence of microstructure, film thickness (20 to 1000 nm) and temperature (-150 to 200°C) on the mechanical properties. Passivated and unpassivated Au and Cu films as well as single crystalline Au films on polyimide substrates were tested. Special care was also dedicated to the microstructural characterization of the samples which was very important for the correct interpretation of the results of the mechanical tests.

Down to a film thickness of about 100 to 200 nm the yield strength increased for all film systems (passivated and unpassivated) and microstructures (polycrystalline and single-crystalline). The influence of different interfaces was smaller than expected. This could be explained by a dislocation source model based on the nucleation of perfect dislocations. For polycrystalline films the film thickness as well as the grain size distribution had to be considered.

For smaller film thicknesses the increase in flow stress was weaker and the deformation behavior changed because the nucleation of perfect dislocations became unfavorable. Instead, the film materials used alternative mechanisms to relieve the high stresses. For regular and homogeneous deformation the total strain was accommodated by the nucleation and motion of partial dislocations. If the deformation was localized due to initial cracks in a brittle interlayer or local delamination, dislocation plasticity was not effective enough to relieve the stress concentration and the films showed brittle fracture. In addition, thermally activated deformation mechanisms were enhanced leading to a strong temperature dependence of the mechanical properties. Based on the experimental results the thickness dependence of the deformation mechanisms, fracture toughness and activation energies could be determined.

Patric Alfons Gruber

Mechanische Eigenschaften von ultradünnen metallischen Schichten ermittelt mit Synchrotronmethoden

176 Seiten, 65 Abbildungen, 13 Tabellen

Kurzzusammenfassung

Eine Grundvoraussetzung, um das Skalierungsverhalten der mechanischen Eigenschaften von ultradünnen Schichten untersuchen zu können, ist eine geeignete Testmethode zur Verfügung zu haben. Deshalb wurden synchrotron-basierte *in situ* Testmethoden entwickelt und optimiert, um die Spannungsentwicklung während isothermer Zugversuche in ultradünnen Metallschichten auf verformbaren Polymersubstraten messen zu können. Dabei wurden sowohl polykristalline als auch einkristalline Schichten berücksichtigt. Diese Methoden wurden eingesetzt, um systematisch den Einfluss von Mikrostruktur, Schichtdicke (20 bis 1000 nm) und Temperatur (-150 bis 200°C) auf die mechanischen Eigenschaften zu untersuchen. Getestet wurden passivierte und unpassivierte Gold- und Kupferschichten sowie einkristalline Goldschichten. Besondere Aufmerksamkeit wurde der Charakterisierung der Mikrostruktur der Proben geschenkt, da diese für die korrekte Interpretation der Testergebnisse sehr wichtig war.

Bis zu einer Schichtdicke von ungefähr 100 bis 200 nm nahm die Fließgrenze für alle Schichtsysteme (passiviert und unpassiviert) und Mikrostrukturen (polykristallin und einkristallin) zu. Der Einfluss der verschiedenen Grenzflächen war jedoch kleiner als erwartet. Dies konnte mit Hilfe eines Versetzungsquellenmodells erklärt werden, welches auf der Nukleierung von vollständigen Versetzungen basiert. Für polykristalline Schichten musste sowohl die Schichtdicke als auch die Korngrößenverteilung berücksichtigt werden.

Für kleinere Schichtdicken wurde der Anstieg der Fließgrenze schwächer und das Verformungsverhalten änderte sich, da die Nukleation von vollständigen Versetzungen zunehmend schwieriger wird. Stattdessen nutzten die Schichtmaterialien andere Verformungsmechanismen, um die hohen Spannungen abzubauen. Eine homogene Verformung wurde durch die Nukleierung und Bewegung von Partialversetzungen erreicht. Wenn die Verformung durch einen Riss in einer spröden Zwischenschicht oder durch eine lokale Ablösung lokalisiert wurde, reichte die Versetzungsplastizität nicht aus, um die Spannungskonzentration abzubauen und die Filme brachen spröde. Außerdem wurden thermisch aktivierte Verformungsmechanismen beschleunigt, was zu einer starken Temperaturabhängigkeit der mechanischen Eigenschaften führte. Basierend auf den experimentellen Ergebnissen konnte die Schichtdickenabhängigkeit der Verformungsmechanismen, der Bruchzähigkeit und der Aktivierungsenergien bestimmt werden.

Danksagung

Die vorliegende Arbeit wurde in der Zeit von April 2002 bis Juni 2007 am Institut für Metallkunde der Universität Stuttgart und am Max-Planck-Institut für Metallforschung in Stuttgart angefertigt.

Herrn Prof. Dr. Eduard Arzt gilt mein besonderer Dank, für die Möglichkeit unter seiner Anleitung zu promovieren, für die Übernahme des Hauptberichts, sowie für die stete Unterstützung und das große Interesse an meiner Arbeit.

Bei Prof. Dr. Ralph Spolenak möchte ich mich ganz herzlich für die Übernahme des Mitberichts sowie für die vielen fruchtbaren Diskussionen, die unerschöpfliche Geduld und die wertvollen Ratschläge, die zum Gelingen dieser Arbeit maßgeblich beigetragen haben, bedanken. Ich hätte mir keinen besseren Betreuer vorstellen können.

Bedanken möchte ich mich auch bei Prof. Dr. Alexander Wanner und Dr. Jochen Böhm für die exzellente Zusammenarbeit beim Aufbau und der Entwicklung der Messmethodik.

Den Herren Ralf Weigel, Dr. Nikolai Kasper und Dr. Andreas Stierle möchte ich für die Bereitstellung der Strahlzeit und die hervorragende Betreuung an der MPI-MF-Beamline bei ANKA danken.

Vielen Dank an Gerhard Adam, Ilse Lakemeyer, Frank Thiele, Dr. Gunther Richter und Dr. Thomas Wagner für die Herstellung der verschiedenen Schichtsysteme.

Sven Olliges sowie Prof. Dr. Heinz Dieter Carstanjen und seinem Team am Pelletron möchte ich für die Messung aller Schichtdicken danken. Sven Olliges hat mich außerdem bei mehreren Strahlzeiten tatkräftig unterstützt. Für seinen unermüdlichen Einsatz möchte ich ihm herzlich danken.

Ich möchte mich auch bei Dr. Christian Solenthaler und Fabian Amstad für die Durchführung der TEM-Untersuchungen an einkristallinen Goldschichten und die hervorragende Zusammenarbeit auf diesem Gebiet bedanken. Es ist immer wieder eine Freude die TEM-Bilder anzusehen.

Mein Dank gilt weiterhin denen, die mich bei der Vor- und Nachbereitung der Messungen am Synchrotron und der Probencharakterisierung in vielfältiger Weise unterstützt haben: Sabine Haag, Birgit Heiland, Hanling Li, Marc Nikolussi, Felix Onuseit, Dr. Steffen Orso, Dr. Gunther Richter, Natascha Sauer, Dr. Linda Sauter, Petra Sonnweber-Ribic sowie Frank Thiele.

Meinen Kommilitonen Petra Sonnweber-Ribic, Steffen Orso und Holger Pfaff möchte ich für die freundschaftliche Unterstützung während der ganzen Zeit danken.

Ich möchte mich bei allen Kolleginnen und Kollegen der Abteilung Arzt für das angenehme Arbeitsklima bedanken.

Nicht zuletzt möchte ich mich bei meiner Frau Simone und bei meinen Eltern für Ihre Unterstützung und Ihr Vertrauen in mich und meine Arbeit bedanken.

Table of contents

1	Introduction	15
2	Literature review and motivation	17
2.1	Technological importance of thin film mechanics	17
2.2	Size effects in thin film plasticity	20
2.3	Cracking of thin films on substrates	25
2.4	Mechanical testing of thin films and small structures	28
2.5	Summary of literature review and aims of this study	35
3	Novel synchrotron-based technique for tensile testing of ultra thin polycrystalline films	38
4	Yield strength and strain hardening of ultra thin Cu films with and without passivation	43
4.1	Introduction	43
4.2	Experimental	45
4.2.1	Sample preparation	45
4.2.2	Microstructural characterization	46
4.2.3	Mechanical testing	47
4.3	Results	49
4.3.1	Microstructure	49
4.3.2	Stress-strain curves	54
4.3.3	Apparent and plane-strain moduli	59
4.3.4	Yield strength	60
4.3.5	Strain hardening	61
4.4	Discussion	62
4.4.1	Low stiffness of Cu films	62
4.4.2	Quantitative evaluation of yield stress data	64
4.4.3	Scaling behavior of yield strength and strain hardening	65
4.5	Summary and conclusion	73
5	Brittle-to-ductile transition in ultra thin Ta/Cu film systems	75
5.1	Introduction	75
5.2	Experimental	77

5.2.1	Sample preparation	77
5.2.2	Mechanical testing	78
5.3	Results	78
5.3.1	Stress-strain curves	79
5.3.2	Fractography	80
5.4	Discussion	84
5.4.1	Statistical approach	84
5.4.2	Energetic approach	88
5.4.3	Linear elastic fracture mechanics	91
5.4.4	Substrate compliance and deformation	94
5.4.5	Strain localization and delamination	96
5.4.6	Plastic deformation and geometrical constraint	97
5.5	Summary and conclusion	100
6	Temperature dependence of mechanical properties in passivated and unpassivated ultra thin Au films	101
6.1	Introduction	101
6.2	Experimental	102
6.2.1	Sample preparation and characterization	102
6.2.2	Tensile testing	103
6.3	Results	106
6.3.1	Microstructure	106
6.3.2	Stress-strain curves and yield strength	107
6.4	Discussion	114
6.4.1	Low and high temperature fracture	114
6.4.2	Thermally activated dislocation glide	115
6.4.3	Role of diffusional creep	119
6.5	Summary and conclusion	123
7	Mechanical properties of ultra thin single crystalline Au films measured by a new synchrotron technique	125
7.1	Introduction	125
7.2	Experimental	127
7.2.1	Sample preparation	127
7.2.2	Mechanical testing	129
7.2.3	TEM investigations	130

7.3	Results	131
7.3.1	Stress-strain curves	131
7.3.2	Yield strength	133
7.3.3	Average peak width	133
7.3.4	Microstructure and defects	134
7.4	Discussion	138
7.4.1	Influence of porosity	138
7.4.2	Deformation mechanisms	141
7.4.3	Scaling behavior of yield strength	143
7.5	Summary and conclusion	147
8	Summary: Novel aspects in the mechanical properties of ultra thin metallic films	148
9	Appendix	152
9.1	Elastic constants for <111> fiber textured Au and Cu	152
9.2	Exemplary AutoIt Macro for the control of a tensile test	154
10	Deutsche Zusammenfassung	157
11	References	164

List of symbols and abbreviations

$2a$	Width of membrane [m]
a	Crack length [m]
A	Area [m ²]
A_{crack}	Crack area [m ²]
b	Magnitude of the Burgers vector [m]
b_N	Magnitude of the Burgers vector for a perfect dislocation [m]
b_p	Magnitude of the Burgers vector for a partial dislocation [m]
c	Numerical constant
C_{ij}	Stiffness coefficients in crystal coordinates [Pa]
C'_{ij}	Stiffness coefficients in sample coordinates [Pa]
d	Grain size [m]
d_{50}	Median grain size [m]
d_{max}	Maximum grain size [m]
d_{mean}	Mean grain size [m]
d_ψ	Lattice spacing at inclination angle ψ [m]
G	Energy release rate [J/m ²]
$g(\alpha, \beta)$	Dimensionless integral of crack opening displacement
h	Film thickness [m]
H	Membrane deflection [m]
k	Boltzmann's constant [$1.381 \cdot 10^{-23}$ J/K]
K_{IC}	Fracture toughness [Pam ^{1/2}]
L	Crack distance [m]
l	Reference length for stress relaxation transverse to the crack [m]
m	Nonlinearity factor for strain transfer at the film/substrate interface
N	Number of obstacles
n	Power-law exponent
p	Pressure [Pa]
P	Porosity [%]
r_{pl}	Radius of plane-strain plastic zone [m]
s	Schmid factor

s_d	Size of dislocation source [m]
S_{ij}	Compliance coefficients in crystal coordinates [Pa^{-1}]
S'_{ij}	Compliance coefficients in sample coordinates [Pa^{-1}]
T	Temperature [K]
U	Strain energy per volume [J/m^3]
V	Volume [m^3]
w	Sample width [m]
W	Elastic energy [J]
Z	Numerical constant
ΔF	Activation energy [eV]
E	Young's modulus [Pa]
E^*	Plane-strain modulus [Pa]
\bar{E}	Effective modulus of the film/substrate composite [Pa]
Ω	Atomic volume [m^3]
α	Numerical constant
α	Weibull exponent (chapter 5)
α_i	Thermal expansion coefficient of the material i [K^{-1}]
β	Weibull scale factor for film strength [Pa] (chapter 5)
β, β_i	Numerical constants ($i = 1, 2, 3$)
δ	Crack opening displacement [m]
δD_{gb}	Grain boundary width times grain boundary diffusivity [m^3/s]
ε	Strain
$\dot{\varepsilon}$	Strain rate [s^{-1}]
ϕ	Angle between normal vectors of the sample and the glide plane [$^\circ$]
γ	Stacking fault energy [J/m^2]
φ	In-plane azimuthal angle [$^\circ$]
κ_i	Power-law exponents ($i = 1, 2$)
λ	Angle between normal vector of the sample and the Burgers vector [$^\circ$]
μ	Shear modulus [Pa]
ν	Poisson's ratio
θ	Bragg angle [$^\circ$]
ρ	Dislocation or twin density [m^{-2}]

List of symbols and abbreviations

σ	Stress [Pa]
σ_{dev}	Standard deviation of mean grain size [m]
σ_{fr}	Fracture stress [Pa]
σ_y	Flow stress [MPa]
τ	Shear stress [Pa]
ψ	Out-of-plane inclination angle [°]
AFM	Atomic Force Microscopy
ANKA	Angströmquelle Karlsruhe
APW	Average Peak Width
CCD	Charge Coupled Device
DC	Direct Current
EBSD	Electron Backscatter Diffraction
FEM	Finite Element Method
FIB	Focused Ion Beam
FWHM	Full Width at Half Maximum
MEA	Microelectrode Array
MEMS	Micro Electro-Mechanical System
MPI-MF	Max-Planck-Institute for Metals Research
RBS	Rutherford Backscattering
RF	Radio Frequency
RMS	Root Mean Square
SEM	Scanning Electron Microscopy
TEM	Transmission Electron Microscopy
UHV	Ultra-High-Vacuum
XRD	X-ray Diffraction

1 Introduction

During the last decades technological progress has been driven predominantly by the modern information and communication technology. The steadily increasing data output and functionality of devices has required an ongoing miniaturization of their structural elements. In the design and manufacturing of actual microelectronic and microelectromechanical systems/MEMS thin metallic films play an important role. Beside the optical, magnetic or electronic properties, which determine the performance of a device, the knowledge of the mechanical properties of thin films is crucial in order to ensure the reliability and functionality of the device during its lifetime.

Like many other properties, the mechanical properties begin to deviate from that of bulk materials when characteristic dimensions become small. Such deviations may occur when either microstructural features or object dimensions approach length scales of defects, defect interactions or deformation mechanisms. Unlike other physical properties, which deviate from continuum models only close to atomistic dimensions, mechanical properties change at surprisingly large length scales, often in the micrometer regime. For thin films this is especially important since films with thicknesses down to several tens of nanometers are widely used. Such thin films sustain very high stresses which can be several times higher than the flow stress of the corresponding bulk material. This has been attributed to constraints on dislocation motion or diffusion imposed by the interfaces with the surrounding layers and to the smaller grain size that is often found in thin films.

The combination of the tremendous technological driving force and wealth of unfamiliar behavior has led to much interest and work in this area. However progress has been slow. This is mostly due to experimental difficulties in measuring the mechanical properties of thin films. Restricted volumes and geometries as well as very small displacements and forces that have to be controlled preclude classical experimental techniques. Many efforts have gone into developing new testing techniques that allow to measure small samples, films and patterned structures by a variety of means with good strain and stress resolution. Nevertheless, until now the ideal testing technique does not exist and many questions concerning the mechanical properties of ultra thin metallic films are still under debate.

A novel synchrotron-based X-ray diffraction technique has been developed by which it is possible to characterize the evolution of mechanical stress in a polycrystalline metallic film thinner than 40 nm during an isothermal tensile test [Böhm et al. 2004]. The metallic films are deposited on compliant polyimide substrates such that the tensile tests can be performed up to total strains of more than 10% and in a temperature range between 110K and 573K. The unique combination of an isothermal test, very small film thickness, short measuring times and high total strain reveals some new aspects and insight in the mechanical properties of thin films which will be discussed in detail in this thesis.

First, in chapter 2 the literature is critically reviewed concerning the technological relevance of thin films, the current understanding of thin film mechanics and the latest trends in mechanical testing of thin films and small structures. Chapter 2 also outlines the motivation for this study. In chapter 3 the principles of the novel synchrotron-based tensile testing technique will be presented. The results of RT tensile tests on Cu, Ta/Cu and Ta/Cu/Ta thin film systems are reported in chapter 4 and 5. Chapter 4 focuses on the size and interface effect on the yield strength of these film systems while chapter 5 deals with the deformation behavior of the different film systems up to high total strains of about 8%. Here, a size effect in crack formation is observed and discussed with respect to fracture mechanics of thin films on substrates. Up to this point the mechanical behavior has been investigated only at room temperature. In chapter 6 a first series of tensile tests at different temperatures on ultra thin Au films is presented and compared to bulk materials; a much stronger temperature dependence on the mechanical properties is found. The investigation of polycrystalline films suffer from the fact that in most cases film thickness and grain size cannot be varied independently and thus the interpretation of the scaling behavior of the mechanical properties is often difficult. In chapter 7 a novel experimental route for the preparation and testing of single crystalline Au films is presented. In combination with TEM investigations a detailed picture of the deformation mechanisms in single crystalline films is obtained. Finally, chapter 8 summarizes and discusses the variety of results and highlights new aspects in the mechanical properties of ultra thin metallic films.

2 Literature review and motivation

The technological importance and the mechanical behavior of thin films as well as current trends in mechanical testing of thin films and small structures, which motivated this study, are introduced in this chapter. Further details required for the interpretation of the experimental results will be given in the corresponding discussion sections in chapter 4 to 7.

2.1 Technological importance of thin film mechanics

On 23 January 1959, Robert Noyce wrote the following sentence in his lab notebook: "... it would be desirable to make multiple devices on a single piece of silicon, in order to be able to make interconnections between devices as part of the manufacturing process, and thus reduce weight, size, etc. as well as cost per active element." With these words, the co-inventor of the integrated circuit spelled out the *Monolithic Idea* which has shaped the microelectronic revolution [Reid 1984]. Ever since, the technology has advanced by miniaturization and building more and more transistors on a single chip. By necessity the interconnect structure has a complex architecture comprising diverse materials and small feature sizes. Figure 2.1a shows a cross-section of an IBM 64-bit high-performance microprocessor chip. The structure is a three-dimensional network of conductor lines embedded in a dielectric matrix, fabricated on the silicon surface that contains the active devices. The conductor lines lie on several levels and are linked by vias. Lithographically defined feature sizes, such as line width and via size, are as small as 100 nm. Films as thin as a few nanometers are used [ITRS 2003].

Traditional interconnect structures use aluminum for the conductor lines, and silica as the dielectric material. To make devices faster, the conductor must have higher conductivity, and the dielectric must have a lower dielectric constant. Copper has been used as the conductor lines in more recent interconnect structures [Rosenberg et al. 2000]. The conductor lines at different levels are linked with copper vias. Liners such as tantalum lie between the conductor lines and the dielectric to prevent copper diffusion into the dielectric and to promote adhesion. Low dielectric constant materials of current use include organic materials such as SiLK [Martin et al. 2000] or a carbon doped silicon oxide. The former is ductile, and the latter is

brittle. Both are compliant compared to silicon dioxide. To further reduce the dielectric constant, other materials, including porous materials, will be used in future interconnects [Morgen et al. 1999].

The *Monolithic Idea* solves one problem but creates another. Making reliable interconnect structures has been a persistent challenge. Stresses result from material deposition and thermal expansion mismatch between the metallic structures and the semiconductor substrate. Material deposition inevitably generates stress, for example deposition of refractory metals such as tungsten usually generates stresses in the GPa range. Materials in interconnect structures, selected to function as conductors, dielectrics or barriers have dissimilar thermal expansion coefficients. On cooling from the fabrication temperature and during service high stresses are generated in the highly organized structures. These can cause deformation, delamination, cracking and void formation. They may also directly affect device performance.

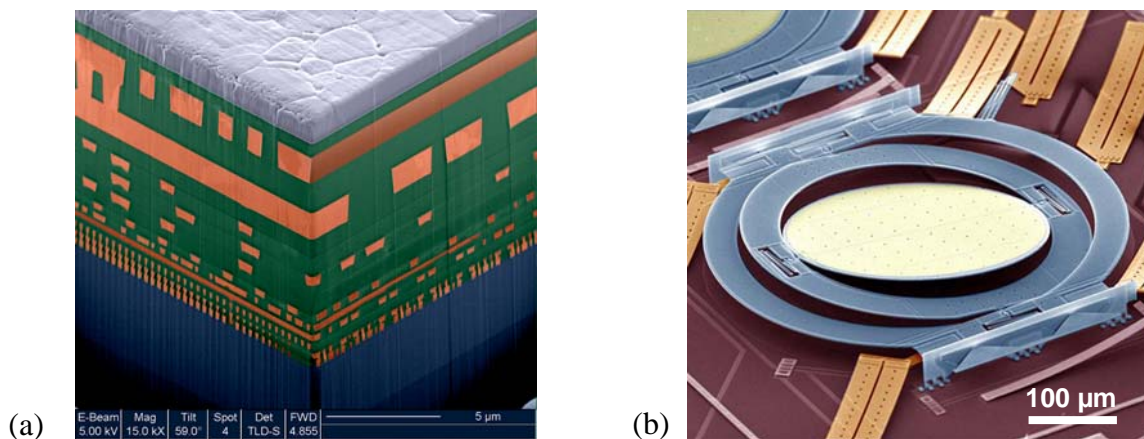


Figure 2.1: (a) Cross-section of 64-bit high-performance microprocessor chip built in IBM's 90 Server-Class CMOS technology with Cu/low-k wiring. The minimum Cu line widths and spaces are $0.12 \mu\text{m}$ [IBM 2005]. (b) Two axis beam steering micro-mirror built using surface micromachining technology [Aksyuk et al. 2002].

Another example out of the domain of microelectromechanical systems/MEMS is shown in figure 2.1b. Here, one can see a surface micromachined mirror used in beam steering optical crossconnects [Aksyuk et al. 2002]. The mechanically movable parts are made out of silicon and are about $1 \mu\text{m}$ thick. The swiveling mirror consists of a silicon plate coated with a very thin Au film ($40 - 80 \text{ nm}$ thick) in order to maximize the reflectivity. Again stresses play an important role, because relaxation of residual stresses in the Au layer can lead to intolerable curvature of the mirror.

So far all examples were based on silicon technology. Flexible electronic circuits on compliant polymeric substrates have recently gained widespread interest for numerous applications. Among these are flexible displays [Chen et al. 2003a, Gelinck et al. 2004], wearable electronics [Post et al. 2000] and flexible microelectrode arrays (MEA) usable for complex in vivo biological applications or retina implants [Meyer 2002, Stett et al. 2003]. Figure 2.2 shows an example for such a flexible display and a flexible MEA. For both applications compliant polyimide substrates are used which are 25 μm and 12 μm thick, respectively, and the conducting material is pure gold. For the active display an additional layer of “electronic ink” [Comiskey et al. 1998] is applied. Similar to the silicon devices high stresses arise during fabrication and service. In addition, due to the high flexibility, devices on compliant substrates have to sustain high strains up to 10%. Here, the question is how far classical and established material systems can be used and how they behave at high strains.

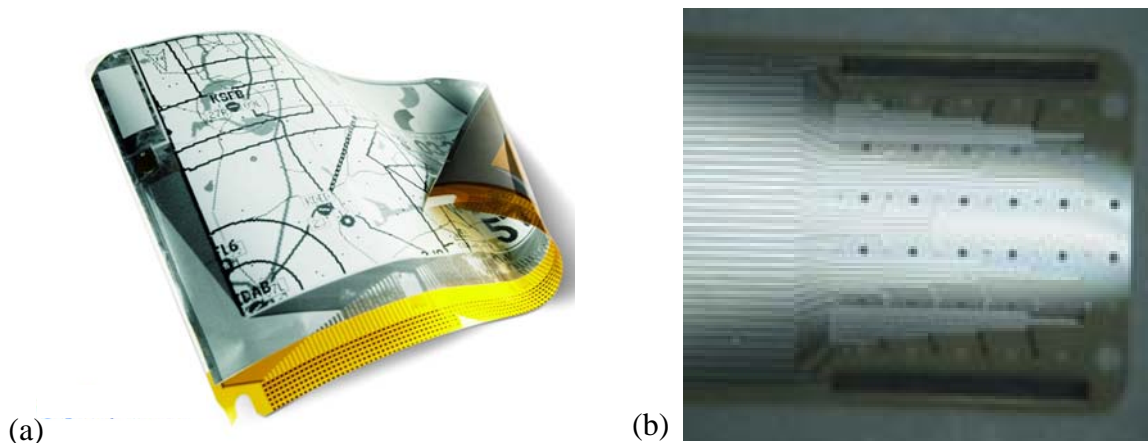


Figure 2.2: (a) Photograph of a flexible display [PolymerVision 2005]. The size of the active display is 4.8” (12.19 cm) and the resolution is 240 x 320 pixels. The minimum rolling radius is 0.75 cm. (b) Photograph of a flexible microelectrode array MEA for in vivo and special in vitro applications [MCS 2006]. It is only 12 μm thick and weighing less than 1g. The electrodes have a diameter of 30 μm with an interelectrode distance of 300 μm . The flexible base is perforated for a better contact with the surrounding tissue.

Independent of application and substrate, the knowledge of the mechanical behavior of the applied materials is crucial to ensure reliability and functionality of a device. A single failure of an individual interconnect line or via, among millions of such micro- and nanofeatures, can destroy the whole device. Such a failure need only to be of the order of 1 μm or less. Traditionally, this problem has been addressed in two ways: by modifying materials in order to enhance thin film strength and interface adhesion, and by rigorous reliability testing to reveal any weak links that can be fixed by altering the design. Among the applied materials the metallic components are most interesting because their mechanical properties strongly

depend on size on one hand but can be influenced and optimized on the other hand. This is due to the complex microstructure of thin metallic structures where anisotropy, grain size and texture play an important role. These parameters can be varied by changing the deposition and heat treatment of the metallic parts. Nevertheless the crosslink between microstructure, mechanical properties and device performance is not clear and more systematic investigations addressing these questions have to be made. These investigations will be difficult and laborious but it is the only way to be able to prescribe efficiently the optimal microstructure and design of a device.

2.2 Size effects on thin film plasticity

Length scales of micro- and nanometers are also of great interest for materials science because many controlling microstructural elements lie in this size regime. In contrast to other physical properties which only change at atomistic length scales, mechanical properties are already affected in the micro and sub-micrometer regime. Microstructural constraints, e.g. due to second-phase particles or grain boundaries as well as geometrical constraints, such as film thickness or line width in small-scale materials may lead to distinct changes in the mechanical properties [Arzt 1998].

Among the mechanical phenomena, plasticity exhibits a particularly strong size effect. Plasticity in thin metallic films is governed by the confinement of dislocation processes to small volumes. As a consequence, flow stresses in sub-micrometer thin films were repeatedly found to be significantly higher than in corresponding bulk materials and increase with decreasing film thickness [e.g. Nix 1989, Arzt et al. 2001, Dehm et al. 2002a, Kraft et al. 2002]. The understanding of the mechanisms responsible for this size effect is still incomplete. It has been suggested that the geometrical constraint in a thin film alter the energetics of dislocation motion. Nix [1989] proposed, based on calculations by Freund [1987], that dislocations moving in a thin film “feel” the presence of a substrate and/or surface passivation/oxide layer. As a dislocation advances on its glide system in the film, it creates additional line length at the interfaces (figure 2.3), which in turn requires an increase in stress to move the dislocation. An energy balance between the work done by the dislocation and the energy stored in the dislocation segments at the interfaces leads to following expression for the stress σ_{Nix} necessary to move a “threading dislocation” under a biaxial stress state:

$$\sigma_{Nix} = \frac{\sin \phi}{\cos \phi \cos \lambda} \frac{\mu_f b}{2\pi(1-\nu_f)} \left[\frac{\mu_s}{\mu_f + \mu_s} \ln \frac{\beta_1 h}{b} + \frac{\mu_p}{\mu_f + \mu_p} \ln \frac{\beta_2 h_p}{b} \right] \cdot \frac{1}{h} . \quad (2-1)$$

Here, the subscripts s, f and p refer to substrate, film and passivation/oxide layer, respectively, h is the thickness, μ the shear modulus, ν Poisson's ratio, b the Burgers vector, and β_1 and β_2 are numerical constants defining the cut-off radii. The angles ϕ and λ describe the orientation between the normal of the sample and the glide plane and the normal of the glide plane and the direction of the Burgers vector, respectively. If no passivation/oxide layer is present, the second term in parentheses can be neglected. According to equation (2-1) an approximately inverse relationship between flow stress and film thickness is expected. While this trend is reflected in many experimental data, quantitative agreement is found only in a few thin film systems [Venkatraman and Bravman 1992], such as epitaxial Al and Cu films on α -Al₂O₃ substrates [Dehm et al. 2002b, Dehm et al. 2003]. In most cases, especially for polycrystalline films, the model strongly underestimates experimental flow stresses as shown in figure 2.4 for Cu thin films. Assuming no grain boundaries, it is also not meant to describe polycrystalline films.

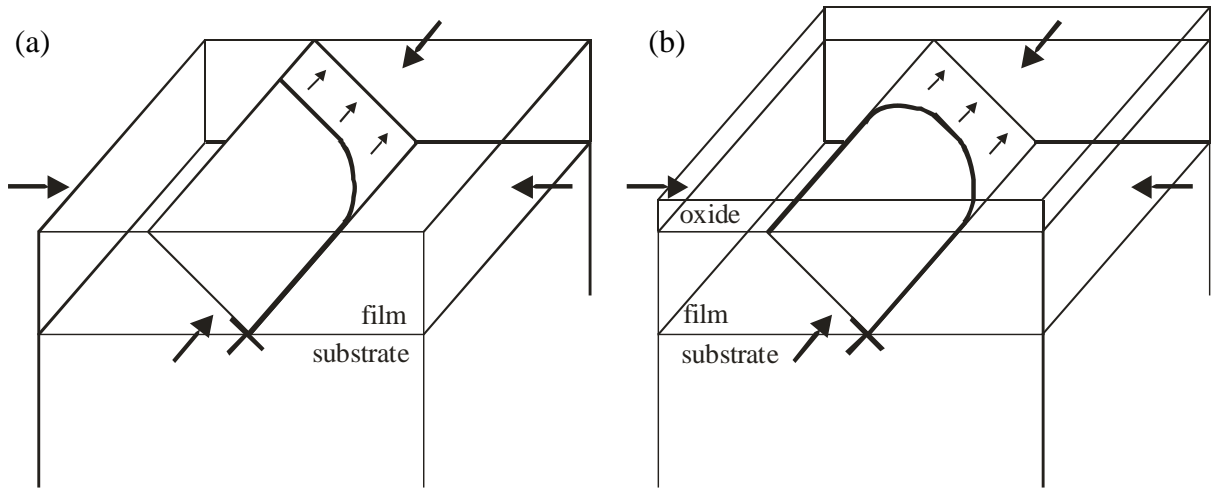


Figure 2.3: Dislocation motion in a film with (a) a free surface and (b) a surface oxide layer fixed to a substrate according to the Nix-Freund model. Additional dislocation segments need to be created at the corresponding interfaces when the dislocation glides through the film. The direction of dislocation movement and the corresponding biaxial stress state are indicated by arrows.

The model by Thompson [1993] considers an additional strengthening effect for polycrystalline films with a columnar grain structure. By assuming that the grain boundaries

are impenetrable for dislocations and that the energies to create dislocation segments at the grain boundaries and the film/substrate interface are approximately equal, equation (2-1) can be modified by a grain size dependent term:

$$\sigma_{Thompson} = \frac{\sin \phi}{\cos \phi \cos \lambda} \frac{\mu_f b}{4\pi(1-\nu_f)} \ln\left(\frac{d}{b}\right) \left(\frac{2}{d \sin \phi} + \frac{1}{h}\right) \quad (2-2)$$

where d is the grain size of the film. Although these assumptions are very extreme with regard to dislocation confinement, equation (2-2) still falls short of experimentally determined flow stresses and its thickness dependence is too weak (figure 2.4a). The Nix-Freund model has also been extended analytically in order to take into account strain hardening and interaction between interfacial dislocations [Nix 1998, Pant et al. 2003]. Thus, flow stresses up to the experimental values can be obtained, but so far the proposed mechanisms have not been confirmed experimentally.

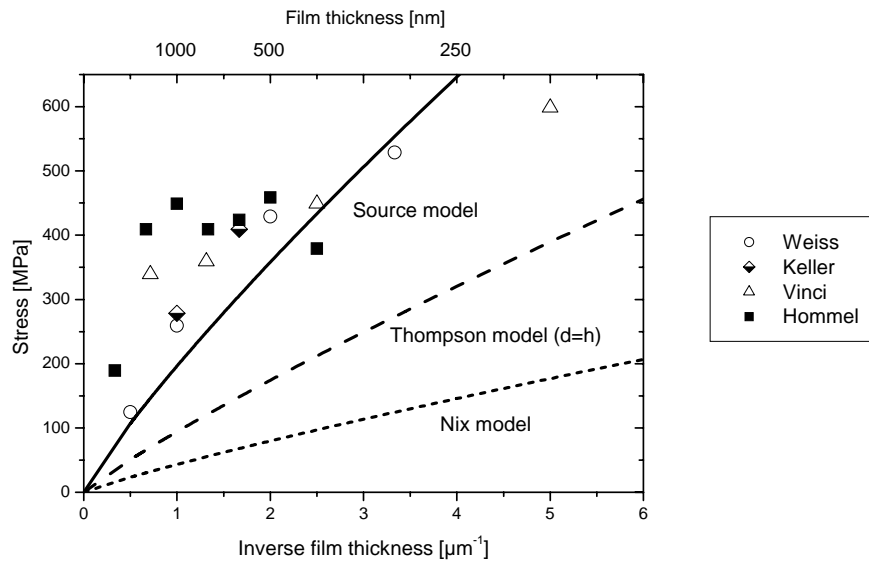


Figure 2.4: Comparison of experimental data for Cu films (room-temperature stress from wafer curvature experiments [Vinci et al. 1995, Keller et al. 1998, Weiss 2000] and stress at 0.5% plastic strain measured in a microtensile test [Hommel and Kraft 2001]) with the predicted values by the Nix-Freund, the Thompson and the Source model. The stress is shown versus the reciprocal value of the film thickness. The Thompson model is calculated assuming that the grain size d is similar to the film thickness h .

So far it has been assumed that enough mobile dislocations exist in the thin films to generate the plastic strains imposed during mechanical testing. Indeed there are various sources for dislocations since defect density, grain boundary volume and interfacial area is huge in a thin

film. However, each source has to fit in the confined geometry and if the source shall be activated several times it must be considerably smaller than film thickness or grain size. Thus, for decreasing dimensions the activation of sources becomes more difficult. Discrete dislocation simulations of the operation of a Frank-Read source in the center of a columnar grain reveal that the size of the most effective dislocation source scales with film thickness or grain size and that the size dependence of the flow stress can be described by an analytical model [von Blanckenhagen et al. 2001, von Blanckenhagen 2002, von Blanckenhagen et al 2003]. Figure 2.4 shows that this analytical solution gives a considerably better description of the experimental results than previous models. These simulations have also been extended to three dimensions. Stress-strain curves, dislocation densities as well as work hardening rates have been calculated [von Blanckenhagen et al. 2004, Espinosa et al. 2005, Espinosa et al. 2006]. The agreement between simulation and experiment is often good which supports the assumption that small-scale plastic deformation may be controlled by dislocation generation rather than dislocation motion. Similar to the dislocation interaction described above the operation of dislocation sources within grains of polycrystalline films has not been observed experimentally to prove or disprove the assumed mechanism.

In contrast, *in situ* transmission electron microscopy (TEM) observations during thermal cycling experiments on cross-sectional thin film samples reveal important mechanisms of interaction between dislocations and film/substrate interfaces. Dislocations moving through a film with an amorphous film/substrate interface deposit no interfacial segments and their motion is not hindered by the interface. The amorphous interface even attracts the dislocation and acts as dislocation sink [Dehm and Arzt 2000, Legros et al. 2003, Legros et al. 2005]. On the other hand, an epitaxial interface is repulsive and stable dislocation segments parallel to the interface are observed [Dehm et al. 2002b, Legros et al. 2003, Legros et al. 2005]. TEM studies also reveal that the dislocation motion is strongly affected by temperature: Dislocation move continuously through the film over distances up to the grain diameter at elevated temperatures, whereas dislocation motion becomes progressively more jerky with decreasing temperature [Kobrinisky and Thompson 2000, Dehm et al. 2001]. The experimental results of Kobrinisky et al. [2001] indicate that the distance between pinning points along the length of mobile dislocation segments increases with film thickness and that it is significantly smaller than the film thickness and average grain size. So far, the physical origin of the pinning points is not clear. If they are related to dislocation interactions, a decrease in pinning distance should be accompanied by an increase in dislocation density. However, the dislocation

density is found to be nearly constant, which might be due to constraints on dislocation multiplication [Dehm et al. 2001]. The TEM observations also suggest that for elevated temperatures stress is relaxed by thermally activated dislocation glide [Kobrinisky and Thompson 2000, Weiss et al. 2001].

A combined study of thermal cycling experiments on unpassivated Cu films using wafer curvature measurements and *in situ* TEM reveal an unexpected behavior. It is found that the room temperature flow stress increases with decreasing film thickness, but exhibits a plateau for films thinner than 400 nm (figure 2.5a) [Balk et al. 2003a]. It is also observed that a new type of dislocation motion occurs in this plateau regime where dislocation motion occurs parallel to the film/substrate interface (figure 2.5b). This “parallel glide” was unexpected since the equibiaxial stress state that exists in the plane of the film should not result in a resolved shear stress in this plane and the corresponding Schmid factor is zero. For films thinner than 200 nm plastic deformation by threading dislocations (figure 2.5c) is completely replaced by parallel glide. This may be due to the fact that the stress required to nucleate and to move threading dislocations becomes too high for the thinnest films and that it is easier to create parallel glide dislocations [Balk et al. 2003a].

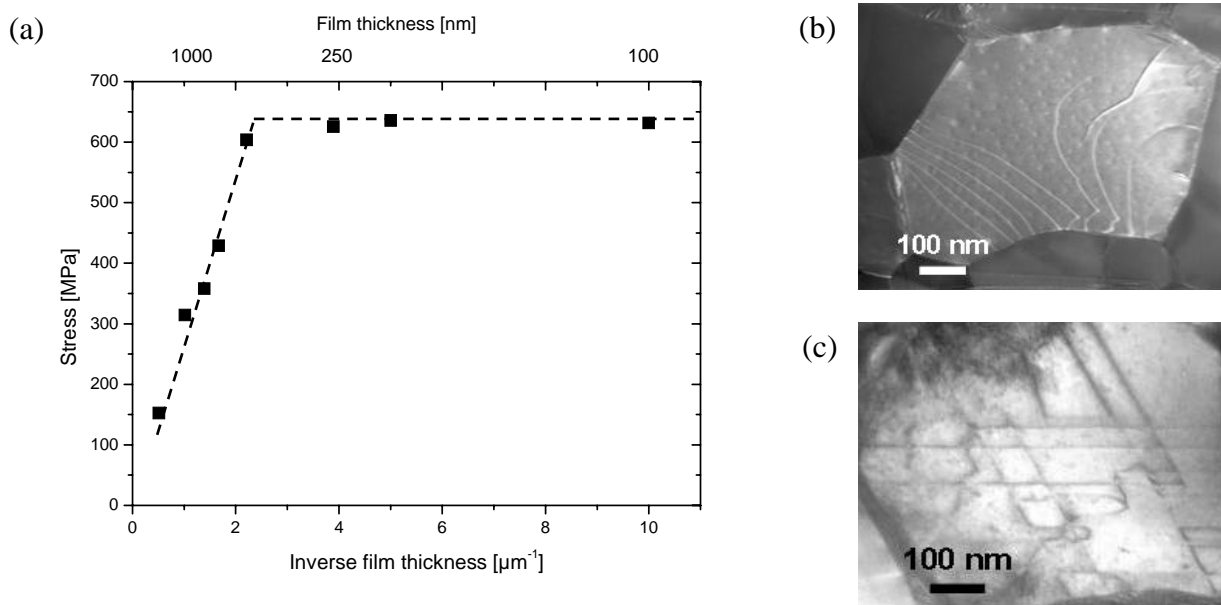


Figure 2.5: (a) Room temperature flow stress from wafer curvature experiments plotted as function of reciprocal film thickness (replotted from [Balk et al. 2003a]). With decreasing film thickness, flow stress initially increases, but then exhibits a plateau at approximately 630 MPa below 400 nm film thickness. (b) Weak beam TEM micrograph showing the arrangement of parallel glide dislocations in a 200 nm thick film. A total of 10 dislocations are emitted sequentially from the source at the lower right triple junction [Balk et al. 2003a]. (c) TEM micrograph of a 500 nm thick film. For thicker films plastic deformation is dominated by threading dislocations. These move on inclined planes and create straight slip traces at the film/substrate interface.

An explanation for this unexpected type of dislocation motion may be constrained diffusional creep [Gao et al. 1999]. The role of diffusional creep in thin films on substrates is still under debate but the fine grain size of most polycrystalline films is expected to enhance diffusional creep processes. According to this model, atoms diffuse from the surface into the grain boundary in order to relieve the tensile stress. Because sliding and diffusion are not allowed at the film/substrate interface, the additional material at the grain boundary creates a crack-like diffusion wedge which can be described as a continuous array of edge dislocations. Ongoing diffusion leads to an increasing stress concentration near the tip of the diffusion wedge (increasing shear stress on grain boundary) and finally to the emission of parallel glide dislocations. The efficiency of this mechanism strongly depends on surface and interface properties because a distinct difference in diffusivity between surface and grain boundary on the one hand, and film/substrate interface on the other, is required. In fact, the presence of a passivation layer on the surface of the film should inhibit diffusional flow from the surface into the grain boundary and thus shut off the nucleation of parallel glide dislocations. This has been demonstrated by Balk et al. [2003a].

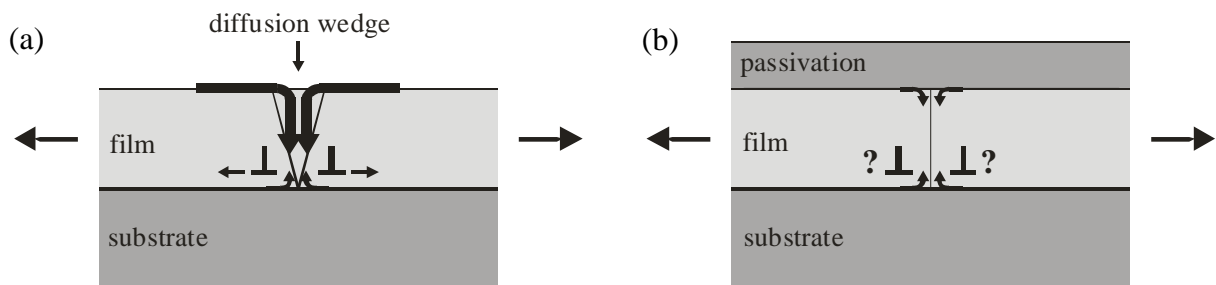


Figure 2.6: Diffusion paths for (a) an unpassivated and (b) a passivated film with columnar grain structure. A distinct difference in diffusivity between surface and film/substrate interface is required in order to form a diffusion wedge and to create a stress gradient along the grain boundary. For the passivated film no generation of parallel glide dislocations is expected.

2.3 Cracking of thin films on substrates

Paradoxically, the high flow stresses found in thin metallic films have become a reliability issue in modern thin film technology because high internal stresses are difficult to relieve and can cause failure by cracking.

The cracking behavior of thin films on substrates differs from bulk behavior due to the small film thickness and the presence of the substrate. In contrast to a bulk specimen, where a

propagating crack of critical size leads to fracture and total failure, a cracked film remains bonded to the substrate. This favors multiple crack formation because a single crack reduces the film stress only locally as a result of the constraining effect of the substrate. Furthermore, thin films on substrates are usually in a biaxial stress state. The constraining effect of the substrate on the released strain energy in a film under biaxial stress compared to a freestanding sheet under uniaxial loading is schematically shown in figure 2.7.

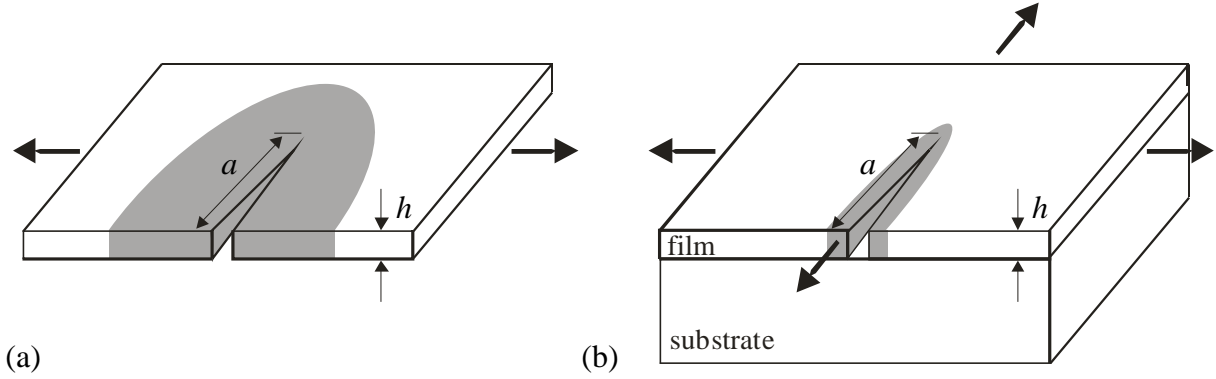


Figure 2.7: Volume of strain energy (marked in grey) released by the formation of a crack is larger in (a) a freestanding film under uniaxial tension than in (b) a film bonded to a substrate subjected to a biaxial film stress.

In a freestanding sheet, the volume V_{sheet} affected by the release of energy due to crack formation scales with the crack length a and the film thickness h according to $V_{sheet} \propto a^2 h$ (figure 2.7a). In contrast, for a film on a substrate, the volume V_{film} in which the strain energy is released yields a stronger influence of the film thickness due to the substrate constraint and scales with $V_{film} \propto ah^2$ (figure 2.7b). For a film bonded to a substrate, the energy W released by the introduction of a crack is given by:

$$W = -\frac{c\sigma_{fr}^2}{E_f^*} ah^2, \quad (2-3)$$

where σ_{fr} is the film fracture stress, c a constant and E_f^* represents the plane-strain elastic modulus of the film. The energy release rate G , is defined as the reduction of the elastic energy associated with the crack per unit area A (where $A \propto ah$), giving:

$$G = -\frac{\partial W}{\partial A}. \quad (2-4)$$

Following this approach, the energy release rate for steady-state cracking is given by:

$$G = Z \frac{\sigma_{fr}^2 h}{E_f^*}. \quad (2-5)$$

This dependency implies that the film thickness plays the role of a critical crack length. When the film thickness is homogenous, the driving force for crack propagation is reached at every site along the film once the stress reaches the fracture stress. The crack propagation parallel to the surface is called channel cracking since the crack forms a channel of constant width as it propagates through the film. The dimensionless number Z depends on the elastic constants of the film and the substrate and must be determined by solving the boundary value problem. When the film and the substrate have similar elastic constants $Z = 2.0$. Beuth [1992] calculated the Z values for a thin film on an infinite substrate with dissimilar elastic constants. When the substrate is stiffer than the film, Z is between 1 and 2. On the other hand, when the substrate is very compliant compared to the film, Z can be 25 and higher.

Even though channel cracking in thin films was extensively studied theoretically [Beuth 1992, Xia and Hutchinson 2000, Begley and Ambrico 2003, Vlassak 2003], little experimental work has been carried out so far. Cracking in thin films is mainly treated as a full elastic problem and it is assumed that the energy release rate is uniform along the crack front (plane-strain state along the complete crack front, even near the surface). As a consequence, the energy release rate and fracture toughness are believed to be independent of film thickness. Some studies report experimental evidence for this assumption for Cr films on Al substrates [Hu and Evans 1989], Ta₂N films on AlN substrates [Moody et al. 1998] and β -NiAl films on Si substrates [Wellner et al. 2004]. All these studies are related to brittle films and thus the assumptions of linear elastic behavior and plane strain conditions may be reasonable. However, for films out of ductile fcc metals such as Al, Au and Cu plastic yielding in front of the crack tip cannot be excluded; here the question is how the plastic zone may develop in such a thin film and whether these assumptions are still reasonable. It is not clear if the theoretical models described above can be adapted to ductile films and very compliant substrates and if the fracture toughness of ductile metallic films is also independent of film thickness. This is of special interest, from both, a fundamental as well as technological point of view, because it is unknown how metallic films on compliant substrates behave at high

total strains. This special material combination is becoming more and more popular for applications such as flexible electronics.

It is obvious from the discussion above that more experimental work is needed in order to obtain a better understanding of the mechanical properties of thin films and small structures. For this, suitable mechanical testing techniques must be available.

2.4 Mechanical testing of thin films and small structures

In the last 20 years several specialized testing techniques have been developed in order to study mechanical properties in small dimensions [Nix 1989, Brotzen 1994, Kraft and Volkert 2001]. The aim of mechanical testing is to determine properties such as Young's modulus, flow stress, fracture strength, creep and fatigue resistance. In some cases, the principles of macroscopic testing can be transferred directly to small dimensions, as for instance in micro tensile testing or nanoindentation. However, very accurate and sensible techniques for measuring forces and strains and innovative ways of sample preparation are often required. In the following, an overview of novel and common techniques for mechanical testing in small dimensions is given, including thermal cycling, nanoindentation, microtensile testing, bulge testing, microbeam bending and microcompression tests.

Unlike bulk samples, many films and small structures are attached to a substrate and are therefore subject to residual stresses. In general, residual stresses develop when the film changes its dimensions relative to the substrate. This usually happens during a temperature change when film and substrate have different thermal expansion coefficients. Usually, the substrate is much thicker than the film and therefore the film must accommodate completely the mismatch with the substrate. These thermal stresses lead to a curvature of the film-substrate composite which can be measured and thus the resulting stresses in the film can be determined [Flinn et al. 1987, Moske and Samwer 1988, Venkatraman and Bravman 1992, Keller et al. 1998]. The thermal cycling method is constrained by the fact that the applied strain and the temperature cannot be varied independently. Also, the maximum strain that can be achieved during a thermal cycle depends on the difference of thermal expansion coefficients of film and substrate and is typically quite small (e.g. less than 1% for Cu on Si). Therefore, despite the simplicity of the measurement, the use of thermal cycling data to obtain reliable film properties is limited.

Hardness measurements are a common technique for characterization of mechanical properties of materials. In a thin film, an indentation of several micrometers may exceed the film thickness and the measured hardness would be a convolution of film and substrate properties. Therefore depth-sensing hardness testing systems have been developed. Such systems measure the indentation depth as function of applied load. With the exact knowledge of the shape of the indenter, it is possible to determine the area under the indenter. Several procedures have been proposed to quantitatively determine the hardness [Oliver and Pharr 1992]. The simplest way to determine hardness is to measure the total indentation depth at maximum load and to correlate them. This value is the classical hardness and includes both elastic and plastic deformation. A more detailed analysis includes the measurement of the contact stiffness between the sample and the indenter tip, which is defined as the incremental load divided by the incremental resulting incremental displacement in the absence of plasticity. The determination of the hardness depends strongly on an accurate measurement of the contact area. However, this is often not straightforward, especially for metals, because material may pile up or sink in in the vicinity of the indent [McElhaney et al. 1998]. In recent years, two major improvements for depth sensing hardness testing have been introduced. First, a procedure for measuring the contact stiffness continuously at any point along the indentation curve and not only at the point of unloading has been developed (continuous stiffness measurement CSM) [Oliver and Pharr 1992]. The second improvement includes the combination of the indenter system with a scanning force microscope (SFM). This setup offers the possibility to image the sample surface prior to testing, to choose the position of indentation and to image the indent after the test [Gerberich et al. 1996, Baker 1997]. Very recently a new setup has been presented which consists of a nanoindenter setup installed in a scanning electron microscope SEM [Rabe et al. 2004, Moser et al. 2005]. Thus it is possible to monitor the contact area as well as deformation behavior *in situ* during the indentation. Despite all methodological improvements hardness stays a rather complex quantity since yielding, strain hardening, viscous flow, cracking or even delamination may all contribute to the deformation process under the indenter tip and the stress state under the tip is non-uniform.

Tensile testing has been rather rarely applied to thin films. This is due to the extreme instability of a freestanding film with submicrometer thickness which makes sample handling very difficult. In addition force and strain measurement is quite tricky [Ruud et al. 1993]. To facilitate sample handling, different experimental routes have been developed in order to use

micromachining techniques, such as lithography and etching, to produce freestanding films attached to silicon frames [Read and Dally 1993, Sharpe and Hemker 2002]. The silicon frames allow for mounting the sample safely into the tensile testing apparatus. Then the parts of the frame parallel to the film are cut such that the support of the silicon frame no longer exists (figure 2.8a). By similar means a variety of samples of different materials has been prepared and tested and minimum thicknesses of about 200 nm could be achieved (e.g. Cu films [Ruud et al. 1993, Read 1998], Al films [Read and Dally 1993, Read et al. 2001], Au films [Emery and Povirk 2003a, Emery and Povirk 2003b]). Haque and Saif have developed an improved micromachined tensile test chip for *in situ* experiments in a scanning or a transmission electron microscope which uses the silicon beams not only for the support of the freestanding sample but also for measuring force and displacement [Haque and Saif 2002]. Thus even 30 – 50 nm thick films can be tested. In figures 2.8b and c SEM pictures of the tensile test chip are shown. The latest design also includes a four-point electrical resistivity measurement capability [Han and Saif 2006].

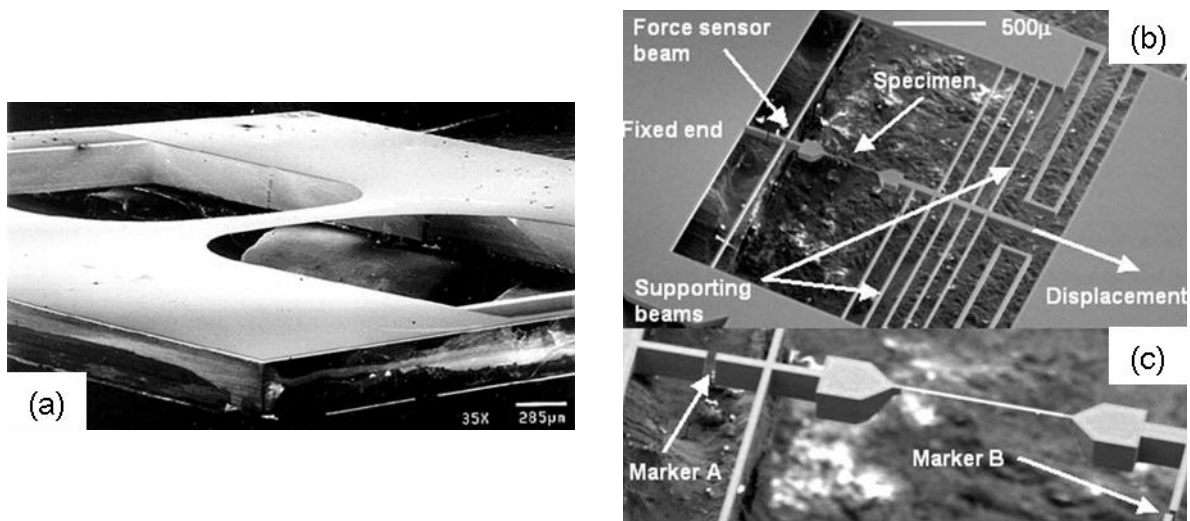


Figure 2.8: (a) Photograph of a polysilicon sample (0.5 μm thick, 600 μm wide) on a supporting silicon frame (1 cm wide and long). After mounting, the two side support strips are cut with a diamond saw. This leaves a completely freestanding tensile specimen [Sharpe 2003]. (b) SEM image of a tensile test chip developed by Haque and Saif [2002]. The freestanding film is attached to the force sensor beam at one end, and a backbone at the other end. The right end of the chip is pulled by a piezoactuator. (c) Zoomed view of freestanding specimen and the displacement markers A and B.

Testing of freestanding films gives insight into the intrinsic properties of the film material and is easier to interpret but sample fabrication and handling remains complicated compared to testing of films on substrates. Therefore it is desirable to test a film that is still attached to a substrate. It is obvious that thus sample handling is no longer a problem. However, a direct

evaluation of the stress is no longer possible since the external load depends on both the stress in the substrate and in the film. There are two main methods used to overcome this problem. The first method is to perform tensile tests on very thin (3.5 μm) polyimide samples with and without film and to calculate the film stress from the small difference between the two macroscopic stress-strain curves [Kang et al. 1997, Macionczyk et al. 1998, Tregilgas and Strumpell 1998, Yu and Spaepen 2004]. This method ignores that the stresses developing in the film during deformation of the composite are biaxial due to the mismatch in Poisson's ratio of film and substrate. Any uncertainties about the thickness and the elastic and anelastic properties of the substrate also affect the stress results.

Another approach has been introduced by Schadler and Noyan [1995], who used *in situ* strain measurements by X-ray diffraction during the tensile test. The standard X-ray technique to measure strains in thin films is the so called $\sin^2\psi$ -method [Noyan and Cohen 1987, Flinn and Chiang 1990, Besser et al. 1994, Kuschke and Arzt 1994]. This method works particularly well when the film has a texture that leads to an isotropic biaxial modulus of the film, which is the case in cubic materials with a (111)-fiber texture [Brantley 1973]. It should be pointed out that this method can be used to determine even more complex stress states like those in patterned and passivated lines [Besser et al. 1994, Kuschke and Arzt 1994]. Stress analysis of untextured or mixed textured films can be complicated and depends on the elastic anisotropy of the film material. The adaptation of the $\sin^2\psi$ -method including grain interaction and elastic anisotropy is given in the literature [Gergaud et al. 1998, Leoni et al. 2001, Welzel et al. 2003, Welzel et al. 2005]. Early experiments with tensile tests combined with X-ray strain measurements have been performed using metallic substrates (e.g. Ni or Al) [Noyan and Sheikh 1992, Kretschmann et al. 1997, Renault et al. 1998]. In recent years, polyimide (Kapton[®] HN, DuPont) has been shown to serve as a better substrate material because this amorphous polymer can be deformed homogeneously up to large strains (>5%) and can be produced with excellent surface quality [Hommel et al. 1999, Kraft et al. 2000]. Also, polyimide can serve as model material for flexible substrates which are important for various applications. The use of an elastic substrate allows the deformation behavior of thin films to be studied, not only in tension but also in compression [Hommel et al. 1999]. This results from the fact that on removing the external load from the film/substrate composite the elastic substrate contracts to its original length. The film, which has been plastically deformed in tension, follows this contraction and is therefore deformed in compression.

Another technique for measuring intrinsic film properties is the bulge test. This technique requires some sample preparation. Free standing films have to be prepared by opening a window in the substrate using micromachining techniques. The freestanding film is deflected by applying a uniform pressure to the film and the mechanical properties are determined from the pressure-deflection behavior. Bulge testing of thin films was first reported by Beams in 1959, as a technique for measuring in-plane mechanical properties of thin films [Beams 1959]. In the beginning the technique suffered from problems related to sample processing, handling and data analysis. The rapid development of silicon micromachining technology has made it possible to manufacture bulge test samples with precisely controlled dimensions. With some care freestanding films as thin as 100 nm can be prepared and tested [Vlassak and Nix 1992]. To explain the experimental data and relate them to the mechanical properties of the tested film, both theoretical and numerical analyses have been conducted. Vlassak and Nix [1992] derived an accurate expression for the elastic load-deflection behavior of square and rectangular membranes following an approach originally developed by Timoshenko [Timoshenko and Woinowski-Krieger 1959]. They also found that once the aspect ratio of the rectangular membrane exceeds 4, the deflection in the center of the membrane is independent of the aspect ratio and plane-strain conditions can be assumed. Thus the deflection can be approximated by the exact solution for an infinitely long rectangular membrane. This mathematical analysis of the bulge test is based on linear elasticity and may not be applied to plastic deformation. Xiang et al. have shown by testing long rectangular Cu membranes and performing a detailed FEM analysis that the analytical stress and strain equations derived by Vlassak and Nix are accurate and that the plane-strain condition is well satisfied even in the plastic regime for materials with strain hardening exponents ranging from 0 to 0.5 as long as the membrane aspect ratio is 4 or greater [Xiang et al. 2005a]. Therefore, information about the initial stress, the elastic constants and yield stress of the membrane can be obtained. By increasing the pressure until the membrane bursts, the fracture strength of the membrane can also be determined.

Beside silicon micromachining techniques the focused ion beam (FIB) technique gains more and more importance as structuring tool in the micrometer and submicrometer regime. In figure 2.9 two examples of samples prepared by FIB are shown. The methodology developed by Uchic and Dimiduk [2005] is based on the preparation of cylindrical samples with uniform cross-section which remain attached to the bulk substrate at one end. These cylinders are tested in uniaxial compression after fabrication using a flat tip nanoindentation device. The

methodology can be used to examine the plastic response of samples of different sizes (figure 2.9a, b). This approach has been adapted to even smaller sample diameters of less than 400 nm [Greer et al. 2005, Volkert and Lilleodden 2006]. In this manner, dimensional size effects at the submicron scale can be explored for single crystals (if the diameter of the column is smaller than the grain size of the material), using a readily interpretable test that minimizes imposed stretch and bending gradients. A second, very similar approach with different sample geometry is the fabrication of microbeams out of a single crystalline film [Motz et al. 2005]. In figure 2.9c an example of a double bending microbeam is shown. Again a nanoindenter setup is used to load the sample and for recording force vs. displacement curves for samples with different beam thickness from 1 to 7.5 μm . The interpretation of the data is not trivial since the stress state in a bent beam is inhomogenous and the stiffness of the indenter and the beam support has to be taken into account as well as a lateral displacement of the loading point during the experiment. The displacement of the beam must be corrected by the indentation depth of the indenter in the beam surface. Therefore a very careful analysis is necessary to obtain correct mechanical data of the sample. Some issues are common for both experimental techniques. Related to the FIB preparation Ga^+ ion implantation and damage in the surface regions of the samples cannot be avoided. Since the cylindrical structures are cut with a nearly perpendicular beam orientation, the affected region is assumed to be only about 15 - 30 nm [Volkert and Lilleodden 2006]. For preparing the microbeam geometry several preparation steps with different inclination angles are necessary; therefore the irradiated surface volume is higher and is assumed to be 300 nm [Motz et al. 2005]. This is crucial, especially when these techniques shall be used for samples with dimensions below 300 nm. Other restrictions are due to the very small dimensions of the samples. First, positioning of the indenter tip relative to the sample becomes difficult and misalignment can lead to a misinterpretation of the experimental data [Greer et al. 2006]. Second, for the evaluation of stress and strain the sample dimensions must be known very accurately; this is not trivial because their determination is not easy and the fabrication by FIB may lead to varying dimensions along the sample. Further the dimensions may change inhomogenously during deformation.

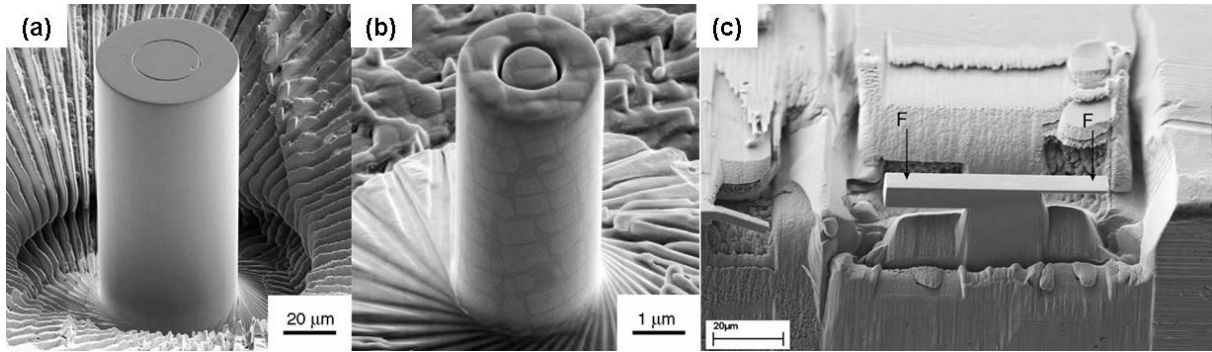


Figure 2.9: (a), (b) 43 μm and 2.3 μm diameter microcompression samples produced by focused ion beam (FIB) milling into a $\text{Ni}_3(\text{Al,Hf})$ single crystal and a single crystal Ni superalloy respectively. The aspect ratio is 1:2 for both pillars. The circular pattern on the top surface of the sample is used for positioning within an automated machining program for the FIB [Uchic and Dimiduk 2005] (c) Double bending microbeam fabricated by FIB machining of a Cu single crystal. Beam thicknesses are between 7.5 and 1.0 μm with widths from 7.5 to 2.5 μm and beam lengths between 20 and 25 μm [Motz et al. 2005].

All of the techniques discussed above are suitable for characterizing plastic behavior of thin film materials. However, only the tensile test of freestanding films, the bulge test for high aspect ratio rectangular membranes and the uniaxial microcompression test provide direct results for the yield or ultimate tensile strength, the elongation to failure and hardening rate. Due to the more complicated loading conditions all other methods require careful analysis techniques for extraction of the materials parameter. Nevertheless the applicability is restricted due to the very complicated sample preparation, involving lithography, etching or FIB. These techniques cannot be applied to all materials and structures, may need the introduction of protective layers or lead to damage or contamination of the sample. Thermal cycling, nanoindentation and tensile testing of thin films on substrates offer the advantage that they do not require further sample preparation than depositing the film on a substrate. This is also attractive since thin films used in actual applications are mostly deposited on substrates. For nanoindentation the substrate can be a problem, because the contribution of the substrate changes as a function of the indentation depth. The influence is enhanced when the mechanical properties of film and substrate are very different, e.g. for very soft films on hard substrates. Then the measured properties depend on the indentation depth even when the tip is far away from the interface between film and substrate.

Another important parameter in the study of mechanical properties of thin films is temperature because deformation mechanisms are expected to be strongly influenced by temperature due to the short diffusion paths. The only technique routinely used at elevated temperatures is thermal cycling, despite the fact that temperature and strain cannot be varied

independently. In order to achieve a more defined experiment, it would be desirable to adapt one of the other techniques to elevated temperatures, but there are only very few experiments described in the literature (tensile testing of freestanding films [Brotzen et al. 1990, Emery et al. 1998, Haque and Saif 2005a], nanoindentation [Lucas and Oliver 1999], bulge test [Hyun et al. 2003, Kalkman et al. 2003, Cieslar et al, 2004]). This is due to experimental reasons: the accuracy of the measuring techniques is strongly influenced by temperature changes and local heating of a sample on the micron scale is very difficult.

So far the ideal testing technique does not exist. Mechanical testing of thin films is a rapidly changing field. Further improvement of existing techniques and development of new ones is necessary to obtain a better understanding of the mechanical properties in small dimensions.

2.5 Summary of literature review and aims of this study

Small is strong – this may be the essence of thin film mechanics, but is smaller even stronger? On one hand it is generally found that the yield stresses of thin metallic films increase with decreasing thickness. While it is clear that this effect must be due to the confinement effects on dislocation processes, understanding of the underlying mechanisms is still incomplete. The literature review shows that the behavior of dislocations near interfaces affects the plasticity in small dimensions in new ways which have not been foreseen by theoretical considerations so far:

- For example unexpected slip systems were discovered in polycrystalline thin films. Their occurrence was attributed to constrained diffusional creep indicating that the geometrical and microstructural constraints may speed up diffusion.
- Discrete dislocation simulations based on the concept of dislocation source activation were conducted in order to better describe experimental values of flow stresses but so far the proposed mechanisms have not been observed experimentally.
- Thermomechanical experiments on very thin films show that the common trend of increasing flow stresses may be stopped for polycrystalline Al and Cu films thinner than 300 nm [Balk et al. 2003a, Dehm et al. 2003]. Due to the temperature variation during the thermal cycle, the limited total strain and the fact that surface diffusivity is completely different for Al and Cu, the origin of the plateau in flow stress for both, Al and Cu films, is not clear.

- On the other hand, it is reasonable that stresses in thin films cannot increase indefinitely. The plastic zone around any stress concentration is confined by the film geometry and the presence of a substrate. If its volume becomes too small for sufficient stress relaxation, the thin film will crack. Similar to plastic deformation, thin film cracking was extensively studied theoretically, but little work was carried out experimentally and experimental data is rare.

It is obvious that much further work is necessary to better understand thin film mechanics. A deeper understanding is not only of great interest in a scientific point of view but the knowledge of mechanical properties of thin films would also help to develop design rules for future micro- and nano-technological devices of high functionality and reliability. Further progress will be possible by developing new testing methods, which is not trivial as shown in the review of common mechanical testing techniques. The key features for a feasible technique are:

- Measurement times should be short in order to study the strain rate dependence.
- Mechanical testing should be performed at constant temperature in order to control temperature and stress separately and to investigate the temperature dependence of different deformation mechanisms.
- Strain should be variable over a wide range.
- Sample fabrication should be easy and flexible with respect to film thickness, film material and interfaces.
- Accurate strain and stress measurement for films as thin as possible.

One of the most promising techniques to fulfill the conditions listed above is the microtensile test of thin metallic films on compliant polyimide substrates combined with a stress measurement by X-ray diffraction [Hommel et al. 1999, Hommel and Kraft 2001]. It is an isothermal testing technique where metallic thin films can be deformed up to total strains of more than 5%. Combined with X-ray diffraction, the complete stress tensor of the metallic film can be determined with high accuracy. Sample fabrication by sputter deposition of metallic films on polyimide substrates is quite simple and various film materials can be tested as single film or layered structure of different film materials. The only drawbacks of this technique are the long measurement time and the unfavorable signal-to-noise ratio in a laboratory X-ray source. Thus the minimum film thickness which can be tested is about 300 nm.

One aim of this study was to develop the microtensile testing technique further by using synchrotron radiation and a simple transmission geometry [Daymond and Withers 1996, Wanner and Dunand 2000] in order to make it feasible for thinner films and to adapt it to different film systems as thin as possible reaching film thicknesses which have not been investigated so far. The novelties of this technique are described in chapter 3. Different testing parameters were varied systematically to get more insight into the deformation behavior of ultra thin metallic films. The role of different interfaces (unpassivated, passivated, amorphous and crystalline interfaces), the deformation behavior at high strains including plastic deformation and cracking, as well as the investigation of deformation mechanisms at different temperatures were of special interest and will be addressed in this study.

Another goal of this study was the extension of the tensile testing technique to single-crystalline films. For this purpose a new experimental route had to be developed in order to prepare a single-crystalline film on a compliant and amorphous polymer substrate. In addition, a different synchrotron X-ray diffraction technique suitable for determination of the stress tensor of a single-crystalline film was established. The best testing techniques are worthless without accurate sample characterization before and after the test. Here, various techniques were employed, including Rutherford backscattering spectrometry RBS (film thickness), atomic force microscopy AFM (grain size), electron backscatter diffraction EBSD (grain size and orientation mapping), scanning electron microscopy SEM (*in situ* tensile testing, crack spacing, crack formation), focused ion beam microscopy FIB (grain size, cross sections) and transmission electron microscopy (grain size, dislocations, twins, pores). By combining the results obtained by the novel synchrotron based testing techniques with sophisticated sample characterization and literature review, new aspects of thin film mechanics were uncovered.

3 Novel synchrotron-based technique for tensile testing of ultra thin polycrystalline films

The X-ray *in situ* tensile testing technique has been shown to work well for polycrystalline metallic films with thicknesses in the micrometer regime [Hommel and Kraft 2001]. Serious experimental problems arise for films considerably thinner than 500 nm. First of all, the X-ray counting times required per data point increase to an impractical level (30 min to 1 h) as the gauge volume is decreased. Second, the signal-to-noise ratio of the diffraction peaks becomes unfavorable since the amorphous polymer substrate gives rise to considerable scattering background.

This problem can be overcome by performing the X-ray strain measurement with synchrotron radiation in which the high photon flux reduces the necessary counting times [Renault et al. 2003, Faurie et al. 2005]. So far the standard X-ray technique to measure the stress evolution in the metallic film is the “ $\sin^2\psi$ method“, which is based on measuring the lattice spacing d_ψ of a selected type of lattice planes (ideally high-indexed planes) at different inclination angles ψ with respect to the sample normal [Noyan and Cohen 1987, Flinn and Chiang 1990, Besser et al. 1994, Kuschke and Arzt 1994]. The $\sin^2\psi$ method is a straightforward technique to measure the biaxial stress existing in a thin film. However, since the specimen must be tilted in order to vary the inclination angle ψ , the measurement procedure is still time consuming. Upon straining the film/substrate composite during the tensile test, the rotational symmetry of the stress state in the film with respect to the sample normal is broken. In order to measure the stress in the transverse direction with the same accuracy as in the longitudinal direction, the complete measurement must be performed in both directions making the whole measurement even more time consuming.

In the framework of this study a novel experimental approach was developed by which it is possible to characterize the biaxial stress state with a single X-ray measurement [Böhm et al. 2004]. This was achieved by measuring the variation of lattice spacing as a function of the in-plane azimuthal angle φ while keeping the inclination angle ψ constant. This could be realized in a well defined transmission geometry [Daymond and Withers 1996, Wanner and Dunand 2000] where the specimen was oriented perpendicular to the incoming X-ray beam.

By using an area detector for recording the diffraction patterns, it was possible to access the whole φ range from 0° to 360° (complete Debye-Scherrer ring) without moving or rotating any component of the experimental setup. Thus the measurement time could be reduced to a minimum (15 to 120 s). In the following and in analogy to the $\sin^2\psi$ method, this procedure is called “ $\sin^2\varphi$ method”. In the presence of a pronounced texture, which was the case for very thin films, intense Debye-Scherrer rings were obtained only if the wavelength of the X-ray beam was adjusted accordingly. For the application of the $\sin^2\varphi$ method to thin films a tuneable X-ray source was required. Beside the favorable high brilliance, this was the second and definitive reason for the necessity of using synchrotron radiation. Because the films tested in this study showed a pronounced $\langle 111 \rangle$ fiber texture, the experimental setup and procedures will be described for this case. Figure 3.1a shows schematically how the wavelength of the X-ray beam is determined by the texture and the lattice spacing of the material under investigation. Due to the $\langle 111 \rangle$ fiber texture, strong diffracted intensities could only be found at ψ angles of 0° and 70.53° . Full Debye-Scherrer rings in transmission geometry could be obtained for $\psi_0 = 70.53^\circ$, corresponding to a Bragg angle of

$$\theta_{111} = 90^\circ - \psi_0 = 19.47^\circ. \quad (3-1)$$

The required wavelength of the X-ray beam for the material under investigation was calculated using Bragg’s equation. Figure 3.1b shows an exemplary diffraction pattern of the complete Debye Scherrer ring of a 50 nm thick Cu film recorded in the normal incidence geometry.

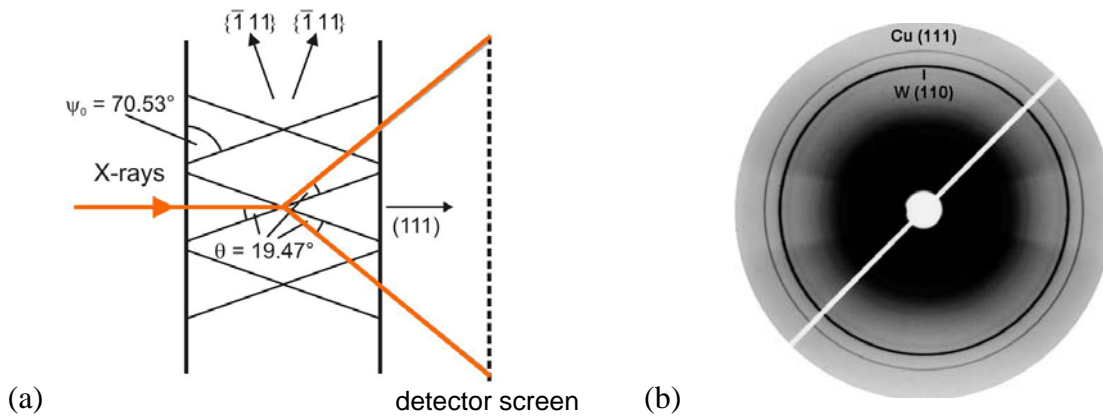


Figure 3.1: (a) Diffraction geometry for obtaining complete Debye-Scherrer rings for inclined $\{111\}$ planes in a $\langle 111 \rangle$ fiber textured film when the specimen is oriented perpendicular to the incident X-ray beam. (b) Diffraction pattern showing Debye-Scherrer rings of the (111) reflection of a 50 nm thick Cu film and the (110) reflection of W powder used as calibration substance.

In order to compensate for the effects of unintentional specimen movements during the tensile test, fine W powder dispersed in vacuum grease and attached to the backside of the polymer substrate was used as calibration substance. The use of a calibration substance was crucial for an accurate strain determination [Wanner and Dunand 2000]. The elastic lattice strains in longitudinal and transverse direction were deduced from the elliptical distortions of the Debye-Scherrer rings (figure 3.2a). The main axes of the ellipses could be obtained by plotting the ring diameter against $\sin^2\varphi$ (figure 3.2b). Since the resolution of the CCD area detector was extremely high, the ring diameter could be evaluated for very small angle increments leading to a superior number of data points, which was at least two orders of magnitude higher than for the classical $\sin^2\psi$ method. Thus, strain resolution better than 10^{-4} was achieved using (111) planes. The software for the analysis of the images from the CCD area detector was developed by Jochen Böhm during his PhD thesis at the University of Stuttgart [Böhm 2004].

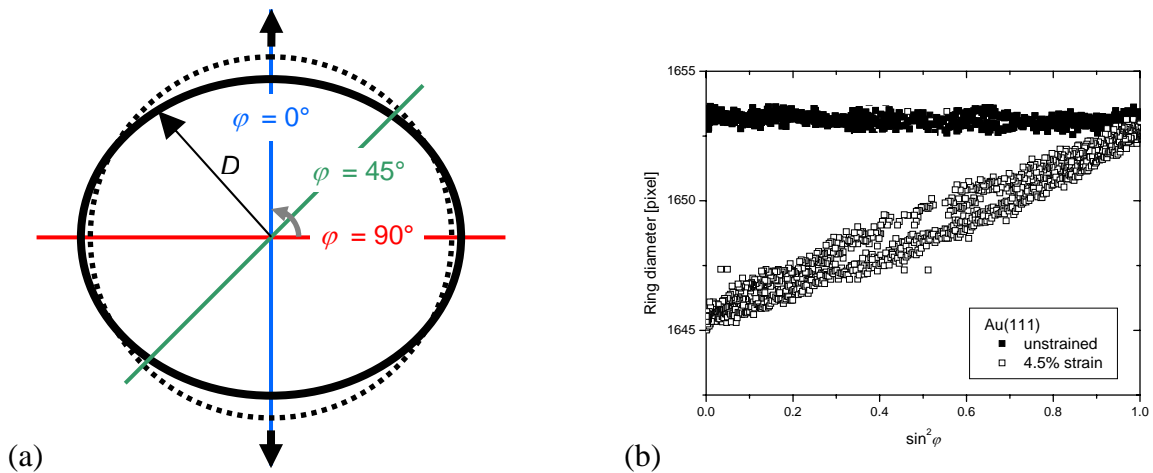
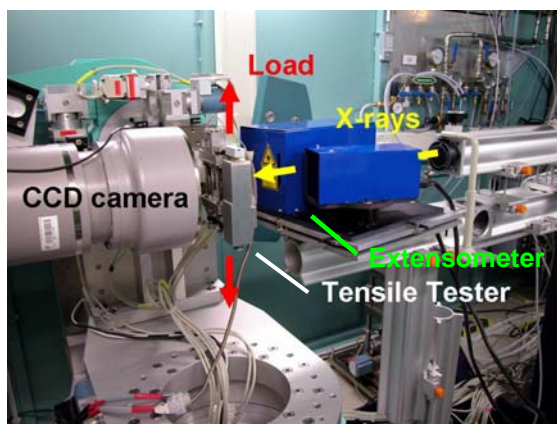


Figure 3.2: (a) Elliptical distortion of a Debye-Scherrer ring under strain (schematically). (b) Diameter of the (111) Debye-Scherrer ring vs. $\sin^2\varphi$ of an 80 nm thick Au film. The two main axes of the ellipse can be obtained by a linear fit and extrapolation to $\sin^2\varphi = 1$ (transverse direction) and $\sin^2\varphi = 0$ (longitudinal direction).

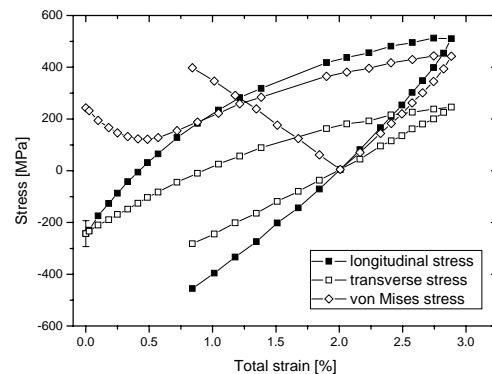
The $\sin^2\varphi$ method has unique features concerning measurement time and accuracy but it has one inherent limitation. Because lattice distortions are only measured in the plane of the film, no unstressed lattice parameter can be determined. Thus, in contrast to the $\sin^2\psi$ method no absolute values for the strain can be obtained. However, it is sufficient to perform a single $\sin^2\psi$ measurement to determine the absolute initial equibiaxial stress state. For the $\langle 111 \rangle$ fiber textured films this was done by measuring the interplanar spacing of (111)-planes at different inclination angles near $\psi_1 = 0^\circ$ and $\psi_2 = 70.53^\circ$. Afterwards, while deforming the sample the $\sin^2\varphi$ method was repeatedly applied to obtain the stress changes in the film. Thus,

we could benefit from the efficiency of the $\sin^2\varphi$ method during the whole tensile test and absolute stress values could be obtained as well. The theoretical considerations for the stress evaluation and the experimental procedure are described elsewhere [Böhm et al. 2004]. Based on error propagation considerations, the error of the initial residual stress measurement ($\sin^2\psi$ method) was estimated to be about ± 50 MPa. The measurement error for the stress changes ($\sin^2\varphi$ method) was only about ± 10 MPa. While the total error thus added up to ± 60 MPa, the relative stress difference between the data points could be determined with very good accuracy which led to well defined stress-strain curves.

In this study different Au and Cu film systems were investigated. The corresponding photon energy for the application of the $\sin^2\varphi$ method was 7.91 keV for Au and 8.92 keV for Cu respectively. The required energy range and the accessibility to a big CCD area detector (MarCCD by Mar, Evanston/IL, USA) made the MPI-MF beamline at the synchrotron radiation source ANKA (Angströmquelle Karlsruhe, Germany) an ideal tool for this kind of measurement. Figure 3.3a shows the experimental setup at the MPI-MF beamline for tensile tests using the $\sin^2\varphi$ method. The screw-driven microtensile tester with a 250 N load cell (Kammrath & Weiss, Dortmund, Germany) was mounted in the center of the diffractometer. For the tensile test, the displacement of the crossheads was increased in steps of 20 to 100 μm . During X-ray exposure, the crosshead position was kept constant. The total strain was measured simultaneously by a laser extensometer (Fiedler Optoelektronik, Germany) or by a two-dimensional optical strain measurement (2D-Strainmaster, LaVision, Göttingen, Germany).



(a)



(b)

Figure 3.3: (a) Experimental setup at the MPI-MF-Beamline for *in-situ* experiments using the $\sin^2\varphi$ method. (b) Stress vs. total strain for a 40 nm thick Au film. The initial residual equibiaxial stress state is determined by a classical $\sin^2\psi$ measurement. In addition, the von Mises stress calculated from the experimental values for longitudinal and transverse stress is plotted in the same graph.

Exemplary results from a tensile test on a 40 nm Au film are presented in figure 3.3b. The sample was loaded to a total strain of 2.9% and subsequently unloaded. In figure 3.2b the stress evolution in the Au film is shown. In the as-deposited state, the film exhibited an equibiaxial compressive stress of about -250 MPa. This was the result of the thermal history during film preparation. During the tensile test a stress increase was observed in the longitudinal as well as the transverse direction. This was due to the dissimilar Poisson's ratios of film and substrate. Both stress-strain curves were nonlinear, indicating that the film underwent plastic deformation. Upon unloading the stress state was again compressive because the metallic film had been deformed plastically in contrast to the fully elastic substrate. Since the complete stress tensor was determined, additional parameters essential for plasticity such as the von Mises stress could be obtained.

With this novel technique, the isothermal mechanical properties of thin metallic films in the thickness regime of 40 nm and less can be measured. The sample preparation is simple and compatible to a wide range of crystalline materials. In addition the deformation behavior at high strains and defined temperatures can be measured. First experiments have shown that a strain resolution significantly better than 10^{-4} is achieved and strain rates up to 10^{-4} s^{-1} are possible. Only the required usage of synchrotron radiation limits the general availability.

4 Yield strength and strain hardening of ultra thin Cu films with and without passivation layers

4.1 Introduction

The smallest line widths and film thicknesses of metallic structures in current microsystems have reached length scales well below 100 nm (90 nm in 2004, 65 nm in 2007, 45 nm in 2010 [ITRS 2003]). Therefore understanding the scaling behavior in the mechanical properties of metallic films on the nanoscale is essential for ensuring the reliability of such structures [Arzt et al. 2001, Dehm et al. 2002a, Kraft et al. 2002], is still incomplete. Compared to preparation and structuring of metallic films, the downscaling of mechanical testing techniques is more challenging and experimental data for films thinner than 100 nm are rare. They are, however, crucial for the validation and extension of current models of thin film mechanical behavior to smaller length scales.

Several specialized techniques have been developed to characterize the mechanical properties of thin films in the micrometer and sub-micrometer regime (for reviews see [Nix 1989, Brotzen 1994, Kraft and Volkert 2001]). In general, the mechanical properties of thin films can be investigated by i) testing of thin films deposited on substrates, which involves minimum sample preparation, but requires significant effort to extract the intrinsic film properties from the experimental data or ii) mechanical characterization of freestanding films, which requires careful specimen processing and handling.

For films thinner than 100 nm both approaches encounter distinct problems. Films on substrates have been tested down to 30 nm by wafer curvature techniques, e.g. [Balk et al. 2003b]. Alternatively, a tensile test approach has been developed to investigate 40 nm thick films on very thin polyimide substrates (3.5 μm thick). Here, the film stresses is estimated from the small difference between the load-strain curve of the film-substrate composite and the substrate [Kang et al. 1997, Tregilgas and Strumpell 1998]. However, the wafer curvature technique suffers from the limitation that strain and temperature evolution are intrinsically coupled leading to complicated stress-temperature curves which are difficult to interpret. On the other hand, the backcalculating approach ignores that the stresses in the film are biaxial

due to the mismatch in Poisson's ratio between film and substrate. Freestanding films down to 30 nm were tested in a tensile test chip developed by Haque and Saif [2002]. Fabricated by micromachining techniques, it consists of the film, Si beams for film support and force and displacement measurement devices. The latest design also includes a four-point electrical resistivity measurement [Han and Saif 2006]. While this is an excellent tool for *in situ* transmission and scanning electron microscopy studies, sample fabrication is complicated and it is tedious to change sample dimensions or the interfacial properties.

All of these methods have provided important information regarding thin film behavior, but a conclusive picture down to nanoscopic film dimensions has not yet been obtained. The reason lies in the difficulty to compare experimental data obtained by different testing techniques under very different testing conditions, e.g. stress state, strain rate, temperature, tested volume, microstructure, interfaces (freestanding, substrate confined, surface oxide/passivation), accessible length scale.

Our group has in recent years developed a novel synchrotron-based testing technique [Böhm et al. 2004], by which it is possible to characterize the stress evolution in metallic films thinner than 40 nm *in situ* during isothermal tensile tests. The samples consist of metallic films deposited on compliant polymer substrates (polyimide foil). Stresses are measured only in the metallic film of interest. Therefore this technique allows the influence of very different interfaces to be investigated: the cases of compliant amorphous polymer substrates as well as polymer substrate and additional stiff crystalline metallic layers on one or both sides are expected to have a strong effect on the film properties [Nix 1989, von Blanckenhagen 2002, Needleman et al. 2006].

In the current study, copper was chosen as a model system for the mechanical behavior of fcc films. For this metal, which does not form a dense natural oxide layer, a first systematic study of different Cu film systems with and without Ta capping or interlayer on polyimide substrates is presented. A representative dataset for Cu films of different surface and interface conditions was obtained by the same testing technique and over a wide range of film thickness between 20 nm and 3 μm . For comparison, a set of freestanding Cu films of similar microstructure and film thickness range (80 to 1000 nm) was tested by a bulge testing technique of our own design. The results are discussed in the light of thin film plasticity models dealing with confinement of dislocation motion [Nix 1989, Thompson 1993] or

dislocation nucleation and interaction [von Blanckenhagen 2002, von Blanckenhagen et al. 2003, Needleman et al. 2006]. It is found that the scaling behavior of mechanical properties cannot be explained by simply considering the film thickness, but the broad grain size distribution in thin films seems to play an important role.

4.2 Experimental

4.2.1 Sample preparation

Different kinds of samples were prepared for the two testing techniques. For tensile testing, films were deposited on 125 μm thick dogbone-shaped polyimide substrates (Kapton® HN) with a gauge section of 6 mm x 20 mm. Prior to film deposition the substrate surface was sputter cleaned using an Ar^+ plasma (105 V, 0.8 A) over 1 min. Different Cu, Ta/Cu and Ta/Cu/Ta film systems were prepared (figure 4.1a-c). Cu as well as Ta films were deposited using a direct-current (DC) magnetron sputter deposition system with a base pressure of 1×10^{-8} mbar, a DC power of 200 W (Cu) or 100 W (Ta) and a Ar pressure of 4.2×10^{-3} mbar. The corresponding deposition rates were 45 nm/min (Cu) and 12 nm/min (Ta). The thickness of the Cu films was varied between 20 and 3000 nm whereas the Ta film thickness was always 10 nm. After deposition all samples were annealed without breaking vacuum at 350°C for 0.5 h to obtain a columnar grain structure and mean grain sizes larger than the film thickness. Higher annealing temperatures were not possible due to the limited thermal stability of the polyimide substrate.

For the bulge test, 80 to 1000 nm thick Cu films were deposited under identical conditions onto commercially available 200 nm thick amorphous SiN_x -membranes (Silson Ltd, Northhampton, England). On the backside of the SiN_x -membrane two windows 1 mm x 4 mm in size [Vlassak and Nix 1992] were produced by photolithography and subsequent anisotropic etching of the (100)-oriented Si wafer. After deposition, the samples were annealed at 500°C for 1h to stabilize the microstructure and to ensure a tensile stress in the Cu film to avoid buckling of the sample. Finally the remaining SiN_x layer was removed in a CF_4/O_2 -plasma over 4 min at a RF-power of 60 to 100 W and a pressure of 2×10^{-1} mbar. Figure 4.1d shows a schematic cross-section through the sample in the area of the freestanding Cu film.

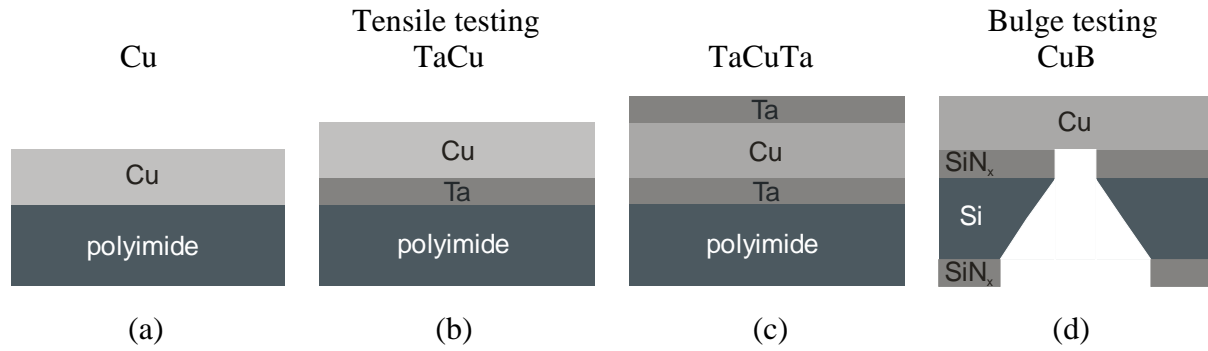


Figure 4.1: Schematic drawing of all samples, (a)–(c) Cu, Ta/Cu and Ta/Cu/Ta film systems on polyimide substrates for tensile testing and (d) freestanding Cu films for the bulge test.

4.2.2 Microstructural characterization

The grain structure of the Cu and Ta/Cu films on polyimide was characterized using electron backscatter diffraction (EBSD) in a scanning electron microscope (SEM) and plan-view transmission electron microscopy (TEM). Films thicker than 160 nm were investigated using an EBSD system (HKL Channel 5) attached to a Leo 1530-VP field emission SEM. The measurements were carried out at a working distance of 13 mm and an accelerating voltage of 20 kV. Areas between $7.5 \times 7.5 \mu\text{m}^2$ and $15 \times 15 \mu\text{m}^2$ were scanned at step intervals of 30 nm to determine grain orientations, size and shape. The data were analyzed using the HKL-software package. Plan-view TEM samples were cut out of the Cu and Ta/Cu films with less than 80 nm thickness and were thinned to electron-transparency by dimpling and ion milling. TEM investigations were carried out using a 200 kV TEM (Phillips CM200, Jeol 2000FX). The grain boundaries from the TEM pictures were drawn manually on a transparency foil, which was digitized and analyzed by a computer software for quantitative image analysis (Leica Quantimet Q5501W). The same procedure was used to analyze micrographs of the freestanding Cu films produced by focused ion beam (FIB) microscopy (FEI FIB 200xP). In order to ensure the identification of all grain boundaries by the channeling contrast in the FIB, images with at least three different tilt angles typically between 0 and 25° were taken and compared. Independent of the imaging technique, several regions of the sample were investigated to obtain reliable and reproducible data (at least 300 to 2000 grains). The grain size was defined as the diameter of a circle with the equivalent area and twin boundaries and boarder grains were ignored.

The thickness of the freestanding Cu films was determined by milling cross-sections in the FIB and measuring the projected film thickness taking into account the tilt angle of 45° . The thickness of the individual layers in the different Cu, Ta/Cu and Ta/Cu/Ta film systems on polyimide was determined by Rutherford backscattering spectrometry (RBS). All RBS measurements were conducted using 2 MeV He^+ ions (6.5MV Pelletron accelerator of the Max Planck Institute for Metals Research). The film thickness of the Ta as well as Cu films could be obtained by fitting the RBS spectra of the Si detector with the X-Rump simulation software (Computer Graphics Service Ltd.) taking into account the scattering geometry, ion species and energy. The energy resolution of the Si detectors used was 20 - 40 keV.

4.2.3 Mechanical testing

The experimental setup and procedure, data acquisition and analysis as well as the unique features concerning the synchrotron-based tensile testing technique are described for Au films in detail elsewhere [Böhm et al. 2004]. All tensile tests were performed at the MPI-MF-beamline of the synchrotron radiation source ANKA (Angströmquelle Karlsruhe). For the study of the different Cu, Ta/Cu and Ta/Cu/Ta film systems on polyimide the energy was adjusted according to the lattice spacing of Cu. For the initial $\sin^2\psi$ -measurement (determination of residual stress) the photon energy was selected to 8.00 keV. For the subsequent $\sin^2\phi$ -measurements (determination of stress evolution during the tensile test) the photon energy was adjusted to 8.92 keV; thus the complete Debye-Scherrer ring of the inclined $\{111\}$ planes of the $\langle 111 \rangle$ fiber textured Cu films could be recorded on the CCD area detector (MarCCD) in a simple transmission geometry [Böhm et al. 2004]. For calibration, tungsten powder was attached to the backside of the polyimide substrate by vacuum grease. During the tensile test the crosshead displacement of the tensile tester (Kammrath & Weiss) was increased in steps between 30 and 100 μm up to maximum displacements of 750 to 1900 μm and subsequently decreased again. For each step a CCD frame was taken. The exposure time was varied between 20 and 120 s with respect to the diffracted signal (longest exposure time for the thinnest films). The elastic lattice strains in longitudinal and transverse direction can be deduced from the elliptical distortions of the Debye-Scherrer rings. For both diffraction geometries ($\sin^2\psi$ - and $\sin^2\phi$ -measurement) the film stress is obtained from the measured elastic strains via Hooke's law [Böhm et al. 2004]. The necessary stiffness matrix for a perfect $\langle 111 \rangle$ fiber texture in the specimen coordinate system and its relationship to the elastic constants in crystal coordinates for Cu are given in

chapter 9.1. The total strain of the samples was measured by a laser-extensometer (Fiedler Optoelektronik). By comparing the film stress measured by synchrotron X-ray diffraction to the total strain of the film-substrate composite, isothermal stress-strain curves for the different specimens could be obtained.

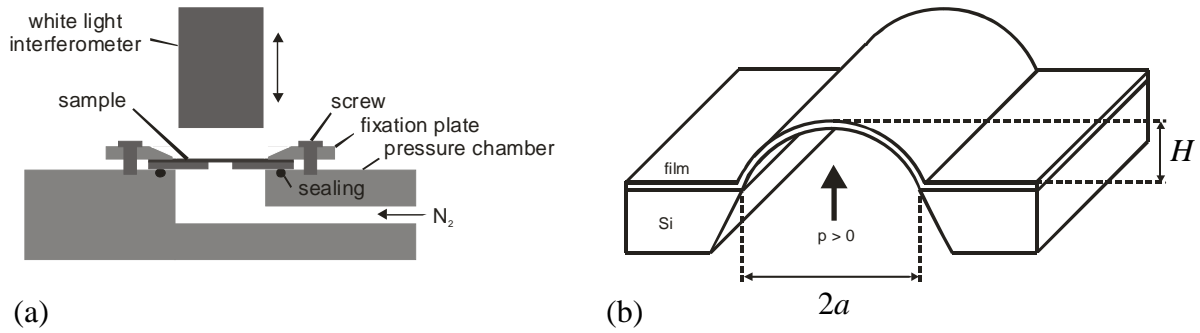


Figure 4.2: Schematic illustration of (a) experimental setup for the bulge test and (b) geometry of membrane deflection under uniform pressure on one side of the freestanding membrane (only a section of the rectangular membrane is shown).

For the bulge testing of the freestanding Cu films a new setup was built (figure 4.2a). With the help of a seal, the samples were fixed by a round plate which was screwed on top of a pressure chamber. The setup was installed on the table of a white light interference microscope (Zygo NewView 5000). The deflection δ of the membrane (figure 4.2b) was determined by measuring the mean height along the center of the membrane. The pressure on the membrane was measured by a capacitive pressure cell (pressure range 1000 mbar, MKS Baratron® 223B) and adjusted by a controller (MKS 250E) equipped with a steerable valve (MKS 248C). In order to vary the dynamic behavior of the pressure system, an additional manual leakage valve was introduced. The accuracy of the pressure control was 1 to 2 mbar. During the bulge test the pressure was varied in steps of 1 to 20 mbar and for each step the membrane deflection was measured. The stress σ and strain ε in the rectangular membrane were determined from the applied pressure p and the membrane deflection H using the following expressions [Xiang et al. 2005a]:

$$\sigma = \frac{p(a^2 + H^2)}{2Hh} \quad \text{and} \quad (4-1)$$

$$\varepsilon = \varepsilon_0 + \frac{a^2 + H^2}{2aH} \arcsin\left(\frac{2aH}{a^2 + H^2}\right) - 1,$$

where h is the film thickness, $2a$ the width of the membrane (figure 4.2b) and ε_0 the residual strain in the film. These equations are valid for elastic and plastic deformation.

4.3 Results

4.3.1 Microstructure

All films showed equiaxed grains with some twinning; several special features were found for each film system. EBSD orientation maps as well as TEM and FIB micrographs are shown in figure 4.3. EBSD measurements revealed that the introduction of the Ta interlayer led to a nearly perfect $\langle 111 \rangle$ fiber texture. The volume fraction of (111) oriented grains (marked in blue in figure 4.3a and b) was found to be 88.7% for a 640 nm thick Cu film on Ta (figure 4.3b) compared to 67.5% for a 160 nm thick Cu film on polyimide (figure 4.3a). Consequently the volume fraction of the second texture component of (100) oriented grains (marked in red) was higher for the 160 nm Cu film (13.7% to 3.8%). In addition to grain orientation the EBSD measurements were used to determine the grain size distribution of Cu and Ta/Cu films thicker than 160 nm (table 4.1).

For thinner films the indexing rate of the EBSD system became too low due to the weak and diffuse Kikuchi patterns. Therefore Cu and Ta/Cu films below 160 nm film thickness were investigated by TEM. Exemplary plan-view TEM micrographs are shown in figure 4.3c and d for a 40 nm thick Cu film and an 80 nm thick Ta/Cu film on polyimide. Due to the Ta interlayer the micrograph of the Ta/Cu film was not as clear as for the Cu film but the Cu grain boundaries could still be detected. Grain size distributions were obtained for both film systems in the thickness regime between 30 and 80 nm (table 4.1).

The freestanding Cu films were analyzed by FIB microscopy. Grains were detected by the channeling contrast in plan-view micrographs (figure 4.3e) for all film thicknesses between 80 and 800 nm. In addition, the FIB system was used to prepare cross-sections of the films (figure 4.3f) in order to determine the film thickness. Beside the film thickness the cross-section also revealed a completely columnar grain structure even for the thickest films as shown for an 800 nm thick film in figure 4.3f. The data for the freestanding Cu films are summarized in table 4.2.

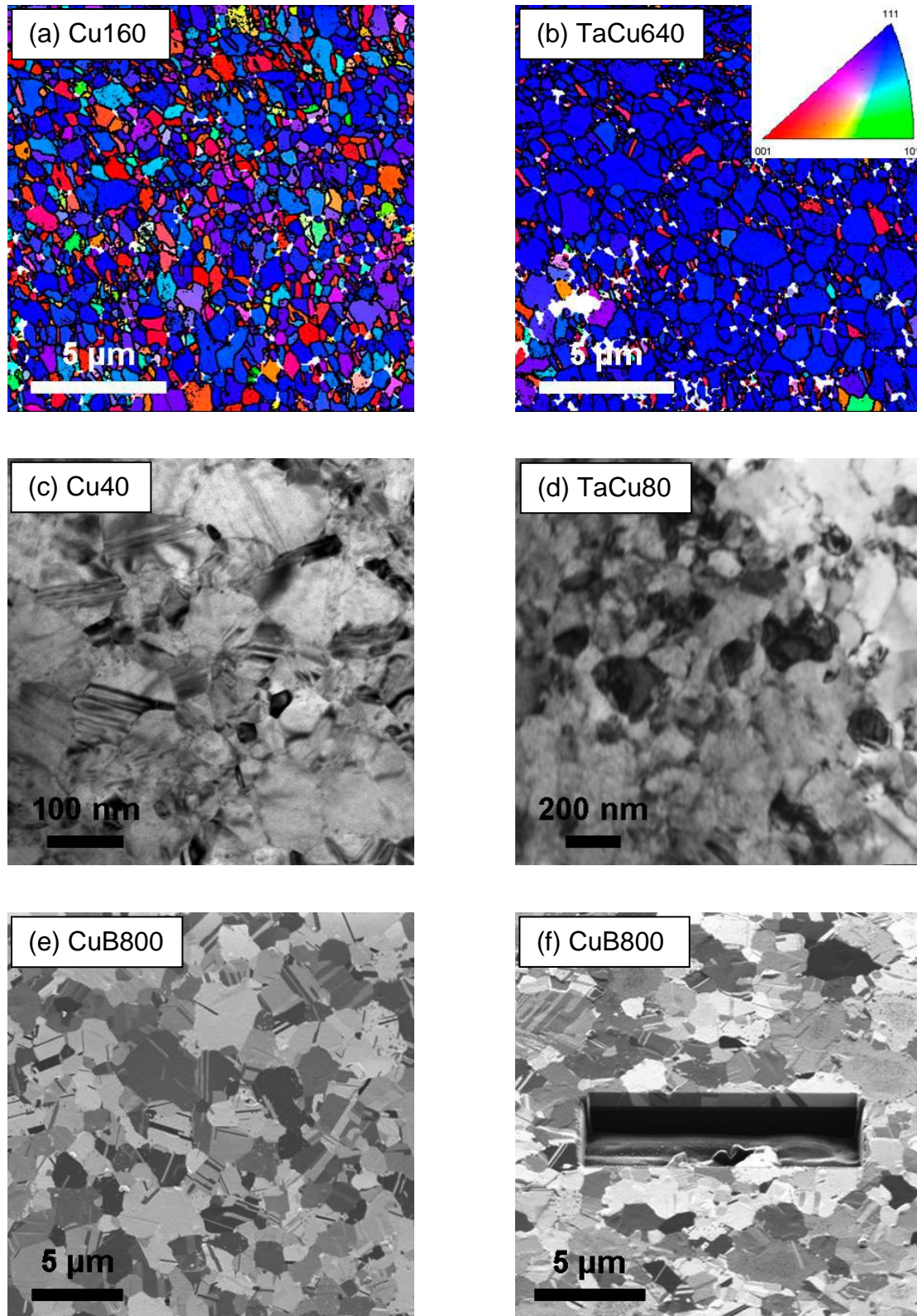


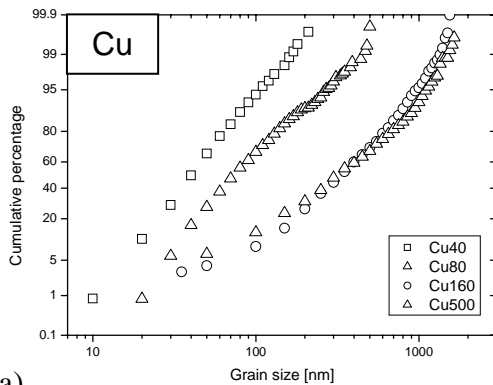
Figure 4.3: Microstructural characterization of the different samples: EBSD orientation maps of (a) a 160 nm thick Cu film and (b) a 640 nm thick Ta/Cu film on polyimide. The orientation normal to the film surface is represented according to the color key shown in the upper right of (b). Both films show a pronounced (111) fiber texture with a small fraction of (100) oriented grains. Non-indexed regions and spots are shown in white. TEM micrographs are of (c) a 40 nm thick Cu film and (d) an 80 nm thick Ta/Cu film on polyimide. Plane-view (e) and cross-sectional (f) FIB image showing an 800 nm thick freestanding Cu film. The cross-section reveals a columnar grain structure.

Table 4.1: Cu and Ta/Cu on polyimide: Median grain size d_{50} , mean grain size d_{mean} , standard deviation σ_{dev} , maximum grain size d_{max} , number of detected grains N and used experimental technique for all Cu and Ta/Cu films on polyimide.

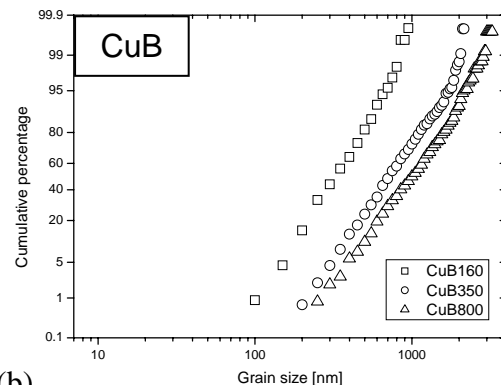
Sample	d_{50} [nm]	d_{mean} [nm]	σ_{dev} [nm]	d_{max} [nm]	N	Method
TaCu30	31	37	23	161	336	TEM
TaCu40	44	53	34	230	387	TEM
TaCu60	58	70	45	310	423	TEM
TaCu80	93	104	49	405	502	TEM
TaCu160	192	252	167	1204	1233	EBS
TaCu320	211	297	283	2273	1457	EBS
TaCu640	197	307	297	2991	1340	EBS
Cu30	29	36	22	159	316	TEM
Cu40	40	48	31	242	348	TEM
Cu60	70	84	54	469	371	TEM
Cu80	75	99	83	581	474	TEM
Cu160	333	407	289	1267	976	EBS
Cu240	303	388	280	1674	1101	EBS
Cu500	325	424	343	1852	499	EBS
Cu1000	293	423	368	2873	885	EBS

 Table 4.2: Freestanding films: Nominal and measured film thickness h , median grain size d_{50} , mean grain size d_{mean} , standard deviation σ_{dev} , maximum grain size d_{max} and number of detected grains N .

Sample	h [nm]		Grain size statistics				
	nominal	measured	d_{50} [nm]	d_{mean} [nm]	σ_{dev} [nm]	d_{max} [nm]	N
CuB80	80	86 ± 10	153	169	84	498	1598
CuB160	160	174 ± 23	323	355	172	1125	2128
CuB250	250	251 ± 20	658	724	378	1865	1711
CuB300	300	296 ± 21	541	595	265	1728	2047
CuB350	350	353 ± 20	753	824	427	2162	1955
CuB400	400	430 ± 24	822	904	429	2788	2379
CuB800	800	812 ± 28	969	1066	582	3581	1235



(a)



(b)

Figure 4.4: Exemplary grain size distributions for (a) Cu films on polyimide and (b) freestanding Cu films. For increasing film thickness the distributions are shifted to higher grain sizes. For films on polyimide this trend stops for film thicknesses above 160 nm; for freestanding films it is valid for all thicknesses up to 800 nm.

4 Yield strength of ultra thin Cu films with and without passivation

The grain size distributions for films on polyimide as well as freestanding films were found to be predominantly lognormal and the median grain size increased with film thickness. Nevertheless, for films on polyimide thicker than 160 nm a distinct deviation from this trend was observed (figure 4.4a). First, many small grains remained after annealing and second, very broad grain size distributions with nearly constant median and mean values were obtained for increasing film thickness. This was attributed to the relatively low annealing temperature of 350°C which is limited by thermal stability of the polyimide substrate. Thus, the mobility of the grain boundaries was low and grains did not grow homogenously. The freestanding Cu films, which could be annealed at 500°C, showed narrower grain size distributions but the increase in grain size became also lower for thicker films (figure 4.4b).

Table 4.3: Nominal and measured Cu and Ta film thicknesses for all Cu, Ta/Cu and Ta/Cu/Ta film systems on polyimide. The error of the RBS measurements was below 2%.

Sample	Ta film thickness [nm]		Cu film thickness [nm]		Ta film thickness [nm]	
	nominal	measured	nominal	measured	nominal	measured
TaCuTa20	10	9	20	15	10	9
TaCuTa40	10	9	40	35	10	9
TaCuTa50	10	9	50	41	10	8+2*
TaCuTa80	10	9	80	71	10	9
TaCuTa100	10	9	100	86	10	8+2*
TaCuTa300	10	8	300	255	10	7+3*
TaCuTa500	10	8	500	422	10	7+3*
TaCuTa750	10	8	750	637	10	7+3*
TaCuTa1500	10	8	1500	900	10	7+3*
TaCu30	10	9	30	22	* Ta ₂ O ₅ layer	
TaCu40	10	9	40	34		
TaCu60	10	9	60	48		
TaCu80	10	9	80	67		
TaCu160	10	8	160	91		
TaCu320	10	8	320	251		
TaCu640	10	8	640	506		
Cu30			30	23		
Cu40			40	31		
Cu60			60	45		
Cu80			80	59		
Cu160			160	120		
Cu240			240	185		
Cu500			500	389		
Cu1000			1000	765		

Analysis of the Ta/Cu films on polyimide gave very similar values for the grain size and grain size distributions. It was not possible to determine the grain size of the Ta/Cu/Ta film systems as all attempts to remove the Ta surface layer in a controlled manner failed. Therefore, it was assumed that the grain size distribution of Cu films with one or two Ta layers was the same.

The thicknesses of Ta and Cu films on polyimide, measured by RBS, are summarized in table 4.3. The difference between nominal and real film thickness was about 10 to 20%. During deposition the film thickness was adjusted via the sputtering time, which apparently gave a systematic offset. For the freestanding films the deposition rate was better calibrated yielding smaller differences between nominal and measured film thickness (table 4.2). The RBS spectra of some Ta/Cu/Ta film systems indicated a 2 to 3 nm thick tantalum oxide layer at the surface.

In figure 4.5 the film thickness is plotted against the median grain size and the aspect ratio between median grain size and film thickness. For films on polyimide, the median grain size at first increases linearly with thickness, followed by a thickness independent grain size for films thicker than 160 nm. In contrast, the grain size of freestanding films increased over the whole thickness regime. This affects the thickness dependence of the aspect ratio between grain size and film thickness: For the freestanding films no systematic trend was observed whereas for the films on polyimide the aspect ratio first increased above 3 for a film thickness of 160 nm and then decreased for the thicker films to below 1. We note that up to this point the grain size was always larger than the film thickness

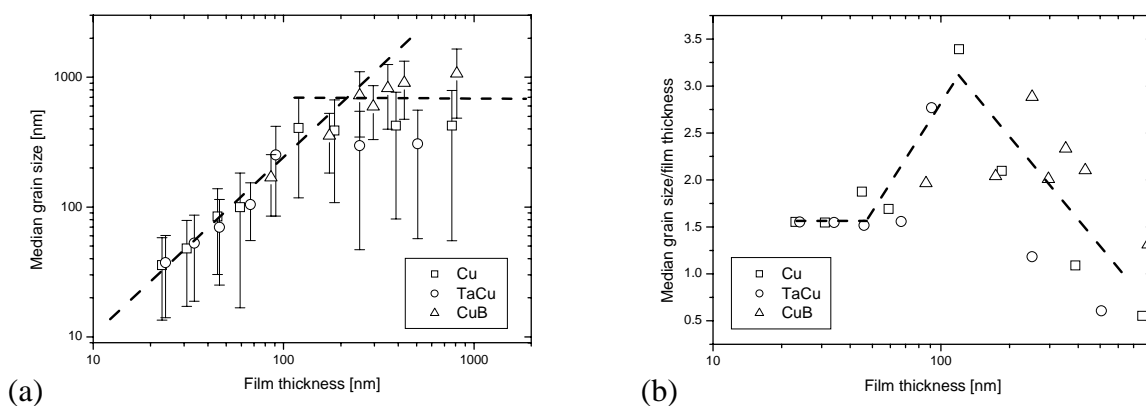


Figure 4.5: (a) Median grain size and (b) median grain size/film thickness vs. film thickness for Cu and Ta/Cu films on polyimide as well as freestanding Cu films. Films on polyimide show a constant grain size for a film thickness above 160 nm whereas the grain size of freestanding films show a linear increase of grain size for all film thicknesses. The film thickness dependence of the aspect ratio of the columnar films also changes for thicknesses above 160 nm.

4.3.2 Stress-strain curves

Figures 4.6 to 4.8 show the results for complete sets of film thicknesses in the range from 20 to 1000 nm for the Cu, Ta/Cu and Ta/Cu/Ta film systems. The stress evolution in the Cu films during external loading in the longitudinal as well as transverse direction is shown. The maximum total strain was varied between 3 and 7%. The overall behavior of Cu films in the different film systems was very similar when the Cu film thickness was above 300 nm, although the absolute stress values were different. First the longitudinal stress increased linearly, followed by yielding and a small strain hardening regime. In almost all cases a plateau stress was found up to the maximum total strain. Upon unloading, again a linear, yielding and strain hardening regime was observed. The stress in the transverse direction was always smaller but of the same sign as the longitudinal stress. It resulted from the mismatch in Poisson's ratio of the Cu film and the polyimide substrate ($\text{Cu}_{(111)[110]}$: 0.51, polyimide: 0.34 [Dupont]).

For Cu films thinner than 200 nm adjacent layers affected not only the absolute stress values but also the shape of the stress-strain curves (compare figures 4.6 to 4.8). Whereas Cu films directly deposited on polyimide showed no distinct change in the stress-strain curve, the introduction of at least one Ta layer gave a sudden stress drop at a total strain of about 2 to 3%. This could be attributed to channel cracking in the Cu films resulting in local stress relaxation and a decrease in the average stress of the film [Gruber et al. 2004]. A more detailed analysis of the fracture behavior combining the stress measurements shown above with results of *in situ* tensile tests in a SEM and fracture toughness calculations is conducted in chapter 5.

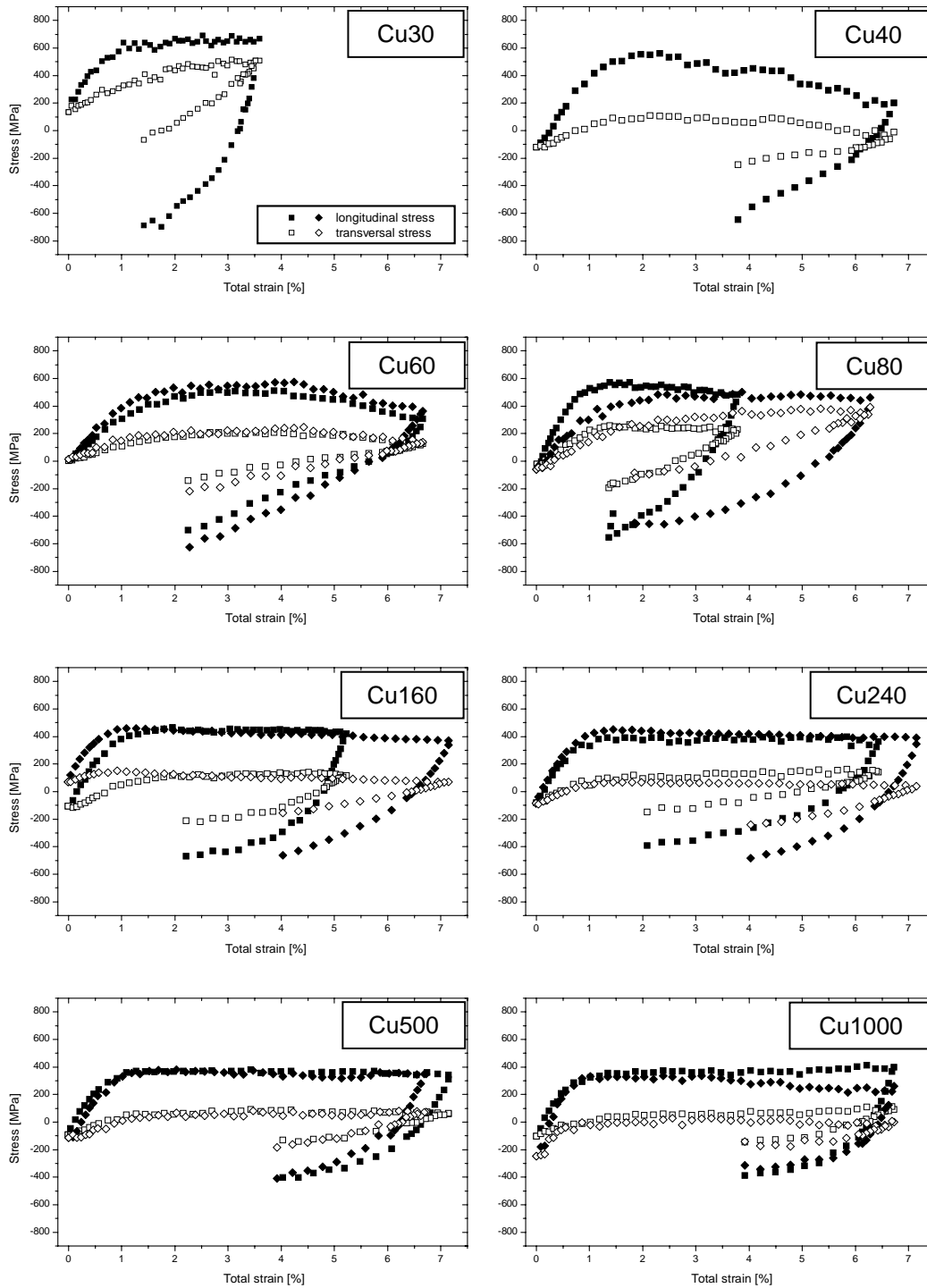


Figure 4.6: Cu films on polyimide: Stress-strain curves for 30 – 1000 nm thick Cu films measured by the synchrotron-based tensile testing technique. Filled symbols represent the longitudinal stress and open symbols represent the transverse stress. One or two samples were measured for each film thickness.

4 Yield strength of ultra thin Cu films with and without passivation

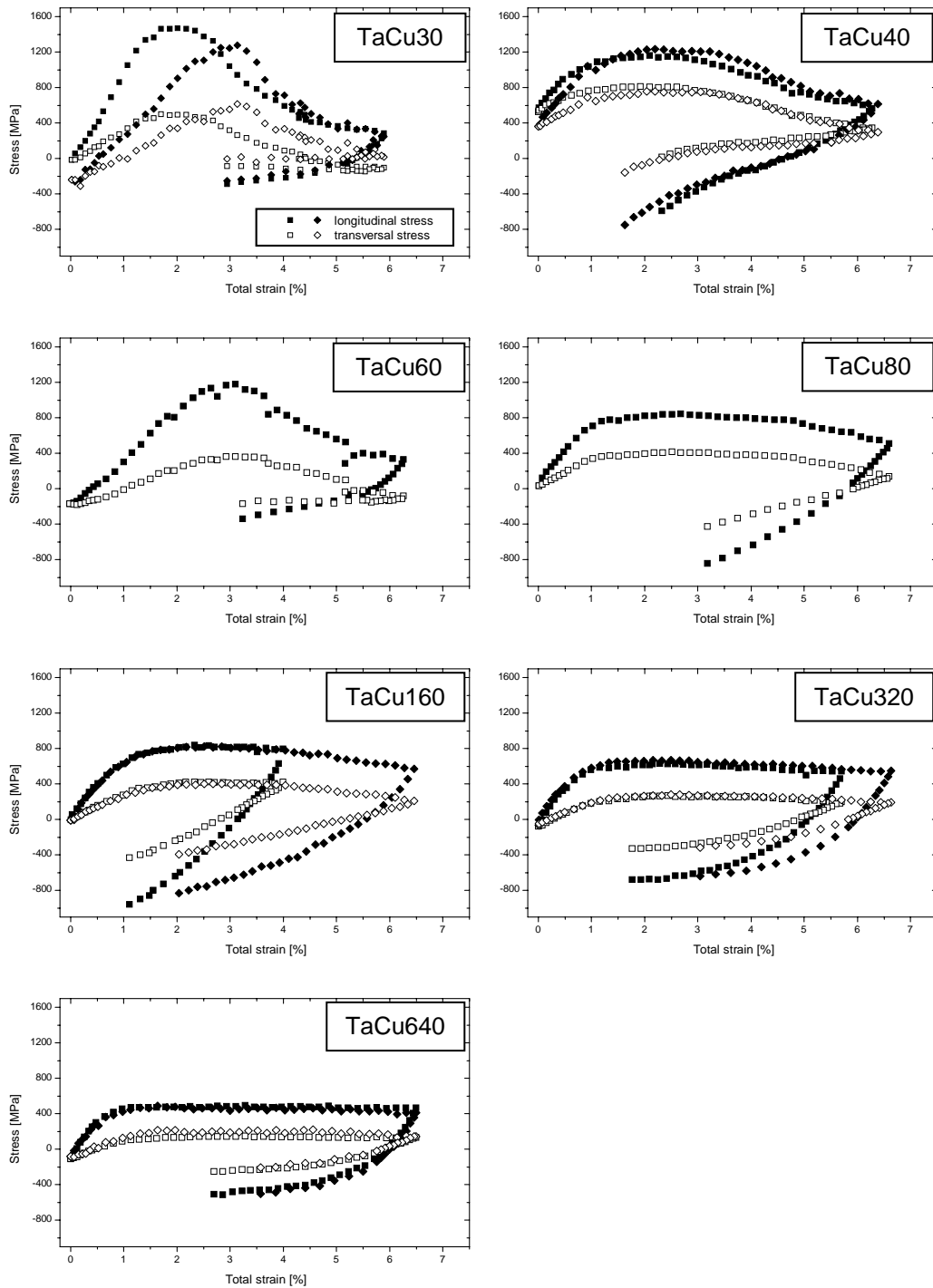


Figure 4.7: Ta/Cu films on polyimide: Stress-strain curves for 30 – 640 nm thick Cu films measured by the synchrotron-based tensile testing technique. Filled symbols represent the longitudinal stress and open symbols represent the transverse stress. One or two samples were measured for each film thickness.

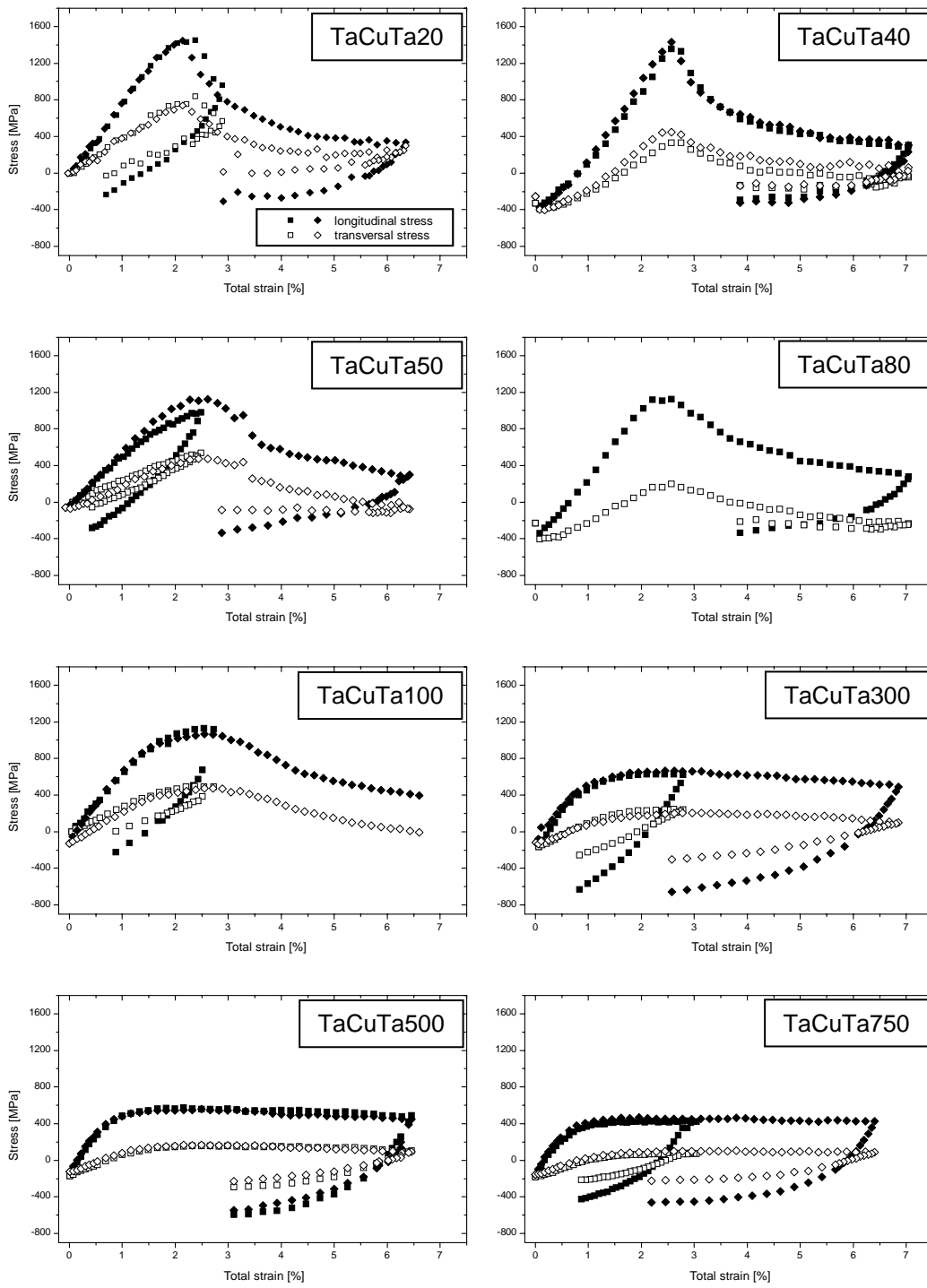


Figure 4.8: Ta/Cu/Ta films on polyimide: Stress-strain curves for 20 – 750 nm thick Cu films measured by the synchrotron-based tensile testing technique. Filled symbols represent the longitudinal stress and open symbols represent the transverse stress. One or two samples were measured for each film thickness.

4 Yield strength of ultra thin Cu films with and without passivation

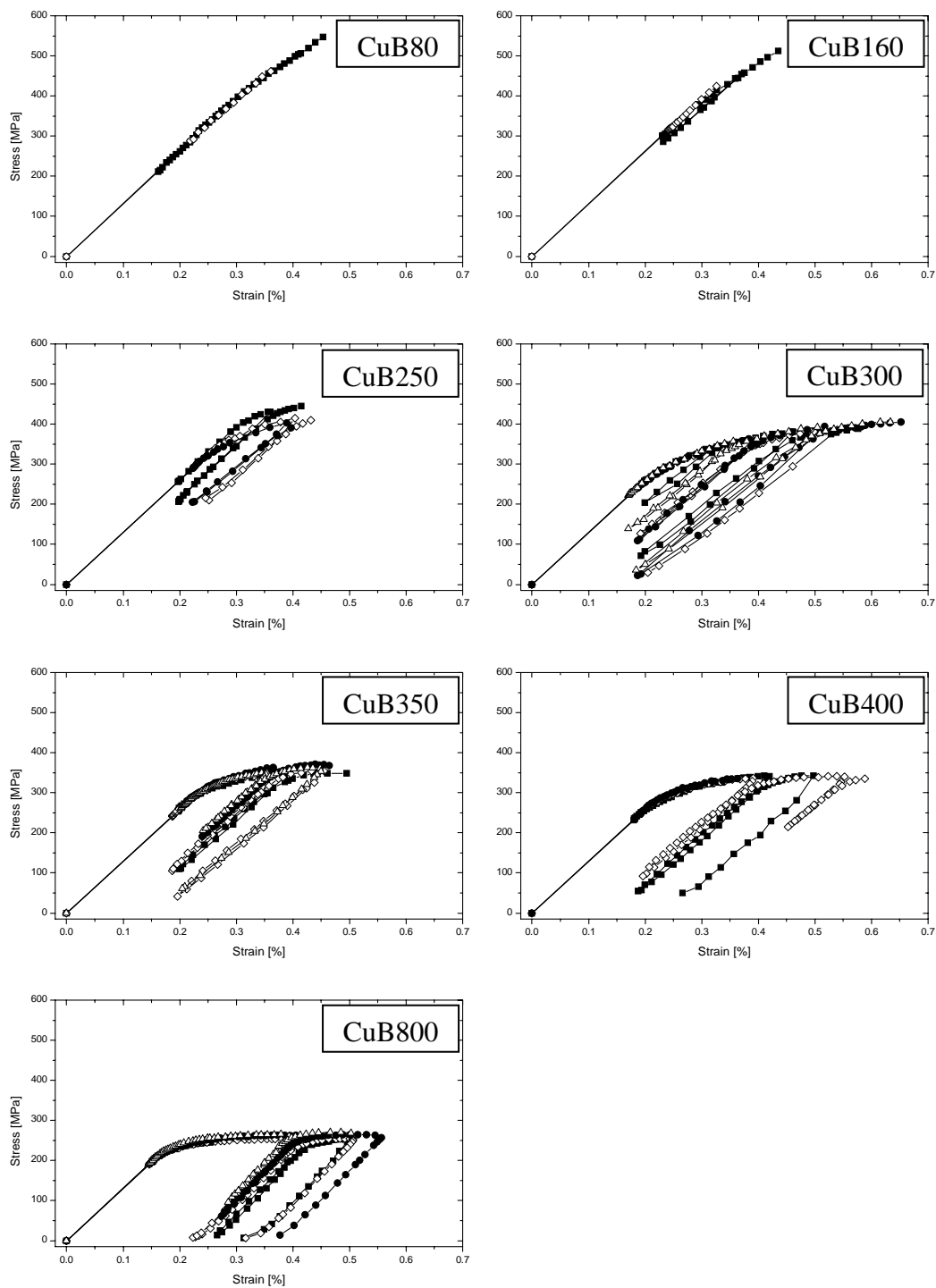


Figure 4.9: Freestanding Cu films: Stress-strain curves for 80 – 800 nm thick Cu films measured by the bulge test. The stress-strain curves are offset by the residual strain in the films (straight line starting from origin). During the bulge test the sample were sometimes unloaded and reloaded again. Up to 4 different films were tested for each film thickness.

The results of bulge tests on freestanding Cu films are shown in figure 4.9. The tests gave a stress-strain curve starting at the equi-biaxial residual stress of the membrane. This stress strain curve was shifted by the equi-biaxial residual strain calculated via Hooke's law from the measured values for the residual stress and the plane-strain modulus. Thus, absolute strain values could be obtained for all samples allowing for direct comparison of the results. During the test the samples were unloaded several times until the freestanding films ruptured. The maximum strain on the samples decreased from around 0.6% for the thicker films to 0.4% for the thinnest films making it difficult to see plastic deformation in the 80 nm thick Cu film. Nevertheless the yield strength for least at 0.1% plastic strain could be determined for all film thicknesses.

4.3.3 Apparent and plane-strain moduli

The initial slope of the longitudinal stress-strain curves in figures 4.6 to 4.8 can be referred to as an apparent modulus. This value may deviate from the real Young's modulus of the film because the film stresses were calculated from the measured lattice strain using the elastic constants for a perfect (111)-fiber texture. No distinct thickness dependence was observed for the film systems on polyimide (figure 4.10a), but with an increasing number of Ta interlayers slightly higher values for the apparent modulus were found. Cu films on polyimide had a mean apparent modulus of 65 ± 15 GPa, whereas it was 69 ± 15 GPa for Ta/Cu films and 80 ± 15 GPa for Ta/Cu/Ta films. The theoretical value for a perfect $\langle 111 \rangle$ fiber texture is 130 GPa. For the bulge tests the plane-strain modulus was determined by analyzing the first unloading segment of the stress-strain curve. This was necessary because of the proximity of residual stresses and flow stress. For the 80 and 160 nm thick films the initial slope was taken because of sample fracture. The values for the plane-strain modulus varied between 117 and 130 GPa and again did not show a clear thickness dependence (figure 4.10b). The plane-strain modulus of a perfect $\langle 111 \rangle$ fiber texture is 181 GPa.

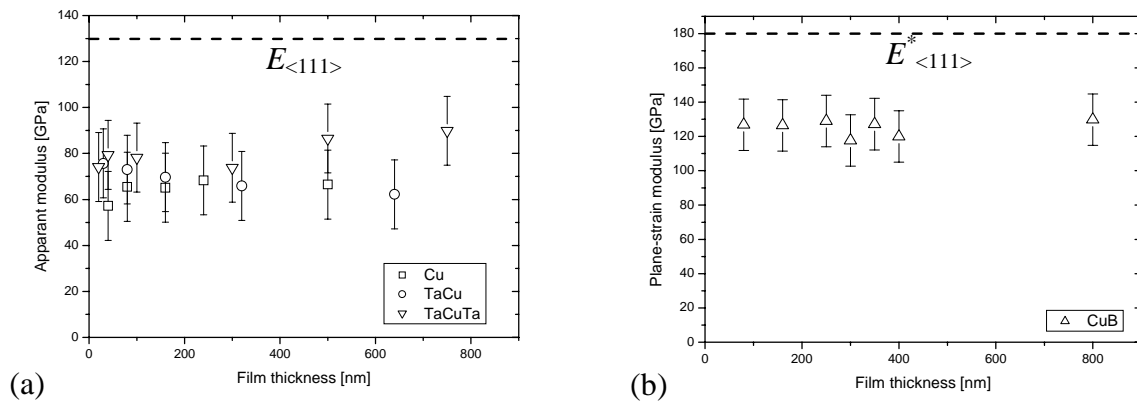


Figure 4.10: Film thickness dependence of (a) the apparent modulus measured with the synchrotron-based tensile testing technique and (b) the plane-strain modulus obtained by the bulge test. For both techniques only a weak thickness dependence of the modulus is found. The dashed lines represent the theoretical values for a perfect <111> fiber texture.

4.3.4 Yield strength

The flow stress for the film systems on polyimide was determined from the von Mises stress at 0.5% plastic strain; this was necessary to account for the biaxial stress state [Böhm et al. 2004]. The stress state for the bulge test is also not uniaxial due to the hindered Poisson's contraction in the membrane. However, the stress perpendicular to the loading axis can be assumed to be equal to half of the stress in loading direction [Xiang et al. 2005a]. Thus the von Mises stress could be calculated. The maximum strain reached during the bulge tests varied with film thickness and was about 0.4%. The only plastic strain value which was reached for all film thicknesses was 0.1%. Therefore the flow stress of the freestanding films was determined for 0.1% plastic strain. The von Mises flow stresses for the tensile and bulge tests are plotted against grain size and film thickness in figure 4.11. For thicker freestanding films, a strong dependence on film thickness was found (slope of -0.4 compared to -0.29 for the grain size). The increase in flow stress was strongly reduced for films thinner than 100 nm (slope of only -0.1 to -0.18). In contrast, the Cu films on polyimide showed a weaker dependence on both grain size and film thickness (slope of -0.14 and -0.12, respectively). The adjacent layers had a strong effect: Freestanding Cu films and Cu films on polyimide showed flow stresses in the range of 250 to 550 MPa, whereas the film systems with at least one Ta layer revealed stresses up to 1300 MPa.

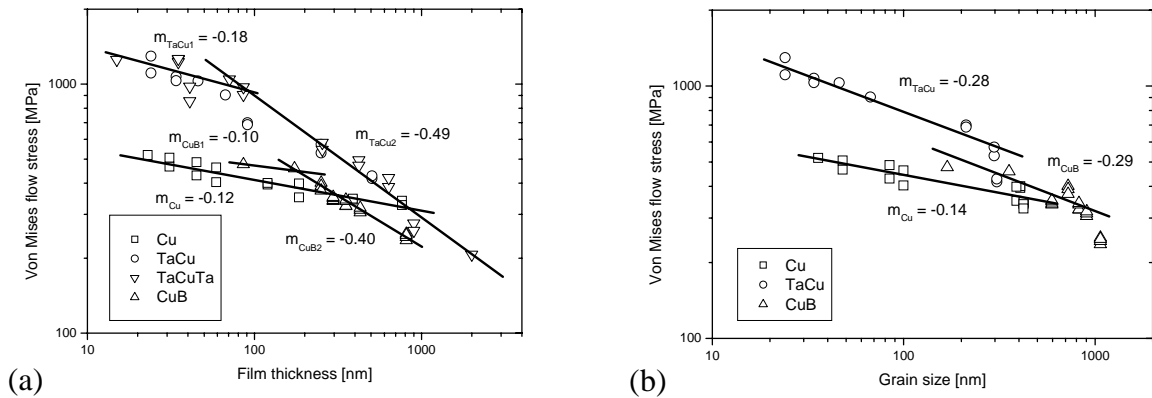


Figure 4.11: Von Mises flow stress vs. (a) film thickness and (b) median grain size for the different film systems. The slopes in the log-log plots for the different film systems indicate a stronger film thickness effect. The introduction of at least one Ta layer gave a distinct increase in flow stress. Data for Ta/Cu/Ta films are not shown in (b) because the grain size could not be measured.

4.3.5 Strain hardening

In order to describe the strain hardening behavior of the different film systems, the difference in stress for two different strain values (0.1 and 0.5% for tensile tests and 0.1 and 0.2% for Bulge tests) was plotted against the film thickness (figure 4.12). Independent of the film system a similar increase of strain hardening was observed with decreasing film thickness down to a thickness of 100 nm (the values for the bulge tests are lower due to the lower difference in permanent strain, but the strain hardening rate is similar). Samples of all film systems below 100 nm thickness show a strongly reduced strain hardening ability.

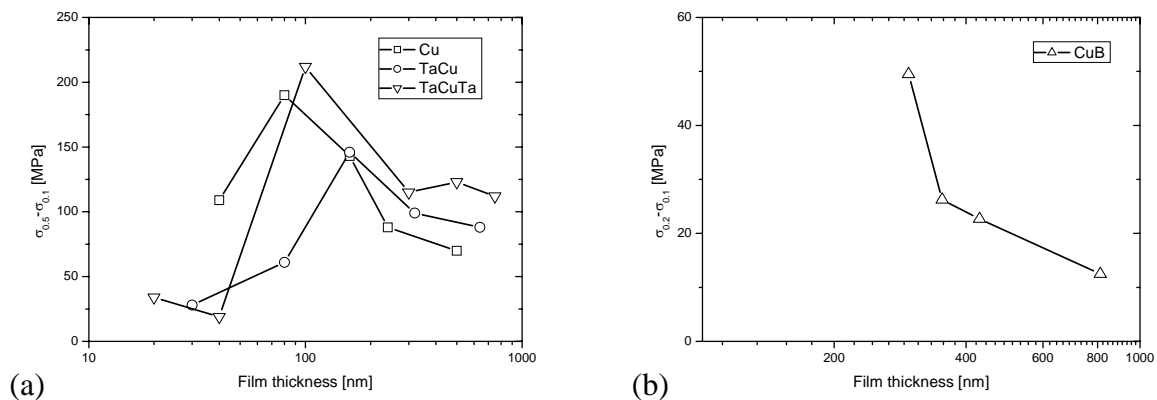


Figure 4.12: Characterization of work-hardening (a) Difference in stress for 0.5 and 0.1% permanent strain for films on polyimide and (b) difference in stress for 0.2% and 0.1% permanent strain for freestanding films vs. film thickness. Note different stress scales. The strain hardening increases for films on polyimide as well as for freestanding films with decreasing film thickness. Similar to flow stress a different behavior is found for films thinner than 100 nm.

4.4 Discussion

4.4.1 Low stiffness of thin Cu films

The apparent moduli as well as the plane-strain moduli obtained were found to be independent of film thickness (figure 4.10). The values are remarkably low and differ for the different film systems and testing techniques. A summary of theoretical and measured values is given in table 4.4. For the Cu films on polyimide the apparent modulus is only about 60% of the value calculated for the given texture of the film. Such a reduction is not unusual: Spaepen et al. found a 20% reduction for tensile tests on electron beam evaporated Cu films on polyimide [Yu and Spaepen 2004] as well as for freestanding Cu films [Huang and Spaepen 2000]. In a detailed study of several plausible mechanisms, like voids, dislocation microplasticity, grain boundary compliance and microcracking, they attributed the stiffness reduction to the imperfection of the grain boundary and the columnar microstructure [Huang and Spaepen 2000]. Similar to their argumentation we can also rule out voids and dislocation microplasticity for our films, since the necessary fraction of voids would be easily detected and no effect of accumulated plastic deformation was found on the measured modulus during multiple loading of the samples.

Compared to their films on polyimide (thickness 0.265 to 2.775 μm and grain size $\sim 1.3 \mu\text{m}$), the contribution of the grain boundaries is expected to be strongly enhanced in our films, which are thinner and have much smaller grain sizes. Given the microstructure of our films, the volume fraction of grain boundaries is about 3 to 10 times higher than in their films. Experiments with a MEMS-based microtensile chip also revealed very low elastic moduli for freestanding Au and Al films with a mean grain size below 100 nm [Haque and Saif 2004]. The reduction was much higher for the Au films and was around 35%. In this study the decrease in stiffness was explained by considering the statistics of the interatomic forces between two atoms in a grain boundary. It was argued that the grain boundary behaves like a softening nonlinear spring. A grain boundary softening mechanism is also expected to depend on grain size. Our films on polyimide show very broad grain size distributions with standard deviations in the range of the grain size. In addition the ratio between grain size and film thickness is not the same for all film thickness (figure 4.5b).

Nevertheless these mechanisms can explain the observed reduction in modulus. The apparent moduli for our Ta/Cu films are about 7% higher than for the Cu films on polyimide. This can be attributed to the stronger <111> fiber texture found in these films which theoretically should lead to an increase in modulus of 11% (table 4.4). An even more pronounced increase in stiffness is found for the Ta/Cu/Ta films. This contribution cannot be due to a change in texture since the texture is defined only by the Ta interlayer. In contrast to the interlayer the surface layer can affect the grain boundary softening by suppressing the crack-like opening of the grain boundary. Thus, in a columnar microstructure the grain boundary is stiffened throughout the whole film thickness.

The plane-strain moduli for the bulge tests are also lower than the calculated values but the difference is only 20%. Two reasons may be responsible for this. Compared to the polyimide substrates used for the tensile test specimens, the surface roughness of the amorphous SiN_x – membranes is very low. This may lead to smoother Cu films, less grain boundary grooving and a better defined film thickness which should enhance the stiffness of the grain boundaries. In addition, the mean grain size is larger (figure 4.4). Based on the measured values for the grain size and film thickness the volume fraction of grain boundaries in these films is estimated to be similar to the films of Yu and Spaepen, who also found a modulus reduction of 20% [Yu and Spaepen 2004].

Table 4.4: Summary of the Young's moduli E and plane-strain moduli E^* , with theoretical values for a <111> and a <100> fiber texture as well as calculated and measured values for the different film systems. The calculation of the moduli is based on the measured texture and on single-crystal elastic constants.

Tensile testing	$E_{\langle 111 \rangle}$ [GPa]	$E_{\langle 100 \rangle}$ [GPa]	E_{calc} [GPa]	E_{measured} [GPa]
Cu	130	69	110.9	65 ± 15
TaCu	130	69	124.0	69 ± 15
TaCuTa	130	69	124.0	80 ± 15
Bulge testing	$E^*_{\langle 111 \rangle}$ [GPa]	$E^*_{\langle 100 \rangle}$ [GPa]	E^*_{calc} [GPa]	E^*_{measured} [GPa]
CuB	181	99	154.4	125 ± 15

4.4.2 Quantitative evaluation of yield stress data

Several studies on the isothermal mechanical properties of Cu films have recently been conducted. In figure 4.13 the longitudinal flow stresses are compared to results from tensile tests [Kraft et al. 2000, Yu and Spaepen 2004] as well as bulge tests on freestanding and passivated Cu films [Vlassak and Xiang 2006]. The present data are believed to be more reliable for the following reason: As shown in figures 4.6 to 4.8 the stress state in the films on polyimide substrates is far from being uniaxial due to the different Poisson's ratio of film and substrate. A biaxial stress state is also induced by bulge testing of rectangular membranes since Poisson's contraction is inhibited by the boundary conditions. This underlines that it is crucial to determine the complete stress state in order to derive the mechanical properties. This is only possible with the synchrotron-based tensile testing technique since the principal stresses in longitudinal and transverse direction are determined with the same accuracy [Böhm et al. 2004].

In figure 4.13 a similar trend is seen in all data. The values however differ substantially between the authors by up to a factor of 1.5. Especially the tensile test data of Cu films on polyimide by Yu and Spaepen [2004] and those by Kraft et al. [2000] are considerably higher than our tensile test results. Besides possible differences in microstructure, the test procedures may be responsible for this. Yu and Spaepen subtracted the contribution of the substrate from the total force and did not consider an initial residual stress. Even for room temperature deposition, compressive stresses of 100 MPa and more would not be uncommon. The consideration of these stresses would decrease their flow stress data to similar values as in our experiments for Cu films on polyimide. The flow stresses obtained by Kraft et al. [2000] do contain the residual stress but generally the determination by X-ray diffraction can be in error by about 50 to 70 MPa. On the other hand, the data by Vlassak and Xiang [2006] obtained in bulge testing of freestanding and passivated films show very good agreement with our results.

Figure 4.13 also shows that the film thickness range well below 100 nm is accessible only by our synchrotron-based tensile testing technique. There, a much reduced thickness dependence of the flow stress is found. In the following, the possible origin of this effect and the influence of different surface and interface conditions will be discussed in the light of established models of thin film plasticity.

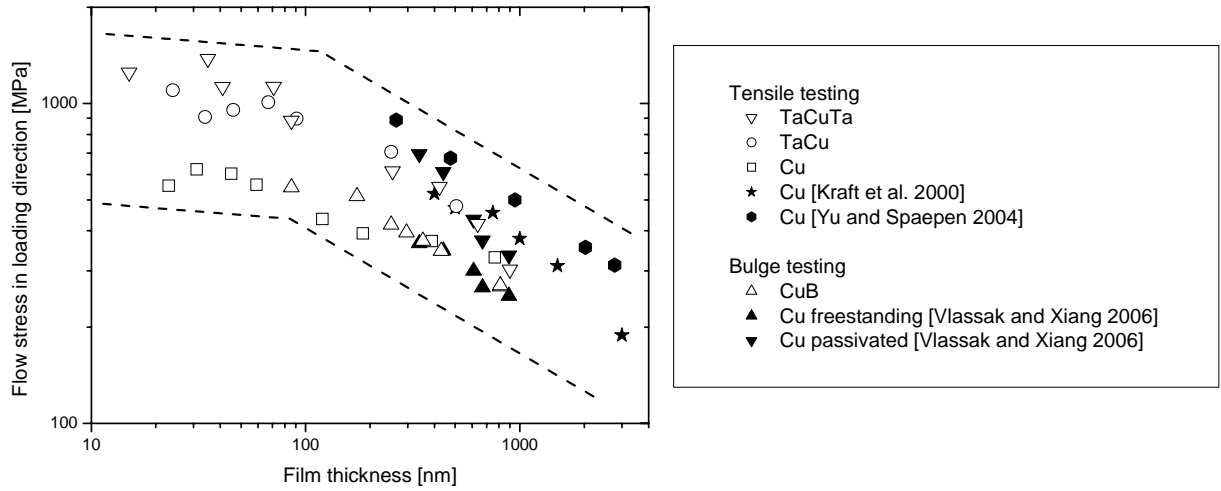


Figure 4.13: Comparison of flow stress data of this study to literature values for different Cu film systems tested by similar isothermal testing techniques. For direct comparability the flow stress in loading direction is plotted against film thickness.

4.4.3 Scaling behavior of yield strength and strain hardening

Mechanisms for the size effect in thin film plasticity can generally be divided into two main categories: (i) glide-controlled mechanisms, i.e., dislocation glide is constrained due to the presence of the substrate or a passivation layer [Nix 1989], grain boundaries [Thompson 1993], interaction between interfacial dislocations [Nix 1998, Pant et al. 2003], or the presence of a highly-stressed boundary layer [Nicola et al. 2003, Needleman et al. 2006]; (ii) nucleation-controlled mechanisms, due to the geometrical constraint on the activation of a dislocation source [von Blanckenhagen et al. 2001, von Blanckenhagen et al. 2003] or the limited number of dislocation sources [Needleman et al. 2006, Greer and Nix 2006].

Commonly the scaling behavior of the flow stress σ_y of thin films is described in a power-law form:

$$\sigma_y = \sigma_0 + c \cdot h^{-n} \quad (2)$$

where σ_0 represents the bulk yield stress, c a numerical constant and h the film thickness. Nix [1989] proposed, based on calculations by Freund [1987], that the origin of hardening in a single crystalline film is induced by the deposition of dislocation segments at the film/substrate interface and at the film surface if the film is oxidized or a passivation layer is present. Energetic considerations yield an exponent n close to 1. In figure 4.14 this model is

applied to the different film systems of this study and compared to the experimental data. It is evident that the Nix model underestimates the experimental observed flow stresses for films thicker than 100 nm whereas for thinner films the experimental values are overestimated. This may indicate that the motion of full dislocations is unfavorable on the small length scale. The model strongly depends on the elastic moduli of the substrate and the passivation layer. If they are low, as for the polyimide substrate, a thickness dependence of the flow stress is still observed but the absolute values for it are much too low, because the deposition of a dislocation segment costs little energy. For the freestanding films no hardening would be expected at all, because dislocations can escape from the film through the free surfaces. The strong influence of interfacial properties on the flow stress, however, is not observed experimentally. Freestanding films as well as films on polyimide do show lower flow stresses than films with one or two Ta layers but the difference is much smaller than predicted by the Nix model. In general, the Nix model is not expected to describe polycrystalline films accurately, as it considers the movement of a single dislocation in a single crystalline film.

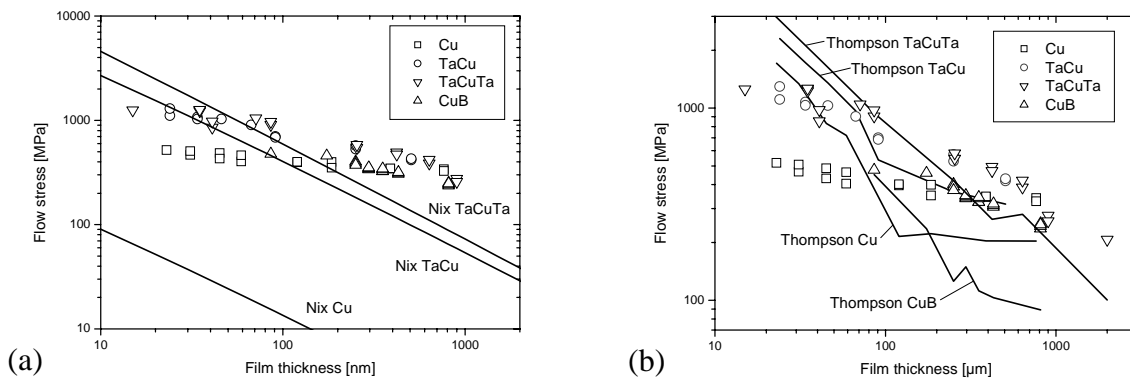


Figure 4.14: Flow stress for the different film systems compared to (a) the Nix model (equation (36) in [Nix 1989]) and (b) the Thompson model (equation (11) in [Thompson 1993]). The following parameters were used for the model calculations: $\sin\phi/(\cos\phi\cos\lambda) = 3.464$, $b = 0.255$ nm, $\beta_s = \beta_o = 2.6$, $\mu_{Cu} = 42$ GPa, $\mu_{Ta} = 69$ GPa, $\mu_{Kapton} = 1$ GPa and $\nu_{Cu} = 0.34$. The values for the Thompson model were calculated for each sample using the corresponding experimental value for the mean grain size. This leads to the unsteadiness of the calculated curves.

Grain boundaries may also be obstacles to dislocation motion. Thompson [1993] extended the Nix model by an additional grain size dependent term assuming that the grain boundaries are impenetrable for dislocations and dislocation segments are created at the grain boundaries as well. The power-law exponent for the grain size dependency is the same as for the thickness dependence according to the Nix model. Figure 4.14b shows the comparison of the experimental data with the calculated values. The calculation was performed for each sample

using the experimental values for film thickness and mean grain size. This led to the nonlinearity of the curves for the Thompson model. Similarly to the Nix model, the Thompson model underestimates the experimental values for film thicknesses above 100 nm and overestimates them for thinner films. Nevertheless, above 100 nm the Thompson model is closer to the experimental values, especially for freestanding films and films on polyimide. By considering both film thickness and grain size, a different scaling behavior for the different film systems is obtained. This indicates that the aspect ratio between film thickness and grain size plays an important role. Compared to the Cu films on polyimide, the freestanding films consist of bigger grains and their grain size increases continuously with film thickness; this leads to a stronger thickness dependence and lower values of the flow stress. Although these trends are captured by the Thompson model, the predicted values are still too low to satisfactorily describe the experimental values.

Dislocation interactions may be a further constraint on dislocation motion. Nix [1998] analyzed theoretically the interaction between moving dislocations and obstacle dislocations. By assuming only repulsive interaction, a flow stress increase of up to a factor of 2.8 was found, which is only true for a completely idealized situation. On the other hand discrete dislocation dynamics simulations of dislocation interactions [Pant et al. 2003] yield smaller stress increases and show that full 3D simulation is necessary to describe thin film behavior.

Another approach based on discrete dislocation dynamics simulations focused on the plastic deformation of metal thin films with a specified set of slip systems [Nicola et al. 2003]. Single crystalline [Nicola et al. 2003] as well as freestanding and passivated polycrystalline films [Needleman et al. 2006] were considered. If a substrate or a passivation layer is present, dislocation pile-up leads to the formation of a boundary layer of high dislocation density. The layer thickness was found to be independent of film thickness and hence gives rise to a thickness effect. For single crystalline films a power-law exponent n of 0.5 was found. For the polycrystalline films with columnar grain structure additional strengthening by the grain boundaries was obtained and the exponent was 1. The simulations for the polycrystalline films were compared to the experimental results from Vlassak and Xiang [2006] and very good agreement for the flow stress at 0.2% permanent strain was obtained. Since the data from Xiang and Vlassak is very similar to our experimental data, the approach from Needleman et al. [2006] may also explain our results. Nevertheless two restrictions must be made. The first is related to the deformation behavior for large strains. The constant pile-up of

dislocations would lead to an ever increasing stress in the boundary layer and distinct strain hardening. This is not observed in our films since the stress runs into a plateau or even decreases for strains above 0.5% (figures 4.6 to 4.9). Note that the stress decrease for the Cu film systems on polyimide is correlated to channel cracking and not to plastic deformation of the Cu films [Gruber et al. 2004]. Nevertheless an initial stress plateau is reached in each sample which is related to plastic deformation before cracking. The different strain hardening behavior is also evident in the comparison of simulated stress-strain curves from Nicola et al. to the experimental data from Xiang and Vlassak (figure 6 and 7 in [Needleman et al. 2006]). There, the simulated stress-strain curves show a clear deviation to higher stress values for strains above 0.3%. The second restriction is the proposed scaling behavior for films with very small grains or very thin film thickness. In the simulations [Needleman et al. 2006], a decreasing film thickness and grain size lead to a dislocation structure with very high back stresses which inhibits dislocation nucleation and results in an even more pronounced size effect. This, again, is not observed in our experiments, where the increase in flow stress becomes much lower for films thinner than 100 nm.

In contrast to the mechanisms proposed by the simulations from Needleman et al. [2006], *in situ* TEM observations on nanoscale Al and Cu thin films revealed decreasing dislocation density and activity with decreasing film thickness [Dehm et al. 2003, Haque and Saif 2005b]. Thus, strain hardening does not seem to be responsible for the higher flow stresses at small film thicknesses. These observations may indicate that the critical parameter for the flow stress of very thin films is dislocation nucleation rather than dislocation motion. Von Blanckenhagen et al. simulated thin film plasticity by considering a Frank-Read source in the center of a columnar grain [von Blanckenhagen et al. 2001]. Discrete dislocation dynamic simulations of the operation of such dislocation sources showed that the size of the most effective dislocation source scaled with the smallest dimension among film thickness h or grain size d ($h/3$ or $d/3$ for a freestanding film, $h/4$ or $d/4$ for a passivated film) [von Blanckenhagen et al. 2001, von Blanckenhagen 2002, von Blanckenhagen et al. 2003]. Using an Orowan equation and the Schmid factor s of the corresponding slip system, the flow stress σ_{source} of the film can be derived analytically from the size of the dislocation source s_d :

$$\sigma_{source} = \frac{1}{s} \cdot \frac{\mu_f b}{2\pi} \cdot \frac{1}{s_d} \ln\left(\frac{\alpha s_d}{b}\right) \quad (4-2)$$

where α is a numerical constant, b is the length of the Burgers vector and μ_f is the shear modulus of the film. In the following the approach according to equation (4-2) will be called source model.

In figure 4.15a the source model for freestanding and passivated films is compared to our experimental results. The calculations were performed with the following parameters for Cu films: $\mu = 42$ GPa, $b = 0.255$ nm, $\alpha = 2.5$ and $s = 0.27$. In contrast to the models from Nix and Thompson, the source model shows good agreement for the absolute values of flow stress as well as the difference between freestanding and passivated films in the thickness regime between 200 and 600 nm. This indicates that on this length scale the flow stress may be determined by the nucleation of dislocations within grains. For thicker films the flow stress is underestimated by the source model. Here, in order to accommodate the external strain more than one dislocation has to be active within a single grain. This may lead to additional contributions by dislocation interactions and pile-up.

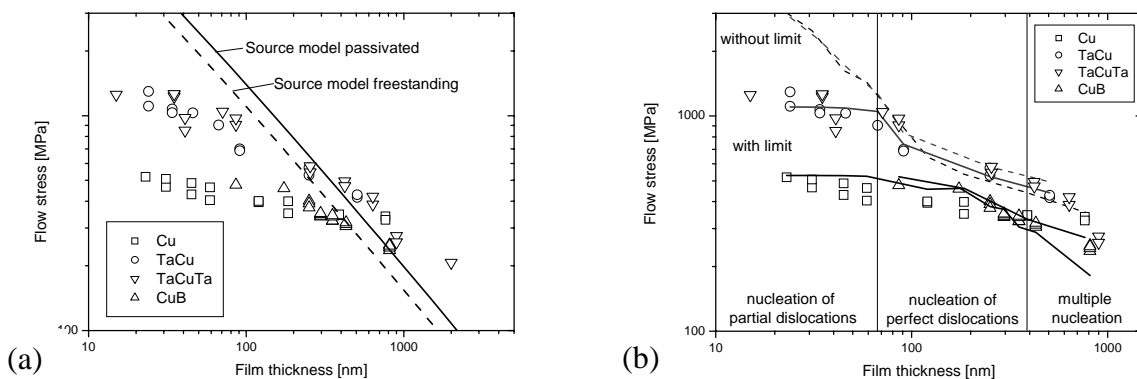


Figure 4.15: Flow stress for the different Cu films systems compared to (a) the source model for freestanding and passivated films and (b) modified versions of the source model taking into account the grain size distribution of the different films with and without an additional stress limitation. Three different deformation mechanisms are assumed: (i) nucleation of partial dislocations at grain boundaries, (ii) nucleation of a perfect dislocation within a grain and (iii) nucleation and motion of more than one dislocation per grain. Details for the model calculations are given in the text.

Although the values of the flow stresses and the difference between the different films systems are captured by the source model, the scaling behavior is still different. Compared to the experimental data the thickness dependence is too strong. Because the grain size distributions are very broad for all of the film systems, it may be not possible to describe the scaling behavior by only considering the film thickness. The dashed lines in figure 4.15b show the scaling behavior of the source model for freestanding and passivated films if the

grain size distribution is considered in addition to the film thickness. The lines are obtained by the following procedure. For every sample of the Cu films on polyimide and the Cu films with a Ta interlayer the flow stress according to the source model is calculated for every grain size of the experimentally determined grain size distribution. This leads to a corresponding flow stress distribution. Afterwards a modified flow stress σ_{mod} for each sample is obtained by weighting the mean value of the flow stress based on the grain size distribution σ_{mean} and the flow stress according to the film thickness σ_h :

$$\sigma_{mod} = \frac{\sigma_h + \sigma_{mean}}{2} = \frac{\sigma_{source}(h) + \frac{\sum_d \sigma_{source}(d)}{N}}{2} \quad (4-3)$$

where h is the film thickness, d the grain size and N is the number of grains of the grain size distribution. The dashed lines represent the linear intersection between the calculated values for the different samples. The implementation of the grain size contribution leads to a more reasonable scaling behavior of the source model over the complete film thickness range down to 100 nm. In the sense of this modified source model the difference between the flow stress at 0.2 and 0.5% permanent strain which was referred to as strain hardening so far is given by the flow stress distribution. Once the stress is high enough to activate all dislocation sources no further strain increase is expected because a sufficient number of dislocations are available to accommodate the increasing external strain. This may also explain the plateaus in the stress-strain curves which are not captured by the other models described above. The well defined plateaus indicate a very homogenous deformation which enforces the argument that each grain has to contribute. It is also important to note that a weak source in a bigger grain is easier to activate but the contribution to the macroscopic deformation is low. Thus, in order to generate the same strain in a bigger grain the source has to be activated several times or more than on source within the grain have to be activated. This may be more difficult than to activate a stronger source in a smaller grain once.

This leads to the last striking feature which is evident in every model discussed so far. All models based on both glide and nucleation of full dislocations strongly overestimate the flow stresses of films thinner than 100 nm. Somehow, a limit for the flow stress has to be implemented in order to describe the flow stress of films thinner than 100 nm. This is also accompanied by two experimental observations, namely the thickness dependence of the flow

stress becomes weaker and the strain hardening or the difference in flow stress at 0.2 and 0.5% permanent strain suddenly breaks down for films thinner than 100 nm (figure 4.12a). This indicates that above a certain stress value an additional deformation mechanism may come into play. The activation of this process should occur for a constant stress and should be independent of film thickness or grain size. This would lead to a limitation for the stress and could explain the weaker thickness dependence of the flow stress for the thinnest films. A reasonable candidate for such a deformation mechanism would be the generation and absorption of extended partial dislocations at grain boundaries. For nanocrystalline metals with grain sizes in the range of several tens of nanometers grain boundaries are highly effective dislocation sinks and sources, and it is generally acknowledged that traditional dislocation sources cease to operate for these materials. By both static [Kumar et al. 2003, Legros et al. 2000] as well as *in situ* TEM observations [Haque and Saif 2004, Haque and Saif 2005b] it is not possible to reveal any evidence of dislocation activity or debris similar to microcrystalline samples. Molecular dynamics simulations suggest that nanocrystalline metals accommodate the applied strain by emission of partial dislocations that run across the grain and are absorbed into the opposing grain boundary [Schiøtz et al. 1998, Derlet and Van Swygenhoven 2002, Yamakov et al. 2002, Frøseth et al. 2004, Van Swygenhoven et al. 2006]. It is still under debate whether the deformation is driven by single or extended partial dislocations [Van Swygenhoven and Weertman 2006].

According to our experiments and the literature we assume that the deformation mechanism changes for grain sizes and film thicknesses below 100 nm. The corresponding stress according to the source model is 1.10 GPa. For comparison the shear stress τ_p and the flow stress σ_p for the nucleation of a partial dislocation in a grain of size d is given by classical dislocation theory [Hirth and Lothe 1992]:

$$\tau_p = \frac{2\alpha'\mu b_p}{d} + \frac{\gamma}{b_p} = s \cdot \sigma_p. \quad (4-4)$$

Here μ is the shear modulus, γ the stacking fault energy and b_p is the magnitude of the Burgers vector for a Shockley partial dislocation. The parameter α' reflects the character of the dislocation and is 0.5 for edge dislocations. Using $\mu = 42$ GPa, $\gamma = 40$ mJ/m², $s = 0.27$ and $b_p = 0.147$ nm for Cu and $d = 100$ nm, σ_p is estimated to be 1.24 GPa. This is slightly higher than the stress for the nucleation of a full dislocation according to the source model. This may

be due to the very simple estimate. Nevertheless it indicates that the choice for the limitation in flow stress is reasonable. The size dependence for the nucleation of partial dislocations according to equation (4-4) is lower than that for full dislocations since the nucleation stress strongly depends on the stacking fault energy which is independent of film thickness. Furthermore, the strongly increasing volume fraction of grain boundaries leads to a nearly unlimited number of nucleation sites and a huge variance in activation stress which may also lower the size dependence. This is also supported by the experimentally observed values for the flow stress of nanocrystalline Cu [Van Swygenhoven and Weertman 2006]. For grain sizes between 100 and 15 nm, flow stresses ranging from 700 to 900 MPa are found which are also lower than the corresponding theoretical values.

In the following a limit in stress of 1.1 GPa is implemented in our modified source model. This means that the contribution of grains or film thicknesses smaller than 100 nm to the average values for the flow stress is limited to this value. The procedure of averaging the flow stress and weighting the film- and grain size effect is identical to the approach without the stress limit. Due to the very broad grain size distributions in our films (even for a 500 nm thick Cu film 15 % of the grains are smaller than 100 nm) the limitation affects more or less all data points in figure 4.15b. For the Cu films on polyimide with at least one Ta layer the introduction of the stress limit of 1.1 GPa leads to a remarkable good agreement to the experimental values over the film thickness regime down to 30 nm. For the freestanding Cu films and the Cu films on polyimide a further reduction of the limit is necessary in order to obtain similar agreement. By reducing the limit to 530 MPa, which corresponds to a length scale of 240 nm according to the source model, the scaling behavior of both the freestanding films and the Cu films on polyimide can be described although their grain size distribution and thickness dependence is very different. The necessary reduction of the limit by 50% indicates that the nucleation of partial dislocations may be easier for films with free surfaces. This is also observed in atomistic computer simulations performed by Hyde et al. [2005]. They investigated the mechanical properties of cylindrical gold nanowires and found that free surfaces act as favorable nucleation sites which can lead to a decrease in flow stress of about 40%. The Cu films on polyimide and the Cu films with at least one Ta layer may also be interpreted as an upper and a lower limit for the flow stress for Cu on the nanoscale since the experimental values for nanocrystalline bulk Cu ranging from 700 to 900 MPa lie in between the two plateau values of the different film systems. This indicates that the nucleation of partial dislocations is affected by the interface stiffness. Weak interfaces (free surface or

compliant substrate) lower the flow stress whereas a hard interface (Ta layer) leads to an increase in flow stress. The nucleation ability of a regular grain boundary lies somewhere in between.

Overall the modified source model with a limitation in flow stress captures the complete scaling behavior of the different films systems for films thinner than 400 nm. However, above 400 nm film thickness the consideration of a single dislocation within a grain is not sufficient and underestimates the experimental values. Here, more than one dislocation must be considered leading to additional hardening by interaction and pile-up of dislocations. This is obviously the upper limit for the validity of the source model also in the modified form. Thus, other models have to be used to describe the deformation behavior of films above 400 nm film thickness. As mentioned earlier in this section the approach by Needleman et al. [2006] would be a very good candidate since it was already used to describe the experimental results for bulge tests on freestanding and passivated Cu films with thicknesses above 0.35 μm .

4.5 Summary and conclusion

Ultra thin Cu film systems with and without passivation have been investigated using a novel synchrotron-based tensile testing technique and bulge testing. The synchrotron-based testing technique allows for the systematic investigation of the influence of different surface and interface conditions on the mechanical properties of thin metal films. The findings can be summarized as follows:

- The measured moduli for all film systems are about 20 to 40% lower than the theoretical values for the corresponding texture. This can be attributed to the enhanced grain boundary volume and the low stiffness of the grain boundaries.
- Freestanding films and films on polyimide substrates behave very similarly and show higher flow stresses than expected. Film systems with one or two Ta layers reveal a large increase in flow stress compared to single Cu layers. Nevertheless the difference between one and two Ta layers is very small.
- The absolute values and scaling behavior of the flow stress can be described for all film systems in the thickness range between 100 and 600 nm by a modified dislocation source model. Therefore the film thickness as well as the grain size distribution must be considered.

- For films thinner than 100 nm the scaling behavior of the flow stress becomes weaker. By assuming an upper limit for the flow stress the transition in the scaling behavior can be described. It is postulated that the reason for the limit in flow stress may be a deformation mechanism which is based on the nucleation and absorption of partial dislocations at the grain boundaries. This would also explain the strongly reduced strain hardening found for these films.

5 Brittle-to-ductile transition in ultra thin Ta/Cu film systems

5.1 Introduction

Flexible electronics have gained widespread interest for numerous applications. Among these are e.g. flexible displays [Chen et al. 2003a, Gelinck et al. 2004], wearable electronics [Post et al. 2000, Bonderover and Wagner 2004], electronic skins [Wagner et al. 2004] or flexible microelectrode arrays (MEA) usable for in-vivo biological applications such as retina implants [Meyer 2002, Stett et al. 2003]. The functional parts of these devices comprise stiff materials (e.g. metals, transparent conductors, and amorphous silicon) deposited on compliant substrates (e.g. polyimide or silicone). When stretched or bent during usage, the compliant substrate usually deforms elastically. Brittle coatings or conducting wires may crack or delaminate as a consequence. Mechanical failure is one of the most critical issues in the development of flexible and stretchable electronics.

On the other hand, the measurement of fracture toughness of thin films is difficult due to small testing volumes and the challenge of handling small samples. In contrast to bulk materials, there is neither a standard procedure nor a commonly accepted methodology to follow. However, increasing efforts have been made and several different test methods are proposed and used. The methodologies employed to measure toughness of thin films are bending, buckling, scratching, indentation and tensile tests [Zhang et al. 2005]. In order to study multiple cracking phenomena of brittle films on compliant substrates, *in-situ* fragmentation tests have been conducted [Handge et al. 2000, Rochat et al. 2003, Xiang et al. 2005b, Heinrich et al. 2006]. This method, in which the progressive development of crack density in the coating is analyzed as a function of substrate elongation, has proven to be very efficient for (i) the determination of the strength distribution in the film as well as the type of strain transfer (linear or nonlinear) between film and substrate [Handge et al. 2000, Handge 2002] and (ii) the calculation and modeling of adhesive and cohesive fracture toughness [Leterrier et al. 1997a, Leterrier et al. 1997b, Rochat et al. 2003, Jansson et al. 2006a, Jansson et al. 2006b]. More direct measurements of fracture toughness of thin films on compliant substrates are possible by bulge testing of circular membranes [Alaca et al. 2002] and a

special buckling test [Chen and Gan 2007]. Here, the fracture toughness is directly obtained from the measured fracture stress and strain, respectively.

In this study we investigate the thickness dependence for multiple cracking of Cu films (34 to 506 nm thick) on polyimide substrates with Ta interlayers (3.5 to 19 nm thick). By combining the results of *in situ* tensile tests in a scanning electron microscope (SEM) and a novel synchrotron-based tensile testing technique [Böhm et al. 2004, Gruber et al. 2004] (chapter 4) on identical samples, various parameters of the fracture behavior are obtained. By the synchrotron technique the stress-strain evolution in the Cu film during cracking is monitored, whereas by SEM tests the crack evolution can be visualized and crack distance as well as crack opening can be quantified. In addition, an energetic approach is proposed, by which the strain energy release rate for a given strain/crack density is estimated from the difference in measured strain energy (area under measured stress-strain curve) and the imaginary strain energy of a fully plastic film (area under imaginary stress plateau). By stepwise integration, the fracture toughness evolution during multiple cracking can be determined. All data provide further insight in the fracture mechanics of thin films on compliant substrates and the role of decreasing ductility in very thin films.

The results are discussed in the light of thin film fracture mechanics models for stiff films on compliant substrates dealing with statistical aspects [Handge et al. 2000, Handge 2002], linear elastic fracture mechanics [Beuth 1992, Xia and Hutchinson 2000], substrate deformation [Beuth and Klingbeil 1996, Vlassak 2003], film/substrate interaction [Begley and Barth-Smith 2005, Begley et al. 2005] as well as strain localization and debonding [Li et al. 2004, Li et al. 2005, Xiang et al. 2005b, Li and Suo 2006]. It seems that the fracture mode in the ductile Cu layer is related to local necking in the regions of initial cracks in the brittle Ta layer. The scaling behavior of fracture toughness and the crack shape imply, however, an increasing inherent brittleness of Cu films with decreasing thickness.

5.2 Experimental

5.2.1 Sample preparation

Two sets of Ta/Cu film systems with varying Cu and Ta film thickness and a set of 10 nm thick Ta films were prepared (figure 5.1). The first Ta/Cu set consisted of 30 to 500 nm thick Cu films deposited on an about 10 nm thick Ta interlayer and the second set covered about 80 nm thick Cu films with 4 to 20 nm thick Ta interlayers. As substrate 125 μm thick dogbone-shaped polyimide foils (Kapton® HN) with a gauge section of 6 mm x 20 mm were used. Prior to film deposition the substrate surface was sputter cleaned for 1 min using an Ar⁺ plasma (105 V, 0.8 A). Cu as well as Ta films were deposited onto the electrically grounded polyimide substrates using a direct-current (DC) magnetron sputter deposition system with a base pressure of 1×10^{-8} mbar, a DC power of 200 W (Cu) an 100 W (Ta) and a Ar pressure of 4.2×10^{-3} mbar. The corresponding deposition rates were 45 nm/min (Cu) and 12 nm/min (Ta), respectively. After deposition all samples were annealed without breaking vacuum at 350°C for 0.5 h.



Figure 5.1: Schematic drawing of the Ta and Ta-Cu film systems investigated. The Ta as well as Cu film thickness was varied.

The film thickness of the individual metallic layers was determined by Rutherford backscattering spectrometry (RBS). All RBS measurements were conducted using 2 MeV He⁺ ions (6.5 MV Pelletron accelerator at the Max Planck Institute for Metals Research). The film thickness of the Cu as well as Ta films could be obtained by fitting the RBS spectra of the Si detector with the X-Rump simulation software (Computer Graphics Service Ltd.) taking into account the scattering geometry, ion species and energy.

5.2.2 Mechanical testing

The experimental procedure and data analysis as well as the unique features concerning the synchrotron-based tensile testing technique are described for Au films in detail elsewhere [Böhm et al. 2004]. The necessary modifications for the adaptation of this technique to Cu films are listed in chapter 3 and 4. All tensile tests were performed at the MPI-MF-beamline located at the synchrotron radiation source ANKA (Angströmquelle Karlsruhe). For the tensile tests of this study the maximum total strain of the samples was increased up to 6.5%. During the tensile test the crosshead displacement of the tensile tester (Kammrath & Weiss) was varied in steps between 30 and 100 μm . The total strain of the sample was measured by a laser-extensometer (Fiedler Optoelektronik). Unfortunately, it was not possible to determine the stress in the Ta layers because the diffracted intensity was below the detection limit.

In addition to the tensile tests at the synchrotron, *in situ* tensile tests in a scanning electron microscope were conducted on the same sets of samples. Here the tensile tester was mounted on the sample stage of an SEM (Leo 1530VP). The samples were loaded in a stepwise manner and SEM images were taken for every step. The total strain on the samples was obtained from the crosshead displacements by calibration with the laser extensometer measurements at the synchrotron. For the SEM tests the maximum total strain was up to 20%. To determine the crack spacing, two different methods were applied. At small strains, cracks did not span the complete width of the SEM images, so the mean crack distance was defined as total crack length (along the film plane) per image area. At large strains, at least 30 cracks were counted along multiple straight lines perpendicular to the cracks, and this number was divided by the total line length. In a similar way, the crack opening was determined for different total strains from the length of these lines within the cracks.

5.3 Results

The following sample denotation will be used to classify the different samples investigated in this study: Ta- x -Cu- y . The variables x and y represent the corresponding Ta and Cu film thickness measured by RBS in nanometers. For all samples the Ta layer lies in between the polyimide substrate and the Cu film.

5.3.1 Stress-strain curves

In the following, results from synchrotron tensile tests on Ta-Cu film systems on polyimide with different Cu and Ta film thickness are presented. The figures 5.2a and b show the stress evolution in the longitudinal as well as transverse direction in a 67 nm and a 506 nm thick Cu film, respectively.

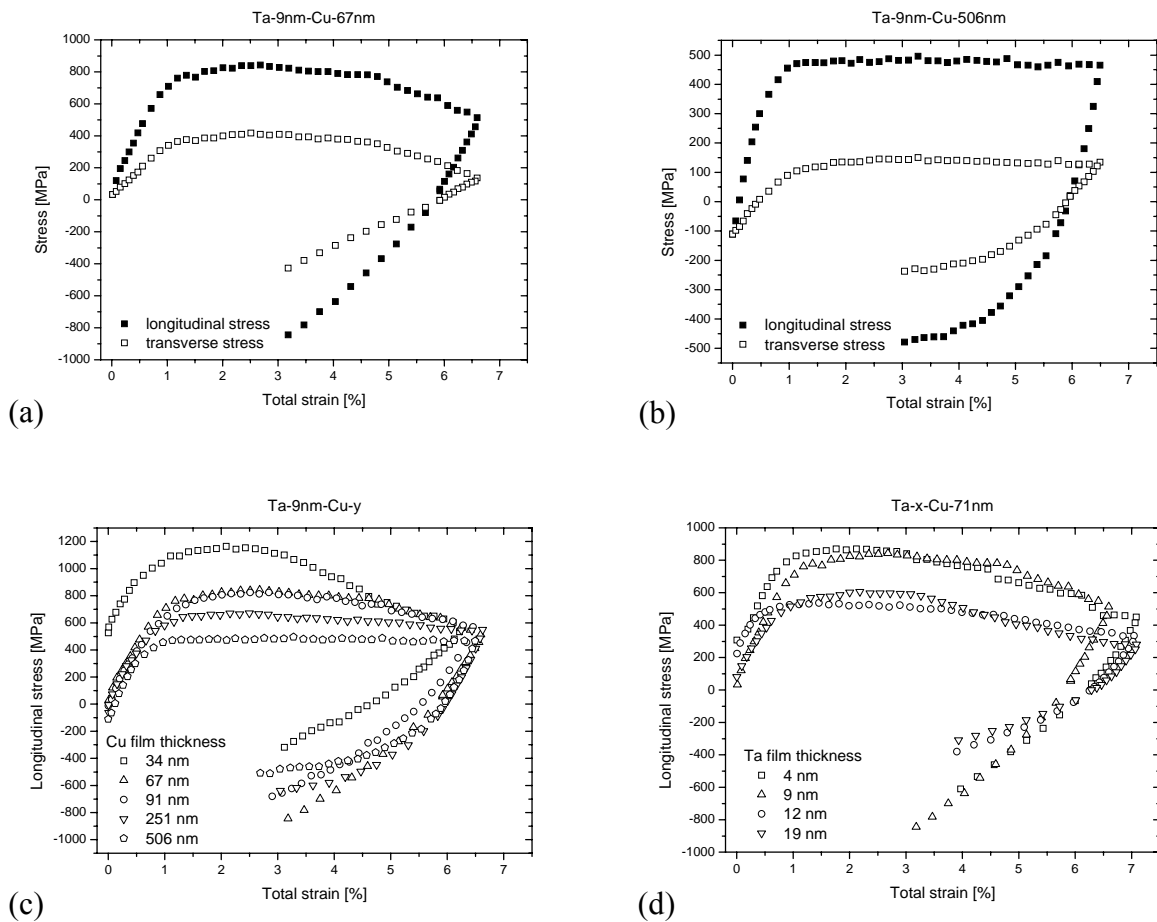


Figure 5.2: Stress-strain curves for different Ta-Cu film systems measured by the synchrotron-based tensile testing technique. The longitudinal (filled symbols) as well as transverse stress (open symbols) is shown for (a) a 67 nm and (b) a 506 nm thick Cu film. Variations in (c) Cu and (b) Ta film thickness influence the maximum stress as well as the amount of stress release. For a clearer overview only the longitudinal stresses are compared.

The overall behavior of both films was similar although the absolute stress values were higher for the thinner film. After the linear elastic regime, the films deformed plastically up to total strains of about 2.5%. For higher strains the longitudinal as well as transverse stress began to decrease. This decrease was much more pronounced for the thinner film. For the thicker film it is almost not visible. Upon unloading, a compressive stress state developed in the Cu films

because they had been plastically deformed, whereas the polyimide substrates deformed elastically during the whole tensile test. The tensile (loading) and compressive (unloading) stresses in transverse direction resulted from the mismatch in Poisson's ratio of Cu and polyimide. Due to the very strong (111) fiber texture the Poisson's ratio of the Cu film in the transverse direction is higher than that of the polyimide (chapter 3 and 4). For direct comparison of samples with different Cu and constant Ta film thickness and vice versa only the longitudinal stresses of each sample are plotted in figures 5.2c and d. For a decreasing Cu film thickness the maximum stress as well as the amount of stress release increased whereas a decreasing Ta film thickness led to an increase in maximum stress but an almost constant stress drop.

5.3.2 Fractography

Figure 5.3 shows a representative set of scanning electron microscopy (SEM) micrographs of one Ta-9nm film and Ta-9nm-Cu-y films with different Cu film thickness. Except for figure 5.3d, all micrographs were taken at a similar total strain between 6.25 and 6.82% under stress. The cracking evolution in all films was very similar. At low strains, short primary cracks nucleated in the film and grew perpendicularly to the loading direction. The length of the cracks was much smaller than the width of the sample. For higher strains, the existing cracks grew further and new cracks nucleated in between the existing cracks. The number of cracks as well as the crack shape depended on film material and film thickness. The Ta-9nm film showed the smallest crack spacing and the cracks were straight. A similar crack shape was observed for the Ta-9nm-Cu-34nm sample but the crack spacing was larger. With increasing Cu film thickness the crack spacing further increased and the cracks became shorter and more and more irregular. For the Ta-9nm-Cu-506nm sample almost no cracks were visible at the surface for a total strain of 6.82%. Figure 5.3d shows a Ta-9nm-Cu-67nm sample strained up to 23.02%. For strains greater than 15%, secondary cracks formed parallel to the loading direction starting at the crack front of a primary crack. It seems that the films delaminated locally along the crack front.

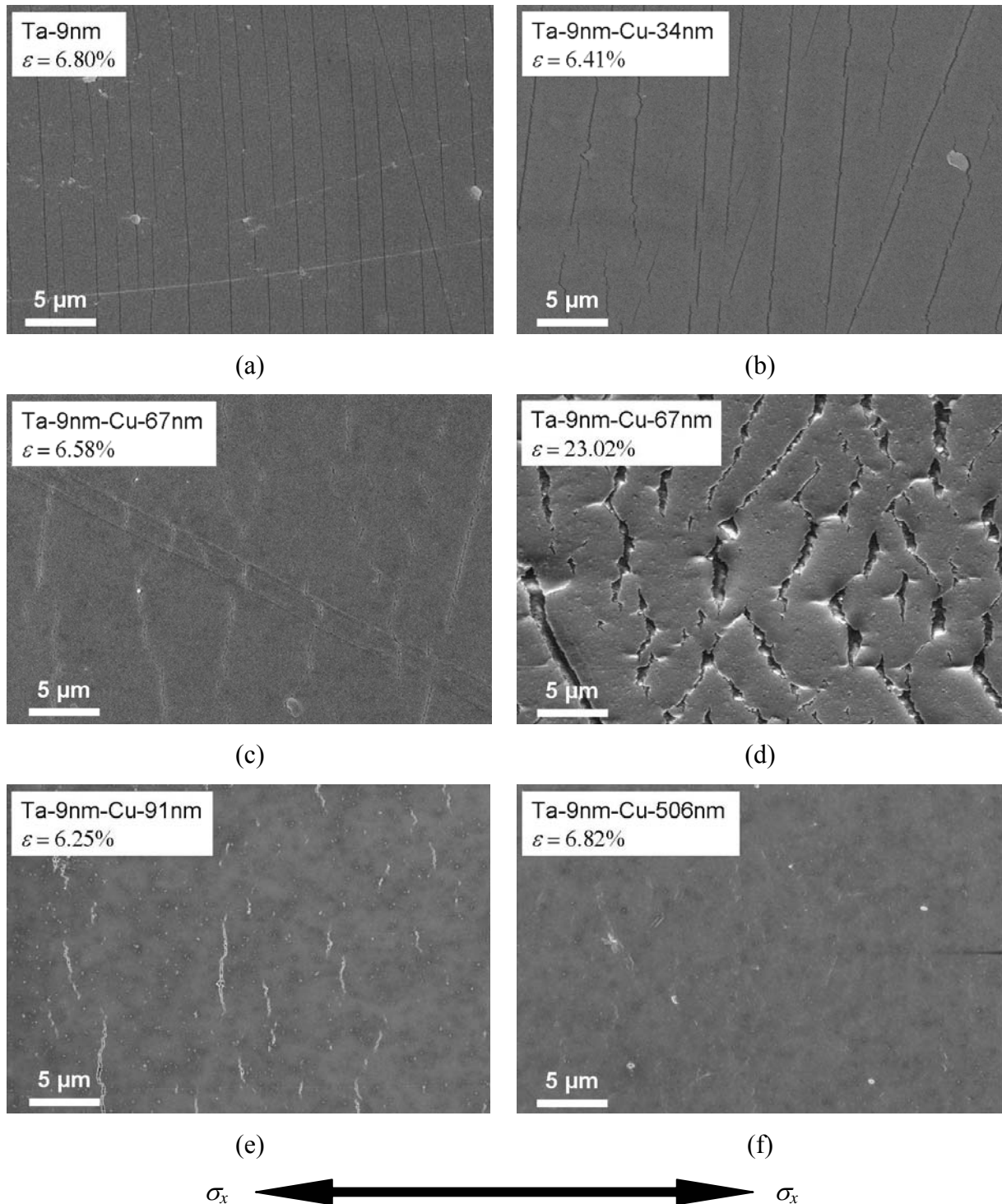


Figure 5.3: SEM micrographs of a Ta-9nm and different Ta-9nm-Cu samples. (a)-(c), (e) and (f) were taken at a similar total strain of about 6.5%. Primary cracks nucleate and grow perpendicularly to the loading direction (black arrow at the bottom). Crack spacing and shape depends on film material and film thickness. (d) Ta-9nm-Cu-67nm sample strained up to 23.02% total strain. Secondary cracks form at the edge of primary cracks. The films seem to delaminate at the crack front.

From the complete set of SEM pictures the mean crack distance L and crack opening displacement δ was determined. In figure 5.4a to 5.4c the mean crack distance is plotted as a function of total strain for the Ta-9nm sample and the different Ta-Cu film systems. The

overall shape was again similar. In the beginning, the crack spacing decreased rapidly with strain. Subsequently the slope changed gradually leading to a smaller slope at larger strains. However, the absolute crack distance is different. An increase in Cu film thickness led to an increase in crack spacing and to higher onset strains for cracking. Thus, for the thicker films the second regime with the smaller slope was not reached for strains up to 20%. On the other hand, an increase in Ta film thickness resulted in a decrease of the initial crack spacing, whereas the final crack spacing was nearly independent of Ta film thickness. In addition, lower onset strains were found for thicker Ta interlayers. For comparison, the initial slope was higher and the crack spacing was much smaller for the Ta-9nm film.

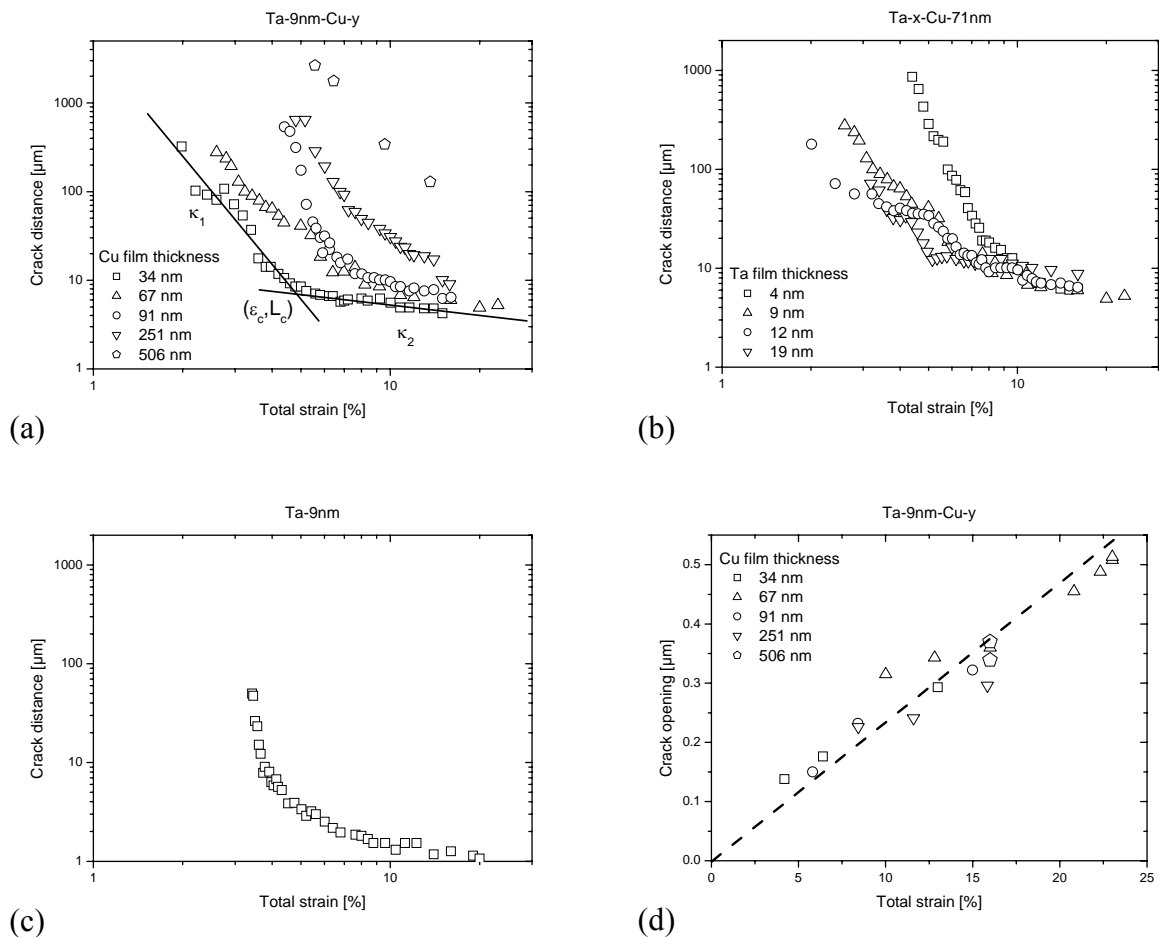


Figure 5.4: Mean crack distance vs. total strain for (a) and (b) Ta-Cu-film systems and (c) for a Ta-9nm sample. The overall shape of the curves is similar whereas absolute values depend on Cu and Ta film thickness. (d) Crack opening vs. total strain for Ta-Cu film systems with varying Cu film thickness. The crack opening increases with strain and is independent of Cu film thickness.

Before and after the change in slope, power-law functions in the form

$$L = c\varepsilon^{-\kappa}, \quad (5-1)$$

where L is the crack distance, ε the total strain and c a constant number, were fitted to the experimental data [Handge et al. 2000, Handge 2002]. The intersection of the two power-law functions was used to define the crossover values for total strain and crack distance, ε_c and L_c , respectively (figure 5.4a). Table 5.1 summarizes the power-law exponents κ_1 (before crossover) and κ_2 (after crossover) and the resulting values of ε_c and L_c . In figure 5.4d the crack opening is plotted against the total strain for different Ta-9nm-Cu film systems. The crack opening increased linearly with strain for all film systems and a linear extension of the data goes through the zero point of both scales. A collection of the values for the initial crack spacing L_0 at the onset of cracking, the intermediate crack spacing L_i at a total strain of about 6.5% (slightly below maximum total strain of synchrotron experiments), the final crack spacing L_f for a total strain of 16% at the end of the tensile tests in the SEM and the initial crack opening displacement δ_0 is given in table 5.2.

Table 5.1: Fragmentation parameters for the different Ta-Cu film systems and the Ta-9nm film. Listed are the two scaling exponents κ_1 and κ_2 as well as the crossover values of the total strain ε_c and crack spacing L_c . The values in brackets are uncertain because the change in slope was not accomplished for these samples. For the Ta-9nm-Cu-506nm sample no change in slope was observed within the investigated strain range.

Sample	κ_1	κ_2	ε_c	L_c [μm]
Ta-9nm-Cu-34nm	4.07 ± 0.47	0.42 ± 0.07	0.049	6.9
Ta-9nm-Cu-67nm	4.39 ± 0.53	0.44 ± 0.08	0.055	8.9
Ta-9nm-Cu-91nm	8.89 ± 0.72	(0.66)	(0.067)	(11.5)
Ta-9nm-Cu-251nm	6.05 ± 0.41	(0.71)	(0.086)	(25.0)
Ta-9nm-Cu-506nm	4.15 ± 0.22			
Ta-4nm-Cu-71nm	8.77 ± 0.51	0.47 ± 0.09	0.075	8.5
Ta-12nm-Cu-71nm	2.34 ± 0.56	0.39 ± 0.08	0.065	8.9
Ta-19nm-Cu-71nm	3.37 ± 0.29	0.42 ± 0.08	0.052	11.1
Ta-9nm	19.58 ± 1.58	0.47 ± 0.12	0.040	2.3

Table 5.2: Initial crack distance L_0 (onset of cracking), intermediate crack distance L_i ($\varepsilon \approx 6.5\%$), final crack distance L_f ($\varepsilon \approx 20\%$) and initial crack opening displacement δ_0 for different Ta-Cu film systems. The values are obtained by analyzing the SEM micrographs by eye and the error is assumed to be 5% for the crack spacing and 10% for the crack opening displacement.

Sample	L_0 [μm]	L_i [μm]	L_f [μm]	δ_0 [nm]
Ta-9nm-Cu-34nm	102.7	6.8	4.7	293
Ta-9nm-Cu-67nm	285.6	15.0	6.4	295
Ta-9nm-Cu-91nm	534.3	26.1	8.1	292
Ta-9nm-Cu-251nm	652.1	193.5	18.7	278
Ta-9nm-Cu-506nm	2696.5	2185.8	128.1	302
Ta-4nm-Cu-71nm	865.0	85.5	6.1	169
Ta-12nm-Cu-71nm	182.8	20.1	6.5	251
Ta-19nm-Cu-71nm	72.5	12.4	9.1	393

5.4 Discussion

5.4.1 Statistical approach

The evolution of the mean crack distance L with total strain ε for the Ta-Cu-film systems and the Ta-9nm sample can be approximated by two power laws both at the onset and the later stage of cracking (figure 5.4a). Handge et al. [2000, 2002] have shown that for thin brittle films on ductile substrates the power-law exponents κ_1 and κ_2 are related to the strength distribution in the film and that they are not independent. The correlation between κ_1 and κ_2 is given by the fact that the stress in the film is locally reduced around a crack. In the initial stage of cracking the average strain in the film equals the total strain of the film/substrate composite. This leads to randomly located cracks according to the local strength of the film, which is given by the statistical distribution of defects in the film. With ongoing sequential cracking and decreasing crack distance, the stress in the film becomes more and more non-uniform with maximum values in the midsection between two preexisting cracks. New cracks form predominantly in the highly stressed regions and thus the location of the cracks is no longer independent. According to the analysis by Handge et al. [2000, 2002], κ_1 is equal to the Weibull exponent α of the strength distribution of the film and κ_2 depends on both, α and m , where m is the nonlinearity parameter of the strain transfer between film and substrate, according to:

$$\kappa_2 = \frac{m\alpha}{(m+1)\alpha+1} = \frac{m\kappa_1}{(m+1)\kappa_1+1} \quad (5-2)$$

For a linear elastic strain transfer $m = 1$, and κ_1 as well as κ_2 depend only on α . On the other hand, $0 < m < 1$ holds for a substrate material which deforms plastically or viscoelastically. By combining the results for κ_1 and κ_2 , one can determine experimentally the parameters for the Weibull distribution of defects and the nature of strain transfer between film and substrate.

Solving equation (5-2) for m and using the experimental values for κ_1 and κ_2 (table 5.1), m is found to be between 0.9 and 1.0 for our Ta and Ta-Cu film systems, at least for the samples where κ_2 could be determined accurately. This indicates a predominantly linear elastic strain transfer between the Ta and Cu films and the polyimide substrate. For the thicker Ta-9nm-Cu films, the transition to the second power-law has not been accomplished (slope is not constant) or has even not been observed in the investigated strain regime up to 20%. This leads to higher apparent κ_2 values and consequently to an increase of m . This would mean that the substrate would harden if the overlaying film becomes thicker, which is not reasonable because the polyimide substrate is still the load bearing part and should not change its properties for any film system investigated. Therefore we assume that the strain transfer is always linear elastic. This is also corroborated by the fact that the crack opening displacement increases linearly with external strain (figure 5.4d).

The experimental values for κ_1 of the Ta-9nm-Cu film systems show no clear trend as a function of Cu film thickness. This may be due to sample preparation. In principle, modern sputtering techniques produce films with very low flaw densities and most defects are located at the film/substrate interface. For our film systems the situation is even aggravated because the Ta films, which are the most brittle part, are located in this area of high defect density. Therefore we assume that the crack nucleation occurs in the Ta Layer. In addition, the dog-bone shaped polyimide substrates have been prepared mechanically which induce some scratches on the substrate surface. Scratches are favorable crack nucleation sites and may broaden the strength and defect distribution of the final film. The occurrence of these additional scratches is not systematic and may explain the inconsistent variation of κ_1 because the defect distribution in the Ta films is similar for all samples due to the constant Ta film thickness. For the Ta-x-Cu-71nm samples the situation is different. Here, the Ta film thickness is varied and thus the number and size of initial defects is changed systematically. It

is reasonable to assume that the initial crack size and size distribution increases with increasing Ta film thickness, which results in lower values for κ_I . Compared to the Ta-Cu film systems the Ta-9nm sample shows a much higher value for κ_I (2 to 6 times higher). Due the brittleness and small thickness of the Ta layer already very small defects lead to immediate cracking, which results in a very narrow strength distribution.

The crossover values for total strain ε_c and crack distance L_c show clearer trends (table 5.1). L_c scales directly with the total thickness of the samples (Ta plus Cu film thickness). This can be attributed to the size of the stress relaxation zone around the cracks which increases with increasing film thickness [Xia and Hutchinson 2000, Handge 2002]. It leads to larger crack spacing because the distance until the stress reaches the fracture stress becomes larger. The scaling behavior of ε_c depends on whether the Ta or Cu film thickness is varied. It decreases with increasing Ta film thickness, which can be explained by the increasing defect size, but increases with increasing Cu film thickness. The latter observation cannot be explained by a Weibull strength distribution because the probability of a critical defect would increase with increasing film thickness leading to decreasing fracture strains [Leterrier et al. 1997b, Rochat et al. 2003].

Let us consider in the following the implications of linear elastic fracture mechanics. Leterrier et al. [1997a, 1997b] have shown that the cohesive strength σ_{max} of a film showing a Weibull-type failure mechanism can be determined by averaging the probabilistic fracture strength of the film:

$$\sigma_{max} = \beta \left(\frac{L_s}{L_0} \right)^{-1/\alpha} \Gamma(1 + 1/\alpha) \quad (5-3)$$

where α is again the Weibull exponent, β the Weibull scale factor for the film strength, $L_0 = 1 \mu\text{m}$ a normalizing length, L_s the crack spacing at saturation and Γ the gamma function. In principle, the Weibull parameters α and β can be derived from linear extrapolation of the initial part of the crack density vs. total strain diagram (this can be obtained by plotting the reciprocal of the crack spacing L) and multiplying the scale parameter for strain ε_{ex} by the Young's modulus of the film [Leterrier et al. 1997b]. For our experiments, α is equal to κ_I , the Young's modulus is 175.7 GPa (plane strain modulus of (111) fiber textured Cu) and the

final crack spacing L_f of our tensile tests is used as L_s . The linear extrapolation of our experimental data leads to very high values for β_{ex} because ε_{ex} strongly increases with increasing Cu film thickness (table 5.3). Therefore, the corresponding fracture strengths $\sigma_{max,ex}$ become also very high. Although ε_{ex} and β_{ex} increase with Cu film thickness, no thickness dependence is found for the fracture strength because the dependence on α is even more pronounced. The absolute values are 2 to 7 times higher than the measured maximum average stresses in the Cu films (figures 5.2a-c). This is due to the fact that the analysis is fully linear elastic and stresses far above the yield strength are allowed in the analysis.

One way to include the effects of plastic deformation is to assume that β is equal to the maximum value of the measured stress-strain curve σ_0 just before the onset of cracking. Doing so, the values for the corresponding fracture strength $\sigma_{max,0}$ show the correct trend (decreasing strength with increasing Cu and Ta film thickness) but now they are 2 to 4 times lower than the experimental stress values. This may be explained by the fact that the local stress around the crack tip may be higher than the average stress in the film and σ_0 does not represent the real fracture strength of the film. It is obvious that the fracture strength of these films cannot be described correctly by a Weibull strength distribution alone. Nevertheless the statistical analysis has provided insight in the defect statistics and size in our films. Another way of including plasticity in the analysis will be shown in the following.

Table 5.3: Summary of results for the statistical analysis. Shape and size parameters of the Weibull distribution α , ε_{ex} and β_{ex} , maximum crack distance L_f , corresponding values of the gamma function $\Gamma(1/1+\alpha)$ and the calculated fracture strengths $\sigma_{max,ex}$ and $\sigma_{max,0}$ according to equation (5-3). σ_0 is the maximum stress of the stress-strain curves as determined from figure 5.2a-c.

Sample	α	ε_{ex}	β_{ex} [MPa]	L_f [μm]	$\Gamma(1/1+\alpha)$	$\sigma_{max,ex}$ [MPa]	σ_0 [MPa]	$\sigma_{max,0}$ [MPa]
Ta-9nm-Cu-34nm	4.07	0.0168	2952	4.7	0.907	1831	1151	714
Ta-9nm-Cu-67nm	4.39	0.0225	3953	6.4	0.911	2360	842	503
Ta-9nm-Cu-91nm	8.89	0.0420	7379	8.1	0.946	5520	822	615
Ta-9nm-Cu-251nm	6.05	0.0447	7854	18.7	0.928	4492	666	381
Ta-9nm-Cu-506nm	4.15	0.0528	9277	128.1	0.908	2617	487	137
Ta-4nm-Cu-71nm	8.77	0.0422	7415	6.1	0.946	5708	872	671
Ta-12nm-Cu-71nm	2.34	0.0169	2969	6.5	0.886	1184	539	215
Ta-19nm-Cu-71nm	3.37	0.0227	3988	9.0	0.898	1863	603	282

5.4.2 Energetic approach

In principle, it is possible to determine the fracture toughness from the fragmentation data by sophisticated finite element modeling [Jansson et al. 2006a, Jansson et al. 2006b]. However, for such an analysis the fracture mechanisms must be known and implemented in the model. In the following, we propose a more direct data analysis approach based on the combination of the results for *in situ* tensile tests in the SEM and the synchrotron. Due to the substrate constraint the stress in the film relaxes only locally around the crack [Beuth 1992, Xia and Hutchinson 2000]. In between the cracks the strain transfer from the substrate to the film is still intact and stress does not relax. Therefore any release in strain energy of the film can be attributed to the crack formation. The strain energy release by cracking can be estimated from the stress-strain curves measured by the synchrotron technique (figure 5.5a). The strain energy U_{strain} stored in the volume of the film is given by the area under the measured stress-strain curve. Experiments on Cu films without cracks have shown that after yielding and strain hardening a stress plateau is reached for strains higher than 1.5% (chapter 4) and remains up to total strains of about 7%.

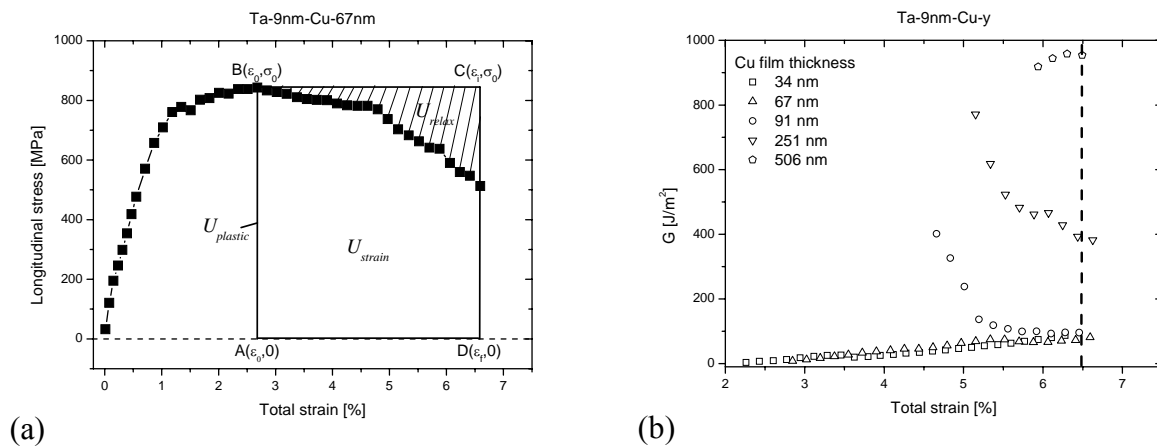


Figure 5.5: (a) Schematic illustration of the data analysis. A constant stress plateau for a film without cracks is assumed. (b) Energy release rate vs. total strain for different Ta-9nm-Cu film systems. For thinner films an increase in energy release rate G is found whereas for thicker films G decreases with strain. At 6.5% total strain G becomes almost constant.

Because the stress decrease in this study always starts at least at 2.5% total strain we assume that the plateau stress has already been reached and without cracking the stress in the film would remain constant. Even for the Ta-9nm-Cu-34nm sample, which showed the highest flow stress, the slope prior to the stress decrease is almost zero (figure 5.2c). Doing so, we can

estimate the strain energy $U_{plastic}$ per volume for a film without cracks and calculate the strain energy U_{relax} per volume released by the cracks:

$$U_{relax} = U_{plastic} - U_{strain} = \sigma_0(\varepsilon_i - \varepsilon_0) - \int_{\varepsilon_0}^{\varepsilon_i} \sigma(\varepsilon) d\varepsilon \quad (5-4)$$

where σ_0 is the longitudinal stress prior to the stress decrease, ε_0 the corresponding strain and ε_i the upper cut-off strain. In order to obtain the energy release rate G for cracking (strain energy release per unit crack area), U_{relax} was related to the created crack area A_{crack} :

$$G = \frac{U_{relax} V}{A_{crack}} = \frac{U_{relax} h w L_i}{h w} = U_{relax} L_i \quad (5-5)$$

where V is the volume around a crack (estimated as distance of $L/2$ on both sides of the crack), h the film thickness, w the width of the sample and L_i the mean crack distance at ε_i . The crack distance is obtained from the *in situ* SEM experiments.

By integration of the stress-strain curves (using Origin® 7 SR2 v7.0383 by OriginLab) and evaluating the crack distance for every strain step, the energy release rate was obtained as a function of total strain. In figure 5.5b the corresponding results for the Ta-9nm-Cu samples are shown. It is evident that the energy release rate increases with Cu film thickness. The thinnest samples also show an increasing energy release rate with total strain. In contrast, the energy release rate decreased with increasing total strain for the samples with 91 nm and 251 nm Cu film thickness. For the thickest sample with 506 nm Cu film thickness again a slight increase is observed. This reflects the different strength distribution in the films. For samples with a broad strength distribution (low κ_I , table 5.1) the energy release rate increases because the maximum defect size in these samples is higher whereas it decreases for samples with a narrow strength distribution (high κ_I).

For a total strain of about 6.5% the energy release rate became almost constant for all samples. The energy release rate at 6.5% total strain is thus taken to calculate the fracture toughness of the Cu films. The relationship between energy release rate and fracture toughness for plane strain is given by [Hertzberg 1989]

$$K_{IC} = \sqrt{\frac{E_f G}{(1 - \nu_f^2)}} \quad (5-6)$$

where E_f and ν_f are the Young's modulus and Poisson's ratio of the film material, respectively. Because of the strong (111) fiber texture of the Cu films the Young's modulus $E_{Cu[110]} = 130$ GPa for the [110] direction and the Poisson's ratio $\nu_{Cu(111),[110]} = 0.51$ for the (111) plane in [110] direction are used (chapter 3 and 4). The necessary parameters from the stress-strain curves, the evaluated values for the strain energies U_{strain} and $U_{relaxed}$ as well as the results for the energy release rate and fracture toughness are listed in table 5.4. The values for the corresponding crack distance L_i can be found in table 5.2. In addition, figures 5.6a and 5.6b show the fracture toughness of the Cu films as function of the Cu and Ta film thicknesses, respectively. The fracture toughness of the Cu films increases roughly linearly with increasing Cu film thickness whereas it decreases with increasing Ta film thickness. The absolute values vary from 2.73 to 12.68 MPam^{1/2}. This is in contrast to existing studies on brittle thin films on substrates where no distinct change in fracture toughness [Moody et al. 1998, Wellner et al. 2004] or a decreasing fracture toughness with increasing film thickness [Leterrier et al. 1997b] has been found. In addition, the absolute values are considerably higher compared to results for 150 nm thick Al films on polyimide ($K_{IC} = 2.04$ MPam^{1/2}) [Alaca et al. 2002] and 0.8 μ m thick Cu-Sn intermetallic films on polyetherimide and polycarbonate substrates ($K_{IC} = 2.63 - 2.83$ MPam^{1/2}) [Chen and Gan 2007]. The reason for these discrepancies will be discussed below in the light of different models for thin film fracture mechanics.

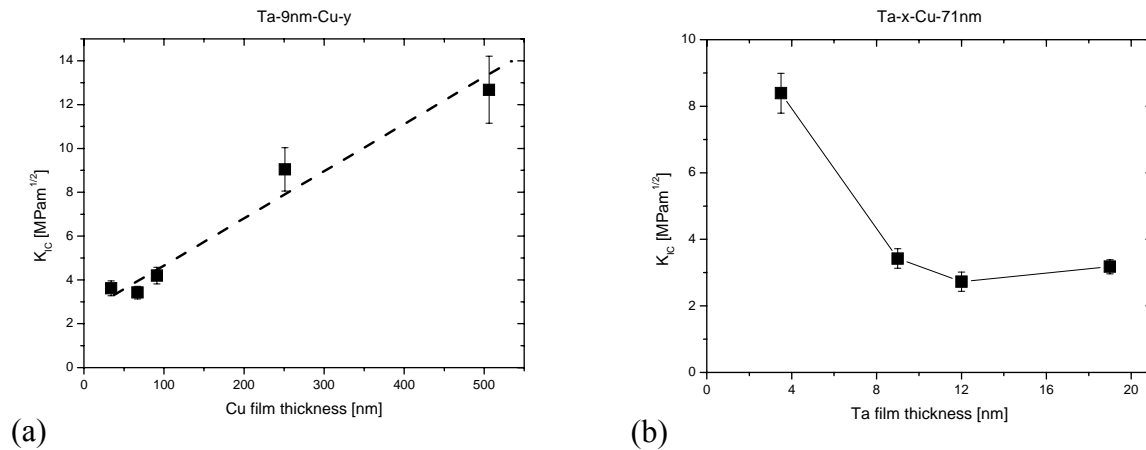


Figure 5.6: Fracture toughness of the Cu films vs. (a) Cu film thickness and (b) Ta film thickness. The fracture toughness of the Cu films depends on Cu as well as Ta film thickness.

Table 5.4: Input data and results for evaluation of energy release rate G and fracture toughness K_{IC} . The parameters σ_0 , ε_0 , ε_i , U_{strain} and U_{relax} are described in the text and schematically shown in figure 5.5a. G and K_{IC} were calculated from these parameters and L_i from table 5.2 according to equations (5-3) and (5-4).

Sample	σ_0 [MPa]	ε_0	ε_i	U_{strain} [MJ/m ³]	U_{relax} [MJ/m ³]	G [J/m ²]	K_{IC} [MPam ^{1/2}]
Ta-9nm-Cu-34nm	1151	0.026	0.063	3138.4	10.9	74 ± 15	3.61 ± 0.34
Ta-9nm-Cu-67nm	842	0.027	0.066	2851.0	4.4	67 ± 12	3.42 ± 0.29
Ta-9nm-Cu-91nm	822	0.028	0.065	2586.4	3.8	100 ± 19	4.19 ± 0.38
Ta-9nm-Cu-251nm	666	0.027	0.066	2400.0	2.4	465 ± 107	9.04 ± 0.99
Ta-9nm-Cu-506nm	487	0.029	0.065	1692.3	0.4	915 ± 234	12.68 ± 1.53
Ta-4nm-Cu-71nm	856	0.027	0.061	2490.5	4.7	400 ± 59	8.39 ± 0.60
Ta-12nm-Cu-71nm	525	0.029	0.060	1449.0	2.1	42 ± 9	2.73 ± 0.29
Ta-19nm-Cu-71nm	603	0.029	0.061	1470.4	4.6	57 ± 11	3.18 ± 0.21

5.4.3 Linear elastic fracture mechanics

Crack propagation in a film bonded to a substrate is a three-dimensional process. Nevertheless, for steady-state, channel cracking of brittle films (no plastic deformation) on substrates can be described analytically by two-dimensional models [Beuth 1992, Xia and Hutchinson 2000]. Xia and Hutchinson [2000] have shown that the longitudinal stress change $\Delta\sigma_x$ (perpendicular to the crack and parallel to the loading axis x) due to stress relaxation at the crack front is

$$\Delta\sigma_x = \sigma_0 \exp(-|x|/l) \quad (5-7)$$

where l is a reference length characterizing the exponential decay of the stress:

$$l = \frac{\pi}{2} g(\alpha, \beta) h. \quad (5-8)$$

Here h is the film thickness. The quantity $g(\alpha, \beta)$ represents the dimensionless integral of the crack opening displacement as defined by Beuth [1992] with α and β being the two Dundur's parameters [Dundurs 1969] characterizing the elastic mismatch between film and substrate.

For a compliant film on a stiff substrate $g(\alpha, \beta)$ is about 0.8 to 1.2 whereas it reaches values of 20 and more when the film is very stiff compared to the substrate [Beuth 1992]. For our case of Ta and Cu films on polyimide $g(\alpha, \beta)$ is estimated to be 15 ($\alpha = 0.97$). Therefore l is about 24 times the film thickness (table 5.5). Subsequently, the average longitudinal stress σ_x in the film can be calculated [Gruber 2004]:

$$\sigma_x = \sigma_0 - \frac{\int_0^{L/2} \Delta \sigma_x dx}{\int_0^{L/2} dx} = \sigma_0 \left(1 + \frac{\exp(-L/2l) - 1}{L/2l} \right). \quad (5-9)$$

In figure 5.7 σ_x is plotted against the total strain and compared to the longitudinal stress measured during the synchrotron experiments for the Ta-9nm-Cu-67nm and Ta-9nm-Cu-251nm sample. The necessary values for σ_0 and l can be found in table 5.4 and table 5.5. The corresponding crack spacing is taken from figure 5.4a.

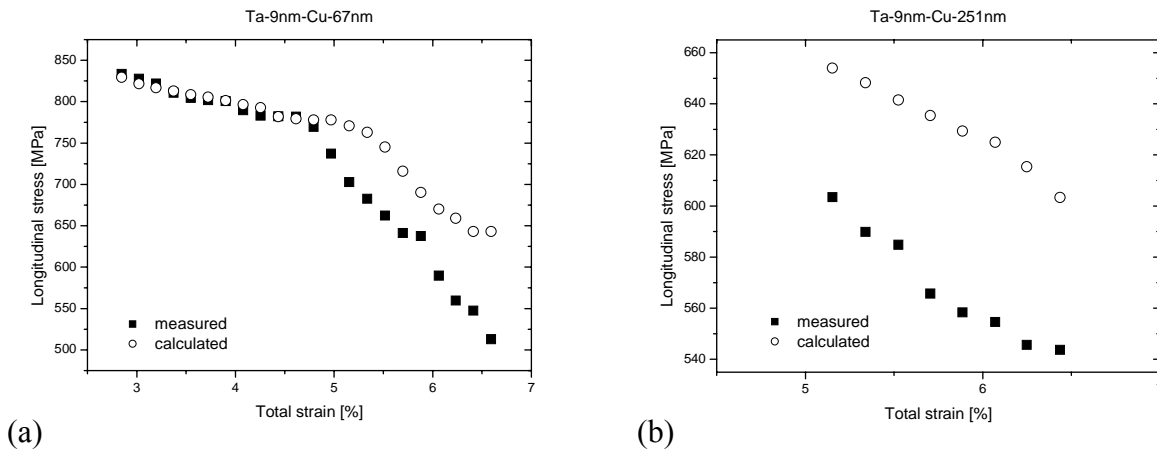


Figure 5.7: Longitudinal stress measured by the synchrotron technique and calculated according equation (5-9) vs. total strain for (a) the Ta-9nm-Cu-67nm and (b) Ta-9nm-Cu-251nm sample. Good agreement between measured and calculated values is obtained in the initial stage of cracking for the thinner sample.

It is evident that the calculated stress values fit well to the experimental values for the thinner sample, at least for the initial stage of cracking. This indicates that in the beginning the thinner sample behaves like a brittle material. For more than 5% total strain the measured stress values begin to deviate and become lower than the calculated ones. This strain level correlates with the transition from the first power-law regime for crack spacing to the second

(the crossover strain ε_c for the Ta-9nm-Cu-67nm sample in figure 5.7a was 0.055, see table 5.1). Here the cracks no longer form independently of each other and the 2D plane strain analysis of a single crack may no longer be valid. In contrast, a discrepancy between calculated and measured values from the beginning is found for the thicker sample. Nevertheless the slope of the stress decrease is similar and the difference between the values is almost constant with considerably lower experimental values.

Table 5.5: Results for the reference length l , the energy release rate G_{Beuth} and fracture toughness $K_{IC,Beuth}$. The values are calculated according to equations (5-6), (5-8) and (5-10). The parameter $g(\alpha, \beta)_{exp}$ represents the necessary value for $g(\alpha, \beta)$ to obtain the experimentally observed energy release rate by equation (5-10).

Sample	l [μm]	G_{Beuth} [J/m^2]	$K_{IC,Beuth}$ [$\text{MPam}^{1/2}$]	$g(\alpha, \beta)_{exp}$
Ta-9nm-Cu-34nm	1.013	6.0	1.03	185
Ta-9nm-Cu-67nm	1.791	6.4	1.06	157
Ta-9nm-Cu-91nm	2.356	8.3	1.20	182
Ta-9nm-Cu-251nm	6.126	14.9	1.62	468
Ta-9nm-Cu-506nm	12.134	16.1	1.68	853
Ta-4nm-Cu-71nm	1.767	7.2	1.13	98
Ta-12nm-Cu-71nm	1.956	2.7	0.69	60
Ta-19nm-Cu-71nm	2.121	3.5	0.78	67

Beuth [1992] has shown that the energy release rate G_{Beuth} associated with the steady-state crack propagation in a brittle film on a substrate of infinite thickness is given by:

$$G_{Beuth} = \frac{\pi (1 - \nu_f^2) \sigma_0^2 h}{2 E_f} g(\alpha, \beta). \quad (5-10)$$

The fracture toughness $K_{IC,Beuth}$ can again be obtained according to equation (5-6). Based on our experimental results $K_{IC,Beuth}$ varies between 0.69 and 1.68 $\text{MPam}^{1/2}$ (table 5.5). Although the observed trends of increasing fracture toughness for increasing Cu film thickness or decreasing Ta film thickness are reproduced by the model it strongly underestimates the experimental values (figure 5.8). This is a very similar argument to the stress calculations above. Both results indicate that stress in the Ta-Cu-film systems is not only released by brittle fracture but additional stress relaxation processes must take place. Possible mechanisms may be substrate deformation [Beuth and Klingbeil 1996, Vlassak 2003, Begley

and Barth-Smith 2005, Begley et al. 2005], strain localization in the film [Li et al. 2004, Li et al. 2005, Xiang et al. 2005b, Li and Suo 2006] or plasticity of the metallic films [Hsia et al. 1994].

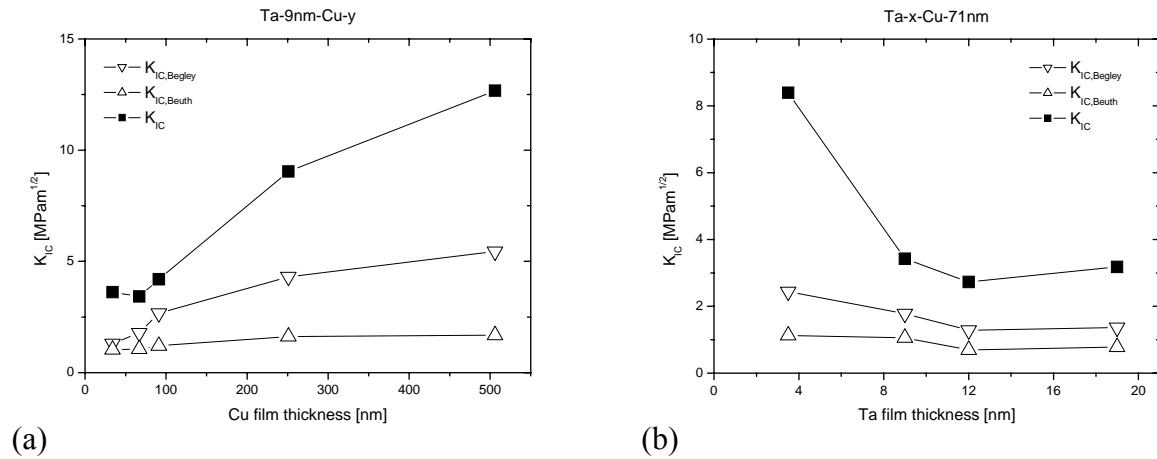


Figure 5.8: Comparison of the experimentally observed fracture toughness K_{IC} and the fracture toughness obtained by the models from Beuth [1992] and Begley et al. [Begley and Barth-Smith 2005, Begley et al. 2005], $K_{IC,Beuth}$ and $K_{IC,Begley}$ (equations (5-10) and (5-13), for samples with (a) varying Cu film thickness and (b) different Ta film thickness.

5.4.4 Substrate compliance and deformation

The energy release rate for channel cracking in a film bonded to a substrate can be significantly affected by the substrate properties. The two-dimensional elastic plane strain analysis presented above has been extended to substrates of finite thickness [Vlassak 2003] and to elastic-plastic substrates [Beuth and Klingbeil 1996]. The corresponding results show that $g(\alpha,\beta)$ can increase by a factor 2 to 3 for very thin substrates ($h_s/h_f < 100$, h_s : substrate thickness) or substrates with low yield strength ($\sigma/\sigma_{y,s} > 2$ with macroscopic stress σ and substrate yield strength $\sigma_{y,s}$). Both is not the case for our Ta-Cu films on polyimide ($h_{polyimide}/h_{Ta-Cu} = 240-3000$, $\sigma/\sigma_{y,polyimide} = 0.6-1$) and the predicted increase of $g(\alpha,\beta)$ is too low to explain the experimental values for the energy release rate. For this $g(\alpha,\beta)$ would have to be 60 to 853 ($g(\alpha,\beta)_{exp}$ in table 5.5) which is 4 to 60 times higher than predicted by the models. In addition $g(\alpha,\beta)$ would have to increase strongly with the film thickness indicating that the increase in energy release rate is rather influenced by the film rather than the substrate properties.

Begley et al. [Begley and Barth-Smith 2005, Begley et al. 2005] have proposed a different approach considering the interaction between the film, the substrate of finite thickness and stiffness as well as the crack spacing and opening. According to their model the effective modulus \bar{E} of the cracked film/substrate composite is lower than that of the intact sample \bar{E}_0 and decreases with increasing crack density (or decreasing crack spacing) [Begley and Bart-Smith 2005]:

$$\bar{E} = \bar{E}_0 \left[1 + 0.2 \left(\frac{h_f \bar{E}_f}{L \bar{E}_s} \right) \left(\frac{\hat{h}_f \bar{E}_f}{\hat{h}_s \bar{E}_0} \right) \right]^{-1}, \quad (5-11)$$

where $\hat{h}_f = h_f / (h_f + h_s)$, $\hat{h}_s = h_s / (h_f + h_s)$, $\bar{E}_f = E_f / (1 - \nu_f^2)$, $\bar{E}_s = E_s / (1 - \nu_s^2)$ and $\bar{E}_0 = \hat{h}_f \bar{E}_f + \hat{h}_s \bar{E}_s$. The subscripts s and f stand for substrate and film, respectively. The pre-factor 0.2 has been determined by finite element modeling. Based on these studies it has been illustrated that the crack opening displacement δ is well approximated by

$$\delta = 0.2 h_f \left(\frac{\bar{E}_f}{\bar{E}_s} \right) \left(\frac{\bar{E}(L_x)}{\bar{E}_0} \right) \varepsilon \quad (5-12)$$

where ε is the total strain imposed on the sample [Begley and Bart-Smith 2005]. If one assumes a uniform crack opening displacement throughout the thickness of the film, the energy release rate for an array of cracks with the final crack spacing L_x is given by

$$G_{Begley} = \sigma_f(L_0) \delta_x = 0.2 h_f \left(\frac{\bar{E}_f}{\bar{E}_s} \right) \left(\frac{\bar{E}(L_x)}{\bar{E}_0} \right) \sigma_f(L_0) \varepsilon(L_x) \quad (5-13)$$

where $\sigma_f(L_0)$ is the stress in the intact portion of the film and δ_x and $\varepsilon(L_x)$ are the crack opening and total strain after the formation of the final set of cracks [Begley et al. 2005]. In order to apply these equations to our experimental data we use the crossover values L_c and ε_c for L_x and $\varepsilon(L_x)$ as well as σ_0 for $\sigma_f(L_0)$. The results of this analysis for the effective moduli \bar{E}_0 and $\bar{E}(L_c)$, crack opening δ_c and energy release rate G_{Begley} are listed in table 5.6 together with the corresponding fracture toughness $K_{IC, Begley}$ obtained by equation (5-6). $K_{IC, Begley}$ is also plotted in figure 5.8.

Table 5.6: Results for the effective moduli \bar{E}_0 and $\bar{E}(L_c)$ for the intact sample and a sample with crack spacing L_c as well as the corresponding crack opening δ_c , energy release rate G_{Begley} and fracture toughness $K_{IC,Begley}$. The parameters are calculated according equations (5-11) to (5-13) and (5-6) using the experimental values L_c , ϵ_c and σ_0 .

Sample	\bar{E}_0 [GPa]	$\bar{E}(L_c)$ [GPa]	δ_c [nm]	G_{Begley} [J/m ²]	$K_{IC,Begley}$ [MPam ^{1/2}]
Ta-9nm-Cu-34nm	2.8852	2.8815	25	29.9	2.29
Ta-9nm-Cu-67nm	2.9318	2.9281	52	43.9	2.78
Ta-9nm-Cu-91nm	2.9650	2.9621	83	68.5	3.47
Ta-9nm-Cu-251nm	3.1855	3.1842	277	184.2	5.59
Ta-9nm-Cu-505nm	3.5361	3.5358	832	405.3	8.44
Ta-4nm-Cu-71nm	2.9304	2.9266	70	61.2	3.28
Ta-12nm-Cu-71nm	2.9401	2.9364	66	35.5	2.50
Ta-19nm-Cu-71nm	2.9512	2.9482	58	34.8	2.47

The values for $K_{IC,Begley}$ vary between 2.29 and 8.44 MPam^{1/2} and are thus closer to the experimental values than that predicted by the Beuth model especially for samples with low Cu film thickness or large Ta film thickness (figure 5.8). In contrast, for samples with larger Cu film thickness or lower Ta film thickness the model underestimates the experimental values more and more. This may indicate that the contribution by the film to the macroscopic mechanical behavior of the sample may have some influence on the fracture toughness, but it is not sufficient to explain the experimental data completely. Another discrepancy between the model and the experimental data is related to the crack opening. According to the model the crack opening should increase with Cu film thickness (equation (5-12) and table 5.6) which is not observed experimentally where the crack opening is the same for all Cu film thicknesses at any total strain (figure 5.4d). Therefore it is questionable if the assumptions made hold for our film systems or if the partial agreement is just fortuitous. At least there must be additional contributions.

5.4.5 Strain localization and delamination

Xiang et al. [2005b] and Li et al. [Li et al. 2004, Li et al. 2005, Li and Suo 2006] have shown that if a metallic film is fully bonded to a polyimide substrate, the substrate suppresses large local elongations in the film. Thus, the film may deform uniformly up to high total strains.

However, if the film debonds locally from the substrate, it becomes freestanding and ruptures at a smaller strain than the fully bonded film. To reduce the rupture strain to a few percent as observed in our experiments (2-4%), the debond length would have to be about 100 times the film thickness [Li et al. 2005]. Such debond lengths are unreasonable for our samples because the ratio between the crack spacing and film thickness L_c/h_f is only 75 to 200, which means that the complete film would have to delaminate. Nevertheless, we expect very local delamination of the film because we assume that crack nucleation starts in the brittle Ta interlayer. The Ta layer is located at the interface to the polyimide substrate where the highest defect density is expected. Thus, the Ta layer is the most likely site of crack initiation. Once the Ta layer fractures the overlaying Cu film becomes freestanding at least across the crack opening (there may be some additional delamination at the film/substrate interface, see figure 5.3d) allowing for strain localization by necking. Subsequently the fracture strain and fracture toughness of the Ta-Cu-film system depends on the ductility of the Cu film (increases with film thickness) and the Ta film thickness (determines initial crack length).

5.4.6 Plastic deformation and geometrical constraint

Xiang et al. [2005b] have shown that Cu films well bonded to a polyimide substrate fracture by a mixture of local thinning and intergranular fracture. In contrast to strain localization, the substrate constraint is less effective in retarding intergranular fracture, because it needs little additional space to proceed. The same argument holds for cleavage fracture, where also no large local elongation occurs. Here, the presence of the substrate can only reduce the driving force for a long channel crack by limiting the crack opening in its wake. It is evident from figure 5.4 that in our Ta- and Ta-Cu film systems all fracture morphologies are present. The contribution of each type strongly depends on film thickness. Very thin Ta and Ta-Cu samples show cleavage fracture with very straight and tiny cracks (figure 5.4a and b), whereas Ta-Cu samples with intermediate thickness rupture by intergranular fracture and local thinning indicated by shorter and wider zig-zag cracks (figure 5.4c and e). The thickest Ta-Cu sample, however, shows only very few and short zig-zag cracks as well as some trenches indicating an increasing tendency of necking (figure 5.4f). In our opinion the gradual change in fracture mechanism must be correlated to the increasing ductility of the Cu films with increasing film thickness because the crack initiation (fracture of brittle Ta interlayer as discussed above) as well as the interface and the substrate properties are the same for all samples. Hsia et al.

[1994] also reported that in very ductile fcc metals cleavage fracture is possible due to dislocation confinement for submicron layers.

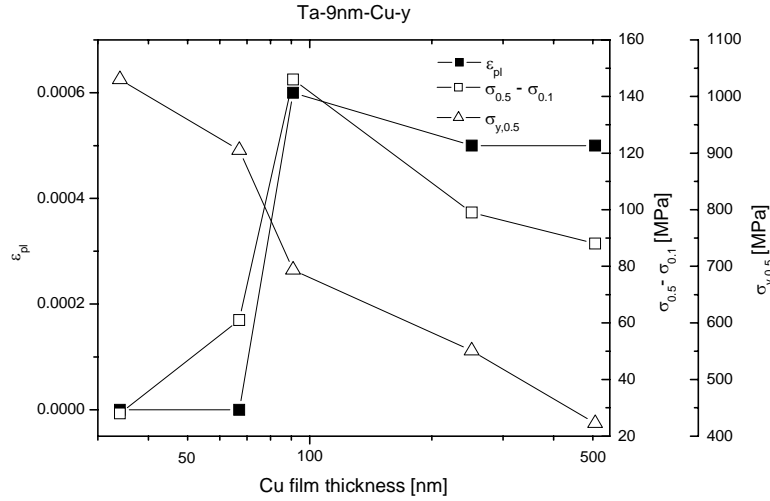


Figure 5.9: Volume averaged plastic strain ϵ_{pl} , strain hardening rate $\sigma_{0.5} - \sigma_{0.1}$ and flow stress $\sigma_{y,0.5}$ for samples with varying Cu film thickness. Strain hardening rate and flow stress are replotted from chapter 4. The volume averaged plastic strain is determined from the initial difference in calculated (according to equation (5-9)) and measured stress divided by the Young's modulus of the Cu film.

In order to quantify the contribution of plastic deformation during cracking of the Ta-Cu film systems, the volume averaged plastic strain ϵ_{pl} was calculated. This was done by dividing the initial difference (first experimental value for crack spacing) between the stress according to the Beuth model (linear elastic, see equation (5-9)) and the experimental values obtained by the synchrotron technique by the Young's modulus of the film ($E_{Cu[110]} = 130$ GPa). In figure 5.9 ϵ_{pl} is compared to the strain hardening rate $\sigma_{0.5} - \sigma_{0.1}$ and the flow stress σ_y of identical samples with varying Cu film thickness (chapter 4). For the two thinnest samples ($h_f < 100$ nm) ϵ_{pl} is zero because no difference between calculated and measures stress is found indicating that these samples show almost perfect brittle fracture. These samples also show a strong decrease in strain hardening and a saturation of flow stress. This is assumed to be correlated to a change in deformation mechanism from full to partial dislocations (chapter 4). The deformation by partial dislocations may not be efficient enough to sustain any crack initiation leading to very brittle fracture behavior. In contrast, for samples with a Cu film thickness above 100 nm ϵ_{pl} is about 0.04 to 0.07% and the strain hardening (peak for $h_f \approx 100$ nm) as well as flow stress decrease with increasing Cu film thickness. Here, dislocation

plasticity seems to relax some stress around the tip of the initial cracks in the Ta interlayer. This leads to the mixture of strain localization and brittle intergranular fracture.

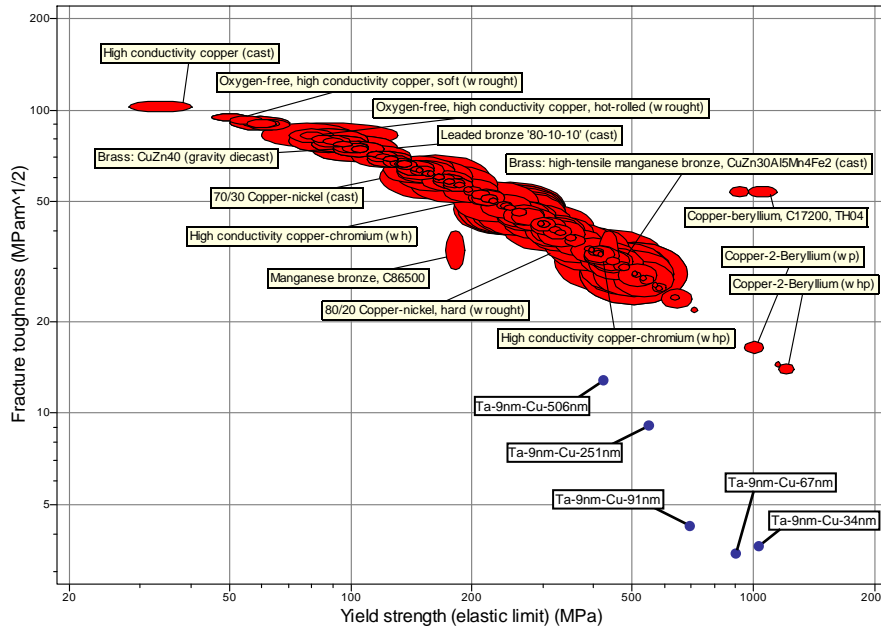


Figure 5.10: Comparison of the measured fracture toughness of different Ta-Cu film systems (blue) to literature data for pure Cu and Cu alloys with similar yield strength (red) [CES Selector Version 4.6.1 by Granta Design Ltd.]

Beside the increasing flow stress the thin film geometry provides an additional effect on the fracture toughness. Compared to Cu alloys of similar flow stress the fracture toughness of the Ta-Cu film systems is considerably lower. On the other hand, the dependence on the flow stress is stronger for the thin film samples (figure 5.10). This may be attributed to the geometrical constraint on the size of the plastic zone. A rough estimation of the radius r_{pl} for the plane-strain plastic zone is given by [Hertzberg 1989]

$$r_{pl} \approx \frac{1}{6\pi} \frac{K_{IC}^2}{\sigma_y^2}. \quad (5-14)$$

Inserting the experimental values for the different Ta-Cu film systems leads to an increasing radius for the plastic zone with increasing Cu film thickness from 0.5 to 36 μm which corresponds to 10 to 40% of the final crack spacing or 10 to 70 times the film thickness. This clearly indicates that the contribution of plastic deformation increases with increasing film thickness and that the fracture toughness is limited by the thin film geometry. The fracture

toughness of the Ta-Cu film systems thus depends on film thickness and is lower than that of a Cu-bulk material of the same strength.

5.5 Summary and conclusion

The cracking behavior of ultra thin Cu films on polyimide substrates with Ta interlayers has been investigated. The combination of *in situ* tensile tests in a SEM and a synchrotron-based tensile testing technique has provided further insight in the fracture mechanics of thin films on compliant substrates:

- Sequential cracking of the films leads to a continuous and distinct decrease in the average stress of the film. Initially the cracks form independently and are located randomly according to strength distribution in the film. Later on the formation of new cracks depends on existing cracks.
- By relating the release in strain energy by cracking, which could be estimated from the stress-strain curves, to the crack area determined from the *in situ* SEM tests, the fracture toughness of the Cu films can be obtained. The fracture toughness increases with Cu film thickness and decreases with increasing Ta film thickness.
- The measured values for the fracture toughness cannot be explained by existing models dealing with linear elastic fracture mechanics, substrate deformation or strain localization in the film.
- The fracture mode of the Cu films seems to be a mixture of local necking and cleavage fracture. The contribution of brittle fracture increases with decreasing Cu film thickness. Films thinner than 100 nm show completely brittle fracture indicating an increasing inherent brittleness of the Cu films.

6 Temperature dependence of mechanical properties in passivated and unpassivated ultra thin Au films

6.1 Introduction

The microstructural and dimensional constraints in polycrystalline thin films strongly influence their mechanical properties [Arzt et al. 2001, Dehm et al 2002a]. The small grain size and film thickness lead to (i) high stresses at low temperatures due to the confinement of either dislocation motion [Nix 1989, Thompson 1993, Nix 1998] or dislocation nucleation and interaction [von Blanckenhagen et al. 2001, Pant et al. 2003, Needleman et al. 2006] (chapter 4) and (ii) increased stress relaxation at elevated temperatures by diffusional flow of matter between the free surface and the grain boundary [Gibbs 1966, Gao et al. 1999]. Thus, the mechanical properties of thin films are expected to depend significantly on temperature.

The only technique which is routinely used to study the deformation of thin films at elevated temperatures is the substrate curvature technique [Nix 1989]. Using this technique several authors have shown that stress relaxation in unpassivated thin films on substrates can occur by diffusional deformation [Vinci et al. 1995, Keller et al. 1998, Weiss et al. 2001, Balk et al. 2003a, Sauter 2006]. Secondly, the presence of a passivation layer on the surface of the film can inhibit diffusional flow and result in the activation of dislocation processes within the grains [Keller et al. 1998, Kobrinsky and Thompson 2000, Kobrinsky et al. 2001, Weiss et al. 2001, Balk et al. 2003a]. Although this technique gave valuable insight in the deformation behavior of thin films on substrates over a wide range of temperatures and needs very little sample preparation, it is limited because it does not allow for independent control of temperature, stress and strain. Thus, it is not possible to obtain comparable data of the same sample at different temperatures.

In order to achieve more defined loading conditions, it would be desirable to adapt other techniques to elevated temperatures. In particular, displacement measurements with a resolution of a few nm are severely influenced by temperature changes due to thermal expansion of the experimental setup. Therefore only very few experiments at elevated temperatures are described in the literature. Among them are nanoindentation creep tests

[Lucas and Oliver 1999], tensile or creep testing of freestanding films [Brotzen et al. 1990, Emery et al. 1998, Haque and Saif 2005a], membrane resonance measurements [Hyun et al. 2003] and bulge tests [Kalkman et al. 2003, Cieslar et al. 2004]. Due to difficulties in data analysis, sample preparation and experimental realization not only the number of testing methods but also the number of tested samples is very small.

Our group has in recent years developed a novel synchrotron-based testing technique [Böhm et al. 2004], by which it is possible to characterize the stress evolution in metallic films thinner than 40 nm during isothermal tensile tests. In the current study heating and cooling capabilities were introduced in the experimental setup to allow for measuring stress-strain curves in a temperature regime from -150°C up to 250°C. The samples consisted of Au film systems with and without additional SiN_x-passivation layers on polyimide substrates. Au was chosen because it does not oxidize and thus can serve as a model system for a free surface. The influence of different surface and interface conditions on the deformation mechanisms of the Au films could systematically be investigated. In this way, the flow stress of the different Au film systems could be systematically determined as functions of film thickness and temperature. The measured flow stresses were used to estimate the activation energies for thermally activated dislocation glide and grain boundary diffusion. This should provide additional information about the correlation of stress, temperature and predominant deformation mechanism.

6.2 Experimental

6.2.1 Sample preparation and characterization

Different Au, AuSiN and SiNAuSiN samples were prepared (figure 6.1). The films were deposited on 125 μm thick dogbone-shaped polyimide substrates (Kapton® HN) with a gauge section of 6 mm x 20 mm. Au as well as SiN_x films were deposited in a direct-current (DC) magnetron sputtering system (DCA Instruments, Finland) with a base pressure of 1x10⁻⁸ mbar. Prior to film deposition the substrate surface was Ar⁺ sputter cleaned for 2 minutes at 200 eV and subsequently heated up to 300°C. Au films were sputtered with a DC power of 100 W, an Ar pressure of 2.5x10⁻³ mbar and a deposition rate of 42 nm/min. The nominal Au film thickness was varied between 80 and 500 nm. The SiN_x inter- and surface layers were

prepared by reactive sputtering with a DC power of 100 W and a N_2 pressure of 3.2×10^{-4} mbar. The Ar flow was adjusted such that the total gas pressure was again 2.5×10^{-3} mbar. In between Au and SiN_x film deposition the gas flow was cut off and the sputter system was pumped for 10 min. The deposition rate for the SiN_x films was 4 nm/min and the nominal film thickness was always 10 nm. Auger electron spectroscopy measurements gave an almost stoichiometric composition of Si_3N_4 . First high resolution transmission electron microscopy images suggested that the films were nanocrystalline with a grain size of about 10 nm.

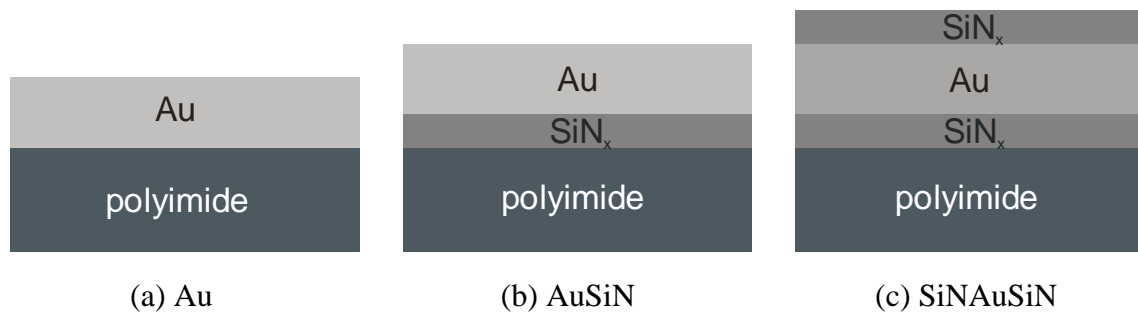


Figure 6.1: Schematic drawing of the different Au, AuSiN and SiNAuSiN samples.

The grain size of the Au films was characterized by focused ion beam (FIB) microscopy and plan-view transmission electron microscopy (TEM). Films thicker than 160 nm were investigated using FIB (FEI FIB 200xP). In order to ensure the identification of all grain boundaries by the channeling contrast in the FIB, images with at least three different tilt angles between 0 and 25° were taken and compared. Plan-view TEM samples were cut out of samples with 80 and 160 nm Au film thickness and were thinned to electron transparency by dimpling and ion milling. TEM investigations were carried out using a 200 kV TEM (Jeol 2000FX). The grain boundaries from FIB and TEM pictures were drawn manually on a transparency foil and scanned in order to determine the area of the grains using commercial software (Leica Quantimet Q5501W). Grain size was defined as the diameter of a circle with the equivalent area and at least 400 grains were evaluated for each film. The thickness of the Au films in the different Au, AuSiN and SiNAuSiN film systems was determined by Rutherford backscattering spectrometry (RBS). All measurements were conducted using 2 MeV He^+ ions (6.5MV Pelletron accelerator of the Max Planck Institute for Metals research). The film thickness was obtained by fitting the RBS spectra with the X-Rump simulation software (Computer Graphics Service Ltd.)

6.2.2 Tensile testing

X-ray diffraction measurements were performed at the MPI-MF-Beamline at the synchrotron radiation source ANKA (Angströmquelle Karlsruhe). The details for the experimental procedure and data analysis of the synchrotron-based tensile testing technique are described for Au films in Reference [Böhm et al. 2004]. Figure 6.2a shows the experimental setup for the transmission geometry used to evaluate the stress evolution during the tensile tests. The microtensile tester (Kammrath & Weiss) is mounted on the sample stage of 2+3 circle diffractometer. The Debye-Scherrer rings of the sample were recorded using a large area CCD detector (MarCCD). For calibration, tungsten powder was attached to the backside of the polyimide substrate by vacuum grease. The total strain of the sample was measured by an optical strain measurement (2D-Strainmaster, LaVision).

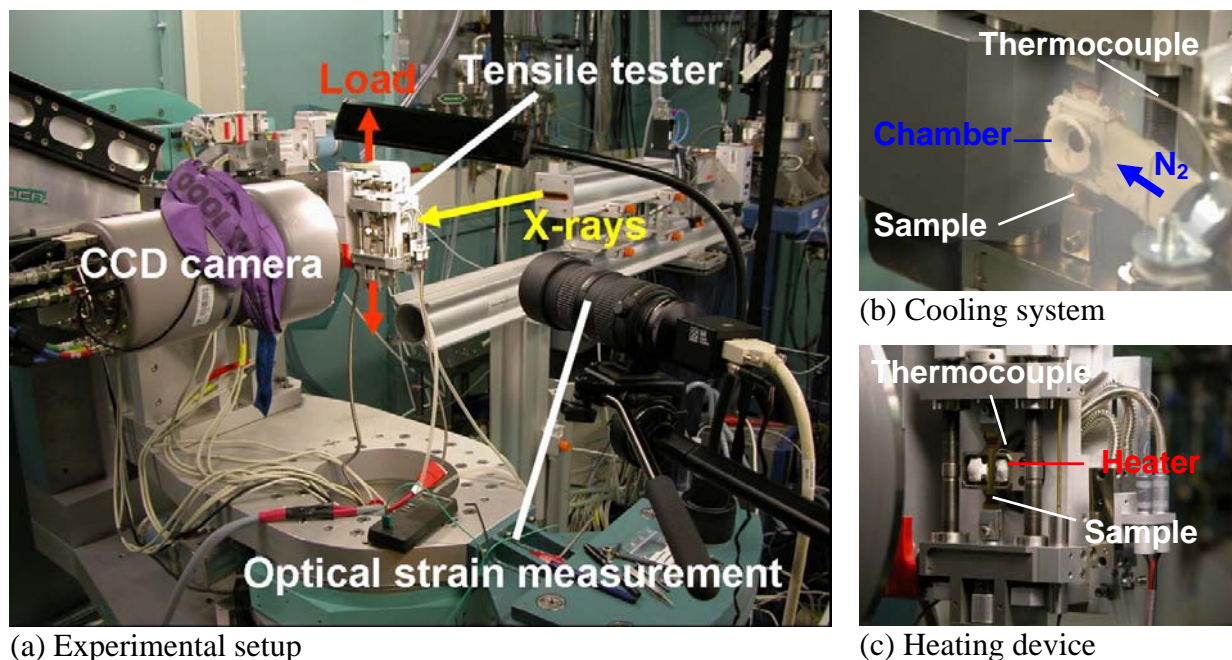


Figure 6.2: (a) Experimental setup at the MPI-MF-Beamline for X-ray measurements in transmission geometry. The Debye-Scherrer rings of the sample and calibration were recorded on a large area CCD camera. The total strain of the sample was measured by optical means. Closer look at (b) the cooling system and (c) heating device. To prevent ice formation during cooling a chamber was built around the sample. The sample temperature was measured by thermocouples.

Two different setups were used to heat and cool the sample. The cooling system consists of a sample chamber with two funnel shaped openings on the back and front side for the X-ray beam and narrow slits at the top and the bottom for the sample (figure 6.2b). The design of the sample chamber was necessary to prevent ice formation on the sample. The chamber was

continuously filled through a flat nozzle with cold N₂ gas which was generated by guiding N₂ gas in a Cu tube coil through a reservoir of liquid N₂. By adjusting the N₂ gas pressure and the dipping depth of the Cu coil in the liquid N₂, almost constant temperatures could be achieved for the period of a tensile test. Using a N₂ pressure of 0.8 bar and dipping the Cu coil completely in liquid nitrogen a sample temperature of -150°C could be realized. The sample temperature was measured by a thermocouple located at the backside of the sample. For heating a commercial heating device (Kammrath & Weiss) was mounted in the backside of the tensile tester (figure 6.2c). It consists of a rounded ceramic heater with a central hole for the incoming X-ray beam (2.8 mm in diameter, X-ray beamsize was 1x1 mm²). Similar to the cooling system a thermocouple was positioned at the backside of the sample to measure the temperature of the sample. Here, the thermocouple was also connected to the control unit of the tensile tester which controlled the temperature. In this study, experiments were performed at five different temperatures ranging from -150 up to 200°C.

Prior to the tensile tests the evolution of thermal stresses in the Au films was characterized. Therefore, a CCD frame was taken every two minutes after starting the heating or cooling until the temperature and stress in the sample became constant. Afterwards the tensile test was performed by increasing the crosshead displacement of the tensile tester in steps between 30 and 100 μm up to a maximum displacement of 1900 μm and subsequent decreasing. Again, a CCD frame was taken for each step. The exposure time was always 30 s in order to ensure almost identical strain rates for all testing temperatures. Small differences occurred because the correlation of crosshead displacement and total strain on the sample varies with temperature and sample. It must be noted that no direct strain measurement was possible for the experiments at low temperatures due to the presence of the sample chamber which covered the sight of the optical strain measurement. Therefore the crosshead displacement was calibrated by tests without sample chamber (the chamber could be demounted from the gas nozzle).

6.3 Results

6.3.1 Microstructure

Exemplary FIB and TEM micrographs of Au and AuSiN samples are shown in figure 6.3. All films had a columnar grain structure with grains that are equiaxed in the plane of the film. Twins are visible in the TEM micrograph of the 80 nm thick Au film whereas twinning seems to be less pronounced in the 160 nm thick films examined by FIB. The introduction of a SiN_x interlayer had no influence on the film microstructure as can be seen in figures 6.3b and c. This was also found for other film thicknesses and films with SiN_x surface and interlayer. Therefore the grain size distributions were only determined for Au samples. The median grain size values were comparable to the actual film thickness and increased linearly with increasing film thickness as long as the film thickness was smaller than 300 nm (figure 6.3d and table 6.1). For the thickest film the grain size stagnated. The mean values of the film thickness, measured by RBS, for different samples of the same nominal thickness are listed in table 6.1. The difference between nominal and real film thickness was about 10%. During deposition the film thickness was adjusted by the sputtering time, which apparently gave a systematic offset.

Table 6.1: Summary of microstructural data of Au samples: Nominal and measured film thickness h , median grain size d_{50} , mean grain size d_{mean} , standard deviation σ_{dev} and number of detected grains N . The error for the measured film thickness is estimated from the deviation between different samples. The error of the RBS measurements was below 2%.

Sample	Film thickness h [nm]		Grain size statistics				
	nominal	measured	d_{50} [nm]	d_{mean} [nm]	σ_{dev} [nm]	d_{max} [nm]	N
Au80	80	73 ± 3	104	126	80	653	610
Au160	160	146 ± 4	170	194	97	640	550
Au240	240	215 ± 6	269	303	155	1313	532
Au320	320	288 ± 13	346	403	215	1568	441
Au500	500	449 ± 11	276	295	121	731	541

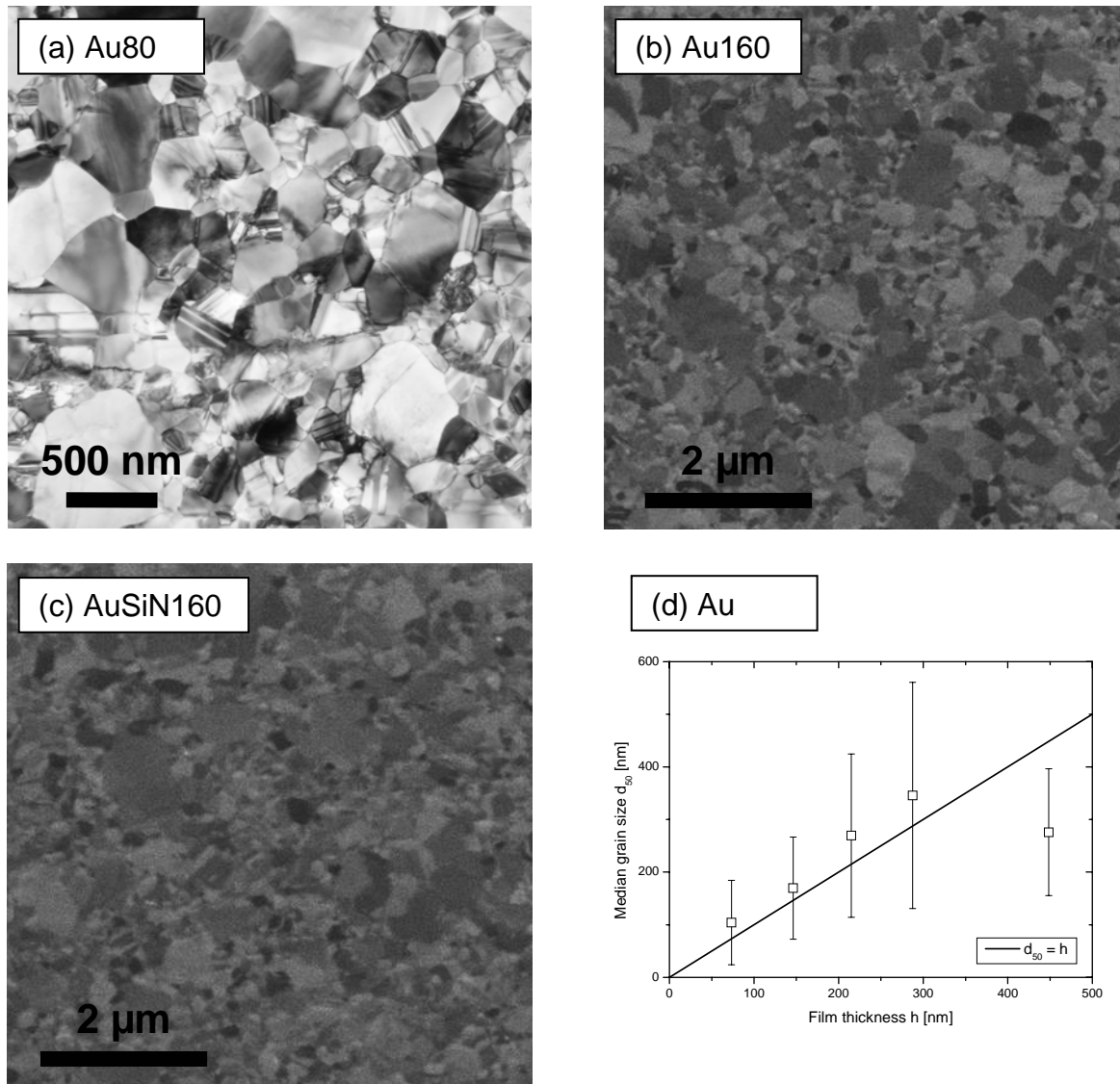
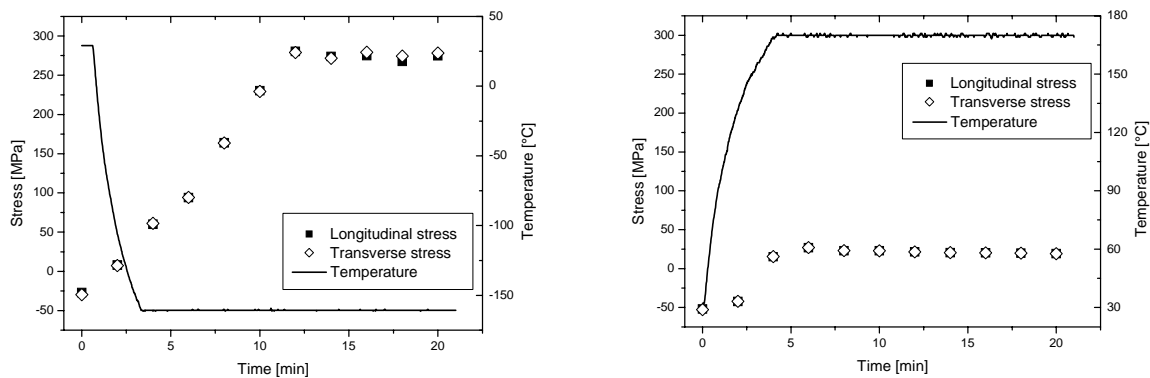


Figure 6.3: Microstructural characterization of the different samples: TEM micrograph of (a) an 80 nm thick Au film and FIB images of (b) a 160 nm thick Au and (c) a 160 nm thick AuSiN film. The microstructure is not affected by the SiN_x layer. (d) Median grain size vs. film thickness for Au samples. Up to 300 nm film thickness the median grain size increases linearly. Above the grain size stagnates.

6.3.2 Stress-strain curves and yield strength

In figure 6.4a and b the evolution of temperature and thermal stresses in 160 nm thick Au films during cooling and heating is shown. In both cases the measured temperature changed faster than the stress state in the film. However, after 4 min (heating up to 150°C) or 12 min (cooling to -150°C) a constant stress level was reached. The stress state remained equibiaxial during the temperature change. In principle, the thermal expansion coefficient of the polyimide is higher than that of the Au film ($\alpha_{PI} = 30 \times 10^{-6} \text{ K}^{-1} > \alpha_{Au} = 14.2 \times 10^{-6} \text{ K}^{-1}$), which should lead to compressive stresses during cooling and tensile stresses during heating. This

was not observed, because the samples were clamped in the tensile tester. Thus a contraction of the substrate during cooling was not allowed which led to a tensile load on the sample (the load cell showed loads of about 10 N). In contrast, the elongation of the substrate during heating is possible and therefore the tensile stresses in the Au film resulted from the lower thermal expansion of the Au film compared to the substrate. Due to the high thermal expansion coefficient of the polyimide substrate the elongation led to a distinct bending of the sample. The bending of the sample had to be compensated by crosshead movement prior to the tensile test to ensure correct loading and straining of the sample.



(a) Au160: Cooling down to -150°C

(b) Au160: Heating up to 150°C

Figure 6.4: Stress and temperature vs. time for 160 nm thick Au films during (a) cooling down to -150°C and (b) heating up to 150°C . An increase in equibiaxial stress is found for both cases.

Two different types of stress-strain curves could be identified. Figure 6.5a shows the stress-strain curve of a 160 nm thick Au film tested at -150°C . After the linear elastic regime, the film deformed plastically up to a total strain of about 2%. For higher strains the longitudinal as well as transverse stress decreased continuously. This stress drop is typical for stress relaxation by sequential cracking of a ductile metallic film on a compliant substrate [Gruber 2004] (chapter 5). Upon unloading compressive stresses developed in the film. The complementary evolution of the transverse stress was due to the mismatch in Poisson's ratio of the Au film and the polyimide substrate [Böhm et al. 2004]. The stress-strain curve of an identical sample tested at 50°C is shown in figure 6.5b. Here, no stress decrease was observed up to a total strain of more than 7%. Instead stress plateaus in tension and compression were found.

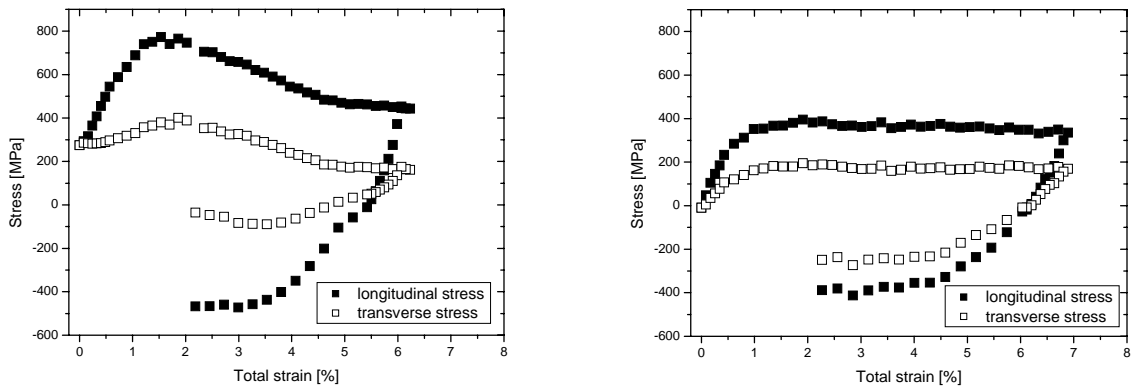
(a) Au160: Tested at -150°C (b) Au160: Tested at 50°C

Figure 6.5: Stress-strain curves for 160 nm thick Au films tested at (a) -150°C and (b) at 50°C . The longitudinal (filled symbols) as well as transverse (open symbols) is shown. The different shapes are typical for all stress-strain curves.

Figures 6.6 to 6.8 show the temperature dependence of the stress-strain curves for all film thicknesses and film systems. Stress-strain curves showing a stress decrease at high total strain were observed for low and high temperatures as well as for samples with and without SiN_x layers. The onset of the stress drop always decreased with increasing temperature. The second type of stress-strain curve without stress decrease was found for Au samples tested at intermediate temperatures and for thicker AuSiN samples. Overall a strong temperature dependence of the stress values was found for all samples.

Consequently also a strong temperature dependence of the flow stresses was observed. The flow stress was determined from the von Mises stress at 0.5% permanent strain. This was necessary to account for the biaxial stress state in the films [Böhm et al. 2004]. In figure 6.9 the von Mises flow stress is shown as function of film thickness and temperature for all film systems. The strongest effects were found for Au samples. Here, the flow stress already decreased significantly for temperatures above 50°C . In addition, the thickness dependence of the flow stress diminished completely. In contrast, samples with SiN_x layers showed much higher flow stresses for the same temperature or film thickness. For 200°C the flow stress of SiNAuSiN samples was still above 300 MPa and still increased with decreasing film thickness. The difference between AuSiN and SiNAuSiN samples was low.

6 Temperature dependence of the mechanical properties of ultra thin Au films

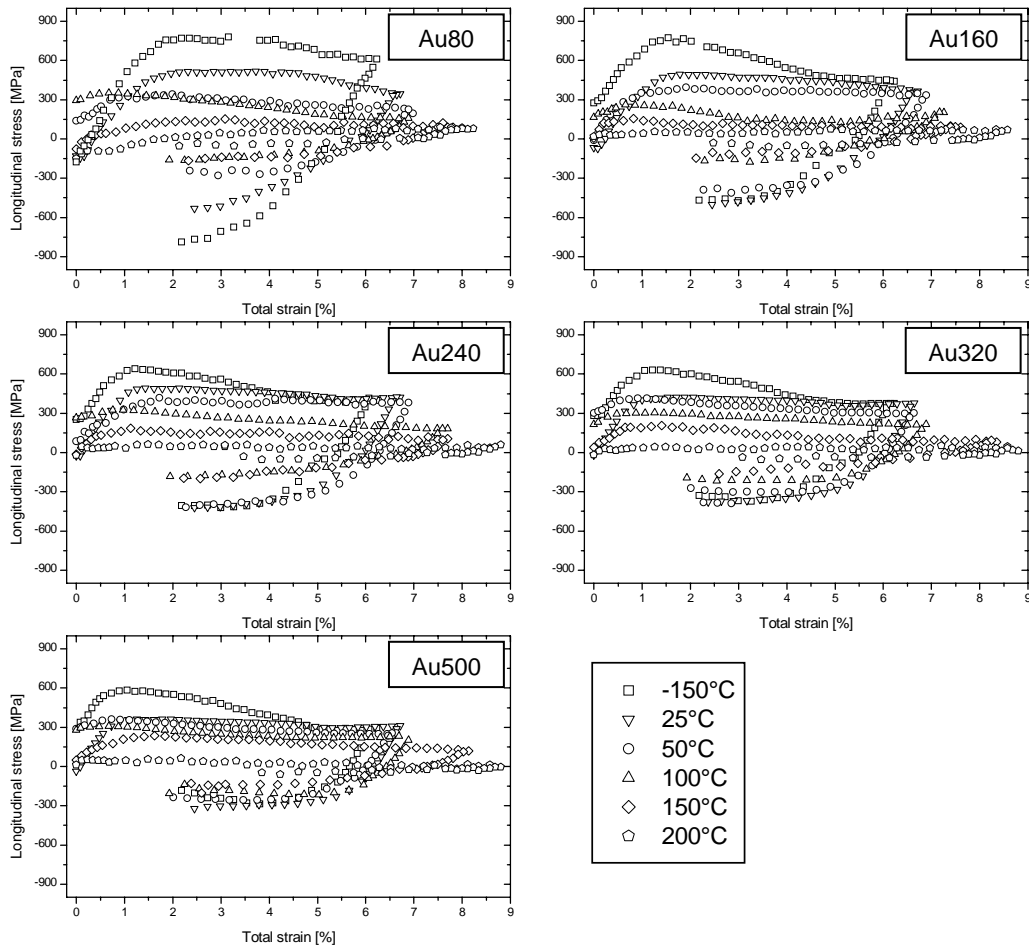


Figure 6.6: Au samples: Stress-strain curves for 80 to 500 nm thick Au films measured at different temperatures ranging from -150°C up to 200°C. For clarity only the longitudinal stress is plotted.

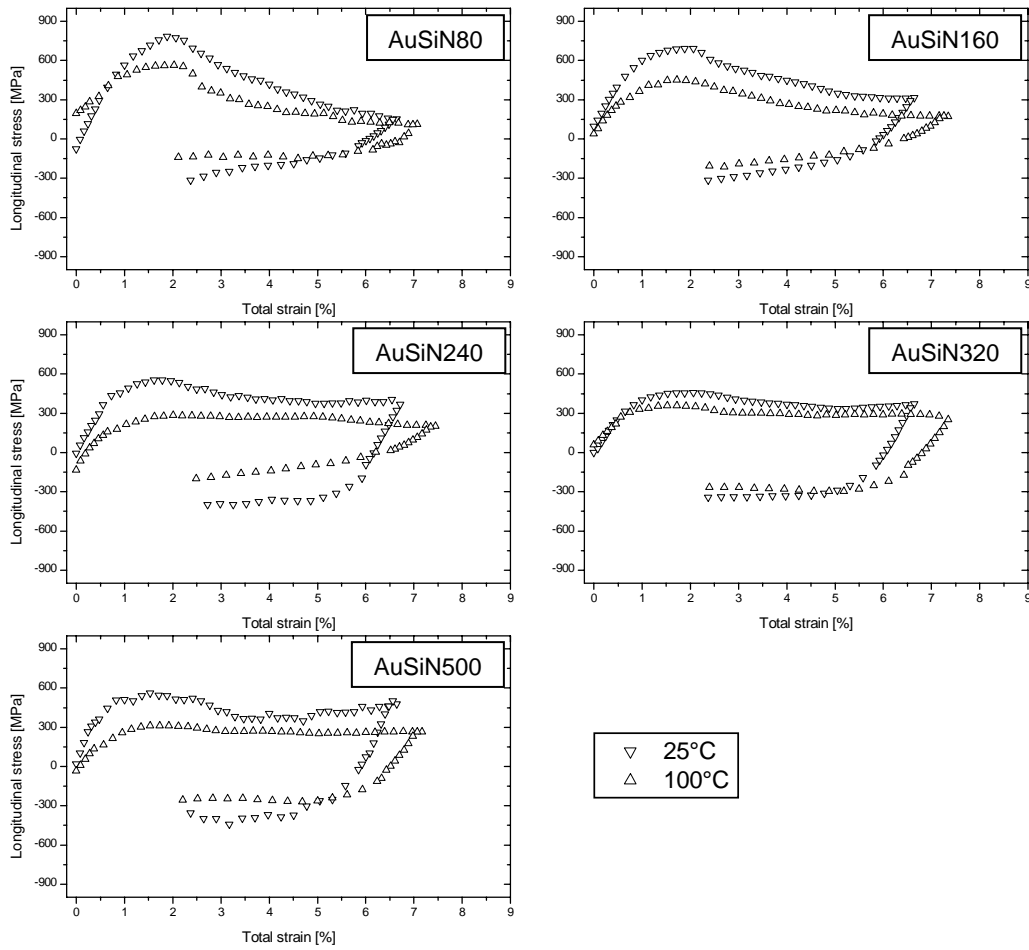


Figure 6.7: AuSiN samples: Stress-strain curves for 80 to 500 nm thick Au films measured at 25°C and 100°C. For clarity only the longitudinal stress is plotted.

6 Temperature dependence of the mechanical properties of ultra thin Au films

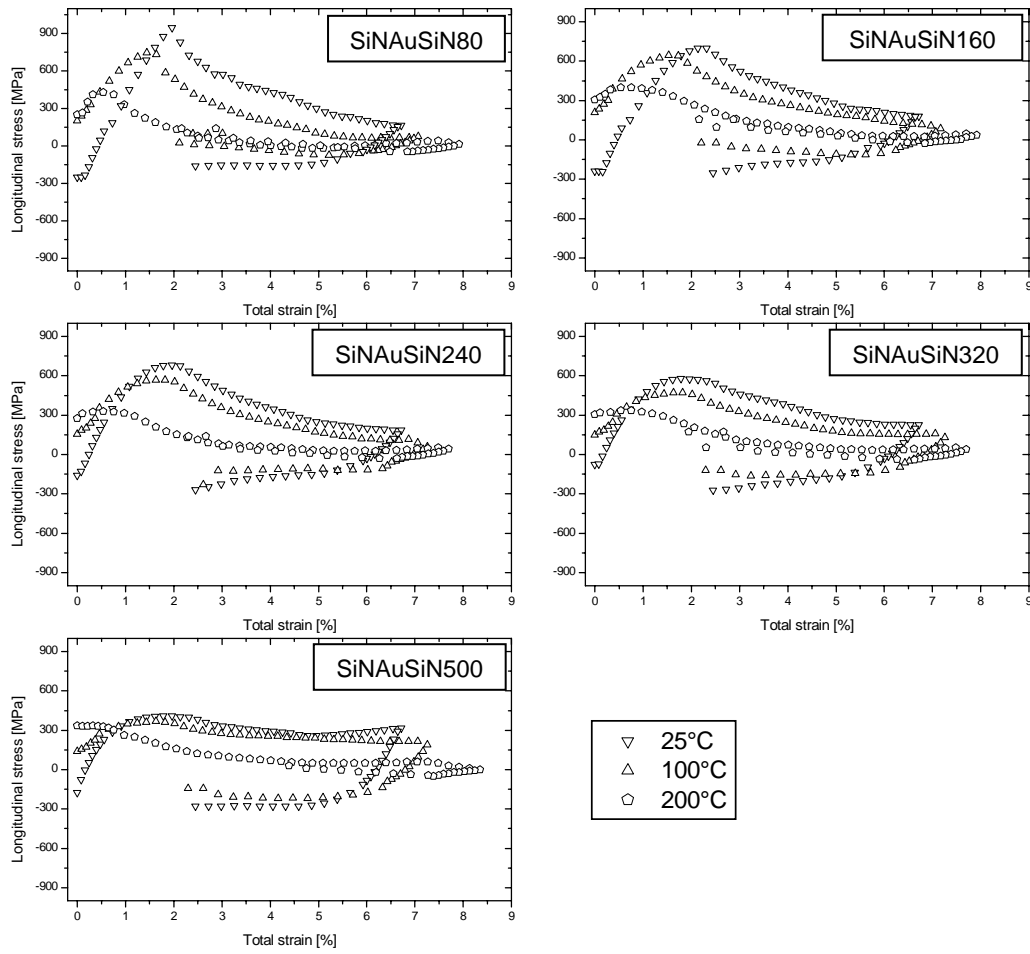
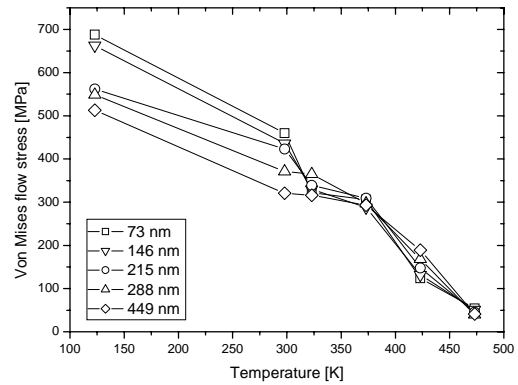
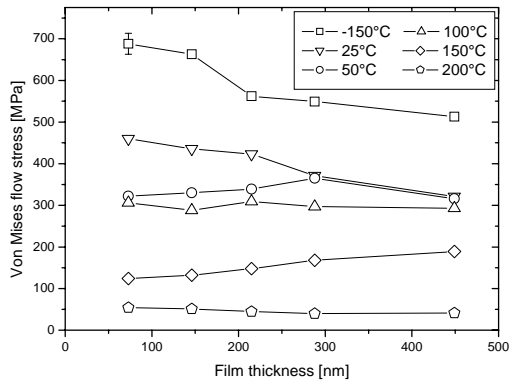
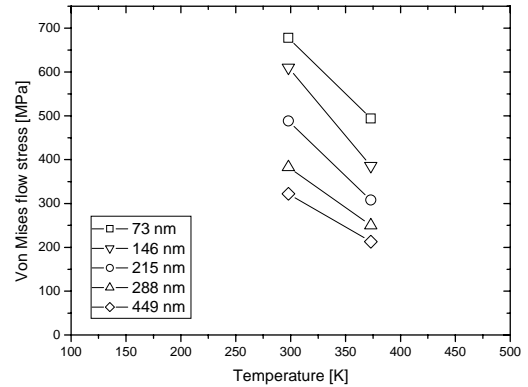
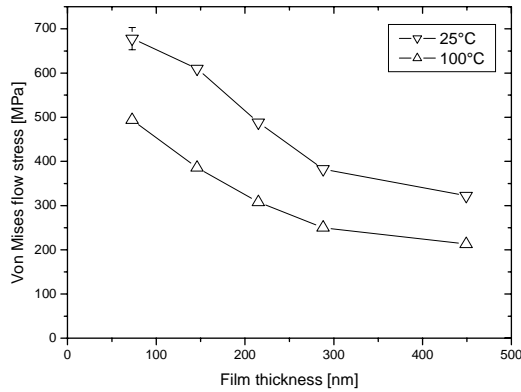


Figure 6.8: SiNAuSiN samples: Stress-strain curves for 80 to 500 nm thick Au films measured at 25, 100 and 200°C. For clarity only the longitudinal stress is plotted.

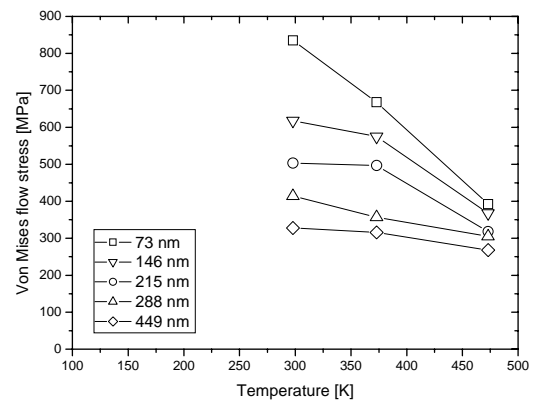
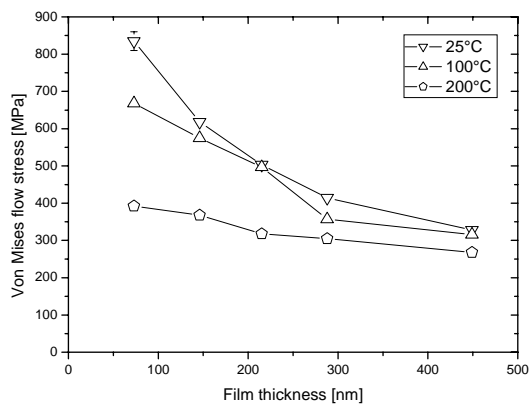
6 Temperature dependence of the mechanical properties of ultra thin Au films



(a) Au



(b) AuSiN



(c) SiNAuSiN

Figure 6.9: Von Mises flow stress as function of film thickness and temperature for (a) Au, (b) AuSiN and (c) SiNAuSiN samples. The flow stress of Au samples shows the strongest dependence on temperature but the lowest thickness dependence.

6.4 Discussion

6.4.1 Low and high temperature fracture

The stress decrease in the stress-strain curves in figures 6.6 to 6.8 can be correlated to sequential channel cracking in the Au films. Due to the substrate constraint cracking leads to local stress relaxation [Beuth 1992, Xia and Hutchinson 2000], which results in a continuous decrease of the average film stress [Gruber 2004] (chapter 5). Fracture was observed at low and high temperatures as well as in samples with and without SiN_x layers. Different mechanisms may be responsible for this. The flow stress of the Au films continuously increases with decreasing temperature indicating that dislocation plasticity is restricted at low temperatures. Thus, stress concentrations around defects in the film may not be relaxed by plastic flow and lead to cracks. The situation is even more critical if SiN_x layers are present. Due to their brittleness they are favorable sites of crack initiation. Once cracked, they generate additional and larger stress concentrations in the sample. This may explain why fracture was more pronounced in AuSiN and SiNAuSiN samples than in Au samples and could be observed at all temperatures.

Lack of adhesion between the films and the substrate may be a second contributor to the fracture process [Li et al. 2005, Xiang et al. 2005b]. If the film is well bonded to the substrate, the substrate constraint suppresses strain localization in the film. On the other hand, if the film locally debonds from the substrate, it becomes freestanding and ruptures at a smaller strain than the well bonded film. The high temperature fracture of our samples may have resulted from a weak interface between the films and the polyimide substrate. The low flow stresses at these temperatures may have enhanced necking of the films and led to the decreasing fracture strain with increasing temperature. However, flow stress could be determined for all samples as fracture always occurred after the macroscopic yield point. The strong temperature dependence of flow stresses will be discussed in the following with respect to thermally activated dislocation glide and diffusional creep.

6.4.2 Thermally activated dislocation glide

The yield strength of most polycrystalline fcc metals does not depend strongly on strain rate and temperature. Nevertheless dislocation glide is a kinetic process and the strain rate $\dot{\epsilon}_{dg}$ for glide in the presence of discrete obstacles is given by [Frost and Ashby 1982]

$$\dot{\epsilon}_{dg} = \dot{\epsilon}_0 \exp\left[-\frac{\Delta F_{dg}}{kT}\left(1 - \frac{s\sigma}{\hat{\tau}}\right)\right], \quad (6-1)$$

where $\dot{\epsilon}_0$ is a characteristic constant taking the initial dislocation density into account, ΔF_{dg} the activation energy at zero stress, $\hat{\tau}$ the critical shear stress which can be interpreted as the flow stress at 0 K, k Boltzmann's constant, T the absolute temperature and s the Schmid factor. From equation (6-1) ΔF_{dg} can be obtained:

$$\Delta F_{dg} = -kT \left[\frac{\ln\left(\frac{\dot{\epsilon}_{dg}}{\dot{\epsilon}_0}\right)}{1 - \frac{s\sigma}{\hat{\tau}}} \right]. \quad (6-2)$$

In the following, equation (6-2) shall be used to determine ΔF_{dg} as function of temperature and film thickness. Therefore $\hat{\tau}$ is determined by extrapolating our flow stress data (figure 6.9a to c) to 0 K and multiplying the corresponding flow stress by s . This is necessary to account for the different strength of the films. The strain rate $\dot{\epsilon}_{dg}$ is replaced by the experimental strain rate of the tensile tests, which was always $5.2 \times 10^{-5} \text{ s}^{-1}$, $s = 0.27$ (for $\langle 111 \rangle$ fiber texture) and $\dot{\epsilon}_0$ is set as 10^{-6} s^{-1} [Frost and Ashby 1982]. Finally ΔF_{dg} is calculated for the von Mises flow stress $\sigma_{y,0.5}$ (figure 6.9a to c).

In figure 6.10 the results for ΔF_{dg} are shown and compared to the von Mises flow stress $\sigma_{y,0.5}$ as well as to the activation energy $\Delta F_{dg,bulk}$ for bulk Au. For Au and AuSiN systems ΔF_{dg} is about 1.0 to $1.3 \pm 0.3 \text{ eV}$ for all temperatures and thicknesses. This is about half of the bulk value, which is 2.01 eV [Frost and Ashby 1982] and would mean that the obstacle strength in thin films is lower than in the bulk material.

6 Temperature dependence of the mechanical properties of ultra thin Au films

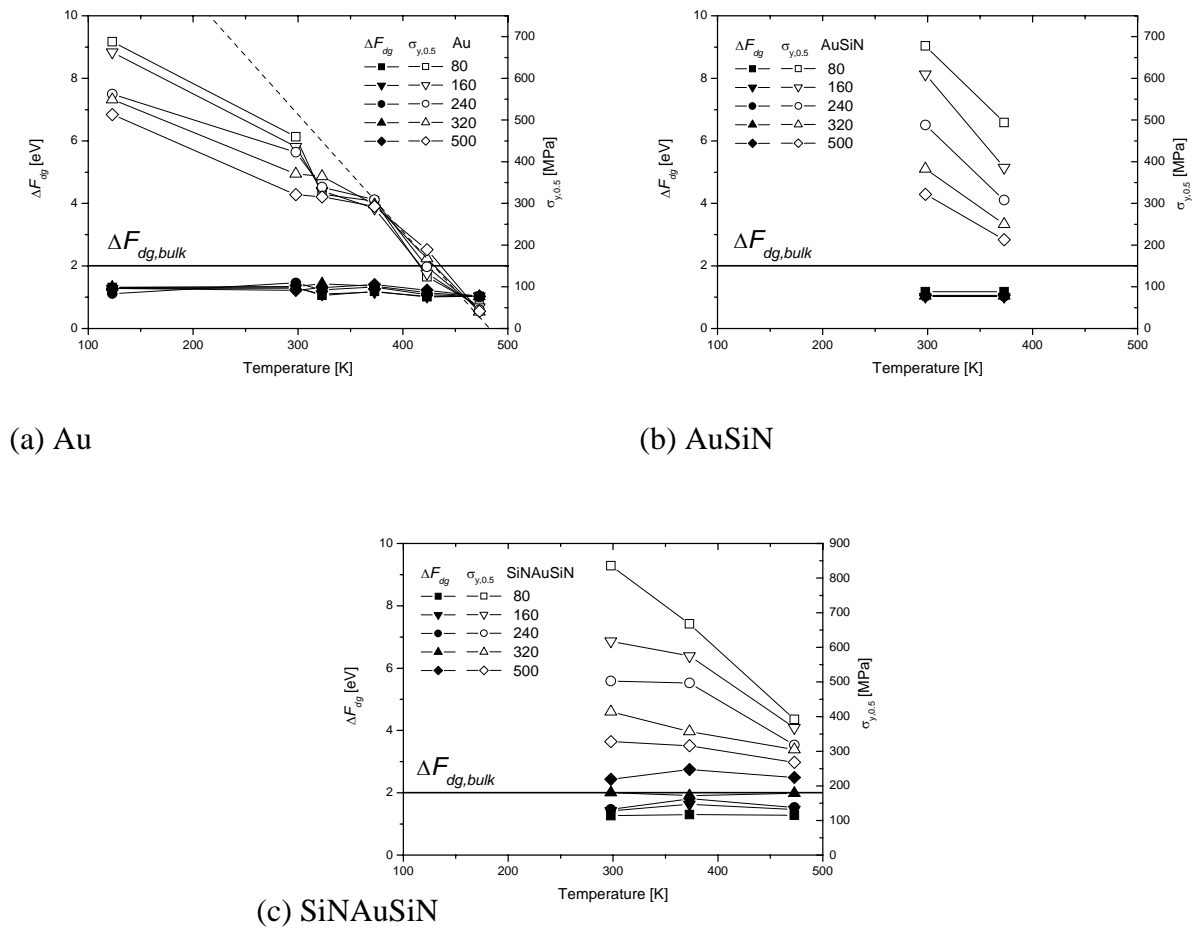


Figure 6.10: Activation energy for dislocation glide according equation (6-2) and von Mises flow stress $\sigma_{y,0.5}$ as function of temperature and film thickness for (a) Au, (b) AuSiN and (c) SiNAuSiN samples. The activation energy $\Delta F_{dg,bulk}$ for bulk Au is 2.01 eV [Frost and Ashby 1982]. Except for Au at high temperatures the constant values for ΔF_{dg} correlate to a constant decrease in flow stress. For Au the flow stress decrease is pronounced for high temperatures (dashed line). For Au and AuSiN samples ΔF_{dg} is lower than $\Delta F_{dg,bulk}$.

This may be due to the free surface in the Au and AuSiN film systems where dislocations can leave the film leading to a lower obstacle density and less obstacle interaction. In contrast, for SiNAuSiN samples, ΔF_{dg} increases with film thickness and reaches $\Delta F_{dg,bulk}$ for thicknesses above 300 nm. Here the columnar grain structure is embedded between two stiff SiN_x layers and dislocations cannot escape from the film. This leads to a pile-up of dislocations at the interfaces and an increasing backstress on other dislocations [Needleman et al. 2006]. The fact that the activation energy is highest for the thickest film indicates that the dislocation density increases with film thickness. In turn, due to the lower activation energy, the temperature dependence of the flow stress is pronounced in the thinner films (figure 6.10c).

Overall the low and constant values for ΔF_{dg} indicate that thermally activated dislocation glide is active in all film systems for all temperatures. However, there seems to be no size effect on obstacle strength. This indicates that the effective obstacle spacing may be smaller than the film thickness or grain size. Indeed, *in situ* TEM experiments for Ag and Cu films on amorphous SiN_x substrates have shown that the pinning distance of moving dislocations is about 70 nm and scales to some extent with film thickness [Kobrinisky et al. 2001]. The correlation between obstacle density and film strength is reflected in $\hat{\tau}$. For pure metals strengthened by work-hardening $\hat{\tau}$ can be estimated by the obstacle spacing l or the dislocation density ρ :

$$\hat{\tau} \approx \frac{Gb}{l} \approx Gb\rho \quad (6-3)$$

where G is the shear modulus and b the Burgers vector. Using $G = 27$ GPa and $b = 0.288$ nm, the obstacle spacing would have to be less than 10 nm or a dislocation density higher than 10^{15} m^{-2} would be necessary to explain the experimental values for $\hat{\tau}$. Both are far from values observed in TEM studies ($l = 50\text{-}70\text{nm}$ [Kobrinisky and Thompson 2000, Kobrinisky et al. 2001, Dehm et al. 2001] and $\rho = 3\text{-}6 \times 10^9 \text{ m}^{-2}$). Therefore, thermally activated dislocation glide may be responsible for the temperature dependence of the flow stress but it cannot fully explain its strong size effect. Additional strength contributions may arise from other mechanisms for thin film hardening. This could be the deposition of misfit dislocations at interfaces [Nix 1989] or grain boundaries [Thompson 1993] or the activation of a dislocation source [von Blanckenhagen et al. 2001, von Blanckenhagen et al. 2003]. The latter is very promising because the size of dislocation sources is similar to the pinning distance of moving dislocations and the corresponding Orowan stresses are close to experimentally observed flow stresses (chapter 4) [von Blanckenhagen et al. 2003]. In this sense, the film thickness and temperature dependence of the flow stress for our Au films may be a combination of dislocation nucleation and subsequent thermally activated dislocation glide.

For Au samples and temperatures above 400 K the decrease in flow stress is even more pronounced (dashed line in figure 6.10a). In addition, the thickness dependence of the flow stress disappears. This may indicate a further change in deformation mechanism which is very efficient for all film thicknesses. For 473 K the flow stresses for Au samples are reduced to 40 to 50 MPa, whereas the flow stresses of SiNAuSiN samples are still 200 MPa and more.

Experimental evidence for a change in mechanism is also given by the evolution of peak-width of the synchrotron experiments with total strain (figure 6.11). The peak-width has been determined from the full width at half maximum of Gauss-fits to radial scans of the Debye-Scherrer rings. The mean of 70 Gauss-fits around the loading axis has been defined as peak-width. Subsequently the peak width has been normalized by the initial peak width. A similar behavior is found for Au samples with 80 and 500 nm film thicknesses. At room temperature, the peak width is constant as long as the film deforms elastically and increases afterwards during plastic deformation. The increase in relative peak width is more pronounced in the thicker film. Peak width reflects the distribution in stress and the grain size of the film as well as the density of statistically stored dislocations. Inhomogeneous stress distributions and local yielding as well as small grains result in peak broadening. Therefore the stronger increase in peak width for the thicker film indicates higher dislocation activity. In contrast, for tensile tests at 150°C, the peak width drops in the beginning and decreases continuously afterwards. The decrease in peak-width is similar for both film thicknesses. Peak refinement by grain growth can be excluded because several annealing experiments at even higher temperatures have not resulted in measurable grain growth. This is in contrast to high temperature tensile tests on freestanding Au films where grain growth was observed [Emery et al. 1998]. Tensile tests on nanocrystalline Al films revealed stress-assisted discontinuous grain growth even at room temperature [Gianola et al. 2006]. For our films, the initial drop in peak width may be attributed to a reduction in dislocation density. The subsequent deformation leads to further relaxation of inhomogeneous stress fields. A plausible candidate for such a deformation mechanism is diffusional creep.

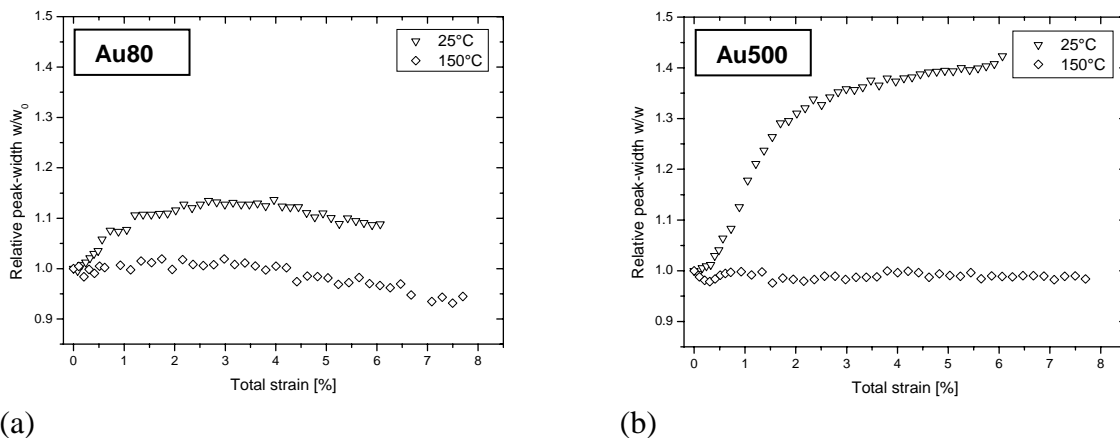


Figure 6.11: Relative peak-width vs. total strain for (a) Au80 and (b) Au500 samples and testing temperatures of 25 and 150°C. The evolution of peak-width is different for low and high testing temperatures.

6.4.3 Role of diffusional creep

Several authors have shown that stress relaxation in thin films on substrates can occur by diffusional deformation where material is transported between the free surface of the film and the grain boundary [Thouless 1993, Kobrinsky and Thompson 1998, Gao et al. 1999, Weiss et al. 2001, Balk et al. 2003a]. All these studies, theoretically as well as experimentally, are related to constrained diffusional creep where diffusion along the film/substrate interface is limited or not allowed. It is questionable if this holds for our Au samples. Following experimental findings indicate that the Au/polyimide interface is weak: (i) the occurrence of fracture at high temperature can only be explained if the film locally debonds and (ii) the further pronounced temperature dependence of flow stress is only found for unpassivated samples. The presence of a stiff SiN_x layer between Au and polyimide cannot suppress the cracking due to its inherent brittleness but it effectively reduces the stress relaxation at high temperatures. The high temperature flow stress of AuSiN samples is much closer to the corresponding values for a SiNAuSiN sample than to that of an Au sample. Therefore we assume that the Au/polyimide interface is too weak to retard interfacial diffusion and will allow interfacial sliding. In the following, we use a model for grain-boundary diffusional creep in a foil with a two-dimensional grain structure without substrate constraint originally developed by Gibbs [1966]. The model is schematically shown for tensile stress in the insert in figure 6.12a. The strain rate $\dot{\epsilon}_{gb}$ is given by

$$\dot{\epsilon}_{gb} = A_{gb} \frac{\delta D_{gb}}{kT} \frac{\Omega}{dh^2} \sigma = C\sigma \quad (6-4)$$

where A_{gb} is a constant of approximately 15, Ω the atomic volume, δD_{gb} the grain boundary width times the grain boundary diffusivity, d the grain size and h the film thickness. The constant C is introduced to facilitate further calculations. The stress-strain curve, as measured in a tensile test, can be calculated by integrating the differential equation:

$$\frac{d\sigma}{dt} = E\dot{\epsilon}_x - E\dot{\epsilon}_{gb}, \quad (6-5)$$

where E is the Young's modulus of the film and $\dot{\epsilon}_x$ is the experimental strain rate. The integration of equation (6-5) leads to:

$$\sigma = \frac{\dot{\epsilon}_x}{C} - \frac{\dot{\epsilon}_x - C\sigma_0}{EC} \exp\left(\frac{EC\epsilon}{\dot{\epsilon}_x}\right), \quad (6-6)$$

which has the functional form

$$y = a + b \exp(-cx) \quad (6-7)$$

and where δD_{gb} can be determined from the constant a , σ_0 from b and E from c , if the stress-strain curve has been fitted according equation (6-7). For the estimation of the grain boundary diffusivity δD_{gb} , $\Omega = 1.694 \times 10^{-29} \text{ m}^3$ and $\dot{\epsilon}_x = 5.2 \times 10^{-5} \text{ s}^{-1}$ were used.

Figure 6.12a shows exemplary fits for two stress-strain curves of Au samples with 500 nm film thickness tested at 25°C and 150°C, respectively. Obviously, the fit describes the experimental data better for the stress-strain curve measured at higher temperature. Because the model only considers elastic deformation and diffusional creep, the unfavorable fit for the room temperature stress-strain curve indicates that diffusional creep is not active at room temperature. This is not unexpected and is also reflected in the estimated values for δD_{gb} (figure 6.12b). They increase strongly for temperatures above 100°C and with increasing film thickness. In the Arrhenius plot for Au240 samples three regimes with different slope can be identified (figure 6.12c). The first two regimes reach from -150°C up to 25°C and from 25°C up to 100°C. The corresponding slopes m_1 and m_2 would give activation energies for grain boundary diffusion of only 0.02 eV and 0.12 eV which again indicate the absence of diffusional creep. The third and steepest regime above 100°C, however, leads to an activation energy of 0.49 eV. The slope of the third regime has been determined for all film thicknesses and is listed together with the corresponding activation energies and pre-exponential factors $\delta D_{0,gb}$ in table 6.2. The activation energy ΔF_{gb} is also plotted against the film thickness in figure 6.12d.

6 Temperature dependence of the mechanical properties of ultra thin Au films

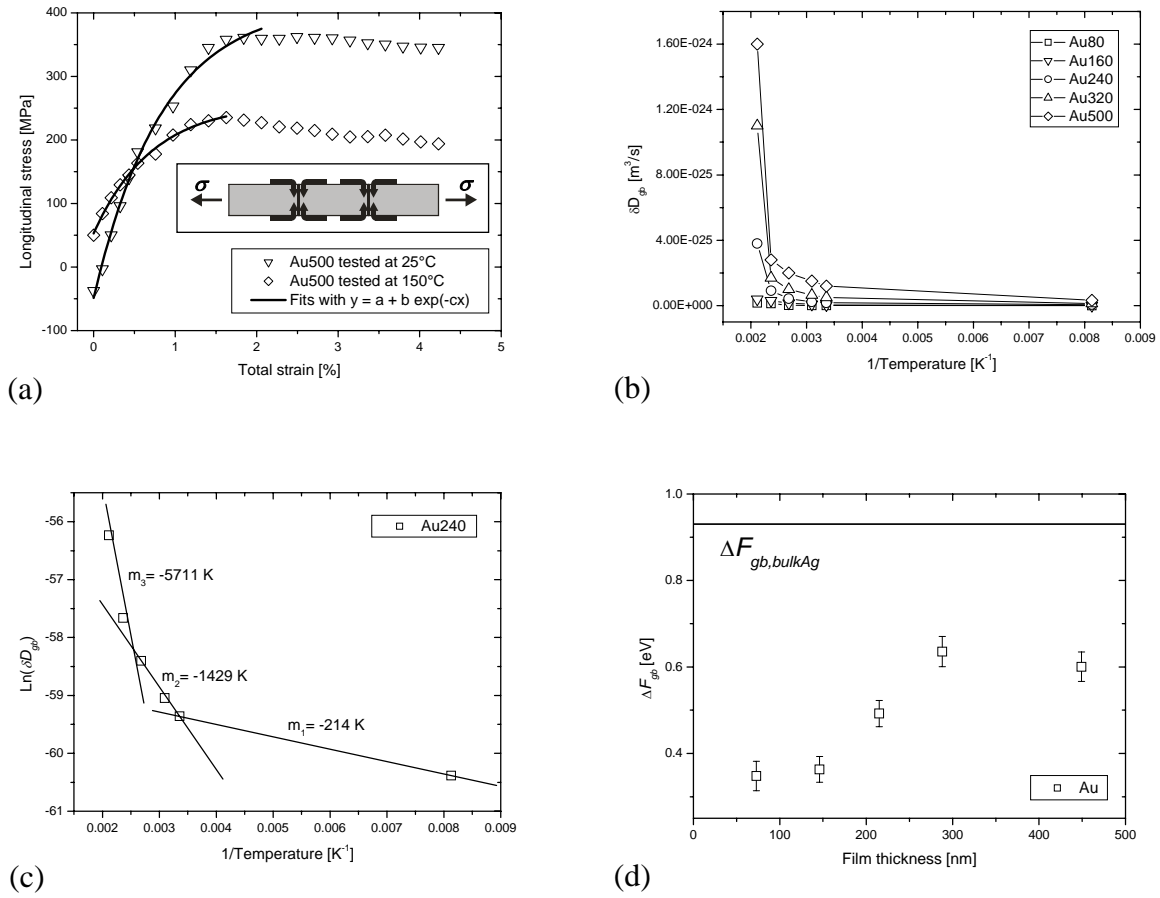


Figure 6.12: (a) Stress-strain curves for Au500 samples tested at 25 and 150°C with corresponding fits according equation (6-7). The insert shows a schematic for grain boundary diffusional creep in a freestanding foil under tensile stress. (b) δD_{gb} vs. reciprocal temperature for Au samples with different film thickness. Grain boundary diffusion is strongly enhanced in thicker films. (c) $\ln(\delta D_{gb})$ vs. reciprocal temperature for Au240 samples. Three different regimes with different slope can be identified. The activation energy has been only determined for the high temperature regime with the highest slope. (d) Activation energy for grain boundary diffusion ΔF_{gb} as function of film thickness.

Table 6.2: Arrhenius data for Au samples: The parameter m_3 represents the slope of the Arrhenius plot for the temperature regime above 100°C. ΔF_{gb} is the activation energy for grain boundary diffusion and $\delta D_{0,gb}$ the corresponding pre-exponential factor.

Sample	m_3 [K]	ΔF_{gb} [eV]	$\delta D_{0,gb}$ [m ³ /s]
Au80	-4036	0.35	1.1×10^{-22}
Au160	-4214	0.36	9.1×10^{-22}
Au240	-5712	0.49	6.7×10^{-20}
Au320	-7372	0.64	6.2×10^{-18}
Au500	-6964	0.60	4.0×10^{-18}

Both the activation energy as well as the pre-exponential factor increase with film thickness. The activation energy increases from 0.35 up to 0.6 eV. This is in any case considerably smaller than reported values for bulk Ag ($\Delta F_{gb,bulkAg} = 0.93$ eV [Frost and Ashby 1982], black line in figure 6.12d) or Cu ($\Delta F_{gb,bulkCu} = 1.06$ eV [Gust et al. 1985]). On the other hand, very similar values of about 0.6 eV have been found experimentally for Ag thin films [Kobrinisky and Thompson 1998] and nanocrystalline Cu [Horváth et al. 1987]. In contrast to ΔF_{gb} , the pre-exponential factors $\delta D_{0,gb}$ are lower than literature values for bulk materials (Ag: 4.5×10^{15} m³/s [Frost and Ashby 1982], Cu: 9.7×10^{15} m³/s [Gust et al. 1985]). This is given by the lower temperature dependence due to the lower activation energy because δD_{gb} for temperatures in the range of our experiments are considerably higher than those of the bulk materials. In figure 6.13a the δD_{gb} values for 80 nm thick Au samples are compared to polycrystalline (pc) [Gust et al. 1985] and nanocrystalline (nc) Cu [Horváth et al. 1987]. For both, nc Cu and Au films δD_{gb} becomes orders of magnitudes higher than for pc Cu at temperatures above 100°C. The high grain boundary diffusivities in nanocrystalline materials have often been attributed to the non-equilibrium structure of grain boundaries in these materials (for reviews see e.g. [Birringer et al. 1988, Würschum et al. 2003]). Similar arguments may also hold for the grain boundaries in our films.

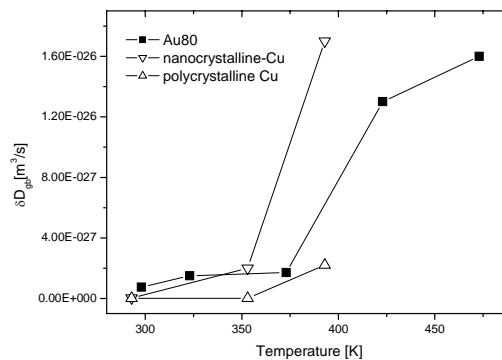


Figure 6.13: δD_{gb} as function of temperature for Au80 samples as well as poly- [Gust et al. 1985] and nanocrystalline Cu [Horváth et al. 1987]. Nanocrystalline Cu shows even higher diffusivities than the Au films.

Another very important diffusion path for diffusional creep in our films is the film substrate interface. For the applicability of the Gibbs model, diffusion along the Au/polyimide has to be faster or at least as fast as grain boundary diffusion. According to the low activation energies and high grain boundary diffusivities it seems that the diffusivity along the interface is

considerably faster. A possible explanation for this may be interfacial sliding. Raj and Ashby [1971] have studied the correlation of sliding at non-planar grain boundaries and diffusional creep as well as elastic accommodation. According to their analysis the sliding rate is higher for a sinusoidal than for a stepped boundary shape and for elastically weak interfaces. In this sense, the interface between an amorphous polymer and a ductile metallic film (like Au on polyimide) is more likely subjected to interfacial sliding than an interface between a metal and ceramic layer (like Au and SiN_x) or a regular grain boundary within the film. For an analytical treatment of this mechanism for our films, the knowledge of the microscopic (“nanoscopic”) structure of the interface would have to be known.

So far, the origin of the increasing grain boundary diffusivity for increasing thickness of the Au films is not clear (figure 6.12b). Any argument given above would help to explain a decrease in diffusivity. However, according to equation (6-4) the strain rate for diffusional creep strongly depends on the film thickness and grain size of the films. In our experiments the strain rate was constant and thus, for increasing film thickness and grain size, the diffusivity must increase as well. If e.g. the inherent diffusivity of the Au films is high enough to accommodate the external strain rate by diffusional creep for a 500 nm thick film, the diffusivity could be lower for a thinner film. In simpler words this means that diffusional creep in thinnest films may be faster than the external strain rate. This could also explain the phenomenon of parallel decrease in diffusivity and activation energy for decreasing film thickness and underlines the dominant role of diffusional creep in thin films with weak interfaces.

6.5 Summary and conclusion

The temperature and thickness dependence of the mechanical properties of passivated and unpassivated Au films has been investigated. Therefore tensile tests have been performed in a temperature range between -150° and 200°C. The findings can be summarized as follows:

- The flow stress strongly depends on temperature and film thickness.
- Fracture occurs at low and high temperatures. Low temperature fracture may be due to decreasing ductility, whereas high temperature fracture may result from decreasing adhesion.

- The temperature dependence of the flow stress can be explained by thermally activated dislocation glide. However, the activation energy is lower than the bulk value due to the different density and arrangement of obstacles in thin films.
- For pure Au films on polyimide the decrease in flow stress is even more pronounced for temperatures above 100°C. Here, the thickness dependence of the flow stress disappears and at 200°C the flow stress is only about 50 MPa. An analysis on the basis of a model for grain-boundary diffusional creep of a freestanding foil give values for the activation energy of about 0.3 to 0.6 eV, which is again considerably lower than for the bulk material. The activation energy as well as the diffusivity decrease with film thickness, which indicates that diffusional creep is strongly pronounced in the thinnest films and may accomplish the complete deformation of the film. This is remarkable because the testing temperatures are only about 0.3 of the homologous temperature.

7 Mechanical properties of ultra thin single crystalline Au films measured by a new synchrotron technique

7.1 Introduction

In principle thin films are particularly well-suited for the systematic study of the scaling behavior of mechanical properties. The preparation of thin films is straightforward and, when deposited on a substrate, thin film samples are easy to handle for mechanical testing [Nix 1989, Kraft and Volkert 2001]. In polycrystalline metallic thin films on substrates, however, the investigation of the dimensional constraints on mechanical properties is complicated due to the presence of grain boundaries. Even if the deposition temperature is sufficiently high to allow for surface diffusion, normal grain growth usually stagnates once the grain size is similar to the film thickness [Mullins1958]. The varying ratio between film thickness and grain size makes it difficult to compare the results from different studies and to separate the effect of film thickness and grain size. Commonly, the scaling behavior of the yield stress with varying film thickness is described in power-law form. Experimental results reveal different exponents ranging from -0.5 to -1 [e.g. Venkatraman and Bravman 1992, Keller et al. 1998, Yu and Spaepen 2004, Vlassak and Xiang 2006]. A similar range is predicted by different models of thin film plasticity. The models considering the movement or nucleation of single dislocations in a confined geometry [Nix 1989, Thompson 1993, Nix 1998, von Blanckenhagen et al. 2001, Espinosa et al. 2005] give an exponent close to -1; in contrast a Hall-Petch like behavior with an exponent of -0.5 [Hall 1951, Petch 1953] is predicted when a pile-up of dislocations at grain boundaries, the film/substrate interface or film surface (if oxidized or passivated) [Nicola et al. 2003, Friedman and Chrzan 1998] is considered. Recent experiments even show that the scaling behavior of the flow stress becomes weaker or disappears for films thinner than 300 nm (chapter 4) [Balk et al. 2003a, Dehm et al. 2003, Emery and Povirk 2003b]. Considering all microstructural parameters (chapter 4) [Keller et al. 1998, Yu and Spaepen 2004] and optimizing the assumptions in simulations [Needleman et al. 2006, Espinosa et al. 2006] may lead to a unified description of the experimental data. In addition the experimental observation of the proposed deformation mechanisms in polycrystalline thin films is difficult [Dehm et al. 2003, Haque and Saif 2004, Haque and Saif 2005b].

The influence of the complicated microstructure can be avoided by investigating epitaxial or single crystalline films. It has been shown by Dehm et al. [2002b, 2003] that the mechanical properties of epitaxial Al and Cu films grown on single crystalline (0001) α -Al₂O₃ substrates can be described quantitatively by the dislocation-based model from Nix and Freund [Nix1989, Freund 1987]. In addition, their *in situ* TEM studies of these films indicate that dislocations channeling through the epitaxial films frequently deposit dislocation segments near the film/substrate interface as assumed in the Nix model. Although the quantitative agreement between model and experiment is good, the thickness dependence of the experimental yield stresses is lower than predicted and shows an exponent closer to -0.5. Due to the rigid alumina substrate mechanical testing has also been limited to substrate curvature measurements during thermal cycling of the film substrate composite. By this method the stress in the film of interest can be varied only by changing the temperature, which in turn influences the deformation mechanisms. Thus experimental data are difficult to interpret. It would be desirable to adapt a more direct mechanical testing technique to single-crystalline films.

In the present study we present an experimental route to prepare single crystalline Au films on compliant substrates which can be tested by a novel synchrotron-based tensile testing technique. The testing technique is based on the availability of (i) polychromatic synchrotron radiation with high brilliance over a wide range of photon energies and (ii) a large-area X-ray detector with high resolution and high sensitivity. The combination of both enables the collection of Laue diffraction patterns and the evaluation of the complete stress tensor of ultra thin films in very short measuring times. Thus the stress evolution in single crystalline films can be monitored during tensile tests and isothermal stress-strain curves for films as thin as 20 nm are obtained for the first time. The mechanical tests are complemented by a detailed transmission electron microscopy (TEM) study on deformed and undeformed films in order to correlate the mechanical data with the microstructure and dislocation mechanisms in the films. It is found that the flow stresses as well as the deformation mechanisms strongly depend on film thickness. For films thinner than 80 nm a plateau in flow stress and an unexpected change in deformation mechanism is identified.

7.2 Experimental

7.2.1 Sample preparation

It is not possible to directly deposit a single crystalline metallic film on an amorphous compliant polymer substrate. Therefore the samples for the tensile tests were prepared in a three step process (figure 7.1). First, the Au films with film thicknesses from 30 to 1000 nm were grown on cleaved and polished (100)-oriented NaCl single crystal substrates (Crystec, Germany) by magnetron sputtering with a base pressure better than 10^{-8} mbar (DCA Instruments). The NaCl substrates were 30 x 30 mm² in size. Six testing areas, 5 mm wide and 8 mm long, were defined by a molybdenum sputtering mask. Prior to deposition the substrate was heated up to 300°C for 60 min. Film deposition was performed at this temperature with a deposition rate of 50 nm/min. In a second step, the samples were spin-coated with a ~8µm thick layer of polyimide using commercial precursors (PI2611, HD Microsystems). The samples with the polyimide layer were cured in a glass oven for 30 min at 200°C in air and for 1 h at 365°C under N₂ atmosphere. The third step was to cut out the different testing areas on the NaCl substrate and to dissolve the NaCl substrate in deionized water. Finally, additional stripes of 125 µm thick polyimide foil (Kapton® HN) were attached at each end and on both sides of the original sample by superglue (UHU Sekunden Alleskleber) in order to adapt the total sample length to the tensile tester (Kammrath & Weiss) and to obtain a suitable clamping area.

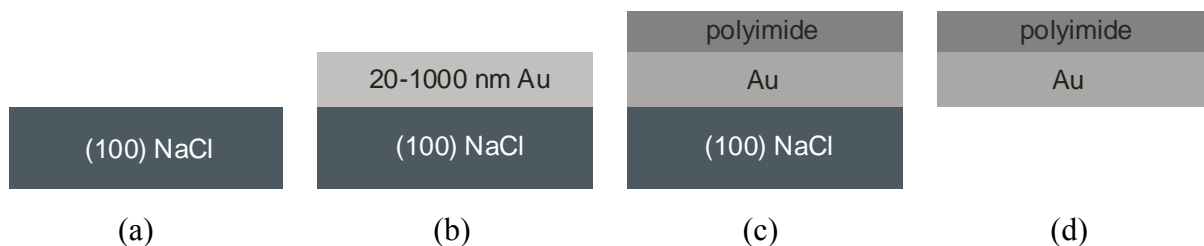


Figure 7.1: Schematic of sample preparation: (a) initial polished NaCl substrate, (b) deposition of epitaxial Au film, (c) spin-coating with polyimide layer and (d) dissolution of NaCl substrate.

The single crystalline films were investigated by electron backscatter diffraction (EBSD) to characterize their quality and the orientation relation between the Au films and the NaCl substrate during film growth. A piece of a NaCl substrate with an uncoated Au film was mounted in a field emission scanning electron microscope (SEM, Leo 1530-VP) equipped with an EBSD system (HKL Channel 5). The measurements were carried out at a working

distance of 13 mm and an accelerating voltage of 20 keV. An area of $1.0 \times 1.95 \text{ mm}^2$ was scanned with a step interval of $10 \text{ }\mu\text{m}$. Data was analyzed using the HKL-software package. All Au films were single crystalline. The films exhibited a cube-on-cube orientation relationship according to $\text{Au}(100)/\text{NaCl}(100)$ and $\text{Au}[100]/\text{NaCl}[100]$ as manifested by the EBSD measurements (figure 7.2). Analysis of the pole figures revealed very similar FWHM values of about 0.3° for both, the Au film and the NaCl substrate. This suggests nearly perfect epitaxial growth of the single crystalline Au film. No domain boundaries were found.

In addition, the initial surface roughness of the NaCl substrate was characterized by atomic force microscopy (AFM). The initial (100) NaCl substrates exhibited a root mean square (RMS) surface roughness of $\sim 12 \text{ nm}$. However, numerous scratches remained after polishing and were also present in the deposited Au film (see figure 7.2a). In addition isolated hillocks were found. As they were not observed on untreated NaCl substrates, they might have formed during substrate heating and cooling.

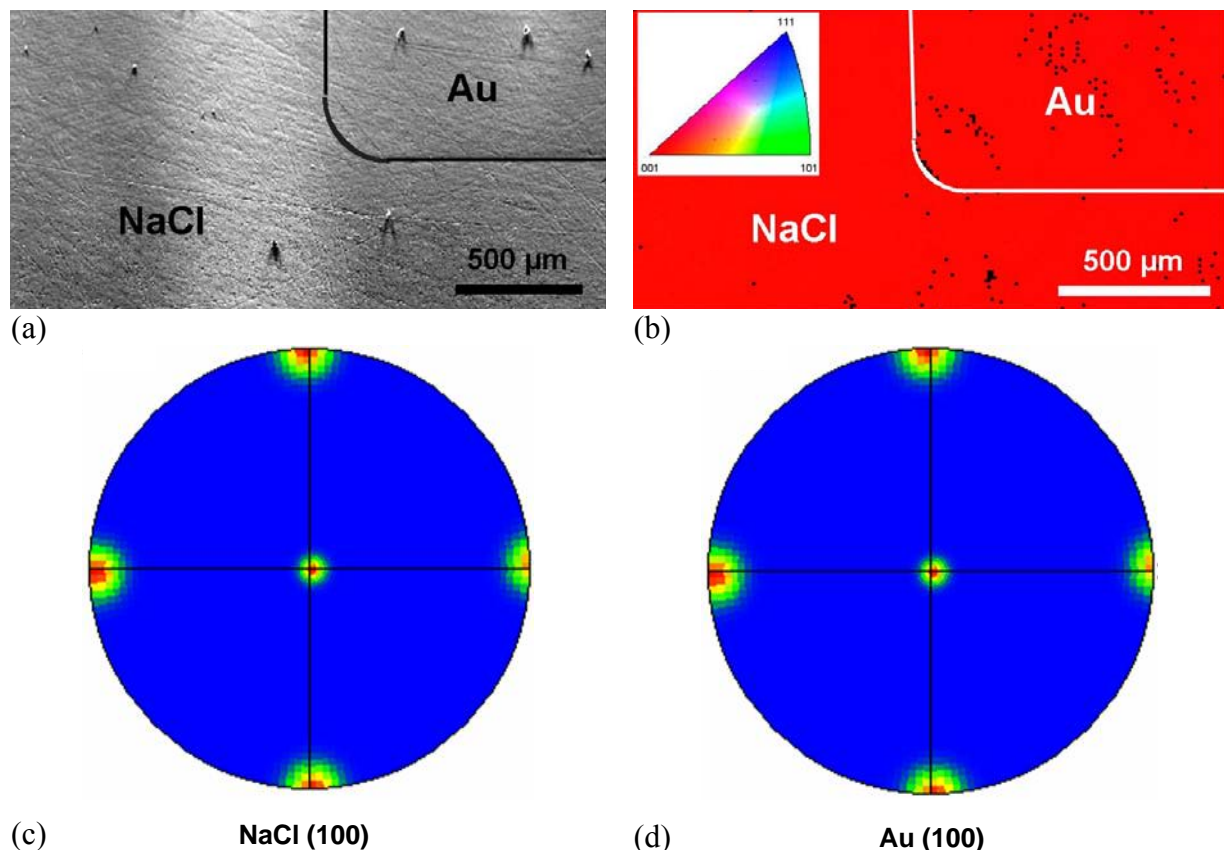


Figure 7.2: (a) SEM image of the surface of a 429 nm thick Au film and the NaCl substrate. (b) EBSD orientation map for Au and NaCl of the same region. The orientation normal to the sample surface is represented according to the colour key in the upper left. Non-indexed spots are shown in black. Au film and NaCl substrate show a (100) orientation. (100) pole figures for (c) the NaCl substrate and (d) the Au film. The FWHM of the centre peak is $0.230 \pm 0.003^\circ$ for the Au film and $0.357 \pm 0.002^\circ$ for the NaCl, respectively.

The thickness of the Au films was determined by Rutherford backscattering spectrometry (RBS) for films transferred to polyimide as well as on NaCl substrates. The RBS measurements were conducted using 2 MeV He⁺ ions (6.5MV Pelletron accelerator of the Max Planck Institute for Metals Research or 6MV Tandem accelerator of the ETH Zurich/Paul-Scherrer-Institute). The film thickness of the Au films was obtained by fitting the RBS spectra with the X-Rump simulation software (Computer Graphics Ltd.).

7.2.2 Mechanical testing

All tensile tests were performed at the MPI-MF-beamline of the synchrotron radiation source ANKA (Angströmquelle Karlsruhe). For the study of the single crystalline films the “pink beam option” of the beamline was used. In this configuration the Rh-coated Si torroidal mirror was left in the beam path in order to focus the beam vertically and to define the energy range of the polychromatic synchrotron radiation (5-18 keV). The spotsize of the X-ray beam was defined by several slit systems to between 0.5 x 0.5 and 1.0 x 1.0 mm². The tensile tester (Kammrath & Weiss) was mounted on the goniometer head such that the loading axis was perpendicular to the incoming X-ray beam (transmission geometry, figure 7.3a). A large area CCD detector (MarCCD) was positioned directly after the tensile tester to capture as many Laue spots as possible (figure 7.3b). For calibration, a Laue diffraction pattern of a 200 μm thin Si wafer was taken after each setup change. During the tensile test the crossheads of the tensile tester were displaced in steps between 30 and 90 μm up to maximum displacements of 1000 μm and subsequently retracted again. For each step a CCD frame was taken. The exposure time was varied between 15 and 120 s according to the diffracted signal (longer exposure time for thinner films). The total strain of the samples was measured by a laser extensometer (Fiedler Optoelektronik).

For the analysis of the Laue diffraction patterns, the XMAS software (X-ray microdiffraction analysis software, Advanced Light Source, Berkeley) was used [Tamura et al. 2003]. It indexes the measured Laue pattern automatically and compares it to that of an unstrained crystal. Laue patterns of the Si wafer were used to calibrate the detector distance, center channel (x and y) and tilt (horizontal and vertical). After calibration, the Laue diffraction patterns of the Au films could be analyzed. The deviations of the Laue spot positions from those of the unstrained crystal were used to calculate the distortion of the crystal unit cell, with a strain resolution of about 10⁻⁴. Subsequently the deviatoric stress tensor was calculated

using the anisotropic stiffness coefficients for the film material and the boundary condition that the stress normal to the surface was zero. By plotting the film stress measured in this way vs. the total strain of the film-substrate composite, isothermal stress-strain curves for the single crystalline Au films were obtained.

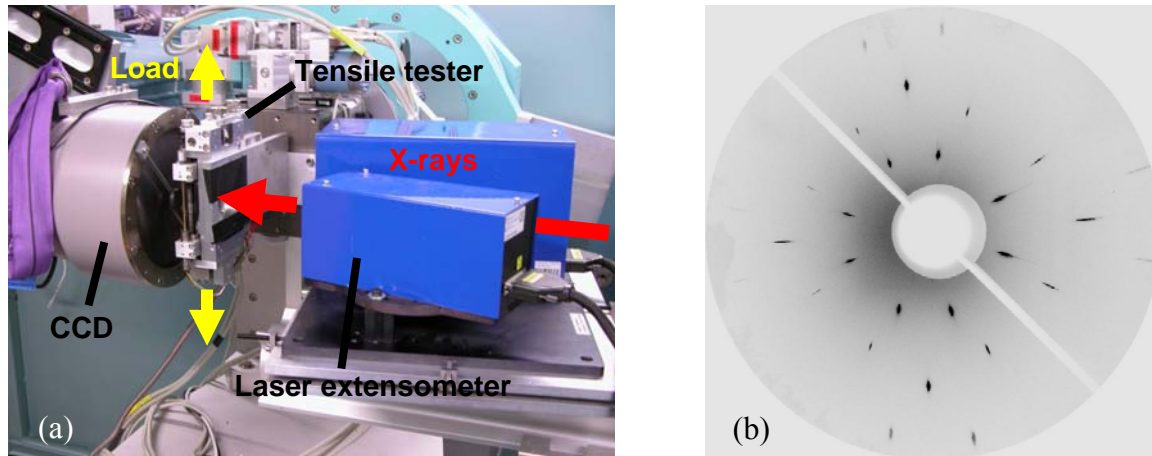


Figure 7.3: (a) Experimental setup at the ANKA MPI-MF-beamline for *in situ* experiments. The total strain of the sample is measured with a laser extensometer and the Laue diffraction patterns are recorded by a large area CCD camera. (b) Exemplary Laue diffraction pattern of a 160 nm thick Au film.

7.2.3 TEM investigations

The TEM studies were performed on plan-view TEM specimens from 30 to 160 nm thick films. The polyimide substrate was removed by etching for 85 min in 20 wt% NaOH at 80°C. Temperature and time were carefully controlled in order to minimize damage to the Au film. In most cases the Au film could be peeled off before the substrate was dissolved. The freestanding pieces of the Au films were carefully removed from the etchant and cleaned in deionised water. Subsequently, the Au pieces were collected with a carbon-coated copper TEM grid and dried for several hours at room temperature. Before use, the TEM grids were hydrophilized for 10 s in an oxygen plasma to ensure good adhesion to the Au film. The microscope (Phillips CM200) was equipped with a video camera (Gatan) and a CCD camera (Gatan2K2K). Bright field images were taken at different magnifications close to the [001] zone axis. Both, deformed and undeformed films were investigated.

7.3 Results

7.3.1 Stress-strain curves

Figure 7.4 shows typical stress-strain curves for the single crystalline Au films for all film thicknesses in the range from 31 to 868 nm. The stress evolution in the Au films during the tensile test in the longitudinal as well as transverse direction is shown. Due to heating and cooling during preparation all samples showed initial stresses between -15 and 60 MPa. For most of the samples the initial stress state was found to be equibiaxial whereas some samples show slightly different stresses in longitudinal and transverse direction. This could be due to anisotropic thermal expansion of the composite of film, substrate and coating but is more likely due to a misalignment of the sample with respect to the calibrated camera distance. The samples were very compliant and therefore sample positioning was a compromise of having a completely flat sample and avoiding any initial external load.

The overall behavior of the Au films was, independent of film thickness, similar although the absolute stress values were very different. First the longitudinal stress increased linearly, followed by a strain hardening regime yielding into a stress plateau which maintained to the maximum strain. Parallel to the longitudinal stresses, transverse stresses arose due to the different Poisson's ratio of the Au film and the polyimide substrate ($\nu = 0.46$ in the (100) plane of a single crystalline Au film and $\nu = 0.30$ for polyimide [HD Microsystems]).

The maximum total displacement was 1000 μm , which corresponds to a maximum total strain of about 4% on the sample. However the stress-strain curves in figure 7.4 show only the data for total strains of up to 2.6-3.8%. The reason for this lies in the fact that the diffraction patterns became more and more unfavorable for data analysis. At the later stages of deformation the samples started to wrinkle, which leads to very broad Laue spots if the amplitude of the wrinkles is similar or smaller than the spot size of the X-ray beam (usually $0.5 \times 0.5 \text{ mm}^2$).

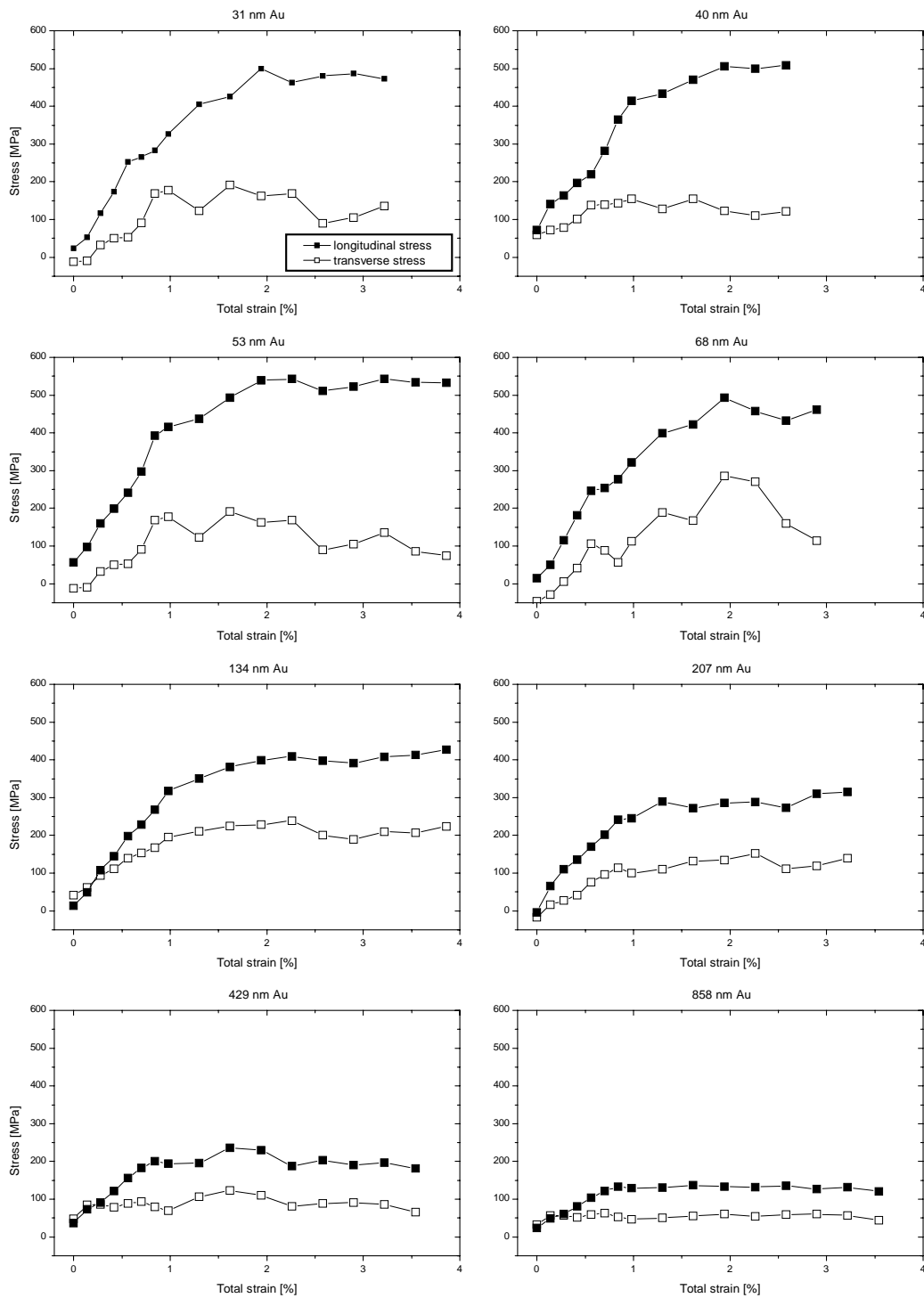


Figure 7.4: Stress-strain curves for 31 – 858 nm thick single crystalline Au films. All data are plotted on the same scale. Filled symbols represent the longitudinal stress and open symbols represent the transverse stress.

7.3.2 Yield strength

Because of the biaxial stress state in the Au films, the flow stress was determined from the von Mises stress at 0.5% permanent strain as shown in figure 7.5a. The corresponding values for the flow stress are plotted versus the film thickness in figure 7.5b. Overall a strong thickness dependence was found for films thicker than 60 nm, whereas for thinner films the flow stress reached a plateau or even decreased. The plateau stress was about 450 ± 50 MPa. The absolute values for the flow stress increased from 116 up to 479 MPa. The error for the flow stress was 20 MPa for 858 nm Au and 50 MPa for films thinner than 200 nm. A linear fit in a double logarithmic plot gave a slope of -0.505 for films thicker than 60 nm.

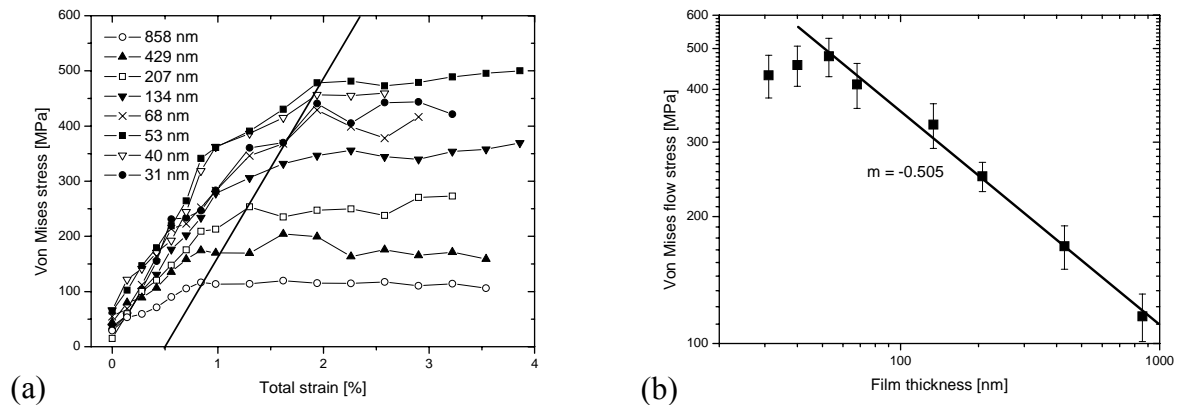


Figure 7.5: (a) Von Mises stress vs. total strain for all thickness from 31 to 858 nm. The solid line has an average slope of all stress-strain curves and marks the flow stress at 0.5% plastic strain. (b) Von Mises flow stress of the single crystalline Au films, determined from (a) vs. film thickness.

7.3.3 Average peak width

An additional parameter which showed a systematic change with applied strain and film thickness was the average peak width (APW). The APW was determined from the full width at half maximum of a 2D Lorentzian fit to the intensity profile of each Laue spot and by averaging over all spots. Figure 7.6a shows an exemplary Laue pattern for a 31 nm thick film. It is evident that the Laue spots are distinct radial streaks. As Laue diffraction patterns from a perfect single crystal or from a single crystal containing randomly distributed dislocations exhibit symmetric peaks, these streaks suggest the presence of unpaired geometrically necessary dislocations [Barabash 2001, Barabash et al. 2002].

In figure 7.6b the corresponding APW values are plotted versus the total strain for three film thicknesses. Overall the APW values increased with decreasing film thickness. As long as the film behaves elastically the APW stays constant, whereas it increases when the film is plastically deformed. This increase was strongly pronounced in the 53 nm thick film. For the thicker films, however, no streaking was observed and the increase for the APW values during deformation was much lower.

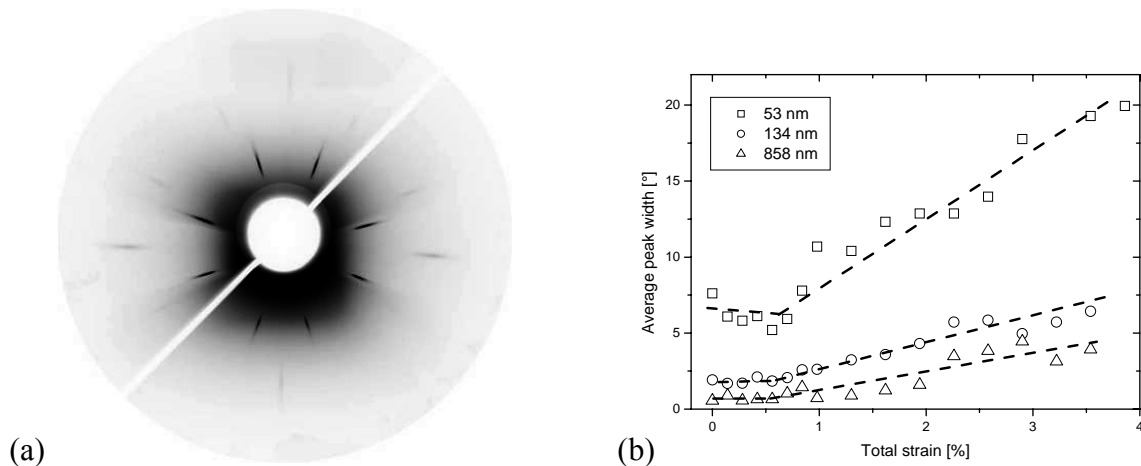


Figure 7.6: (a) Laue diffraction pattern showing the radial peak broadening for a 31 nm thick film. (b) Average peak width vs. total strain for different film thicknesses. The thinnest film shows a pronounced peak broadening during plastic deformation.

7.3.4 Microstructure and defects

Here we report the results of a detailed TEM study on deformed and undeformed films. A separate study performing *in situ* TEM straining experiments on the same films is presented by Oh et al. [2007].

Figure 7.7 shows an overview of an undeformed 40 nm thick Au film. The bright contrasts in the TEM micrograph originated from voids in the film. They were predominantly square in shape. In addition, twin boundaries (narrow lines) were present on inclined $\{111\}$ planes running along perpendicular $\langle 110 \rangle$ directions. The rounded lines and the changing dark-bright contrast were bend contours.

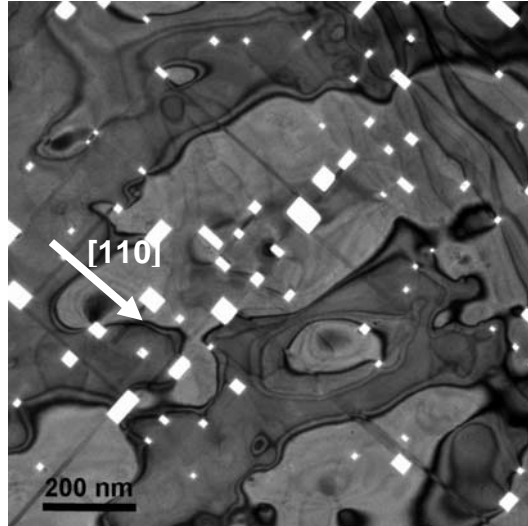


Figure 7.7: TEM image of an undeformed 40 nm thick Au film giving an overview over the microstructure containing rectangular holes, a perpendicular network of twins along (110) directions and bend contours.

Figure 7.8 shows a comparison of deformed films with different film thickness ranging from 31 to 53 nm. Compared to the undeformed film in figure 7.7a, the twin density in the 40 nm thick film was higher after deformation. The microstructure of the different film thicknesses looked very similar, however the porosity as well as the twin density decreased with increasing film thickness. In 53 nm and 68 nm thick films only few voids were observed and thicker films were found to be completely dense. The twins formed a dense network with parallel and perpendicular twins under 45° to the loading axis (which was the [100] direction). Most of the twins started and ended at voids or another twin.

The bright contrast of the voids allowed automatic detection by a computer software for quantitative image analysis (Leica Quantimet Q5501W). The porosity of the film was determined by the area fraction of the voids and the pore size was taken as the diameter of a square with the equivalent area (aspect ratio of the holes was 0.96-1.01). In addition, the mean distance of the pores was evaluated by the intercept method. The interpore distance L was defined by

$$L = \frac{l - Nd}{N} \quad (7-1)$$

where N is the number of pores, l is the measurement length and d is the pore size. The results of the quantitative analysis are summarized in table 7.1 and figure 7.9a.

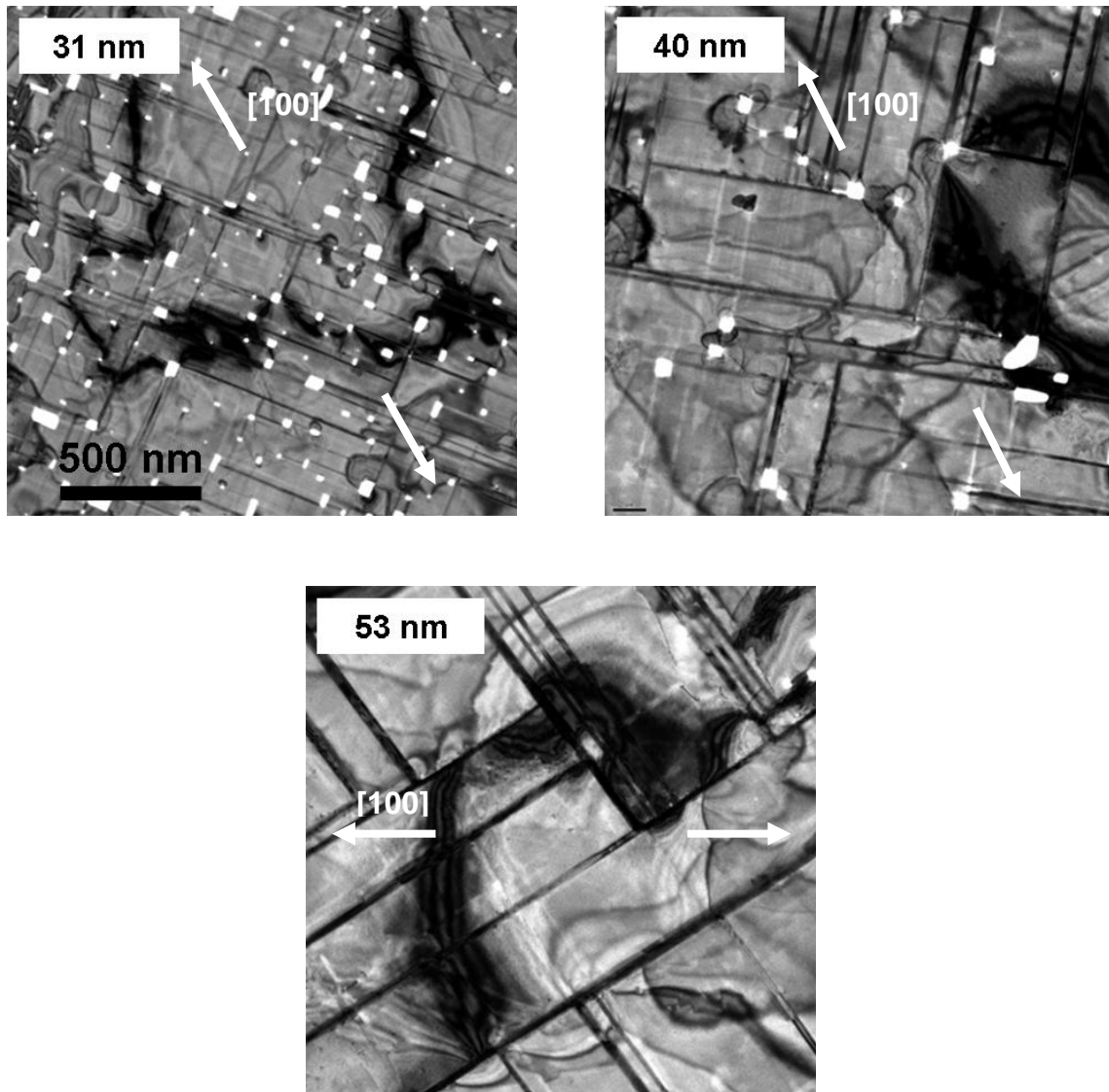


Figure 7.8: TEM images of deformed films with different film thickness. The magnification is identical for all three pictures. Porosity and twin density increases with decreasing film thickness. The [100] tensile axis is shown by white arrows.

In contrast to the voids, twins were found for all film thicknesses up to 160 nm. For the quantitative analysis, the twin density was determined by visual inspection. Because the brightness spectrum of the twins reached from black to white an upper and a lower bond for the twin density was determined counting lines of any brightness and only counting very dark lines, respectively. Still, one has to keep in mind that not all twins are visible in a plan-view TEM picture. Nevertheless the observed trends were clear even within the large error bars, which were considered to be very conservative. The twin density decreased with increasing film thickness and the deformation during the tensile test resulted in an increase in twin density by a factor of 1.5 to 2 (table 7.1 and figure 7.9b).

Table 7.1: Results of the quantitative evaluation of pore size and twin density for deformed and undeformed films and different film thicknesses (mean pore size d , standard deviation Δd , maximum pore size d_{max} , minimum pore size d_{min} , pore distance L , porosity P , twin density ρ , maximum twin density ρ_{max} , minimum twin density ρ_{min}).

Pores						
Film thickness [nm]	d [nm]	Δd [nm]	d_{max} [nm]	d_{min} [nm]	L [nm]	P [%]
31	44.2	27.0	223.4	7.6	823.9	4.80
40	84.5	39.6	211.1	27.7	3314.5	2.87
Twins						
Film thickness [nm]	ρ [10^{12} m^{-2}]	ρ_{max} [10^{12} m^{-2}]	ρ_{min} [10^{12} m^{-2}]			
31	19.06	13.34	24.77			
40	4.71	3.29	6.12			
53	2.41	1.69	3.14			
134	0.053	0.037	0.069			
40*	3.16	2.21	4.11			
53*	1.04	0.73	1.35			

* undeformed

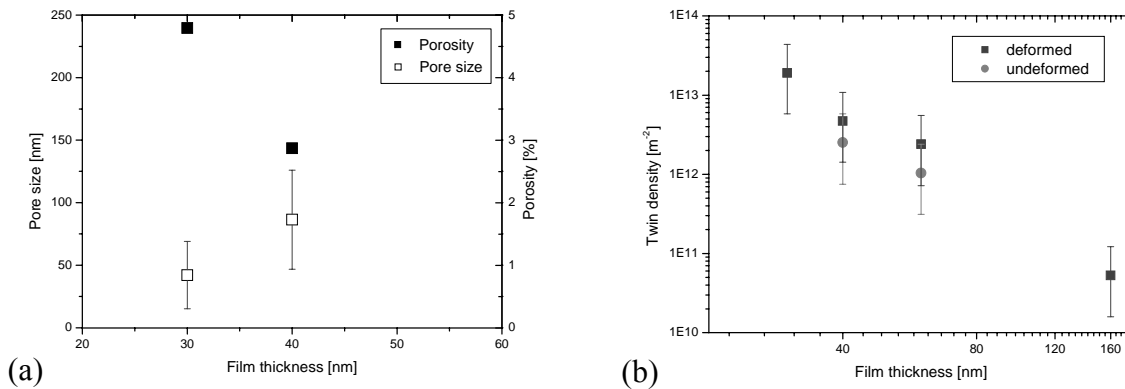
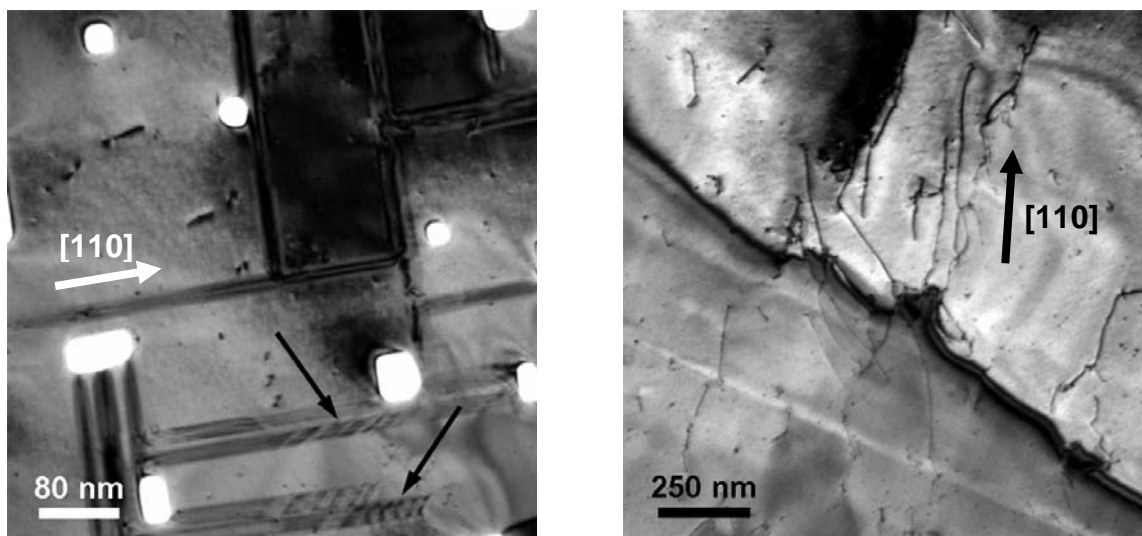


Figure 7.9: (a) Pore size, porosity and (b) twin density as function of film thickness. Porosity and twin density decrease with increasing film thickness. Deformed films show higher twin densities than undeformed films.

Figure 7.10a shows a higher magnification of some twins in a 31 nm thick film. The twins consisted of a pile-up array of partial dislocations. The distance between the partials decreased along the slip plane and the density was highest at the leading front of the array. At the trailing end the stacking fault ribbons became wider. In many cases, the leading dislocations appeared as an extended partial dislocation which was bounded by a very narrow stacking fault. The stacking fault between two partials appeared as a parallel triple fringe pattern (bright-dark-bright-dark-bright). The fringes corresponded to the sites where the stacking fault intersected the film at its bottom and top.

Perfect dislocations gliding on an inclined $\{111\}$ plane usually intersect the free surface of the Au film and the Au/polyimide interface. In the thinnest films these dislocations did not leave a slip trace at the surface nor a dislocation segment near the interface to the polyimide substrate. They usually appeared as short curly fibers which were about half the film thickness long. However, in thicker films considerably longer fibrous objects were found (figure 7.10b for 68 nm thick film). These fibers were much larger than the projected distance of an inclined $\{111\}$ plane and their orientation was not well-defined. The origin of these fibers could not be finally identified in this study. It may be multiple cross-slip of a single dislocation but it could also be the result of the interaction of several dislocations.



(a)

(b)

Figure 7.10: TEM images showing dislocation activity in (a) a 31 nm thick film and (b) a 68 nm thick film. The thinner film deforms predominantly by extended partial dislocations (black arrows in (a)) whereas the thicker film also shows glide of perfect dislocations. The black line crossing the image is a bend contour.

7.4 Discussion

7.4.1 Influence of porosity

The rounded square shape of the pores indicates that they are residues from the growth process. The voids may originate from the partial wetting behavior of Au on NaCl. In the initial stages Au islands are formed which have to overgrow the surface roughness of the substrate. The NaCl substrates were cleaved from a bigger crystal which results in a terraced surface with cleaving steps along defined crystallographic directions. This may explain the

perfect orientation and regular shape of the voids. Once the film is thicker than the height of the surface steps the islands can coagulate and form a dense film. This is the case for films thicker 60 nm. However the homogeneity of the film thickness will be affected by this mechanism.

The presence of the voids will lower the measured average stress in the films. To obtain the true value for the film stress, we aim to perform a correction. Any open discontinuity in a thin film bonded to a substrate, e.g. a crack or a pore, leads to local stress relaxation. The size of the relaxation zone depends on the elastic mismatch between film and substrate. Xia and Hutchinson [2000] developed a two dimensional model to describe the stress relaxation by channel cracks oriented perpendicular to the loading axis x . According to their analysis the stress change is

$$\Delta\sigma_x = -\sigma_0 \exp\left(-\frac{|x|}{l}\right) \quad (7-2)$$

where σ_0 is the initial stress and l is a reference length which characterizes the exponential decay of the stress with increasing distance x from the crack:

$$l = \frac{\pi}{2} g(\alpha, \beta)h. \quad (7-3)$$

Here h is the film thickness and $g(\alpha, \beta)$ is a function introduced by Beuth [1992] to describe the energy release rate of the channel crack and to capture the effect of the elastic mismatch between film and substrate. If we insert the Young's moduli and Poisson's ratios of Au and PI2611 ($E_{Au(100)} = 43$ GPa, $\nu_{Au(100)} = 0.46$, $E_{PI2611} = 8$ GPa, $\nu_{PI2611} = 0.34$) we obtain $\alpha = 0.72$, $g(\alpha, \beta) = 2.8$ [Beuth 1992] and $l \approx 4.4h$.

In order to estimate the influence of the voids in our films, we assume a pore geometry and a stress relaxation zone as shown in figure 7.11a. The relaxation zone is assumed to be $2l$ wide. The complete sample is represented considering the area around the pore at a distance of $L/2$ where L is the distance between two pores. Thus we have to consider three areas (note that due to the thin film geometry, area and volume fractions are identical), namely the area of the holes A_p , the area of the relaxed zone A_{relax} and the area of the unrelaxed zone $A_{unrelax}$:

$$\begin{aligned}
 A_p &= d^2 \\
 A_{relax} &= \left(\frac{4l + d\sqrt{2}}{\sqrt{2}} \right)^2 - A_p \\
 A_{unrelax} &= A_{ges} - A_{relax} - A_p = (L + d)^2 - A_{relax} - A_p
 \end{aligned} \tag{7-4}$$

where d is the pore size.

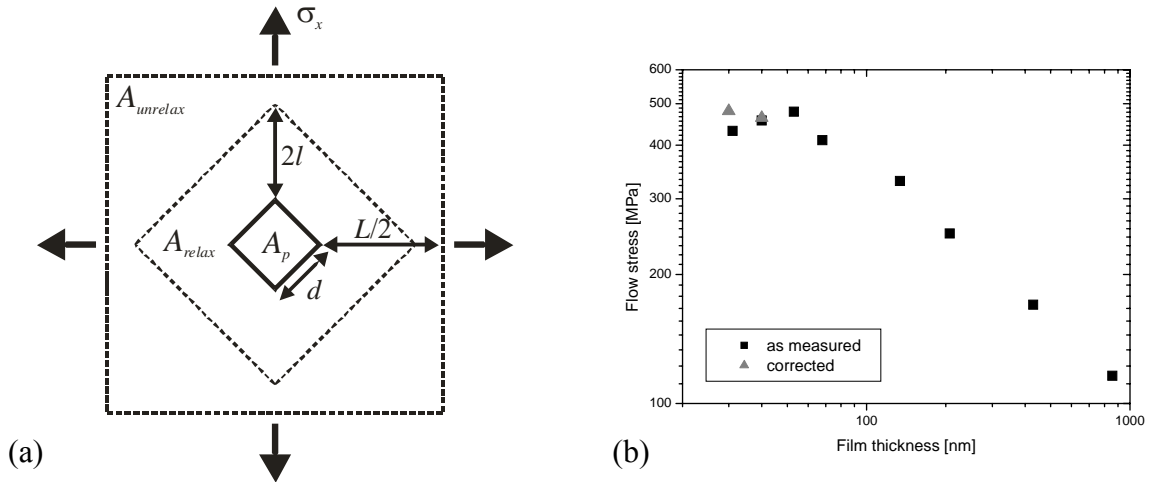


Figure 7.11: (a) Schematic drawing of pore geometry with stress relaxation zone A_{relax} and unrelaxed zone $A_{unrelax}$ used for the estimation of the film stress for a dense film from the measured average stress σ_x . (b) Corrected and measured flow stress versus film thickness. Even with correction according equation (7-6) no further increase in flow stress is obtained.

The mean stress in the relaxed zone A_{relax} can be calculated by integrating equation (7-2) over $2l$:

$$\sigma_{relax} = \sigma_0 - \frac{\int_0^{2l} \Delta\sigma_x dx}{\int_0^{2l} dx} = \sigma_0 \left(1 + \frac{\exp(-2) - 1}{2} \right) = 0.568\sigma_0 \tag{7-5}$$

and thus the mean stress σ_{mean} of the sample (identical to the measured flow stress) as well as the unreleased stress σ_0 can be obtained:

$$\sigma_{mean} = \frac{A_{unrelax}}{A_{ges}} \sigma_0 + \frac{A_{relax}}{A_{ges}} \sigma_{relax} = \left(\frac{A_{unrelax}}{A_{ges}} + 0.568 \frac{A_{relax}}{A_{ges}} \right) \sigma_0$$

$$\sigma_0 = \frac{\sigma_{mean}}{\frac{A_{unrelax}}{A_{ges}} + 0.568 \frac{A_{relax}}{A_{ges}}} \quad (7-6)$$

In figure 7.11b the calculated unrelaxed flow stresses for the porous 31 and 40 nm thick films (d and L are taken from table 7.1) are plotted together with the measured flow stresses for all film thicknesses. Even after considering the porosity and additional stress relaxation around the pores no increase in flow stress is found in films thinner than 80 nm. Instead the flow stress plateau is confirmed since the contribution by the correction is bigger for the 31 nm thick film due to the higher porosity. This is remarkable since the estimate made above assumes stress relaxation in the complete area around the pore. Thus the estimate for the stress relaxation is an upper limit since a pore under biaxial stress also shows local stress concentrations which have not been considered. On the other hand stress concentrations at the pores could also help to lower the average yield stress since they are favorable nucleation sites for dislocations.

7.4.2 Deformation mechanisms

The quantitative analysis of the twins revealed a high twin density for undeformed films. There may be two reasons for this. First, the Au films grew in a cube-on-cube orientation relationship on the NaCl substrate (figure 7.2). This was not expected because the lattice misfit in this direction is large (lattice parameter of NaCl is 5.641 Å whereas that of Au is only 4.07 Å; along the (110) direction the misfit would be only 2%). One way to accommodate this misfit may be the introduction of twins. However, the twin density strongly depends on film thickness and above 160 nm film thickness hardly any twins were found. Because the lattice misfit is independent of the film thickness, there seems to be other, more efficient mechanisms to accommodate the large lattice misfit.

One has to keep in mind that also nominally undeformed films have undergone two temperature cycles on the NaCl substrate during sample preparation. After deposition they were cooled down from 300°C and during curing of the polyimide they were heated up to 365°C and cooled down again. Due to the different thermal expansion coefficients of Au (α_{Au}

= $14 \cdot 10^{-6} \text{ K}^{-1}$) and NaCl ($\alpha_{\text{NaCl}} = 44 \cdot 10^{-6} \text{ K}^{-1}$) this corresponds to thermal strains of 0.8 and 1.0%, respectively. This means that if twinning is an active deformation mechanism, twins could have been introduced during these preparation steps. During the tensile test the films were deformed to total strains of about 3-4% which gave an additional increase of the twin density by a factor of 2. The argument that twinning is pronounced in thinner films is also confirmed by the observed changes in the average peak width of the Laue spots. Especially the radial width of the Laue spots was affected which reflects the out-of-plane orientation of the illuminated volume. For films thinner than 80 nm the initial peak width as well as the increase in peak width during deformation were larger. This can only be attributed to twin formation since the Laue spots are not affected by an increased density of statistical dislocations [Barabash 2001, Barabash et al. 2002]. In contrast, thicker films show no pronounced increase in peak width. Here the deformation during the tensile test is accommodated by perfect dislocations.

In situ TEM investigations show that deformation by partial dislocations becomes dominant as the film thickness decreases. The appearance of partial dislocations was first observed in the 80 nm thick films [Oh et al. 2007]. Chen et al. [2003b] proposed a dislocation-based model to explain the preference for deformation twins and stacking faults in nanocrystalline Al when the grain size decreases to tens of nanometers. In their model, they compared the critical shear stress to nucleate a perfect dislocation with the stress required to initiate a Shockley partial dislocation and a stacking fault and obtained the following equation for the critical feature size h_c below which the nucleation of partial dislocations is more favorable:

$$h_c = \frac{2\alpha' \mu (b_N - b_p) b_p}{\gamma} \quad (7-7)$$

For Au, the shear modulus μ is 27 GPa, the stacking fault energy $\gamma = 40 \text{ mJ/m}^2$, and the magnitude of the Burgers vectors of the perfect dislocation and Shockley partial dislocation are $b_N = 0.288 \text{ nm}$ and $b_p = 0.166 \text{ nm}$, respectively. The parameter α' reflects the character of the dislocation with $\alpha = 0.5$ for edge and 1.5 for screw dislocations. Taking these values, the critical feature size is calculated to be between 14 and 44 nm. This is slightly smaller than the transition point between 80 and 160 nm observed in our experiments. This may be due to the very simple estimate. However, it is evident that the twins and stacking faults start and end at voids or at another twin or stacking fault. This indicates that they are not nucleated

homogeneously but at stress concentrations. Since there are many feasible sites for stress concentrations (pores, surface steps, twins) present in the thinnest films, the transition to deformation and nucleation of partial dislocations may be easier than assumed in the simple model.

7.4.3 Scaling behavior of yield strength

Nix [1989] proposed, based on calculations by Freund [1987] that the origin of hardening in a single crystalline film is induced by the deposition of dislocation segments at the film/substrate interface. An energy balance between the work done by the dislocation and the energy stored in the dislocation segments gave the following expression for the flow stress of the film:

$$\sigma_{Nix} = \frac{\sin \phi}{\cos \phi \cos \lambda} \frac{\mu_f b}{2\pi(1-\nu_f)} \frac{1}{h} \left[\frac{\mu_s}{\mu_f + \mu_s} \ln\left(\frac{\beta h}{b}\right) \right] \quad (7-8)$$

where ϕ and λ are the angles between the normal vectors of the film and the glide plane, and between the normal vector of the film and the Burgers vector b , respectively, μ_f is the shear modulus of the film, μ_s that of the substrate and ν_f is the Poisson's ratio of the film. β is a numerical constant that defined the outer cut-off radius of the dislocation and h is the film thickness. Quantitative agreement between this model and experimental flow stress data was found for epitaxial Al and Cu films grown on single crystalline (0001) α -Al₂O₃ substrates [Dehm et al. 2002b, Dehm et al. 2003].

Although long dislocation segments were also found for our films, at least for films thicker than 160 nm, the Nix model strongly underestimates our experimental data (figure 7.12a). Because of the low modulus of the polyimide substrate, the predicted values are much too low. Therefore, in our films the effect of misfit dislocations, if they exist, cannot be stress-determining. Additional contributions by blocking at the twin boundaries are also unlikely to explain the discrepancy between the model and the experimental data because the twin spacing is much bigger than the film thickness. The TEM images also show neither threading dislocations depositing long dislocation segments at the film/substrate interface nor any interaction or pile-up of perfect dislocations.

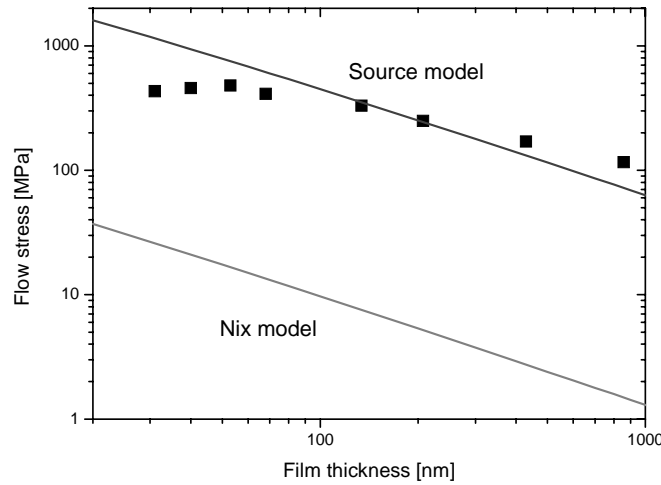


Figure 7.12: Flow stress for the single crystalline Au films compared to the Nix model (equation (7-8)) for a polyimide substrate and the Source model for a freestanding film (equation (7-9)). The following parameters were used for the calculation of the models: $\sin\phi/(\cos\phi\cos\lambda) = 2$, $b = 0.288$ nm, $\beta = 2.6$, $\mu_{Pt2611} = 2.96$ GPa, $\mu_{Au} = 27$ GPa, $\nu_{Au} = 0.42$, $s = 0.5$ and $\alpha = 2.5$.

In order to accommodate the homogeneous macroscopic deformation many different slip systems must contribute. This indicates that the scaling effect of the flow stress may not be the result of constraints on dislocation motion but rather of constraints on the nucleation of dislocations. Von Blanckenhagen et al. [2001] simulated thin film plasticity by considering a Frank-Read source in the center of a columnar grain. The source configuration was chosen such that the activation energy was minimized. Discrete dislocation dynamics simulations of the operation of such dislocations sources revealed that the size s_d of the most effective dislocation source scales with the smaller dimension among film thickness h and grain size d . For a freestanding film s_d was found to be $h/3$ or $d/3$. Using an Orowan equation and the Schmid factor s of the corresponding glide system the flow stress of the film σ_{source} can be derived analytically from the size of the dislocation source s_d :

$$\sigma_{source} = \frac{1}{s} \frac{\mu_f b}{2\pi s_d} \ln\left(\frac{\alpha s_d}{b}\right) \quad (7-9)$$

where α is a numerical constant, b is the magnitude of the Burgers vector and μ_f is the shear modulus of the film. For a single crystalline film the only varying parameter is the film thickness, therefore the source size is assumed to be $h/3$. In figure 7.12 the source model is compared to the experimental data. In contrast to the Nix model the source model shows good

agreement, especially for thicknesses between 160 and 500 nm. Below, it overestimates the flow stress whereas for thicker films it yields lower flow stresses. Overall this indicates that the flow stress is reasonably well described by the nucleation stress of single dislocations.

However for thinner films we have seen that the deformation is carried increasingly by partial dislocations which normally have an even higher nucleation stress than the full dislocations. Nevertheless, at local stress concentrations they can be nucleated. Since in the thinnest films many additional stress concentrations are present due to the presence of pores, the nucleation of partial dislocations may be easier than assumed. For the thicker films the nucleation is easier due to the decreased constraint on the dislocation source. In this case many dislocations are generated at relatively low stresses and the dislocation density may become high enough that the dislocations interact or pile-up. This may lead to backstresses that affect the nucleation of further dislocations as proposed by Nicola et al. [2003].

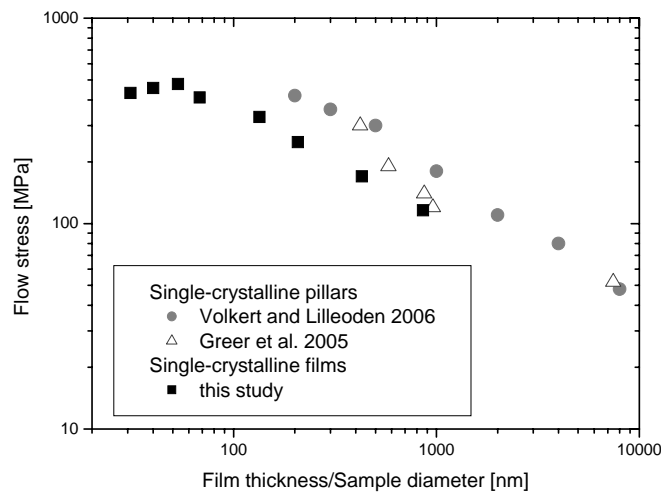


Figure 7.13: Comparison of the flow stress data of this study to literature values of uniaxial compression tests on single crystalline Au pillars [Greer et al. 2005, Volkert and Lilleoden 2006]. The data is plotted against the film thickness and sample diameter, respectively.

It is instructive to compare our results with those of the nanocompression test. Greer et al. [2005] as well as Volkert and Lilleoden [2006] used a focused ion beam (FIB) to cut single crystalline Au pillars out of a macroscopic Au sample. Subsequently, pillars were tested with a nanoindenter equipped with a flat punch in a uniaxial compression test. The diameter of the pillars varied between 180 nm and 8 μm . In figure 7.13 the flow stresses obtained from these nanocompression tests are compared to the data of our single crystalline films. It is evident

that both testing techniques result in a very similar scaling behavior of the flow stress, but the absolute values are lower for our films by a factor of 1.5. Greer et al. [Greer et al. 2005, Greer and Nix 2006] proposed a dislocation starvation mechanism to explain the hardening in the Au pillars; it is assumed that the dislocations leave the crystal at the free Au surface before they have the chance to multiply or interact. Thus, new dislocations have to be nucleated to accommodate further strain. Volkert and Lilleoden [2006] also discussed a dislocation source-limited behavior due to the loss of dislocations by the sample surfaces. They argued that the reduced dislocation density in a small column leads to lower internal stresses and therefore the external stress required to nucleate a dislocation source may be higher. Both explanations are very similar to the argumentation of the source model and should not result in much higher stresses. However, it could be that the higher surface to volume ratio in the pillars compared to our films and the 3D geometry of the pillars may influence the effective size of the dislocation source. In order to explain the discrepancy the source size for the pillars would have to be 1/10 of the pillar diameter. A general issue for pillars prepared by Ga⁺ ion beam sputtering in the FIB is the creation of a heavily damaged, implanted layer on the side walls of the columns. It is assumed that this layer is about 15-30 nm thick, which would be a remarkable volume fraction for pillars smaller than 300 nm. If the layer is sufficiently strong to block the dislocations from leaving the pillar, the resulting pile-up could lead to large backstresses on the nucleation of further dislocations until the stress is high enough to break through the boundary layer. The role of the boundary layer is still under debate but recent white beam Laue microdiffraction measurements of Au and Al pillars indicate that the FIB preparation influences the microstructure of the pillar and generates distinct strain gradients [Maaß et al. 2006].

Compared to the nanocompression test, the *in situ* tensile testing technique presented here enables the investigation of much smaller feature sizes. In addition the testing and handling of the samples is very easy. Provided that polychromatic synchrotron radiation is available, films as thin as some tens of nanometers can be investigated. The detailed analysis of Laue diffraction patterns yields the complete stress tensor and also gives additional information on the microstructural changes during deformation. However in order to take full advantage of the technique and to investigate solely a film thickness effect, ultra thin films with a homogeneous thickness and better microstructure (no pores and growth twins) would be required.

7.5 Summary and conclusion

A novel experimental route has been presented to prepare single crystalline Au films on a compliant polyimide substrate. The films have been tested by isothermal tensile testing and the stress in the film was obtained by white beam Laue diffraction. A detailed TEM study on the thinnest films gave additional insight in the microstructure and the deformation mechanisms in the films. The findings can be summarized as follows:

- Single crystalline Au films can be obtained by magnetron sputtering on NaCl substrates and transferred to compliant polyimide substrates. Films thinner than 80 nm show square shaped holes which result from the cleaved surface of the NaCl substrate.
- Isothermal stress-strain curves are obtained for films as thin as 30 nm. The flow stress of the films increases with decreasing film thickness but for films thinner than 80 nm constant or even decreasing flow stress values are found.
- This change in behavior is correlated to a transition in the dominating deformation mechanism from perfect dislocations to partial dislocations. The presence of voids and twins facilitate the nucleation of these partial dislocations.
- Good agreement is obtained by comparing the experimental data to a dislocation source model postulated by von Blanckenhagen et al. [2001].
- A comparison to the data of nanocompression tests on single crystalline micropillars shows that the flow stresses for the single crystalline films are lower. This may be due to the different surface-to-volume ratio or the different surface conditions in the micropillars caused by FIB preparation. However, smaller length scales are accessible with our synchrotron-based technique.

8 Summary: Novel aspects in the mechanical properties of ultra thin metallic films

The goal of this thesis was to develop a basic understanding of the plasticity of ultra thin metallic films. An accurate measurement of the mechanical properties of the films was the first step toward that objective. Therefore synchrotron-based *in situ* tensile testing techniques were developed and optimized in order to characterize the biaxial stress evolution in ultra thin metallic films on compliant polymer substrates during isothermal tensile tests. Experimental procedures for polycrystalline as well as single crystalline films were established. Thereby, the variable wavelength of the synchrotron radiation was the key feature for the experiments. For polycrystalline films monochromatic X-rays of defined energy were necessary to adapt for the very strong <111> fiber texture in the films, whereas a polychromatic X-ray beam was used for single crystalline films. The stress determination during the tensile tests was realized in a transmission geometry. Thus, no sample rotation or tilting was necessary and the whole information could be recorded on a big CCD area detector during a single X-ray exposure (15 to 120 s, complete Debye-Scherrer rings for polycrystalline films and Laue patterns for single crystalline films). In this way, the complete stress tensor of polycrystalline as well as single crystalline films with film thicknesses down to 20 nm could be measured with a strain resolution of 10^{-4} and at strain rates up to 10^{-4} s^{-1} . By these techniques, a unique field of testing parameters for ultra thin metallic films, like microstructure (interfaces, polycrystalline, single crystalline), temperature and deformation behavior at high total strains was established.

Metal films were either deposited on compliant polyimide substrates or on NaCl substrates. The latter substrate was chosen to grow epitaxial Au films. These were subsequently coated with a polyimide layer. In a final step, the NaCl substrate could be dissolved in water and the single crystalline Au film remained on the polyimide layer. Polycrystalline Cu and Au films with and without passivation layers (Ta for Cu and SiN_x for Au) were prepared on polyimide substrates in order to investigate the role of different interfaces on the mechanical properties. In addition, freestanding Cu films were prepared and tested by Bulge testing. Special care was dedicated to the microstructural characterization of the samples which was very important for the correct interpretation of the results of the mechanical tests.

In figure 8.1 the room temperature flow stresses of the different Cu and Au film systems are plotted against the film thickness and compared. The behavior for polycrystalline Cu and Au films was very similar. The influence of different interfaces was much smaller than expected. The biggest effect was found for films with one stiff interlayer (TaCu or AuSiN). Films on polyimide behaved like freestanding films and showed lower flow stresses, whereas samples with an additional surface passivation (TaCuTa, SiNAuSiN) showed no further increase in flow stress. This indicated that the deformation behavior was not predominantly influenced by the interfaces, but that it was also determined by mechanisms within the grains and in the grain boundaries.

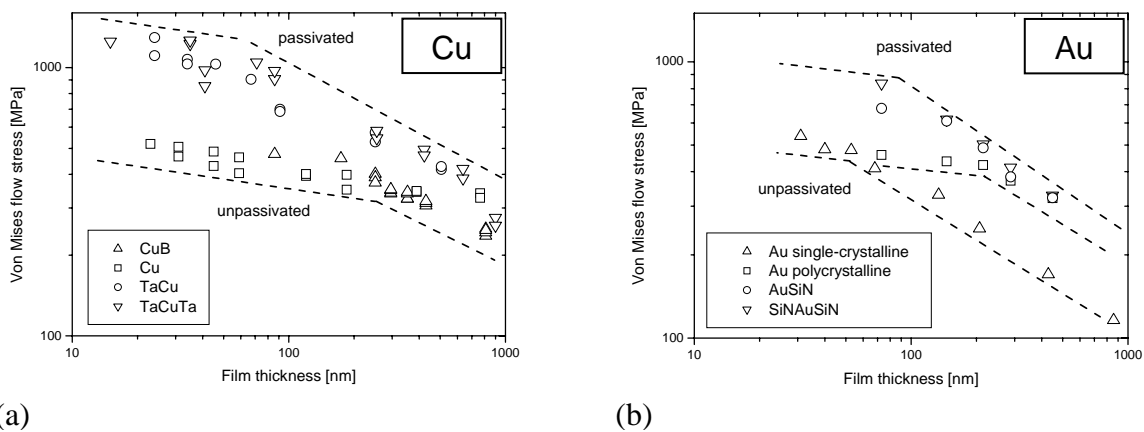


Figure 8.1: Room temperature flow stress for the (a) Cu and (b) Au film systems investigated in this study. The difference between passivated and unpassivated samples is similar for both materials. Below 100 nm film thickness, single crystalline Au films become as strong as polycrystalline Au films. In addition, a lower thickness dependence is found on this length scale for all film systems.

The scaling behavior of the flow stress could be described in the thickness regime between 100 and 600 nm by a modified dislocation source model which considers the activation of Frank-Read sources in the grains of the film. Anyway, it was not sufficient to implement only the film thickness, but the complete grain size statistics had to be considered to get good agreement to the experimental data. The yield stress of films thinner than 100 nm, however, could not be predicted accurately by the model. A limit in nucleation stress had to be introduced, as the model predicted unreasonably high nucleation stresses for the smallest grains. This indicated that the nucleation of perfect dislocations became unfavorable for feature sizes below 100 nm and that a different deformation mechanism might be responsible for the stress plateau. The nucleation stress for partial dislocations was very close to the observed plateau stress. Therefore, it was argued that the smallest grains in the film deform predominantly by

partial dislocations similar to first observations in nanocrystalline materials. This would also explain the strongly reduced strain hardening found for these films.

The proposed deformation by partial dislocations was also confirmed by the study of the single crystalline Au films. Here, the film thickness was the only microstructural parameter of relevance. For thicker films, the flow stress of the single crystalline films was lower than that for polycrystalline ones due to the missing constraint by the grain boundaries. However, the flow stress of the single crystalline films reached an almost identical stress plateau if the film thickness was below 100 nm (figure 8.1b). Transmission electron microscopy investigations on single crystalline films thinner than 160 nm showed an increasing density of twins. The twins resulted from the motion of partial dislocations on parallel glide planes. Pile-ups of partial dislocations within the twins were also found. No deformation twins were found in thicker single crystalline films which indicated a transition in deformation mechanism from perfect to partial dislocations if the film thickness or grain size is below 100 nm.

The tensile testing technique on polyimide substrates also allowed for investigating the deformation behavior of the metallic films at high total strains. Doing so, sudden stress decreases were found for film systems with weak adhesion or brittle surface or interlayers. This could be correlated to sequential cracking of the films. For TaCu samples with a Ta interlayer a detailed analysis of the cracking behavior was conducted. By combining the results of the *in situ* experiments at the synchrotron with those of *in situ* tests in a scanning electron microscope the strain energy per volume released by cracking as well as the crack area could be determined. Thus, it was possible to estimate the fracture toughness of the Cu films. It was found that the fracture toughness increases with film thickness. A comparison to existing models of thin film fracture mechanics showed the fracture mode of the thinnest films is brittle whereas it becomes more and more ductile if the film thickness increases. Figure 8.2a shows a comparison of flow stress and fracture toughness for TaCu films as a function of film thickness. The fracture toughness was minimal where the flow stress reached the plateau, which indicated that the constraint in plasticity was responsible for the decreasing fracture toughness of the thinnest films. However the dimensional constraint by the film thickness on the plastic zone should also have had an effect because Cu alloys of same strength show much higher fracture toughnesses than the Cu films in the TaCu film systems.

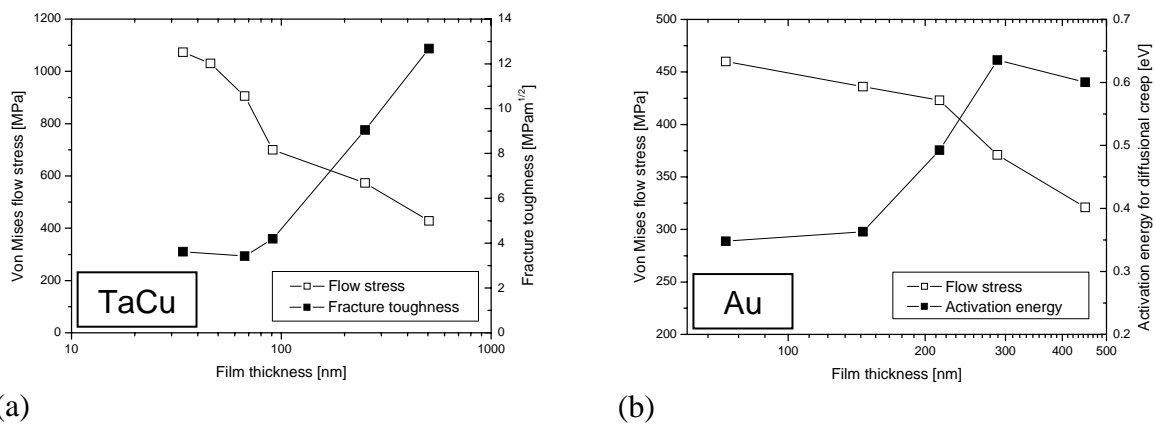


Figure 8.2: (a) Fracture toughness and flow stress of Cu films in TaCu samples and (b) activation energy for diffusional creep and flow stress for Au samples vs. film thickness. For both the flow stress increases with film thickness whereas the fracture toughness or activation energy decreases.

In order to investigate the temperature dependence of the mechanical properties heating and cooling devices were implemented in the experimental setup. Experiments in a temperature range between -150°C and 200°C showed a strong temperature dependence of the flow stress for passivated and unpassivated Au films. For passivated films and unpassivated films at temperatures below 100°C the temperature dependence could be explained by thermally activated dislocation glide. Above 100°C the temperature dependence of the yield stress for unpassivated films became even more pronounced. The size effect in yield stress disappeared completely and flow stresses of the bulk material were reached. This could be attributed to diffusional creep, which was inhibited in passivated films. The activation energy for diffusional creep increased with film thickness and decreased with increasing flow stress (figure 8.2b). In any case, it was always lower than the corresponding activation energy for the bulk material indicating that diffusional flow is facilitated in thin films with free surfaces.

Overall one can say that by using the synchrotron-based tensile testing techniques the scaling behavior of the mechanical properties could systematically be investigated for films thinner than 100 nm. It was found that the flow stress did not increase irresistibly. Instead the thickness dependence became lower below 100 nm film thickness. On this length-scale the nucleation of perfect dislocations becomes unfavorable and partial dislocations are more likely nucleated. Tensile tests to higher total strains and at different temperatures did also show that the brittleness and the temperature dependence of the flow stress are strongly enhanced in ultra thin films. In this sense, one may conclude: Small is strong, but smaller is not always stronger...

9 Appendix

9.1 Elastic constants for <111> fiber textured Au and Cu

For a cubic material exhibiting a perfect <111> fiber texture the relationship between the elastic constants in specimen coordinates and those in crystal coordinates can be obtained by coordinate transformation [Besser et al. 1994]:

$$\begin{aligned}
 C'_{11} &= \frac{C_{11} + C_{12} + 2C_{44}}{2}, \\
 C'_{12} &= \frac{C_{11} + 5C_{12} + 2C_{44}}{6}, \\
 C'_{13} &= \frac{C_{11} + 2C_{12} - 2C_{44}}{3}, \\
 C'_{15} &= \frac{C_{11} - C_{12} - 2C_{44}}{\sqrt{3}\sqrt{6}}, \\
 C'_{25} &= \frac{-C_{11} + C_{12} + 2C_{44}}{\sqrt{3}\sqrt{6}}, \\
 C'_{33} &= \frac{C_{11} + 2C_{12} + 4C_{44}}{3}, \\
 C'_{44} &= \frac{C_{11} - C_{12} + C_{44}}{3}, \\
 C'_{46} &= \frac{-C_{11} + C_{12} + 2C_{44}}{\sqrt{3}\sqrt{6}}, \\
 C'_{66} &= \frac{C_{11} - C_{12} + 4C_{44}}{6}.
 \end{aligned}$$

The elastic constants of Au in crystal coordinates are $C_{11} = 186$ GPa, $C_{12} = 157$ GPa and $C_{44} = 42$ GPa [Goens and Weerts 1936]. The stiffness and compliance matrices of a <111> fiber textured polycrystalline Au film in sample coordinates are thus

$$C'_{ij} = \begin{pmatrix} 214 & 148 & 139 & 0 & -13.0 & 0 \\ 148 & 214 & 139 & 0 & 13.0 & 0 \\ 139 & 139 & 223 & 0 & 0 & 0 \\ 0 & 0 & 0 & 23.7 & 0 & 13.0 \\ -13.0 & 13.0 & 0 & 0 & 23.7 & 0 \\ 0 & 0 & 0 & 13.0 & 0 & 32.8 \end{pmatrix} \text{GPa}$$

and

$$S'_{ij} = \begin{pmatrix} 12.4 & -7.06 & -3.30 & 0 & 10.6 & 0 \\ -7.06 & 12.4 & -3.30 & 0 & -10.6 & 0 \\ -3.30 & -3.30 & 8.60 & 0 & 0 & 0 \\ 0 & 0 & 0 & 53.9 & 0 & -21.3 \\ 10.6 & -10.6 & 0 & 0 & 53.9 & 0 \\ 0 & 0 & 0 & -21.3 & 0 & 38.9 \end{pmatrix} \text{TPa}^{-1}.$$

The elastic constants of Cu in crystal coordinates are $C_{11} = 168$ GPa, $C_{12} = 121$ GPa and $C_{44} = 75$ GPa [Goens and Weerts 1936]. The stiffness and compliance matrices of a $\langle 111 \rangle$ fiber textured polycrystalline Cu film in sample coordinates are thus

$$C'_{ij} = \begin{pmatrix} 220 & 104 & 86.6 & 0 & -24.2 & 0 \\ 104 & 220 & 86.6 & 0 & 24.2 & 0 \\ 86.6 & 86.6 & 237 & 0 & 0 & 0 \\ 0 & 0 & 0 & 40.7 & 0 & 24.2 \\ -24.2 & 24.2 & 0 & 0 & 40.7 & 0 \\ 0 & 0 & 0 & 24.2 & 0 & 57.8 \end{pmatrix} \text{GPa}$$

and

$$S'_{ij} = \begin{pmatrix} 7.69 & -3.84 & -1.41 & 0 & 6.87 & 0 \\ -3.84 & 7.69 & -1.41 & 0 & -6.87 & 0 \\ -1.41 & -1.41 & 5.26 & 0 & 0 & 0 \\ 0 & 0 & 0 & 32.8 & 0 & -13.8 \\ 6.87 & -6.87 & 0 & 0 & 32.8 & 0 \\ 0 & 0 & 0 & -13.8 & 0 & 23.1 \end{pmatrix} \text{TPa}^{-1}.$$

9.2 Exemplary AutoIt Macro for the control of a tensile test

AutoIt macros (AutoIt V2.64, Hidden Soft, Jonathan Benett & Team, free available from <http://www.autoitscript.com/AutoIt/downloads.php>) were used to control the tensile tester and the CCD camera. AutoIt is a simple tool that can simulate keystrokes, mouse movements and window commands (maximize, minimize, wait for, etc.). The desktop of the Linux workstation of the CCD camera was displayed on the PC of the tensile tester by VNC (VNC V3.3.3.2, AT&T Laboratories Cambridge, free available from <http://www.cl.cam.ac.uk/research/dtg/attarchive/archive/vnc/>). Thus, the software of the CCD camera (MarCCD, M. Blum, marresearch) and of the tensile tester (DDS32 V2.0, Kammrath & Weiss) could be controlled on the PC. The AutoIt macro just simulated the mouse clicks to take an image and to move the motor of the tensile tester after activating the corresponding window. The macro was varied with respect to the exposure time, step widths and number of cycles:

```
SetEnv, exptime, 30000

WinActivate, DDS32
WinActivate, Motor Control

;Bild aufnehmen
WinActivate, marccd's X desktop (ankamf6:4)
sleep, 500
LeftClick, 526,256

sleep, 1000

; Bild aufnehmen - 20 s
sleep, %exptime%
WinActivate, DDS32           ; DDS32 aktivieren
WinActivate, Motor Control
sleep, 500

; ----- BELASTUNG
; 7 Steps in 30 µm Schritten
SetEnv, Steps, 7
SetEnv, steplen, 3000

repeat, %Steps%

; motor forward
LeftClick, 26,52
; motor reverse
;LeftClick, 63,51

sleep, %steplen%
LeftClick, 103,51; motor stop
Send, {F5}
; View All

;Bild aufnehmen
WinActivate, marccd's X desktop (ankamf6:4)
```

```

sleep, 500
LeftClick, 526,256

sleep, 1000

; Bild aufnehmen - 20 s
sleep, %exptime%
WinActivate, DDS32
WinActivate, Motor Control
sleep, 500
endrepeat
; -----

; ----- BELASTUNG
; 35 Steps in 60 µm Schritten
SetEnv, Steps, 35
SetEnv, steplen, 6000

repeat, %Steps%

; motor forward
LeftClick, 26,52
; motor reverse
;LeftClick, 63,51

sleep, %steplen%
LeftClick, 103,51; motor stop
Send, {F5}
; View All

;Bild aufnehmen
WinActivate, marccd's X desktop (ankamf6:4)
sleep, 500
LeftClick, 526,256
sleep, 1000

; Bild aufnehmen - 20 s
sleep, %exptime%
WinActivate, DDS32
WinActivate, Motor Control
sleep, 500
endrepeat
; -----

; ----- ENTLASTUNG
; 10 Steps in 30 µm Schritten
SetEnv, Steps, 10
SetEnv, steplen, 3000

repeat, %Steps%

; motor forward
;LeftClick, 26,52
; motor reverse
LeftClick, 63,51

sleep, %steplen%
LeftClick, 103,51; motor stop
Send, {F5}
; View All

```

```
;Bild aufnehmen
WinActivate, marccd's X desktop (ankamf6:4)
sleep, 500
LeftClick, 526,256
```

```
sleep, 1000
```

```
; Bild aufnehmen - 20 s
sleep, %exptime%
WinActivate, DDS32
WinActivate, Motor Control
sleep, 500
endrepeat
```

```
; -----
```

```
; ----- ENTLASTUNG
```

```
; 13 Steps in 100 µm Schritten
SetEnv, Steps, 8
SetEnv, steplen, 10000
```

```
repeat, %Steps%
```

```
; motor forward
;LeftClick, 26,52
; motor reverse
LeftClick, 63,51
```

```
sleep, %steplen%
LeftClick, 103,51; motor stop
Send, {F5}
; View All
```

```
;Bild aufnehmen
WinActivate, marccd's X desktop (ankamf6:4)
sleep, 500
LeftClick, 526,256
```

```
sleep, 1000
```

```
; Bild aufnehmen - 20 s
sleep, %exptime%
WinActivate, DDS32
WinActivate, Motor Control
sleep, 500
endrepeat
```

```
; -----
```

```
MsgBox, 0, STATUS, Messung beendet!
```

10 Deutsche Zusammenfassung

Einleitung

Der technologische Fortschritt der letzten Jahrzehnte wurde im Wesentlichen durch die moderne Informations- und Kommunikationstechnologie geprägt. Die immer größer werdenden Datenmengen und zunehmende Funktionalität der Geräte erfordert eine weiterführende Miniaturisierung der elektronischen Bauelemente. In der Herstellung von mikroelektronischen und mikroelektromechanischen Systemen spielen dünne Metallschichten eine wichtige Rolle. Neben den optischen, magnetischen oder elektronischen Eigenschaften, die die Funktionalität des Bauteils bestimmen, ist die Kenntnis der mechanischen Eigenschaften von dünnen Schichten entscheidend, um die Zuverlässigkeit und Funktionalität des Bauteils über dessen Lebensdauer hinweg zu gewährleisten.

Die mechanischen Eigenschaften verändern sich, wenn mikrostrukturelle Parameter oder die Objektgröße selbst Längenskalen im Mikrometerbereich erreichen [Arzt 1998]. Für dünne Metallschichten ist dies von besonderer Bedeutung, da bereits Schichten mit Schichtdicken im Bereich unter 100 nm im Einsatz sind [ITRS 2003]. In solch dünnen Schichten herrschen häufig sehr hohe mechanische Spannungen, die um ein Vielfaches höher sein können, als die Fließgrenze des entsprechenden Massivmaterials. Dies wird häufig auf die Einengung der Versetzungsbewegung zurückgeführt [Nix 1989, Thompson 1993, Arzt et al. 2001, Dehm et al. 2002a]. Die zugrunde liegenden Mechanismen sind allerdings noch nicht vollständig verstanden.

Dies liegt nicht zuletzt daran, dass es experimentell sehr schwierig ist, die mechanischen Eigenschaften dünner Metallschichten zu messen [Kraft and Volkert 2001]. Die Einschränkungen bezüglich des Volumens und der Abmessungen der Proben sowie die sehr kleinen Verschiebungen und Kräfte, die beherrscht werden müssen, verhindern, dass klassische Messmethoden einfach auf dünne Schichten übertragen werden können. Viele neue Testmethoden wurden vorgeschlagen, allerdings gibt es bis heute keine ideale Testmethode, und viele Fragen der mechanischen Eigenschaften von dünnen Metallschichten sind nach wie vor ungeklärt.

Experimentelle Methoden

Synchrotronmethoden

Das Ziel dieser Arbeit war die Plastizität von ultradünnen Metallschichten genauer zu untersuchen. Dafür wurden neue synchrotron-basierte *in situ* Testmethoden entwickelt und optimiert, um die Entwicklung von mechanischen Spannungen in ultradünnen Metallschichten auf verformbaren Polymersubstraten während isothermer Zugversuche messen zu können. Es wurden experimentelle Verfahren für polykristalline und einkristalline Schichten aufgestellt. Dabei spielte der einstellbare Wellenlängenbereich der Synchrotronstrahlung eine Schlüsselrolle. Für polykristalline Schichten wurde monochromatische Röntgenstrahlung verwendet, deren Wellenlänge exakt auf die starke $\langle 111 \rangle$ Fasertextur und das Schichtmaterial abgestimmt wurde. Für einkristalline Schichten wurde hingegen ein polychromatischer Röntgenstrahl eingesetzt. Die Ermittlung der Gitterdehnungen in den Metallschichten erfolgte in einer Transmissionsgeometrie, d.h. die Probe stand senkrecht zum Röntgenstrahl und wurde von diesem durchstrahlt. Auf der Rückseite der Probe konnten die Beugungsbilder mit einem großen Flächendetektor aufgenommen werden (komplette Debye-Scherrer Ringe für polykristalline Schichten bzw. Laue Aufnahmen für einkristalline Schichten). Im Gegensatz zu der klassischen röntgenographischen Spannungsmessung mit der sog. $\sin^2\psi$ -Methode war keine Rotation oder Kippung der Probe notwendig, um die Gitterdehnung in verschiedenen Kristallorientierungen messen zu können. Die notwendige Information konnte mit einer einzigen Röntgenmessung (15 bis 120 s) ermittelt werden. Für polykristalline Schichten wurden die Gitterdehnungen aus der elliptischen Verzerrung der Debye-Scherrer Ringe ermittelt, während jene für die einkristallinen Schichten aus der Verschiebung der Laue Peaks bestimmt wurden. Die Spannungen wurden jeweils auf Basis der gemessenen Gitterdehnungen mit Hilfe des Hookeschen Gesetzes berechnet. Auf diese Weise konnten alle Komponenten des Spannungstensors sowohl für polykristalline als auch für einkristalline Schichten bis zu einer Schichtdicke von etwa 20 nm mit einer Dehnungsauflösung von etwa 10^{-4} und Dehnraten bis zu 10^{-4} s^{-1} gemessen werden. Die Messungen wurden an der MPI-MF-Beamline an der Angströmquelle Karlsruhe (ANKA) durchgeführt. Mit Hilfe dieser Methoden konnte ein neues Feld von Testparametern, u. a. Mikrostruktur (verschiedene Grenzflächen, polykristallin, einkristallin), Testtemperatur und Verformungsverhalten bei hohen Dehnungen für ultradünne Metallschichten erschlossen werden. Zum Vergleich wurden zusätzlich

Membrantests an freistehenden Metallschichten durchgeführt. Dabei wurde die Membranauslenkung als Funktion des angelegten Druckes mit Hilfe eines Weisslicht-interferenzmikroskops gemessen und daraus die Schichtspannung berechnet.

Probenherstellung und -charakterisierung

Alle Metallschichten wurden mittels Magnetron-Sputtern im Ultrahochvakuum ($< 10^{-8}$ mbar) hergestellt. Für die polykristallinen Proben wurden knochenförmige 125 μm dicke Polyimidsubstrate (Kapton® HN, DuPont) mit einem Messbereich von 6 mm x 20 mm verwendet. Vor der Schichtabscheidung wurde die Substratoberfläche gereinigt und über 1 min mit einem Ar^+ Plasma behandelt. Verschiedene Au und Cu Schichtsysteme mit und/oder ohne zusätzliche Zwischen- und Deckschichten (Ta für Cu und SiN_x für Au) wurden hergestellt, um den Einfluss der verschiedenen Grenzflächen auf die mechanischen Eigenschaften zu untersuchen. Die Schichtdicken der Au und Cu Schichten wurden im Bereich von 20 bis 1000 nm variiert, während die Zwischen- und Deckschichten immer zwischen 5 und 25 nm dick waren. Um eine möglichst große Korngröße zu erreichen, wurden die Au Schichten bei einer Substrattemperatur von 300°C abgeschieden. Die Cu Schichten wurden hingegen bei Raumtemperatur hergestellt und nach der Schichtherstellung 30 min bei 350°C ausgelagert. Die Cu Schichten für den Membrantest wurden unter identischen Bedingungen auf kommerziell erhältliche, amorphe SiN_x -Membranen abgeschieden. Um eine freistehende Schicht zu erhalten, wurde die SiN_x -Membran auf der Rückseite der Cu Schicht mit einem CF_4/O_2 -Plasma entfernt (4 min, ca. 100 W). Da einkristalline Schichten nicht direkt auf amorphen Polymersubstraten hergestellt werden können, wurden hierfür Steinsalzsubstrate verwendet. Auf diesen konnten einkristalline Au Schichten (30 bis 1000 nm dick) hergestellt werden. Diese wurden anschließend mit einem Polyimidfilm (PI2611, HD Microsystems) beschichtet. Nach der Aushärtung des Polyimids konnte das Steinsalzsubstrat in Wasser aufgelöst werden. Die Haftung der einkristallinen Au Schichten auf dem Polyimidfilm war so gut, dass mit den so hergestellten Proben Zugversuche durchgeführt werden konnten.

Die Charakterisierung der Mikrostruktur erfolgte mittels verschiedenster Methoden, unter anderem RBS (Schichtdicke), EBSD (Korngröße und -orientierung), FIB (Korngröße, Querschnitte, Schichtdicke) und TEM (Korngröße, Versetzungen, Zwillinge, Poren). Die

Untersuchung der Mikrostruktur war für die Interpretation der Ergebnisse der mechanischen Tests sehr wichtig. Polykristalline Schichten zeigten im untersuchten Schichtdickenbereich durchweg eine kolumnare Kornstruktur mit mittleren Korngrößen, die immer etwas größer als die entsprechende Schichtdicke waren. Die Auswertung der Korngrößenverteilungen ergab jedoch sehr breite Verteilungen, d.h. obwohl der Medianwert etwas größer als Schichtdicke war, gab es immer einen großen Anteil an sehr kleinen Körnern. Die Mikrostruktur der einkristallinen Schichten im Schichtdickenbereich unterhalb von 160 nm zeigte eine mit abnehmender Schichtdicke zunehmende Zwillingsdichte und Porosität. Die Poren ergaben sich aus der Oberflächenbeschaffenheit der Steinsalzsubstrate und dem Inselwachstum der einkristallinen Au Schichten. Die Oberfläche der Substrate wies Spaltstufen auf, die terrassenförmig entlang bestimmter kristallographischer Richtungen angeordnet waren. Ab einer gewissen Schichtdicke konnte sich über die Spaltstufen hinweg eine geschlossene Schicht bilden. Die Zwillinge hingegen wurden nicht während der Schichtherstellung gebildet, sondern entstanden während der Verformung der einkristallinen Schichten. Zusätzlich zu den statischen Untersuchungen im REM, FIB und TEM wurden auch *in situ* Zugversuche im REM durchgeführt. Hier stand das Bruchverhalten bei hohen Dehnungen von polykristallinen Cu Schichten mit einer spröden Ta Zwischenschicht im Vordergrund. Dabei wurde die Rissbildung und die Entwicklung der Rissdichte untersucht.

Ergebnisse und Diskussion

Plastizität ultradünner Kupferschichten mit und ohne Passivierung

Die Membrantests und Zugversuche an verschiedenen Cu Schichtsystemen mit und ohne Ta Zwischen- oder Deckschicht zeigten Unterschiede im Skalierungsverhalten der Fließgrenze für die einzelnen Schichtsysteme. Cu Schichten auf Polyimid verhielten sich wie die freistehenden Cu Schichten und zeigten unerwartet hohe Fließspannungen. Zusätzliche Ta Schichten führten zu einem deutlichen Anstieg der Fließgrenze, allerdings gab es keinen Unterschied zwischen den Schichtsystemen mit nur einer Ta Zwischenschicht und solchen mit einer Ta Zwischen- und Deckschicht. Die Ergebnisse deuten daraufhin, dass das Verformungsverhalten nicht primär durch die Grenzflächen beeinflusst wird, sondern dass Verformungsmechanismen innerhalb der Körner und an den Korngrenzen festigkeitsbestimmend sind. Das Skalierungsverhalten der Fließspannungen konnte im

Schichtdickenbereich zwischen 100 und 600 nm mit einem modifizierten Versetzungsquellenmodell beschrieben werden. Nach diesem Modell wird die Fließspannung des Materials durch die für die Aktivierung einer Frank-Read Quelle im Innern eines Korns benötigte Spannung bestimmt. Allerdings reichte die Berücksichtigung der Schichtdicke alleine nicht aus, um die experimentellen Ergebnisse zu erklären. Erst unter Einbeziehung der Korngrößenverteilung konnten die Absolutwerte und das Skalierungsverhalten der Fließspannung für alle Schichtsysteme richtig wiedergegeben werden.

Die Fließspannungen für Schichten mit Schichtdicken von weniger als 100 nm konnten aber auch mit diesem Modell nicht beschrieben werden. Es musste zusätzlich noch ein oberes Limit für die Nukleierungsspannung eingeführt werden, da das Modell für die kleinsten Körner extrem hohe Spannungen voraussagt. Dies deutet daraufhin, dass die Nukleierung von vollständigen Versetzungen in den kleinsten Körnern zu schwierig wird und dass ein anderer Verformungsmechanismus möglicherweise günstiger wird. Da die Nukleierungsspannung von Partialversetzungen sehr gut mit der für die Beschreibung der experimentellen Daten notwendigen Maximalspannung korreliert, könnte die Verformung durch Partialversetzungen eine mögliche Erklärung für das veränderte Skalierungsverhalten der Fließspannung sein. Außerdem könnte ein solcher Verformungsmechanismus auch die stark reduzierte Verfestigung in diesen Schichten erklären.

Spröd-duktil Übergang in ultradünnen Ta/Cu Schichtsystemen

Die Ta Zwischen- und Deckschichten beeinflussten nicht nur die Fließspannungen der Cu Schichten, sondern führten bei Dehnungen von mehr als 2.5% zu einer plötzlichen Abnahme der Schichtspannungen. Dies konnte auf Rissbildung in den Cu Schichten zurückgeführt werden. Dieses Phänomen wurde für Cu Schichten mit einer Ta Zwischenschicht genauer untersucht. Durch die Kombination der Ergebnisse von Zugversuchen am Synchrotron und im Rasterelektronenmikroskop an identischen Proben konnten die bei der Rissbildung freiwerdende Verzerrungsenergie sowie die zugehörige Rissfläche ermittelt werden. Damit war es möglich, die Bruchzähigkeit der Cu Schichten zu bestimmen. Dabei kam heraus, dass die Bruchzähigkeit der Cu Schichten mit zunehmender Schichtdicke ansteigt. Der Vergleich mit bestehenden Modellen zur Bruchmechanik von dünnen Schichten zeigte, dass die dünnsten Cu Schichten völlig spröde brechen, während das Bruchverhalten mit zunehmender

Schichtdicke immer duktiler wird. Die Schichtdicke hat dabei nicht nur einen Einfluss auf die Versetzungsplastizität, sondern schränkt auch die Ausdehnung der plastischen Zone ein. Dies führt zu einer weiteren Erniedrigung der Bruchzähigkeit im Vergleich zu Massivmaterialien gleicher Festigkeit.

Temperaturabhängigkeit der mechanischen Eigenschaften von ultradünnen Au Schichten

Mit Hilfe der neuen synchrotron-basierten Messmethode kann auch die Temperaturabhängigkeit der mechanischen Eigenschaften untersucht werden. Dazu wurden Zugversuche an passivierten und unpassivierten Au Schichten im Temperaturbereich zwischen -150 und 200°C durchgeführt. Dabei wurde festgestellt, dass die Fließspannung für alle Schichtsysteme eine starke Temperaturabhängigkeit zeigt. Rissbildung wurde bei tiefen und hohen Temperaturen beobachtet. Mögliche Ursachen hierfür sind die abnehmende Duktilität bei tiefen Temperaturen bzw. mangelnde Haftung bei höheren Temperaturen. Die Temperaturabhängigkeit der Fließspannung für passivierte Schichten und für unpassivierte Schichten unterhalb von 100°C konnte mit thermisch aktiviertem Versetzungsgleiten erklärt werden. Die ermittelten Aktivierungsenergien waren allerdings kleiner als die des entsprechenden Massivmaterials. Dies liegt vermutlich an der unterschiedlichen Dichte und Anordnung der Hindernisse. Unpassivierte Au Schichten zeigten oberhalb von 100°C eine noch stärkere Temperaturabhängigkeit der Fließspannung. Dabei ging die Schichtdickenabhängigkeit der Fließspannung vollständig verloren. Dies konnte auf Diffusionskriechen zurückgeführt werden, das in den passivierten Schichten unterdrückt wurde. Die ermittelte Aktivierungsenergie für Diffusionskriechen nahm mit der Schichtdicke zu. Sie war jedoch für alle Schichtdicken deutlich niedriger als die Aktivierungsenergie des Massivmaterials. Dies deutet daraufhin, dass die Diffusion in dünnen Schichten mit freien Oberflächen erleichtert wird.

Mechanische Eigenschaften ultradünner einkristalliner Au Schichten

Einkristalline Schichten sind besonders für die Untersuchung der Schichtdickenabhängigkeit der Fließspannung geeignet, da hier die Schichtdicke der einzige relevante mikrostrukturelle

Parameter ist. Insgesamt zeigten die einkristallinen Schichten jedoch eine ähnliche Schichtdickenabhängigkeit wie die polykristallinen Schichten. Für dickere Schichten war die Fließspannung der einkristallinen Schichten deutlich geringer als die der polykristallinen Au Schichten. Dies liegt an der breiten Korngrößenverteilung in den polykristallinen Schichten. Aufgrund der homogenen Verformung durch das Polyimidsubstrat sind alle Körner der Schicht gezwungen, an der Verformung mitzuwirken, d.h. auch in den Körnern, die kleiner als die Schichtdicke sind, müssen Versetzungen nukleiert werden. Dies führt im Mittel zu höheren Fließspannungen. Für Schichtdicken kleiner 100 nm zeigen die einkristallinen und die polykristallinen Schichten allerdings fast identische Fließspannungen. Die Schichtdickenabhängigkeit ging in beiden Fällen deutlich zurück.

Untersuchungen im Transmissionselektronenmikroskop (TEM) an verformten und unverformten einkristallinen Au Schichten im Schichtdickenbereich von 30 bis 160 nm zeigten eine zunehmende Zwillingsdichte mit abnehmender Schichtdicke. In verformten Schichten war die Zwillingsdichte ebenfalls höher. Die Zwillinge wurden durch die Bewegung von Partialversetzungen auf parallelen Gleitebenen gebildet. Innerhalb der Zwillinge wurde häufig ein Aufstau von Partialversetzungen gefunden. In dickeren einkristallinen Schichten (≥ 240 nm) wurden keine Zwillinge mehr beobachtet. Daher scheint für Schichtdicken kleiner 160 nm der vorherrschende Verformungsmechanismus von vollständigen Versetzungen zu Partialversetzungen hin zu wechseln.

Zusammenfassung

Durch den Einsatz der neu entwickelten Synchrotronmethoden konnte das Skalierungsverhalten der mechanischen Eigenschaften von ultra dünnen Metallschichten im Schichtdickenbereich unterhalb von 100 nm systematisch untersucht werden. Dabei hat sich gezeigt, dass die Fließspannung mit abnehmender Schichtdicke nicht unaufhörlich zunimmt. Stattdessen wird die Schichtdickenabhängigkeit unterhalb von 100 nm deutlich schwächer. In diesem Größenbereich wird die Nukleierung von vollständigen Versetzungen zunehmend schwieriger, und es werden eher Partialversetzungen gebildet. Zugversuche zu höheren Dehnungen und bei verschiedenen Temperaturen haben außerdem gezeigt, dass die Sprödigkeit und die Temperaturabhängigkeit der Fließspannungen in diesem Größenbereich stark zunehmen.

11 References

- Aksyuk V.A., Arney S., Basavanhally N.R., Bishop D.J., Bolle C.A., Chang C.C., Frahm R., Gasparyan A., Gates J.V., George R., Giles C.R., Kim J., Kolodner P.R., Lee T.M., Neilson D.T., Nijander C., Nuzman C.J., Paczkowski M., Papazian A.R., Ryf R., Shea H. and Simon M.E. [2002]. 238x238 surface micromachined optical crossconnect with 2dB maximum loss, in *Optical Fiber Communications Conference. (OFC). Postconference Technical Digest. Postdeadline Papers (IEEE Cat. No.02CH37339). Opt Soc. America. Part vol.2, 2002, FB9-1-3 vol.*
- Alaca B.E., Selby J.C., Saif M.T.A. and Sehitoglu H. [2002]. Biaxial testing of nanoscale films on compliant substrates: Fatigue and fracture. *Review of Scientific Instruments* 73(8), 2963-70.
- Arzt E. [1998]. Size effects in materials due to microstructural and dimensional constraints: a comparative review. *Acta Materialia* 46(16), 5611-26.
- Arzt E., Dehm G., Gumbsch P., Kraft O. and Weiss D. [2001]. Interface controlled plasticity in metals: dispersion hardening and thin film deformation. *Progress in Materials Science* 46(3-4), 283-307.
- Baker S.P. [1997]. Between nanoindentation and scanning force microscopy: measuring mechanical properties in the nanometer regime. *Thin Solid Films* 308-309, 289-96.
- Balk T.J., Dehm G. and Arzt E. [2003a]. Parallel glide: unexpected dislocation motion parallel to the substrate in ultrathin copper films. *Acta Materialia* 51(15), 4471-85.
- Balk T.J., Dehm G. and Arzt E. [2003b]. Parallel glide: a fundamentally different type of dislocation motion in ultrathin metal films, in *Multiscale Phenomena in Materials - Experiments and Modeling Related to Mechanical Behavior. Symposium. San Francisco, CA*, eds. H. M. Zbib, D. H. Lassila, L. E. Levine & K. J. Hemker.
- Barabash R. [2001]. X-ray and neutron scattering by different dislocation ensembles. *Materials Science & Engineering A* 309(Special Issue SI), 49-54.
- Barabash R.I., Ice G.E., Larson B.C. and Yang W.G. [2002]. Application of white x-ray microbeams for the analysis of dislocation structures. *Review of Scientific Instruments* 73(3), 1652-4.
- Beams J.W. [1959]. Mechanical properties of thin films of gold and silver, in *Structure and Properties of Thin Films*, eds. C. A. Neugebauer, J. B. Newkirk & D. A. Vermilyea John Wiley and Sons.
- Begley M.R. and Ambrico J.M. [2003]. Channel cracking during thermal cycling of thin film multi-layers. *International Journal of Fracture* 119(4-vol.120), 325-38.
- Begley M.R. and Bart-Smith H. [2005]. The electro-mechanical response of highly compliant substrates and thin stiff films with periodic cracks. *International Journal of Solids & Structures* 42(18-19), 5259-73.

- Begley M.R., Bart-Smith H., Scott O.N., Jones M.H. and Reed M.L. [2005]. The electro-mechanical response of elastomer membranes coated with ultra-thin metal electrodes. *Journal of the Mechanics & Physics of Solids* 53(11), 2557-78.
- Besser P.R., Brennan S. and Bravman J.C. [1994]. An X-ray method for direct determination of the strain state and strain relaxation in micron-scale passivated metallization lines during thermal cycling. *Journal of Materials Research* 9(1), 13-24.
- Beuth J.L., Jr. [1992]. Cracking of thin bonded films in residual tension. *International Journal of Solids and Structures* 29(13), 1657-75.
- Beuth J.L. and Klingbeil N.W. [1996]. Cracking of Thin Films Bonded to Elastic-Plastic Substrates. *Journal of the Mechanics & Physics of Solids* 44(9), 1411-28.
- Birringier R., Hahn H., Hofler H., Karch J. and Gleiter H. [1988]. Diffusion and low temperature deformation by diffusional creep of nanocrystalline materials. *Diffusion and Defect Data - Solid State Data, Part A (Defect and Diffusion Forum)* A59, 17-31.
- Böhm J. [2004]. In situ tensile testing at the limits of X-ray diffraction - A new synchrotron-based technique, PhD Thesis: University of Stuttgart, Stuttgart, Germany.
- Böhm J., Gruber P., Spolenak R., Stierle A., Wanner A. and Arzt E. [2004]. Tensile testing of ultrathin polycrystalline films: a synchrotron-based technique. *Review of Scientific Instruments* 75(4), 1110-19.
- Bonderover E. and Wagner S. [2004]. A woven inverter circuit for e-textile applications. *IEEE Electron Device Letters* 25(5), 295-7.
- Brantley W.A. [1973]. Calculated elastic constants for stress problems associated with semiconductor devices. *Journal of Applied Physics* 44(1), 534-5.
- Brotzen F.R. [1994]. Mechanical testing of thin films. *International Materials Reviews* 39(1), 24-45.
- Brotzen F.R., Rosenmayer C.T., Cofer C.G. and Gale R.J. [1990]. Creep of thin metallic films. *Vacuum* 41(4-6), 1287-90.
- Chen Y., Au J., Kazlas P., Ritenour A., Gates H. and McCreary M. [2003a]. Flexible active-matrix electronic ink display. *Nature* 423, 136.
- Chen M., Ma E., Hemker K.J., Sheng H., Wang Y. and Cheng X. [2003b]. Deformation twinning in nanocrystalline aluminium. *Science* 300(5623), 1275-7.
- Chen Z. and Gan Z.H. [2007]. Fracture toughness measurement of thin films on compliant substrate using controlled buckling test. *Thin Solid Films* 515(6), 3305-9.
- Cieslar M., Oliva V., Karimi A. and Martin J.L. [2004]. Plasticity of thin Al films as a function of temperature. *Materials Science & Engineering A* 387-389, 734-7.
- Comiskey B., Albert J.D., Yoshizawa H. and Jacobson J. [1998]. An electrophoretic ink for all-printed reflective electronic displays. *Nature* 394, 253-5.

- Daymond M.R. and Withers P.J. [1996]. A synchrotron radiation study of transient internal strain changes during the early stages of thermal cycling in an Al/SiCW MMC. *Scripta Materialia* 35(10), 1229-34.
- Dehm G. and Arzt E. [2000]. In situ transmission electron microscopy study of dislocations in a polycrystalline Cu thin film constrained by a substrate. *Applied Physics Letters* 77(8), 1126-8.
- Dehm G., Balk T.J., Edongue H. and Arzt E. [2003]. Small-scale plasticity in thin Cu and Al films. *Microelectronic Engineering* 70, 412-24.
- Dehm G., Balk T.J., von Blanckenhagen B., Gumbsch P. and Arzt E. [2002a]. Dislocation dynamics in sub-micron confinement: recent progress in Cu thin film plasticity. *Zeitschrift fur Metallkunde* 93(5), 383-91.
- Dehm G., Wagner T., Balk T.J., Arzt E. and Inkson B.J. [2002b]. Plasticity and interfacial dislocation mechanisms in epitaxial and polycrystalline Al films constrained by substrates. *Journal of Materials Science & Technology* 18(2), 113-17.
- Dehm G., Weiss D. and Arzt E. [2001]. In situ transmission electron microscopy study of thermal-stress-induced dislocations in a thin Cu film constrained by a Si substrate. *Materials Science and Engineering A* 309-310, 468-72.
- Derlet P.M. and Van Swygenhoven H. [2002]. The role played by two parallel free surfaces in the deformation mechanism of nanocrystalline metals: a molecular dynamics simulation. *Philosophical Magazine A* 82(1), 1-15.
- Dundurs J. and Bogy D.B. [1969]. Edge-bonded dissimilar orthogonal elastic wedges under normal and shear loading. *Journal of Applied Mechanics* 36(3), 650-2.
- DuPont Materials data sheet No. H-38492-2 for Kapton®, DuPont de Nemours GmbH, Bad Homburg, Germany.
- Emery R., Simons C., Mazin B. and Povirk G.L. [1998]. High temperature tensile behavior of free-standing gold films, in *Thin-Films-Stresses and Mechanical Properties VII. Symposium. Boston, MA*, eds. R. C. Cammarata, M. Nastasi, E. P. Busso & W. C. Oliver.
- Emery R.D. and Povirk G.L. [2003a]. Tensile behavior of free-standing gold films. Part I. Coarse-grained films. *Acta Materialia* 51(7), 2067-78.
- Emery R.D. and Povirk G.L. [2003b]. Tensile behavior of free-standing gold films. Part II. Fine-grained films. *Acta Materialia* 51(7), 2079-87.
- Espinosa H.D., Berbenni S., Panico M. and Schwarz K.W. [2005]. An interpretation of size-scale plasticity in geometrically confined systems. *Proceedings of the National Academy of Sciences of the United States of America* 102(47), 16933-8.
- Espinosa H.D., Panico M., Berbenni S. and Schwarz K.W. [2006]. Discrete dislocation dynamics simulations to interpret plasticity size and surface effects in freestanding FCC thin films. *International Journal of Plasticity* 22(11), 2091-117.

- Faurie D., Renault P.O., Le Bourhis E. and Goudeau P. [2005]. Determination of elastic constants of a fiber-textured gold film by combining synchrotron x-ray diffraction and in situ tensile testing. *Journal of Applied Physics* 98(9), 93511-1-9.
- Flinn P.A. and Chien C. [1990]. X-ray diffraction determination of the effect of various passivations on stress in metal films and patterned lines. *Journal of Applied Physics* 67(6), 2927-31.
- Flinn P.A., Gardner D.S. and Nix W.D. [1987]. Measurement and interpretation of stress in aluminum-based metallization as a function of thermal history. *IEEE Transactions on Electron Devices* ED-34(3), 689-99.
- Freund L.B. [1987]. The stability of a dislocation threading a strained layer on a substrate. *Journal of Applied Mechanics* 54(3), 553-7.
- Friedman L.H. and Chrzan D.C. [1998]. Continuum analysis of dislocation pile-ups: influence of sources. *Philosophical Magazine A* 77(5), 1185-204.
- Froseth A.G., Derlet P.M. and Van Swygenhoven H. [2004]. Dislocations emitted from nanocrystalline grain boundaries: nucleation and splitting distance. *Acta Materialia* 52(20), 5863-70.
- Frost H.J. and Ashby M.F. [1982]. *Deformation-Mechanism Maps: The Plasticity and Creep of Metals and Ceramics*: Pergamon Press.
- Gao H., Zhang L., Nix W.D., Thompson C.V. and Arzt E. [1999]. Crack-like grain-boundary diffusion wedges in thin metal films. *Acta Materialia* 47(10), 2865-78.
- Gelinck G.H., Edzer H., Huitema A., Veenendaal E.V., van Cantatore E., Schrijnemakers L., van der Putten J., Geuns T.C.T., Beenhakkers M., Giesbers J.B., Huisman B.H., Meijer E.J., Benito E.M., Touwslager F.J., Marsman A.W., van Rens B.J.E. and De Leeuw D.M. [2004]. Flexible active-matrix displays and shift registers based on solution-processed organic transistors. *Nature Materials* 3(2), 106-10.
- Gerberich W.W., Nelson J.C., Lilleodden E.T., Anderson P. and Wyrobek J.T. [1996]. Indentation induced dislocation nucleation: the initial yield point. *Acta Materialia* 44(9), 3585-98.
- Gergaud P., Labat S. and Thomas O. [1998]. Limits of validity of the crystallite group method in stress determination of thin film structures. *Thin Solid Films* 319, 9-15.
- Gianola D.S., Van Petegem S., Legros M., Brandstetter S., Van Swygenhoven H. and Hemker K.J. [2006]. Stress-assisted discontinuous grain growth and its effect on the deformation behavior of nanocrystalline aluminum thin films. *Acta Materialia* 54(8), 2253-63.
- Gibbs G.B. [1966]. Diffusion creep of a thin foil. *Philosophical Magazine* 13(123), 589-&.
- Goens E. and Weerts J. [1936]. The main resilience constants of monocrystal of copper, gold and lead. *Physikalische Zeitschrift* 37.
- Greer J.R. and Nix W.D. [2006]. Nanoscale gold pillars strengthened through dislocation starvation. *Physical Review B* 7324(24), 5410.

- Greer J.R., Oliver W.C. and Nix W.D. [2005]. Size dependence of mechanical properties of gold at the micron scale in the absence of strain gradients. *Acta Materialia* 53(6), 1821-30.
- Greer J.R., Oliver W.C. and Nix W.D. [2006]. Corrigendum to "Size dependence in mechanical properties of gold at the micron scale in the absence of strain gradients" [Acta Mater 53 (6) (2005) 1821-1830]. *Acta Materialia* 54(6), 1705.
- Gruber P., Böhm J., Wanner A., Sauter L., Spolenak R. and Arzt E. [2004]. Size Effect on Crack Formation in Cu/Ta and Ta/Cu/Ta Thin Film Systems, in *Nanoscale Materials and Modeling - Relations Among Processing, Microstructure and Mechanical Properties. Symposium. San Francisco, CA*, eds. P. M. Anderson, T. Foecke, A. Misra & R. E. Rudd.
- Gust W., Mayer S., Bogel A. and Predel B. [1985]. Generalized representation of grain-boundary self-diffusion data. *Journal De Physique* 46(NC-4), 537-44.
- Hall E.O. [1951]. The deformation and ageing of mild steel: III Discussion of results. *Proceedings of the Physical Society. Section B* 64, 747-53.
- Han J.H. and Saif M.T.A. [2006]. In situ microtensile stage for electromechanical characterization of nanoscale freestanding films. *Review of Scientific Instruments* 77(4), 45102-1-8.
- Handge U.A. [2002]. Analysis of a shear-lag model with nonlinear elastic stress transfer for sequential cracking of polymer coatings. *Journal of Materials Science* 37(22), 4775-82.
- Handge U.A., Leterrier Y., Rochat G., Sokolov I.M. and Blumen A. [2000]. Two scaling domains in multiple cracking phenomena. *Physical Review E (Statistical Physics, Plasmas, Fluids, and Related Interdisciplinary Topics)* 62(6), 7807-10.
- Haque M.A. and Saif M.T.A. [2002]. Mechanical behavior of 30-50 nm thick aluminum films under uniaxial tension. *Scripta Materialia* 47(12), 863-7.
- Haque M.A. and Saif M.T.A. [2004]. Deformation mechanisms in free-standing nanoscale thin films: A quantitative in situ transmission electron microscope study. *Proceedings of the National Academy of Sciences of the United States of America* 101(17), 6335-40.
- Haque M.A. and Saif M.T.A. [2005a]. Thermo-mechanical properties of nano-scale freestanding aluminum films. *Thin Solid Films* 484(1-2), 364-8.
- Haque M.A. and Saif M.T.A. [2005b]. In situ tensile testing of nanoscale freestanding thin films inside a transmission electron microscope. *Journal of Materials Research* 20(7), 1769-77.
- HD Microsystems. Manufacturers data sheet of PI2611 type polyimide, HD MicroSystems Ltd.
- Heinrich M., Gruber P., Orso S., Handge U.A. and Spolenak R. [2006]. Dimensional control of brittle nanoplatelets. A statistical analysis of a thin film cracking approach. *Nano Letters* 6(9), 2026-30.

- Hertzberg R.W. [1989]. *Deformation and Fracture Mechanics of Engineering Materials*: John Wiley & Sons, Inc.
- Hirth J.P. and Lothe J. [1992]. *Theory of Dislocations*, Malabar, UK: Krieger Publishing.
- Hommel M. and Kraft O. [2001]. Deformation behavior of thin copper films on deformable substrates. *Acta Materialia* 49(19), 3935-47.
- Hommel M., Kraft O. and Arzt E. [1999]. A new method to study cyclic deformation of thin films in tension and compression. *Journal of Materials Research* 14(6), 2373-6.
- Horvath J., Birringer R. and Gleiter H. [1987]. Diffusion in nanocrystalline material. *Solid State Communications* 62(5), 319-22.
- Hsia K.J., Suo Z. and Yang W. [1994]. Cleavage due to dislocation confinement in layered materials. *Journal of the Mechanics and Physics of Solids* 42(6), 877-96.
- Hu M.S. and Evans A.G. [1989]. The cracking and decohesion of thin films on ductile substrates. *Acta Metallurgica* 37(3), 917-25.
- Huang H. and Spaepen F. [2000]. Tensile testing of free-standing Cu, Ag and Al thin films and Ag/Cu multilayers. *Acta Materialia* 48(12), 3261-9.
- Hyde B., Espinosa H.D. and Farkas D. [2005]. An atomistic investigation of elastic and plastic properties of Au nanowires. *Jom* 57(9), 62-6.
- Hyun S., Brown W.L. and Vinci R.P. [2003]. Thickness and temperature dependence of stress relaxation in nanoscale aluminum films. *Applied Physics Letters* 83(21), 4411-3.
- IBM [2005]. <http://www-03.ibm.com/press/us/en/photos/.wss?topic=6>, IBM Corporation, USA.
- ITRS [2003]. The International Technology Roadmap for Semiconductors, Lithography, in *2003 Edition International Technology Roadmap for Semiconductors*.
- Jansson N.E., Leterrier Y. and Manson J.A.E. [2006a]. Modeling of multiple cracking and decohesion of a thin film on a polymer substrate. *Engineering Fracture Mechanics* 73(17), 2614-26.
- Jansson N.E., Leterrier Y., Medico L. and Manson J.A.E. [2006b]. Calculation of adhesive and cohesive fracture toughness of a thin brittle coating on a polymer substrate. *Thin Solid Films* 515(4), 2097-105.
- Kalkman A.J., Verbruggen A.H. and Janssen G. [2003]. High-temperature bulge-test setup for mechanical testing of free-standing thin films. *Review of Scientific Instruments* 74(3), 1383-5.
- Kang Y.S., Ho P.S., Knipe R. and Tregilgas J. [1997]. Film thickness effect on tensile properties and microstructures of submicron aluminum thin films on polyimide, in *Thin Films: Stresses and Mechanical Properties VI. Symposium. San Francisco, CA*, eds. W. W. Gerberich, H. Gao, J. E. Sundgren & S. P. Baker.

- Keller R., Baker S.P. and Arzt E. [1998]. Quantitative analysis of strengthening mechanisms in thin Cu films: effects of film thickness, grain size, and passivation. *Journal of Materials Research* 13(5), 1307-17.
- Kobrinisky M.J., Dehm G., Thompson C.V. and Arzt E. [2001]. Effects of thickness on the characteristic length scale of dislocation plasticity in Ag thin films. *Acta Materialia* 49(17), 3597-607.
- Kobrinisky M.J. and Thompson C.V. [1998]. The thickness dependence of the flow stress of capped and uncapped polycrystalline Ag thin films. *Applied Physics Letters* 73(17), 2429-31.
- Kobrinisky M.J. and Thompson C.V. [2000]. Activation volume for inelastic deformation in polycrystalline Ag thin films. *Acta Materialia* 48(3), 625-33.
- Kraft O., Freund L.B., Phillips R. and Arzt E. [2002]. Dislocation plasticity in thin metal films. *MRS Bulletin* 27(1), 30-7.
- Kraft O., Hommel M. and Arzt E. [2000]. X-ray diffraction as a tool to study the mechanical behaviour of thin films. *Materials Science and Engineering A* 288, 209-16.
- Kraft O. and Volkert C.A. [2001]. Mechanical testing of thin films and small structures. *Advanced Engineering Materials* 3(3), 99-110.
- Kretschmann A., Kuschke W.M., Baker S.P. and Arzt E. [1997]. Plastic deformation in thin copper films determined by X-ray micro-tensile tests, in *Thin Films: Stresses and Mechanical Properties VI. Symposium. San Francisco, CA*, eds. W. W. Gerberich, H. Gao, J. E. Sundgren & S. P. Baker.
- Kumar K.S., Suresh S., Chisholm M.F., Horton J.A. and Wang P. [2003]. Deformation of electrodeposited nanocrystalline nickel. *Acta Materialia* 51(2), 387-405.
- Kuschke W.M. and Arzt E. [1994]. Investigation of the stresses in continuous thin films and patterned lines by X-ray diffraction. *Applied Physics Letters* 64(9), 1097-9.
- Legros M., Dehm G. and Balk T.J. [2005]. In-situ TEM study of plastic stress relaxation mechanisms and interface effects in metallic films, in *Thin Films-Stresses and Mechanical Properties XI. Symposium. San Francisco, CA*, eds. T. E. Buchheit, A. M. Minor, R. Spolenak & K. Takashima.
- Legros M., Dehm G., Balk T.J., Arzt E., Bostrom O., Gergaud P., Thomas O. and Kaouache B. [2003]. Plasticity-related phenomena in metallic films on substrates, in *Multiscale Phenomena in Materials - Experiments and Modeling Related to Mechanical Behavior. Symposium. San Francisco, CA*, eds. H. M. Zbib, D. H. Lassila, L. E. Levine & K. J. Hemker.
- Legros M., Elliott B.R., Rittner M.N., Weertman J.R. and Hemker K.J. [2000]. Microsample tensile testing of nanocrystalline metals. *Philosophical Magazine A* 80(4), 1017-26.
- Leoni M., Welzel U., Lamparter P., Mittemeijer E.J. and Kamminga J.D. [2001]. Diffraction analysis of internal strain-stress fields in textured, transversely isotropic thin films: theoretical basis and simulation. *Philosophical Magazine A* 81(3), 597-623.

- Leterrier Y., Boogh L., Andersons J. and Manson J.A. [1997a]. Adhesion of silicon oxide layers on poly(ethylene terephthalate). I. Effect of substrate properties on coating's fragmentation process. *Journal of Polymer Science, Part B (Polymer Physics)* 35(9), 1449-61.
- Leterrier Y., Andersons J., Pitton Y. and Manson J.A. [1997b]. Adhesion of silicon oxide layers on poly(ethylene terephthalate). II. Effect of coating thickness on adhesive and cohesive strengths. *Journal of Polymer Science, Part B (Polymer Physics)* 35(9), 1463-72.
- Li T., Huang Z.Y., Suo Z., Lacour S.P. and Wagner S. [2004]. Stretchability of thin metal films on elastomer substrates. *Applied Physics Letters* 85(16), 3435-7.
- Li T., Huang Z.Y., Xi Z.C., Lacour S.P., Wagner S. and Suo Z. [2005]. Delocalizing strain in a thin metal film on a polymer substrate. *Mechanics of Materials* 37(2-3), 261-73.
- Li T. and Suo Z. [2006]. Deformability of thin metal films on elastomer substrates. *International Journal of Solids & Structures* 43(7-8), 2351-63.
- Lucas B.N. and Oliver W.C. [1999]. Indentation power-law creep of high-purity indium. *Metallurgical and Materials Transactions A* 30(3), 601-10.
- Maass R., Grolimund D., Van Petegem S., Willmann M., Jensen M., Van Swygenhoven H., Lehnert T., Gijs M.A.M., Volkert C.A., Lilleodden E.T. and Schwaiger R. [2006]. Defect structure in micropillars using x-ray microdiffraction. *Applied Physics Letters* 89(15), 151905-1-3.
- Macionczyk F., Bruckner W. and Reiss G. [1998]. Stress-strain curves by tensile testing of thin metallic films on thin polyimide foils: Al, AlCu, CuNi(Mn), in *Thin-Films-Stresses and Mechanical Properties VII. Symposium. Boston, MA*, eds. R. C. Cammarata, M. Nastasi, E. P. Busso & W. C. Oliver.
- Martin S.J., Godschalx J.P., Mills M.E., Shaffer E.O., II and Townsend P.H. [2000]. Development of a low-dielectric-constant polymer for the fabrication of integrated circuit interconnect. *Advanced Materials* 12(23), 1769-78.
- McElhaney K.W., Vlassak J.J. and Nix W.D. [1998]. Determination of indenter tip geometry and indentation contact area for depth-sensing indentation experiments. *Journal of Materials Research* 13(5), 1300-6.
- MCS [2006]. <http://www.multichannelsystems.com/products/meaprobes/meatypes/meatypes/flexmeas.htm>, MCS Multi Channel Systems GmbH, Reutlingen, Germany.
- Meyer J.U. [2002]. Retina implant - a bioMEMS challenge. *Elsevier, Sensors and Actuators A* 97-98, 1-9.
- Moody N.R., Medlin D., Boehme D. and Norwood D.P. [1998]. Film thickness effects on the fracture of tantalum nitride on aluminum nitride thin film systems. *Engineering Fracture Mechanics* 61, 107-18.
- Morgen M., Ryan E.T., Jie-Hua Z., Chuan H., Taiheui C. and Ho P.S. [1999]. Low dielectric constant materials for advanced interconnects. *Jom* 51(9), 37-40.

- Moser B., Kuebler J., Meinhard H., Muster W. and Michler J. [2005]. Observation of instabilities during plastic deformation by in-situ SEM indentation experiments. *Advanced Engineering Materials* 7(5), 388-92.
- Moske M. and Samwer K. [1988]. New UHV dilatometer for precise measurement of internal stresses in thin binary-alloy films from 20 to 750 K. *Review of Scientific Instruments* 59(9), 2012-17.
- Motz C., Schoberl T. and Pippan R. [2005]. Mechanical properties of micro-sized copper bending beams machined by the focused ion beam technique. *Acta Materialia* 53(15), 4269-79.
- Mullins W.W. [1958]. The effect of thermal grooving on grain boundary motion. *Acta Metallurgica* 6(6), 414-27.
- Needleman A., Nicola L., Xiang Y., Vlassak J.J. and Van der Giessen E. [2006]. Plastic deformation of freestanding thin films: Experiments and modeling. *Journal of the Mechanics and Physics of Solids* 54(10), 2089-110.
- Nicola L., Van der Giessen E. and Needleman A. [2003]. Discrete dislocation analysis of size effects in thin films. *Journal of Applied Physics* 93(10), 5920-8.
- Nix W.D. [1989]. Mechanical properties of thin films. *Metallurgical Transactions A* 20(11), 2217-45.
- Nix W.D. [1998]. Yielding and strain hardening of thin metal films on substrates. *Scripta Materialia* 39(4/5), 545-54.
- Noyan I.C. and Cohen J.B. [1987]. *Residual Stress: Measurement by Diffraction and Interpretation*: Springer.
- Noyan I.C. and Sheikh G. [1993]. X-ray tensile testing of thin films. *Journal of Materials Research* 8(4), 764-70.
- Oh S.H., Legros M., Kiener D., Gruber P. and Dehm G. [2007]. In situ TEM straining of single crystal Au films on polyimide: Thickness dependent deformation mechanism. *submitted to Acta Materialia*.
- Oliver W.C. and Pharr G.M. [1992]. An improved technique for determining hardness and elastic modulus using load and displacement sensing indentation experiments. *Journal of Materials Research* 7(6), 1564-83.
- Pant P., Schwarz K.W. and Baker S.P. [2003]. Dislocation interactions in thin FCC metal films. *Acta Materialia* 51(11), 3243-58.
- Petch N.J. [1953]. The cleavage strength of polycrystals. *Journal of the Iron and Steel Institute* 174(1), 25-8.
- PolymerVision [2005]. <http://www.polymervision.com/assets/downloadablefile/display2-12955.jpg>, Polymer Vision, Eindhoven, Netherlands.
- Post E.R., Orth M., Russo P.R. and Gershenfeld N. [2000]. E-broidery: design and fabrication of textile-based computing. *IBM Systems Journal* 39(3-4), 840-60.

- Rabe R., Breguet J.M., Schwaller P., Stauss S., Haug F.J., Patscheider J. and Michler J. [2004]. Observation of fracture and plastic deformation during indentation and scratching inside the scanning electron microscope. *Thin Solid Films* 469-470, 206-13.
- Raj R. and Ashby M.F. [1971]. On grain boundary sliding and diffusional creep. *Metallurgical Transactions* 2, 1113-27.
- Read D.T. [1998]. Tension-tension fatigue of copper thin films. *International Journal of Fatigue* 20(3), 203-9.
- Read D.T., Cheng Y.W., Keller R.R. and McColskey J.D. [2001]. Tensile properties of free-standing aluminum thin films. *Scripta Materialia* 45(5), 583-9.
- Read D.T. and Dally J.W. [1993]. A new method for measuring the strength and ductility of thin films. *Journal of Materials Research* 8(7), 1542-9.
- Reid T.R. [1984]. *The Chip*, New York: Simon & Shuster.
- Renault P.O., Badwai K.F., Bimbault L., Goudeau P., Elkaim E. and Lauriat J.P. [1998]. Poisson's ratio measurement in tungsten thin films combining an X-ray diffractometer with in situ tensile tester. *Applied Physics Letters* 73(14), 1952-4.
- Renault P.O., Villain P., Coupeau C., Goudeau P. and Badawi K.F. [2003]. Damage mode tensile testing of thin gold films on polyimide substrates by X-ray diffraction and atomic force microscopy. *Thin Solid Films* 242(2), 267-73.
- Rochat G., Leterrier Y., Fayet P. and Manson J.A.E. [2003]. Mechanical analysis of ultrathin oxide coatings on polymer substrates in situ in a scanning electron microscope. *Thin Solid Films* 437(1-2), 204-10.
- Rosenberg R., Edelstein D.C., Hu C.-K. and K.P. R. [2000]. Copper Metallization for High Performance Silicon Technology. *Annual Review of Materials Science* 30, 229-62.
- Ruud J.A., Josell D., Spaepen F. and Greer A.L. [1993]. A new method for tensile testing of thin films. *Journal of Materials Research* 8(1), 112-17.
- Sauter L. [2006]. Microstructural and film thickness effects on the thermomechanical behavior of thin Au films, PhD Thesis: University of Stuttgart, Stuttgart, Germany.
- Schadler L. and Noyan I.C. [1995]. Quantitative measurement of the stress transfer function in nickel/polyimide thin film/copper thin film structures. *Applied Physics Letters* 66(1), 22-4.
- Schiotz J., Di Tolla F.D. and Jacobsen K.W. [1998]. Softening of nanocrystalline metals at very small grain sizes. *Nature* 391, 561-3.
- Sharpe W.N. [2003]. Murray lecture - Tensile testing at the micrometer scale: Opportunities in experimental mechanics. *Experimental Mechanics* 43(3), 228-37.
- Sharpe W.N., Jr. and Hemker K.J. [2002]. Mechanical testing of free-standing thin films, in *Surface Engineering 2001 - Fundamentals and Applications. Symposium . Boston, MA*, eds. M. Wen Jin, A. Kemar, G. L. Doll, Y. T. Cheng, S. Veprék & T. W. Chung.

- Stett A., Egert U., Guenther E., Hofmann F., Meyer T., Nisch W. and Haemmerle H. [2003]. Biological application of microelectrode arrays in drug discovery and basic research. *Analytical and Bioanalytical Chemistry* 377, 486-95.
- Tamura N., MacDowell A.A., Spolenak R., Valek B.C., Bravman J.C., Brown W.L., Celestre R.S., Padmore H.A., Batterman B.W. and Patel J.R. [2003]. Scanning X-ray microdiffraction with submicrometer white beam for strain/stress and orientation mapping in thin films. *Journal of Synchrotron Radiation* 10, 137-43.
- Thompson C.V. [1993]. The yield stress of polycrystalline thin films. *Journal of Materials Research* 8(2), 237-8.
- Thouless M.D. [1993]. Effect of surface diffusion on the creep of thin films and sintered arrays of particles. *Acta Metallurgica et Materialia* 41(4), 1057-64.
- Timoshenko S. and Woinowski-Krieger S. [1959]. *Theory of Plates and Shells*: McGraw-Hill.
- Tregilgas J.H. and Strumpell M. [1998]. Tensile testing of ultra-thin-film materials deposited on polyimide for MEMS applications, in *Microelectromechanical Structures for Materials Research. Symposium*. San Francisco, CA, eds. S. Brown, J. Gilbert, H. Guckel, R. Howe, G. Johnson, P. Krulevitch & C. Muhlstein.
- Uchic M.D. and Dimiduk D.M. [2005]. A methodology to investigate size scale effects in crystalline plasticity using uniaxial compression testing. *Materials Science & Engineering A* 400-401, 268-78.
- Van Swygenhoven H., Derlet P.M. and Froseth A.G. [2006]. Nucleation and propagation of dislocations in nanocrystalline fcc metals. *Acta Materialia* 54(7), 1975-83.
- Van Swygenhoven H. and Weertman J.R. [2006]. Deformation in nanocrystalline metals. *Materials Today* 9(5), 24-31.
- Venkatraman R. and Bravman J.C. [1992]. Separation of film thickness and grain boundary strengthening effects in Al thin films on Si. *Journal of Materials Research* 7(8), 2040-8.
- Vinci R.P., Zielinski E.M. and Bravman J.C. [1995]. Thermal strain and stress in copper thin films. *Thin Solid Films* 262(1-2), 142-53.
- Vlassak J.J. [2003]. Channel cracking in thin films on substrates of finite thickness. *International Journal of Fracture* 119(4-vol.120), 299-323.
- Vlassak J.J. and Nix W.D. [1992]. A new bulge test technique for the determination of Young's modulus and Poisson's ratio of thin films. *Journal of Materials Research* 7(12), 3242-9.
- Vlassak J.J. and Xiang Y. [2006]. Bauschinger and size effects in thin-film plasticity. *Acta Materialia* 54(20), 5449-60.
- Volkert C.A. and Lilleodden E.T. [2006]. Size effects in the deformation of sub-micron Au columns. *Philosophical Magazine* 86(33-35), 5567-79.

- von Blanckenhagen B. [2002]. Versetzungen in dünnen Metallschichten, PhD Thesis: University of Stuttgart, Stuttgart, Germany.
- von Blanckenhagen B., Arzt E. and Gumbsch P. [2004]. Discrete dislocation simulation of plastic deformation in metal thin films. *Acta Materialia* 52(3), 773-84.
- von Blanckenhagen B., Gumbsch P. and Arzt E. [2001]. Dislocation sources in discrete dislocation simulations of thin-film plasticity and the Hall-Petch relation. *Modelling and Simulation in Materials Science and Engineering* 9(3), 157-69.
- von Blanckenhagen B., Gumbsch P. and Arzt E. [2003]. Dislocation sources and the flow stress of polycrystalline thin metal films. *Philosophical Magazine Letters* 83(1), 1-8.
- Wagner S., Lacour S.P., Jones J., Hsu P.H.I., Sturm J.C., Li T. and Suo Z.G. [2004]. Electronic skin: architecture and components. *Physica E* 25(2-3), 326-34.
- Wanner A. and Dunand D.C. [2000]. Synchrotron X-ray study of bulk lattice strains in externally loaded Cu-Mo composites. *Metallurgical and Materials Transactions A* 31(11), 2949-62.
- Weiss D. [2000]. Deformation Mechanisms in Pure and Alloyed Copper Films, PhD Thesis: University of Stuttgart, Stuttgart, Germany.
- Weiss D., Gao H. and Arzt E. [2001]. Constrained diffusional creep in UHV-produced copper thin films. *Acta Materialia* 49(13), 2395-403.
- Wellner P., Kraft O., Dehm G., Andersons J. and Arzt E. [2004]. Channel cracking of β -NiAl thin films on Si substrates. *Acta Materialia* 52(8), 2325-36.
- Welzel U., Leoni M. and Mittemeijer E.J. [2003]. The determination of stresses in thin films; modelling elastic grain interaction. *Philosophical Magazine* 83(5), 603-30.
- Welzel U., Ligot J., Lamparter P., Vermeulen A.C. and Mittemeijer E.J. [2005]. Stress analysis of polycrystalline thin films and surface regions by X-ray diffraction. *Journal of Applied Crystallography* 38, 1-29.
- Würschum R., Herth S. and Brossmann U. [2003]. Diffusion in nanocrystalline metals and alloys—a status report. *Advanced Engineering Materials* 5(5), 365-72.
- Xia Z.C. and Hutchinson J.W. [2000]. Crack patterns in thin films. *Journal of the Mechanics and Physics of Solids* 48(6-7), 1107-31.
- Xiang Y., Chen X. and Vlassak J.J. [2005a]. Plane-strain bulge test for thin films. *Journal of Materials Research* 20(9), 2360-70.
- Xiang Y., Li T., Suo Z.G. and Vlassak J.J. [2005b]. High ductility of a metal film adherent on a polymer substrate. *Applied Physics Letters* 87(16), 61910.
- Yamakov V., Wolf D., Phillpot S.R., Mukherjee A.K. and Gleiter H. [2002]. Dislocation processes in the deformation of nanocrystalline aluminium by molecular-dynamics simulation. *Nature Materials* 1(1), 45-8.

- Yu D.Y.W. and Spaepen F. [2004]. The yield strength of thin copper films on kapton. *Journal of Applied Physics* 95(6), 2991-7.
- Zhang S., Sun D., Fu Y.Q. and Du H.J. [2005]. Toughness measurement of thin films: a critical review. *Surface & Coatings Technology* 198(1-3), 74-84.